THE UNIVERSITY *of* EDINBURGH

Coda wave interferometry and relative source location

Youqian Zhao

THE UNIVERSITY *of* EDINBURGH

Thesis submitted for the degree of
Doctor of Philosophy

University of Edinburgh
School of Geosciences

Year of Submission 2019

Abstract

A wide range of applications requires relative locations of sources of energy to be known accurately. Most conventional location methods are either subject to errors that depend strongly on inaccuracy in the model of propagation velocity used, or demand a well-distributed network of surrounding seismic stations in order to produce reliable results. A source location method based on coda wave interferometry (CWI) is relatively insensitive to the number of seismic stations and to the source-to-station azimuthal coverage. It therefore opens new avenues for research, for applications in areas with unfavourable recording geometries, and for applications which require a complementary method.

CWI uses scattered waves in the coda of seismograms to estimate the small differences between two seismic states, and currently has three types of applications: estimating bulk velocity change of the medium, scatterer displacement, and source location perturbation. When used for source location, CWI is used to estimate the distances between pairs of sources with similar mechanism (equivalent to estimating location perturbation of the same source), which are then used jointly to determine the relative location of a cluster of sources using a probabilistic framework as an optimization problem. However, estimating source separation is a relatively new type of application of CWI. In the first part of this thesis, the performance of CWI is tested in models with varying complexities and types: from point-scatterer media as assumed in the CWI theory, to layered media as in classic Earth models, to media with combinations of point-scatters and layers, and finally to the more realistic Marmousi model. This thesis also presents the first elastic case of testing CWI to estimate source separation in synthetic experiments. The study contributes to better understand and interpret the source separation estimates and therefore relative locations using CWI.

The second part of this thesis validates the location algorithm with synthetic data. When applied to real seismic data, the algorithm is found to suffer from the impact of large difference in the dominant wavelength of recordings made on different instruments. This thesis introduces a new formulation for the optimization problem to account for data from multiple station channels. In addition, it proposes a way to standardize the selection of parameters when implementing the method. The

algorithm is applied to a micro-seismic dataset of mining induced events recorded in Nottinghamshire, England. The earthquake location results are highly consistent when using different individual seismometer channels, showing that it is possible to locate event clusters with a single-channel seismometer. These microseismic events have shorter distinguishable codas in recorded waveforms, and hence fewer recorded scattered waves than those that have been used to test this method previously. Thus, the potential applications of this cost-effective method are extended to seismic events over a wider range of magnitudes.

Given the advantages of this location method, it has been applied only once in literature other than in this thesis. It is likely that one reason that it is not used more widely is the lack of reliable code that implements this multistage method. This thesis develops a well-commented MATLAB code called *CWIcluster* that does so, accompanied by a clear and thorough user manual. It implements the location method in three stages: classifying events into clusters, computing inter-source separations using CWI, and estimating their relative locations. Each stage can be implemented in an automated sense given criteria chosen by the user. It is shown that the location algorithm is able to correct bias (underestimation) in the CWI separation estimates to some extent.

The third part of this thesis returns to the three basic types of applications of CWI. Standard CWI methods require an assumption that a single type of perturbation has taken place in the system (as do most other methods that measure changes in a seismic system). However, in reality more than one type of perturbation can occur simultaneously. This thesis proposes a general treatment to account for multiple types of perturbations, allowing each type to be recognized and estimated with the effects of others being compensated. The appendices include a co-authored submitted paper that examines the influence of velocity change and source location perturbation on one another in the context of a rock-physics laboratory.

Overall this thesis intensively tests the relatively new method of coda wave interferometry to estimate inter-source separations in various environments, and explores its potential to detect multiple types of perturbations that have occurred simultaneously, thus extending our understanding of the set of CWI methods in general. In addition, it validates the relative location method based on CWI and provides ways to improve the original method, as well as a way to assess the quality of results when applied to real data. Finally, it presents a new freely-available code package to implement the location method, which the authors hope will introduce this method more widely in both academia and industry.

Lay summary

Finding accurate locations of seismic sources is essential for a wide range of seismological, industrial and other applications. Examples include discriminating earthquake fault and auxiliary planes from the sequences of aftershocks or foreshocks, studying earthquake interaction and recurrence, modeling earthquake hazards, and monitoring seismic activity during and after geothermal projects and hydraulic fracturing. Conventional methods for estimating relative locations of seismic events that use the first arrivals of seismograms usually demand a well-distributed seismic station network. Their performance deteriorates where a sufficient number of seismic stations with a good source-to-receiver azimuthal coverage is unavailable.

An alternative location method that uses a different part of seismograms, the coda, does not have such demands. Coda is the later part of a seismogram and is generated by scatterered waves. It is discarded in many seismological applications due to its complex appearance with few uniquely identifiable arrivals. In fact, usually these waves have travelled a large area during propagation, hence contain more information than the direct wave (first arrival of seismograms). Coda wave interferometry (CWI) can extract the location constraints of a cluster of events using the coda of seismograms and solve for their relative locations in a probabilistic framework. It has been shown to be able to locate a cluster of earthquakes with a single seismic station.

In this thesis I show a second case of application of this novel location method. The data I use are recorded from microearthquakes that have shorter distinguishable coda in their waveforms than those used previously. Thus, the potential applications of this non-demanding method are extended to seismic events over a wider range of magnitudes. Despite the advantages of this method, the uptake in its use has been

limited to two papers in the literature (one is Chapter 4 of this thesis). In part this may be because the algorithm requires unfamiliar methods which are not painless to program. In this thesis I develop a well-commented and easily editable MATLAB code package that implements this multistage method in an automated sense, accompanied by a clear and thorough user manual.

I also test this method in a series of numerical experiments in media of various types and complexities, which contributes to better understanding and interpretation of results of this method when applied to real data.

Estimating constraints on locations of two sources is equivalent to estimating the displacement of one source whose location is changed to another position. Except for estimating change in source location, CWI can also be used to estimate small changes in velocity and scatterer locations in the propagating medium. The standard CWI methods require an assumption that a single type of perturbation (source location, velocity or scatter locations) has taken place in the system, which is not necessarily the case in reality. I provide a treatment that does not require this assumption, which accounts for multiple types of perturbations, allowing each type to be recognized and estimated with the effects of others being compensated.

Acknowledgement

First and foremost, I would like to thank my supervisor Prof. Andrew Curtis, for giving me the opportunity to undertake this project and to work with him. Without his invaluable guidance and encouragement throughout my PhD, I would never have gone this far with my work and been presenting this thesis. From working with him, I have also learnt so much beyond doing research – constant excellence, genuine curiosity and kindness, all of which I would like to pack with me for future adventures.

Thanks also goes to my supervisor Dr. Giovanni Meles, who has generously helped me with mathematics and programming in the early stage, which is crucial in the realization of the core algorithm used in this project. I also thank my supervisor Dr. Brian Baptie, who provided me with the data to test the algorithm, and gave me the chance to work in the adorable British Geological Survey (BGS) building in my second year.

I would also like to acknowledge the University of Edinburgh and BGS for their funding for my research.

I would like to express my deepest gratitude to my parents, who always give me the freedom to make my own decisions in life (even when I was a kid, or a teenager!), and selflessly support me on anything I choose to do. It is their encouragement and constant faith in me that made me believe that I CAN follow my dreams.

Last but not least, I would like to say thank you to my husband Jacques, who has given me immense support along this journey, who has helped me grow as a person, who I have experienced so many ups and downs during these years with that I cannot value more.

Declaration

I declare that this thesis had been composed solely by myself and that it has not been submitted, either in whole or in part, in any previous application for a degree. Except where otherwise acknowledged, the work presented is entirely my own.

Youqian Zhao

Contents

List of Figures

List of Figures

the travel-time changes $\sigma_\tau{}^2$ of each time-window, the solid line (black) shows the least-square fit, and dashed line marks the level of the y-intercept of the fit.

Figure 6-26: Estimated velocity change using CWI in a medium with 600 point-scatterers. The dots and bars show the means and standard deviations of estimates over the six sources obtained from individual receivers; the solid line and the shade show the mean and standard deviations of the estimates over all receivers; and the dashed line shows the true velocity change.

List of Tables

1

Introduction

1.1 Previous study on coda

In highly heterogeneous media, seismic waveforms consist of directly arriving phases followed by a long train of chaotic-looking signals. These late arrivals constitute the *coda* of the waveform. The coda is dominated by waves that have been scattered by the heterogeneities in the medium single or multiple times. Figure 1-1a shows a modeled waveform that contains a direct arrival, a wave travelling directly from the source to the receiver. The waveform in Figure 1-1b contains a direct arrival, and subsequent arrivals with much lower amplitude, which should result mainly from single scattering at the modeled point scatterers due to their low amplitude and a limited time length. Figure 1-1c shows a waveform of a microearthquake recorded in New Ollerton, England. The direct P- and S-arrivals can be identified easily, and the subsequent arrivals whose amplitude decays gradually with time should mainly be generated by multiple scatterering in the medium. In most seismological applications, such as reflection and refraction seismology, the coda is discarded due to the complexity in its analysis. However, the coda contains information independent of that provided by early arrivals, in that coda waves travel in a larger region in the medium than direct or early arriving waves, hence have the potential to be used either individually in processing or as a complement to first arrivals and primaries (waves that have been reflected upward once).

The idea of studying seismic coda germinated in the late 1960s, when Aki (1969) analyzed coda waves of small local earthquakes. He suggested that the coda waves are backscattered waves from a multitude of randomly-distributed heterogeneities in the subsurface, and the energy contained in coda waves of a local earthquake is a function of time measured from the origin of the earthquake. Specifically, the later a wave is recorded, the greater the number of scatterers it encounters. He proposed that

the late portions of a waveform could be considered as an averaging effect over numerous samples of the heterogeneities in the medium, hence could be treated in a statistical model, wherein the properties of the medium are characterized with a small number of statistical parameters (Aki, 1969; Aki & Chouet, 1975). The statistical treatment inspired other authors like Chouet (1976) who validated Aki's statistical model with observational data. Their works laid the foundation of many subsequent studies that apply modeling techniques such as Finite Difference (Frankel & Clayton 1986; Stam 1995) and Foldy methods (Kelner et al. 1999; Snieder et al. 2002; Lombaert at el. 2007) to model the Earth's subsurface to generate scattered waveforms.

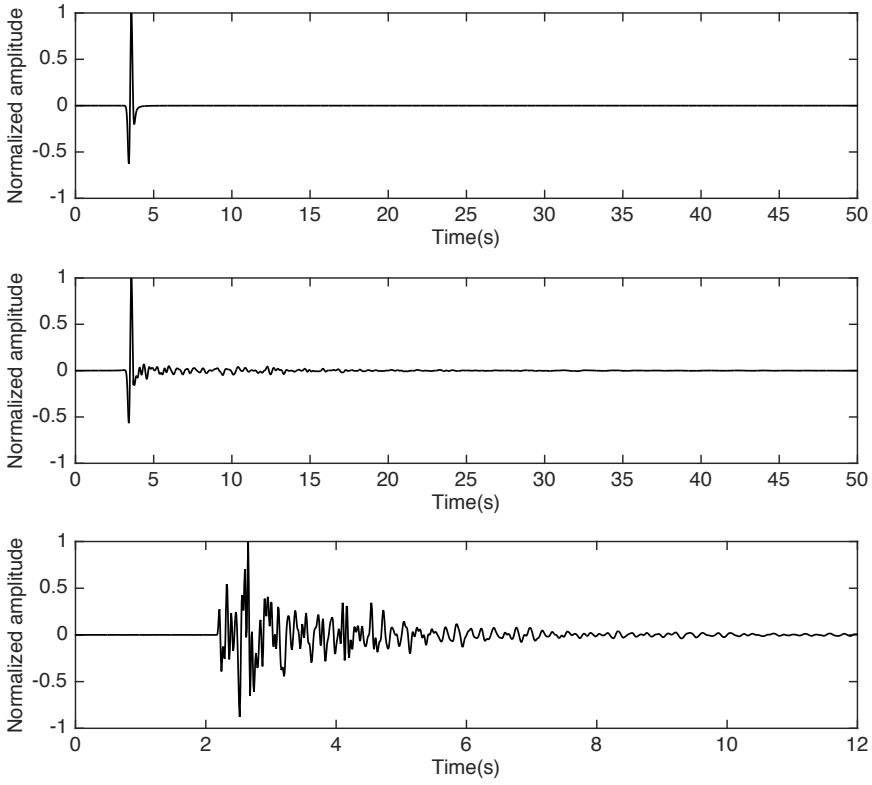

Figure 1-1: Demonstration of direct arrival (panel a), single scattered arrivals (panel b), and multiple scattered arrivals (panel c). Waveforms shown in panels (a) and (b) are modeled using the Foldy code (Galetti, et al., 2013), panel (c) is a recorded waveform of a microearthquake in New Ollerton, England.

Aki and his collaborator's first studies on coda (Aki 1969; Aki & Chouet 1975) as well as some later works (e.g. Roberts et al., 1992) used the amplitude of the waves, while the phase information was considered by other pioneers of coda studying. Poupinet et al. (1984) exploited the sensitivity of coda waves and estimated the velocity change of S-wave in the Calaveras fault zones from the phase shifts in seismograms recorded with the same station before and after the Coyote Lake, California, earthquake. Two waveforms were excited by a pair of microearthquakes on the same segment of the fault, and they found one seismogram were like the other with some time delay, regardless the difference in amplitude. They identified the different length of delay along the seismogram by computing the crosscorrelation in the frequency domain in a moving window, and the time delay data were used to estimate the changes in seismic velocity. The idea of their approach (Poupinet et al. 1984; Ratdomopurbo & Poupinet, 1995) is similar to that of a technique proposed approximately a decade ago by Snieder et al. in 2002 - Coda wave interferometry (CWI) (Snieder et al., 2002). An advance of their method is that the way to extract the difference between waveforms may be more effective. In this project, we apply CWI to determine the separation between a pair of energy sources, which will then be used to solve for the relative locations of the sources. This is a relatively new application of the CWI theory, however, it shares a common methodology to obtain differences between waveforms with the original applications of CWI for estimating variations in seismic velocity of the medium. In the next section, we provide a review of the relatively short history of the CWI technique.

1.2 Coda wave interferometry

Coda is highly repeatable in a stable seismic system, where the properties and position of source, propagating medium and the receiver stay unchanged. Once a small perturbation occurs, the difference between coda in the waveforms recorded at the same position before and after the perturbation reveals the change that has occurred in the system, while the early arrivals are often not able to "feel" it. The top plot of Figure 1-2 (a) shows a synthetic seismogram of waves that have traveled through a medium with a large number of point-scatterers as heterogeneities, the middle plot shows a waveform propagated in the same medium and was recorded at the same receiver, while the source is slightly displaced to its close neighbourhood. Not surprisingly, the two waveforms are very similar to each other as indicated in the bottom plot where one overlaps the other. Details of the first arrivals and the coda are shown in panel (b) and (c), respectively, which clearly show that the slight perturbation having almost no detectable influence on the early arrivals are significantly magnified in the coda. In other words, the commonly-desired first arrivals cannot be used in such cases where the changes in the system are small, while coda waves are shown to be more capable of identifying these changes.

The example above visualizes the extreme sensitivity of coda. Coda wave interferometry (CWI) is the technique that exploits and makes use of the sensitivity of coda to estimate small temporal changes in seismic systems. Three major types of applications have been developed – (1) monitoring the change in seismic velocity, (2) estimating the displacement of scatterers in the medium and (3) determining the perturbation in source location. CWI identifies the type and amount of the small perturbation by measuring the phase shifts of arrivals in the coda in a statistical fashion. Specifically, this is done by computing the crosscorrelation of the two

waveforms within successive non-overlapping windows along their codas in the time domain. The statistical parameters describing the shifts of phases in a time-window are obtained by manipulating the crosscorrelation and autocorrelation of the two waveforms, hence can be derived simply from waveform data. They are then related to one of the three types of perturbations. Thus the perturbations mentioned above can be extracted.

In the paper that first introduced CWI, Snieder et al. (2002a) determined the non-linear dependence of seismic velocity of Elberton granite on temperature. They were able to estimate the velocity change due to a temperature difference as small as 5°C, while in most of the previous laboratory experiments, the temperature discrepancy that could be identified from velocity change was about 100°C. Their experimental results also revealed a reversible and an irreversible mechanism of the velocity change in the granite under heating. Their work demonstrated the ability of CWI to identify minute changes in the medium through variations in bulk velocity. This idea was then implemented in a sequence of intriguing studies and applications. Outside the laboratory, Gret et al. (2005) carried out a controlled stress-change experiment in a mining environment, in which they used CWI to monitor *in situ* temporal stress variation by measuring time-lapse velocity changes. Using the CWI technique, a well-developed daily cyclic velocity change was found from a continuous monitoring near the Xiaojiang fault zone in Kunming, China, which showed highly consistency among components and stations (Wang et al., 2008).

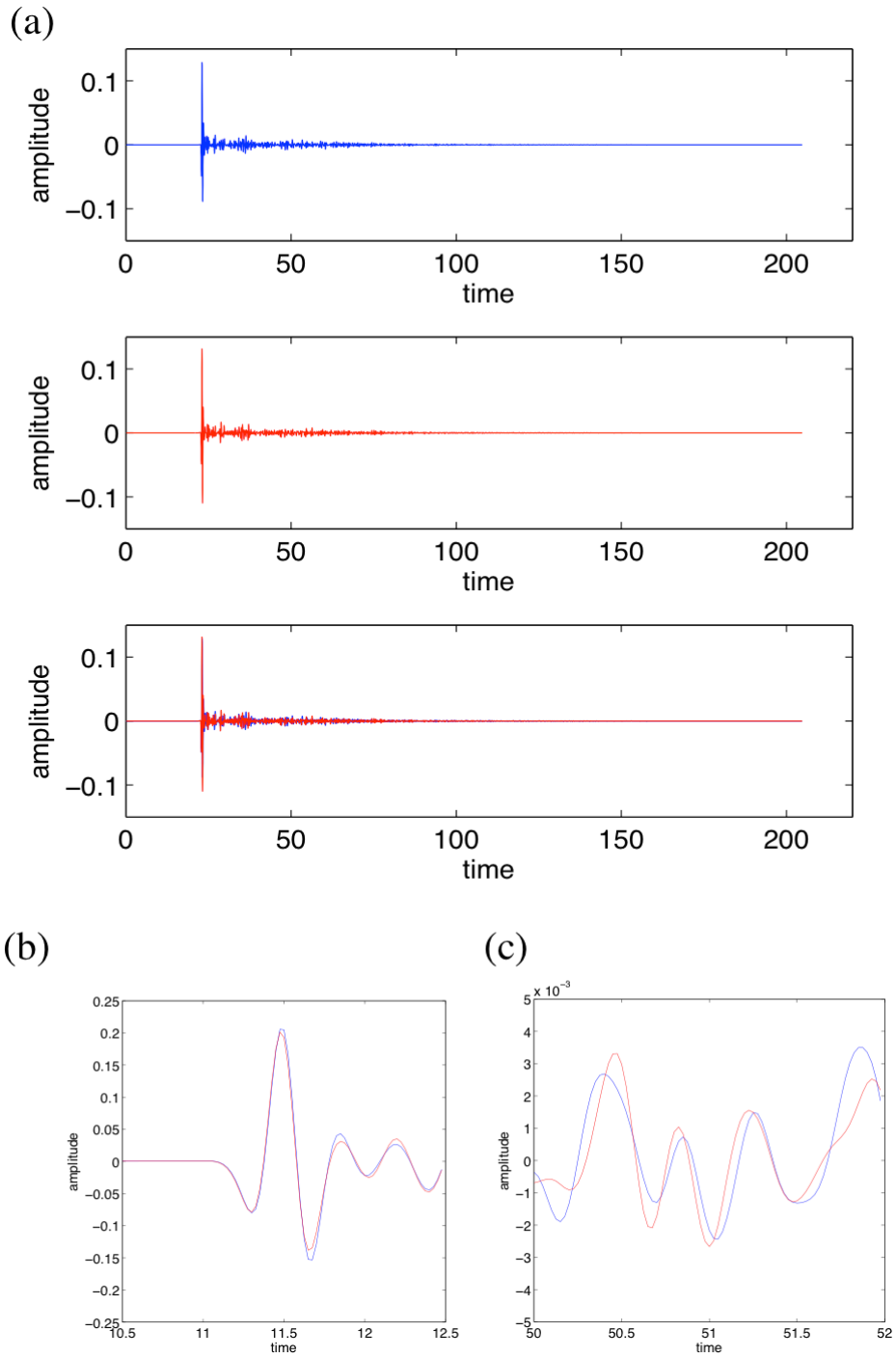

Figure 1-2: Scattered waveforms. (a) displays the original waveform on the top, the waveform obtained after perturbing the source in the middle, and their superposition at the bottom. (b) and (c) are 2-second zoom-ins around the first arrivals and from the coda of the two waveforms.

Applications of CWI to measure minute velocity variations have also contributed to studies on volcanoes. Wegler et al. (2006) applied CWI to the waveforms recorded by the permanent stations installed at the Merapi volcano, Indonesia, before its eruption in 1998. The waves were excited by airguns placed in water basin dug in the side of the volcano, each of which generated highly repeatable waveforms (Wegler et al., 1999). They observed an increase in shear wave velocity prior to the eruption, which correlated the incremental activity of seismicity during the same period. This indicated the increasing pressure inside the volcanoes as the elastic velocity in rocks is known to grow proportionally with increasing stress. Their interpretation agrees with that make by Poupinet et al. (1984) on the shear-wave velocity change before the earthquake on the Calaveras fault, California. A growth in seismic velocity before volcanic eruption was also observed by Nagaoka et al. (2010) at Mt. Asama, Japan. According to Battaglia et al. (2012), CWI can also be used as a tool to reveal the earthquake-volcano interaction by monitoring the velocity change in the surrounding areas. They demonstrate that in the cases where large earthquakes occur around a volcano, the interior of the volcano is affected by the passage of large amplitude seismic waves, whether any observable change in the eruptive activity is induced. The original CWI technique requires an assumption of a constant portion of velocity change. Pacheco and Snieder (2005) extended the theory by relating localized velocity change in the medium to the differences in recorded waveforms.

As mentioned above, CWI can also be used to identify other types of changes in a system. Gret et al. (2005) observed rapid temporal changes in the Mount Erebus Volcano, Antarctica, from the deteriorating correlation of the signals recorded during a particularly active period of the volcano. Explosive gas bubbles in the lava lake that generated repeatable explosions were used as the passive source, and since the lake was of relatively small size, both the source location and mechanism were

considered unchanged. The reason for this change involving medium velocity change was also excluded because the phase shift did not show a trend linearly increasing with travel time, which characterizes velocity change by CWI. They therefore suggested the decorrelation of coda is for the change in scattering properties of the interior of the volcano.

Applications of CWI that involves inferring displacement of scatterers in the medium can be used to monitor the turbulence of a fluid containing or seeded by small buoyant particles that scatters waves (Snieder, 2004). In the field of geophysics, this application may be relevant to the scenario in which a strongly scattering region of the Earth is strained leading to the movement of the interior heterogeneities, however this potential type of application has not been put into practical use in geophysics so far. A more detailed discussion on discriminating different types of changes using CWI is provided in Chapter 6.

Another type of application of CWI is to estimate the separation between a pair of energy sources with similar mechanisms. Its study interests commenced when Sineder and Vrijlandt (2005) derived the geometric constraints on their relative locations for different types of sources, including point force, explosion, and double-couple (for earthquakes) sources, from the crosscorrelation of coda of waveforms recoded at the same station. Their derivation is based on the assumption of identical mechanism of sources. Highly correlated early arrivals in the waveforms of aftershock sequences and induced microseismicities in hydrocarbon reservoirs often show a high level of similarity in source mechanism (Ealdhauser & Ellsworth, 2000; Sinieder & Vrijlandt, 2005; Gnyp, 2013; van der Woerd et al., 2014). However, there are occasions where the deviations in source mechanism cannot be ignored which leads to large errors in separation estimates. Robinson et al. (2007b)

developed an extension of CWI to accommodate the mechanism change for double-couple sources. Their new theory allows the change in strike, dip and rake of the double couple to be evaluated before they reach a set of crossovers, giving new potential of CWI in use of relative source location.

Robinson et al. (2007a) observed that the source separation estimates using CWI show a probabilistic character. Robinson et al. (2011) established a Bayesian framework of the CWI separation that describes and quantifies its probabilistic nature. These works lead to a novel source location technique (Robinson et al., 2013), a probabilistic approach that solves for the relative location of a cluster of earthquakes through optimization, with inter-source separation data computed directly from seismic waveform using the CWI theory. Thus, CWI could be used as a complement to the conventional earthquake location methods (Poupinet et al., 1984; Fremont & Malone, 1987; Waldhauser & Ellsworth 2000, 2002). In particular, the most applicable range of CWI is where the inter-source distance is small compared to the dominant wavelength of the seismic waves, while it is extremely difficult for traditional approaches to attain an accuracy smaller than these separations.

1.3 Relative source location

Relative location of earthquakes is essential in a variety of applications, such as imaging fault planes with sequences of aftershocks and/or foreshocks (Got et al., 1994; Dodge et al., 1995; Waldhauser & Ellsworth, 2002; Shearer et al., 2005), studying earthquake interaction and recurrence (Chen et al., 2013), and monitoring induced microseismicity (Ake et al., 2005; Fronhlich & Brunt, 2013; Ellsworth 2013). The relative locations of a group of earthquakes could be obtained from absolute

locations. However, the quality of absolute locations found in each case depends heavily on the velocity model used, the number of stations available, and source-to-receiver distances and azimuths. In seismological applications, earthquake location uncertainties are therefore usually of the order of kilometers (Shearer, 1999). Besides, in regions with multiple earthquakes, the events can have influence on the location of their neighbours (Pavlis, 1992).

The location errors can be significantly depressed by directly calculating the relative location from the travel-times or waveforms so that the location errors can be reduced to a few or a few tens of meters. Douglas (1967) first improved the standard absolute location method described by Jeffreys (1959) by accounting for azimuth-dependent travel-time variation by estimating the epicenters for seven events simultaneously. A station correction term is added to the equation of condition for calculating the corrections of hypocenter locations from the initialization and in each iteration, as suggested by Cleaty and Hales (1966). This also gives the residual in station corrections and the residual of the original times. This method is called Joint Epicenter Determination (JEP). Although it estimates the depths of the earthquakes, the solution is poor, and only when the depths are constrained *a priori* the locating process, the convergence can be reached rapidly. Dodge et al. (1995) made a radical step forward of this method by using the crosscorrelation picked traveltimes, and obtained relative location errors of less than 100m horizontally and 200m vertically, while the estimates given by its predecessor (Douglas, 1967) was about 1km in the horizontal direction. This is the Joint Hypocenter Determination (JHD) method widely used to estimate the relative location of earthquakes in swarms. JHD applies the technique proposed by VanDecar and Crosson (1990) for estimating the relative arrival times of tele-seismicity, where cross-correlation is calculated between all possible event pairs and the obtained delay times are converted to

absolute times by aligning them in the natural time order, which are then inverted for hypocenter locations and station corrections. Bhattacharya et al. (2005) used the JHD method to relocate a set of earthquakes in northeast India with both *P* and *S*-wave arrivals, and their lateral variation in velocity inferred from the resultant station correction is comparable to the result of the local earthquake tomography method.

However, as other applications relying on crosscorrelating waveforms to obtain travel time differences, the JHD method is only able to locate events that are limited in a small volume to ensure the similarity in the waveforms. If the earthquakes interested are sparsely distributed, in other words, the inter-event separations are not small compared to the dominant wavelength, these methods would fail. Another approach to determine the relative location of earthquakes in a cluster is the master event approach (Harris, 1987; Deichmann & Garcia-Fernandez, 1992; Deichmann & Giardini, 2009), which suffers even more from large inter-event distances. It requires the existence of a master event to have a waveform sufficiently similar to that of all the other events, so that the differential traveltime between the master event and the others can be computed from crosscorrelation, which is not always possible, and the errors due to correlated noise in the master event are transferred to all differential traveltime measurements through the crosscorrelations, thus severely deteriorate the location results.

The Double-Difference (DD) method developed by Waldhauser and Ellsworth (2000) partly overcomes the aforementioned problem of the limited inter-event distance with its ability to construct links between multiple event clusters and between clusters and individual events, though it also involves waveform crosscorrelation to compute differential traveltimes between event pairs. “Double-difference” refers to the residual between observed and theoretical differential traveltimes of a pair of

earthquakes recorded at a common station. The DD method determines the relative event location by minimizing the double-difference of pairwise events through adjusting the vector difference between their hypocenters. Within an earthquake swarm, the event separations can be determined to the accuracy of the crosscorrelation data. Catalog traveltime data are used to connect different event clusters. For individual events that are not inside any swarm, Waldhauser and Ellsworth (2002) also compute the double-difference between these events and between events in clusters with them. Thus by combining the traveltime data derived in two ways, the DD method is capable of relocating earthquakes distributed over large distances.

The DD method is currently one of the most widely used approaches to locate earthquakes in a cluster or in multiple clusters in a region with dense seismic stations in a network. However, in areas without a large number of seismic stations or good source-to-station azimuthal coverage, like intra-plate regions, the performance of the DD method deteriorates (Robinson et al. 2013). In such circumstances, the CWI-based relative source location method (Robinson et al., 2013) can be particularly useful. This technique uses inter-source separation data calculated with CWI, which has been shown to give stable measurements among stations. It applies waveform crosscorrelation as the DD method, the JHD method and the master event approach do, however does not require multiple stations. This is because the CWI-based method extracts useful information from a larger proportion of the waveform, rather than only one or two phases (*P* and/or *S* arrivals) like the conventional methods. Robinson et al. (2013) established a probabilistic formulation to solve for the relative location of a cluster of earthquakes as an optimization problem, in which the most probable combination of event locations is found at the global minimum of the objective function. The second part of this thesis will focus

on this novel source location method.

1.4 The claim

In this thesis, I re-validate the usage of coda wave interferometry (CWI) for estimating the separation between a pair of sources with identical source mechanism with synthetic waveforms generated with a simple and exact modeling method, the Foldy code (Galetti et al., 2013). The underestimating tendency in estimates of larger separations is observed as described by Snieder and Vrijlandt (2005) and Robinson et al., (2007; 2011).

To understand factors that influence the performance of CWI in estimating inter-source separations, I conduct a series of synthetic tests in media with various types and complexities. These experiments are original: testing different properties of the scatterers on the performance of CWI in point-scatterer media; testing CWI in media consisting of horizontal layers; testing CWI under the influence of both point scatterers and layers; and finally testing CWI in the more realistic Marmousi2 model. It is found that the accuracy and precision of CWI estimates improves with increasing number of point scatterers until a limit is met; and CWI gives estimates with lower uncertainty when the scatterers with higher intensity are applied. In a point-scatterer medium with favorable parameters, CWI produces a virtually exact estimate of the source separation between a pair of events with a true separation $\delta_{true} \leq 0.25\lambda_d$, after which it has an increasing trend of underestimation, and for $\delta_{true} \geq 0.4\lambda_d$ CWI only gives an estimate of the lower bound of the separation. As the theory of CWI assumes point scatterers in its derivation, these results are then used as reference when examining the performance of CWI in other types of media. Layer structure is found to disrupt the estimation to an extent depending on the event

pair locations relative to the orientation of the layers, and the source-to-receiver locations relative to the orientation of the layers. However the estimation is remarkably improved when a small number of point-scatterers is included. Tests in the Marmousi2 model reveal that in more complex structures, CWI separation estimates have a similar level of accuracy to that obtained in the point-scatterer media, even when the assumptions in the theory does not adequately describe the data. This study contributes to better understanding and interpretation the source separation estimates and therefore relative locations using CWI.

For a cluster of seismic sources, the inter-source separation estimates can be used to estimate their relative locations, using a probabilistic framework developed by Robinson et al. (2013). They also demonstrate that the CWI-based location method is able to determine the relative location of a cluster of earthquakes using a single seismic station. In this thesis, I validate this novel location method for a second time both synthetically and using real seismic data. While the method has been shown to produce reasonable results on larger earthquakes, I test this method for microseismic events with shorter distinguishable coda in recorded waveforms, and hence fewer scattered waves. The location results are highly consistent when using different individual seismometer channels, showing that it is possible to location event clusters with a single-channel seismometer. The potential applications of this cost-effective method are thus extended over a wider range of magnitudes. In this thesis, I also provide two improvements to the original method: to account for the impact of large difference in the dominant wavelength of recording made on different instruments, I introduced a new formulation for the optimization problem; to avoid the vagaries of trial-and-error method in parameter selection when applying CWI, I presented a systematic approach which helps standardize the method, and also allows CWI techniques to be automated.

Given the advantages of this location method, it is likely that it only has two published applications (Robinson et al., 2013; Zhao et al., 2017, i.e. Chapter 4 of this thesis) is in part because the algorithm requires unfamiliar methods to be used, and is therefore also partly due to the lack of a readily available, easily editable code. To this end, I developed such a code called *CWIcluster* in MATLAB that implements the method, accompanied by replicable examples with both synthetic and real data, and a user manual. A way to assess the location results is also introduced. The code has been made available at *www.geos.ed.ac.uk/eip/codes.html*.

I also wrote a user manual for the location code (see Appendix 1), which thoroughly explains the methods and algorithms used in the functions and scripts contained in the code package, and demonstrates in detail how the they are used to produce the results of the synthetic and real-data examples presented in Chapter 5.

Presently, when applying CWI to estimate changes in a seismic system, one assumes that a single type of change (medium velocity change, source location perturbation or scatterer displacement) has occurred. However, in reality more than one type of perturbation can occur simultaneously. In this thesis, I study a series of scenarios with numerical experiments where one type of change is accompanied by another, explored their applicable range, and how the effect of the undesired type of perturbation can be compensated. Finally, I propose a general treatment for scenarios where the types of changes that have occurred is unknown, how to distinguish them and estimate the change of interest with the effect of others compensated.

In a co-authored article (Singh et al., 2019), where changes in wave velocity and source locations are measured with the CWI method using laboratory rock physics data, I use *CWICluster* code package to estimate the relative locations of the acoustic

emissions (sources) and find that the estimated event locations form a pattern that is very similar to that formed by the actual locations of the sources applied in the experiment.

Chapters 3, 4, 5, and 6 are written in a manner that is common to published papers, where "we" refers to the first author, me, and the co-author(s). The co-authored article is provided as Appendix 2.

1.5 Thesis outline

This thesis consists of eight chapters, of which this Introduction is the first. The others can essentially be divided into three parts, corresponding to studies that focus on estimating source separation using CWI in *Part 1* (Chapter 2-3), relative source location based on CWI in *Part 2* (Chapter 4-5), and discriminating different types of perturbations using CWI methods in *Part 3* (Chapter 6), respectively:

Chapter 2 provides an introduction to the theory of coda wave interferometry with a brief derivation, and shows how it can be used to estimate the separation between a pair of energy sources. To validate the theory, I present the results of a synthetic example in a 2D acoustic point-scatterer medium, where the waveforms are modeled using the Foldy method (Foldy, 1945, Galetti et al, 2013). The underestimation tendency of CWI estimates is observed, and the consistency among results given by individual receivers at different locations is examined. It is found that estimates of individual receivers vary to some extent, which could be because the distribution of scatterers are insufficiently isotropic, rendering different scattering behaviour (in a statistical sense) towards individual receivers.

In *Chapter 3* I conduct a series of synthetic experiments to test the performance of CWI to estimate inter-source separations in models with various types and complexities. To begin with, a range of point-scatterer media is used to examine how different properties of point scatterers influence the CWI estimation. Since the theory of CWI assumes point scatterers in its derivation, results obtained in point-scatterer media with favorable parameters are then used as reference when examining the performance of CWI in other types of media: layered media, scatterer-layer media and the Marmousi model. It is demonstrated that within the applicable range, CWI is able to produce reliable estimates of source separations in media more complex and realistic structures, even when the assumptions in the theory does not adequately describe the data. I also present the first elastic test on CWI to estimate source separations in a synthetic experiment. The results of this study will help understand and interpret the source separation estimates using CWI in applications with real data. Parts of the work in this Chapter has been prepared to submit for publication as:

- Zhao, Y., A. Curtis, and J. Singh, 2018, Estimating the distance between pairs of energy sources using coda wave interferometry in models with varying complexities and types of prior information.

Chapter 4 focuses on using the inter-source separation obtained using CWI to estimate the relative location of a cluster of events. The location algorithm uses a probabilistic framework established with the empirical relations between measured and actual source separations and solves for the relative event locations as an optimization problem. The algorithm is presented, together with two improvements I introduce in this thesis. I validate the location algorithm with both synthetic and microearthquake data. The work in this Chapter has been published as:

- Zhao, Y., A. Curtis, and B. Baptie, 2017, Locating microseismic sources with a single seismometer channel using coda wave interferometry: Geophysics, **82**,

A19-A24.

Chapter 5 presents a MATLAB code called *CWIcluster* that implements the source location algorithm introduced in *Chapter 4*. The code implements the location method in three steps: classifying events into clusters with the given waveforms recorded by one or multiple seismic station channels, estimating inter-source separations using CWI, and then estimating the relative source locations by solving a minimization problem. Each step can be implemented in an automated sense given criteria chosen by the user. Replicable examples with both synthetic and real data are presented in the Chapter. It is demonstrated that the location method is able to correct for the underestimation bias of the CWI method to some extent. This code is accompanied by a thorough user manual, and has been made available at *www.geos.ed.ac.uk/eip/codes.html*. The work in this Chapter has been accepted for publication as:

- Zhao, Y. and A. Curtis, 2019, Relative source location using coda wave interferometry: method, code package, and application to mining induced earthquakes: Geophysics, 84, No.3 (May-June) P1-12.

Chapter 6 returns to the three basic types of applications of CWI. Standard CWI methods require an assumption that a single type of perturbation has taken place in the system (as do most other methods that measure changes in a seismic system). However, in reality more than one type of perturbation can occur simultaneously. This Chapter proposes a general treatment to account for multiple types of perturbations, allowing each type to be recognized and estimated with the effects of others being compensated. The work in this Chapter is under preparation for submission for publication as:

- Zhao, Y. and A. Curtis, 2018, Discriminating different types of perturbations in a seismic system using coda wave interferometry.

Chapter 7 discusses the current limitations of the location method, and provide suggestions for its improvements and further studies.

Chapter 8 summarizes the main conclusions that can be drawn from the work presented in this thesis and the contributions to the field of research.

Appendix 1 provides the user manual of the location code *CWICluster* introduced in Chapter 5.

Appendix 2 is a co-authored article on the applications of CWI to monitor changes in velocity and source locations in experimental rock physics.

2

CODA WAVE INTERFEROMETRY

2.1 Introduction

Geophysical applications of coda wave interferometry (CWI) that involve detecting subtle velocity variations have become a booming field of research (Poupinet, 1984; Gret et al., 2005; 2006; Peng and Ben-Zion, 2006; Wegler et al, 2006; Larose and Hall, 2009; Battaglia et al, 2012) since the introduction of its standard formulation by Snieder et al. (2002). Another type of CWI application measures changes in source location by estimating the separation between two identical sources, introduced by Snieder and Vrijlandt (2005). They derived the separation between a pair of sources given geometric constraints on their relative location for different types of source (point force, explosion, and double-couple earthquakes) in terms of the crosscorrelation of coda in the waveforms recorded at the same station. Their derivation is based on the assumption that the two events are of identical source mechanism. Highly correlated early arrivals in the waveforms of aftershock sequences and induced microseismicity in hydrocarbon reservoirs or mining sites often show a high level of similarity in source mechanism (Waldhauser & Ellsworth, 2000; Snieder & Vrijlandt, 2005; Gnyp, 2013; van der Woerd et al., 2014). Coda waves sample a larger region of the propagating medium, and therefore contain more information than the first or early arrivals used by conventional methods. Hence CWI requires fewer stations and source-to-station azimuthal coverage than conventional methods. The most applicable range of CWI is where the inter-source distance is small compared to the dominant wavelength of the seismic waves; by contrast it is difficult for traditional approaches to attain an accuracy smaller than these separations.

In this chapter, I first present the theory of CWI in Section 2.2, focusing on estimating source separations. I then introduce an efficient and exact modeling method called the Foldy method (Foldy, 1945; Groenenboom and Snieder, 1995;

Galetti et al., 2013) in Section 2.3, which I use for numerical examples. In Section 2.4 I validate my implementation of the theory in a numerical experiment with waveforms generated using the Foldy method. In Section 2.5 I discuss a potential source of error of the modeling method and the limitations of the tests.

2.2 Theory of coda wave interferometry

The theory of CWI is based on scattering path summation, whereby the scattering wavefield can be represented as (Snieder, 1999):

$$\boldsymbol{u}(t) = \sum_{T} \boldsymbol{A}_T(t) \tag{2.1}$$

which states that the total wavefield $\boldsymbol{u}(t)$ at a given position can be written as the superposition of waves $\boldsymbol{A}_T(t)$ that travel along all possible trajectories in the medium, where the subscript T is associated with each trajectory. This expression of wavefield considers point-scatterers, or scattering at boundaries, so the wave path can be "counted", hence a sum is used. In the real Earth, heterogeneities that cause scattering may be far more complex. For a medium that contains only point scatters as heterogeneities, the trajectory of a wave is linked by a sequence of scatterers, through which a wave propagates from a source to a receiver, as shown in Figure 2-1. The trajectories T in equation 2.1 include the direct wave, singly-scattered waves, and multiply-scattered waves. CWI does not require information on the number of trajectories or what each trajectory is. For elastic waves, mode conversions occur at the scatterers. In that case, $\boldsymbol{A}_T(t)$ includes both P-wave and S-wave segments of a trajectory.

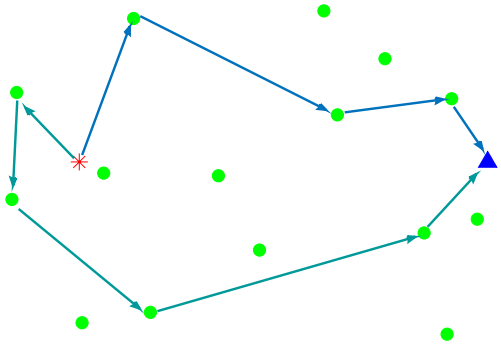

Figure 2-1 Sketch of wave trajectories. The star, triangle, and dots represent the source, receiver, and point-scatterers, respectively. The blue and cyan line segments with arrows indicate two possible wave trajectories in this medium.

Once a perturbation occurs, either in wave propagation velocity, scatterer positions or source location, the wavefield recorded at a given position changes correspondingly. It is shown by Snieder (2006) that the changes in the waveform caused by these perturbations is dominated by the change in the traveltime perturbation of the waves, provided that the scattering mean free path, the average distance between scatters, is much larger than a wavelength. The wavefields recorded before and after the perturbation can therefore be denoted

$$\boldsymbol{u}^{(u)}(t) = \sum_{T} \boldsymbol{A}_T(t), \tag{2.2}$$

and

$$\boldsymbol{u}^{(p)}(t) = \sum_{T} \boldsymbol{A}_T(t - \tau_T), \tag{2.3}$$

where the superscripts (u) and (p) means "unperturbed" and "perturbed", respectively, and τ_T is the change in the travel-time because of the perturbation of the wave propagating along trajectory T. Note that as CWI analyze the coda in seismograms where the amplitude of the arrivals are lower than the early arrives, it is

usually required that the recordings of the first event (including coda) should be finished before the start of the second event. Also, there should be no further events overlapping the part of the seismogram of the second event being analyzed.

The form of equation 2.3 implies that the shape and amplitude of the waves contained in $\boldsymbol{u}(t)$ do not change. However, this is not the case when the perturbation causes a dispersive change in the waves. In that case, equation 2.3 can still be taken as a good approximation for the perturbed wavefield if the waveform has been filtered with a pass band that is sufficiently small so that the dispersion can be ignored within the band (Snieder, 2006).

In general, the travel-time change τ_T depends on the trajectory T, so the travel-time changes of the waves arriving within a given time interval have a certain distribution, which reflects how the system is perturbed. In other words, the type (velocity change, scatterer displacement, and source displacement) and magnitude of the perturbation can be estimated from the distribution of τ_T. Specifically, the mean $\langle\tau_T\rangle$ and variance ${\sigma_\tau}^2$ statistics of the traveltime change of the waves arriving at a receiver within a certain time window are used in CWI to make such estimates. These statistics are extracted from the crosscorrelation of the unperturbed and the perturbed waveforms.

The differences between a pair of waveforms are measured by their time-shifted crosscorrelation coefficient

$$R^{(t,t_\omega)}(t_s) = \frac{\int_{t-t_\omega}^{t+t_\omega} u^{(u)}(t')u^{(p)}(t'+t_s)dt'}{\sqrt{\int_{t-t_\omega}^{t+t_\omega} {u^{(u)}}^2(t')dt' \int_{t-t_\omega}^{t+t_\omega} {u^{(p)}}^2(t')dt'}}, \tag{2.4}$$

where t_s is the time shift of the two waveforms in the correlation. The crosscorrelation is computed over a time window with a length of $2t_\omega$ with center

time t. The denominator is the square root of the product of the autocorrelation of the two waveforms, which normalizes the crosscorrelation, thus the coefficient $R^{(t,t_\omega)}$ has a maximum of 1. Inserting the expression of the unperturbed and the perturbed waveforms 2.2 and 2.3 into the numerator of the correlation coefficient, gives

$$N(t_s) = \sum_{TT'} \int_{t-t_\omega}^{t+t_\omega} \boldsymbol{A}_T(t')\boldsymbol{A}_{T'}(t' + t_s - \tau_T)dt', \tag{2.5}$$

which leads to a double sum $\sum_{TT'}$ over the trajectories, along which the waves arriving within the time window $(t - t_\omega, t + t_\omega)$. T refers to the trajectories before the perturbation, and T' after. The double sum $\sum_{TT'} = \sum_{T=T'} + \sum_{T\neq T'}$ consists of diagonal terms (for $T = T'$) and cross terms (for $T \neq T'$). If the cross terms are uncorrelated, they are assumed to contribute zero to the double sum term. Snieder (2004) investigated the validity of ignoring slightly correlated off-diagonal terms by comparing the magnitude of the non-diagonal and the diagonal terms and found that their ratio is inversely proportional to the square root of the frequency bandwidth of the waveform and the time window length. That is to say, in order to ignore the cross terms, the frequency band and the time window must be sufficiently large, yet the time window cannot be unboundedly large.

The integral inside the summation is the crosscorrelation of the waves travelling along individual trajectories according to the definition of crosscorrelation, i.e. $\int_{t-t_\omega}^{t+t_\omega} \boldsymbol{A}_{T_i}(t')\boldsymbol{A}_{T_i}(t' + t_s - \tau_T)dt' = C_T(t_s - \tau_T)$. Thus the numerator of the correlation coefficient can be written as:

$$N(t_s) = \sum_T C_T(t_s - \tau_T). \tag{2.6}$$

Similarly, the denominator is therefore:

$$D(t_s) = \sum_T C_T(0). \tag{2.7}$$

Hence, the correlation coefficient becomes:

$$R^{(t,t_\omega)}(t_s) = \frac{\sum_T C_T(t_s - \tau_T)}{\sum_T C_T(0)}. \tag{2.8}$$

The mean and variance of the travel-time change derivation of $\langle \tau_T \rangle$ and ${\sigma_\tau}^2$ is the key to estimate small changes in a seismic system using CWI. For equation 2.8 to be written in a form more convenient to derive ${\sigma_\tau}^2$, another assumption is made that the waves travelling along different trajectories arriving within a given time window have a power spectrum with the same shape (Snieder, 2006). This is valid in scenarios where the waves are excited by sources located in close proximity to each other with identical mechanism. Also, since scattering is usually frequency-dependent, the waves have to have been scattered the same number of times, the time window therefore must be sufficiently small. Note that to omit the cross terms in the double sum in $N(t_s)$, there is a trade-off to consider in the decision about the length of the time window to use when implementing CWI. I developed an approach to systematically select the length of time windows, which is described in Chapter 5.

As the Fourier transform of the power spectrum is autocorrelation in the time domain, the assumption implies that the autocorrelations are also the same after normalization. Hence, in a time window with a suitable size, the crosscorrelation function can be expressed by a "common" normalized autocorrelation function $C(t)$, and a parameter I_T that accounts for the intensity of waves along different trajectories, i.e.

$$C_T(t) = I_T C(t), \qquad \text{where } C(0) = 1, \tag{2.9}$$

and for autocorrelation $C_T(0) = I_T$. Hence, the correlation coefficient can be written as

$$R^{(t,t_\omega)}(t_s) = \frac{\sum_T I_T C(t_s - \tau_T)}{\sum_T I_T}. \tag{2.10}$$

In equation 2.10, the correlation coefficient is expressed as an average of the common normalized autocorrelation weighted by the intensity of waves along different trajectories. It is also assumed that the traveltime change of waves along different trajectories does not fluctuate dramatically within a time window, so the

common normalized autocorrelation can be approximated as its second-order Taylor expansion, i.e. $C(t) = C(t=0) + \dot{C}(t=0)t + \frac{1}{2}\ddot{C}(t=0)t^2$, where the dots denote time derivatives. Since an auto-correlation function is an even function, its first-order time derivative is an odd function, giving $\dot{C}(t=0) = 0$. According to equation 2.9 $C(t=0) = 1$, the Taylor approximation becomes

$$C(t) = 1 + \frac{1}{2}\ddot{C}(t=0)t^2. \tag{2.11}$$

$\ddot{C}(t=0)$ can be obtained by differentiating the normalized auto-correlation twice, after which $C(t)$ becomes

$$R^{(t,t_\omega)}(t_s) = 1 - \frac{1}{2}\overline{\omega^2}\frac{\sum_T I_T(t_s - \tau_T)^2}{\sum_T I_T}, \tag{2.12}$$

where t is replaced with $t_s - \tau_T$, and $\overline{\omega^2} = -\ddot{C}(0) = \frac{\int_{t-t_\omega}^{t+t_\omega} \ddot{u}^2(t')dt'}{\int_{t-t_\omega}^{t+t_\omega} u^2(t')dt'}$ is the mean-squared angular frequency, which can readily be computed from the waveforms. The maximum of $R^{(t,t_\omega)}(t_s)$ can then be found with differentiation and is obtained for $t_s = \frac{\sum_T I_T \tau_T}{\sum_T I_T}$, i.e.

$$t_s = \langle \tau_T \rangle_{(t,t_\omega)}, \tag{2.13}$$

where the average is based on wave intensity of each trajectory, i.e.

$$\langle \tau_T \rangle_{(t,t_\omega)} = \frac{\sum_T I_T \tau_T}{\sum_T I_T}, \tag{2.14}$$

where the subscript means that the mean is taken oven the employed time window $(t - t_\omega, t + t_\omega)$. Substituting equation 2.13 into the weighted average term of 2.12, the latter becomes $\frac{\sum_T I_T (t_s - \langle \tau_T \rangle_{(t,t_\omega)})^2}{\sum_T I_T}$, which is the variance ${\sigma_\tau}^2$ of the travel-time change along different trajectories. Thus the maximum of the correlation coefficient is related to the variance ${\sigma_\tau}^2$, i.e. (Snieder, 2006)

$$R^{(t,t_\omega)}{}_{max} = 1 - \frac{1}{2}\overline{\omega^2}{\sigma_\tau}^2{}_{(t,t_\omega)}, \tag{2.15}$$

The correlation coefficient can be computed from equation 2.4 and hence its maximum $R^{(t,t_\omega)}{}_{max}$, the corresponding shift time $t_{max} = \langle \tau_T \rangle_{(t,t_\omega)}$, and the

variance $\sigma_\tau{}^2$ of the traveltime change can readily be obtained.

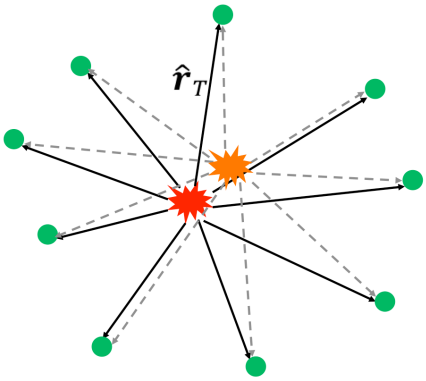

Figure 2-2: Wave paths from sources (stars) to the first scatterers (dots) in possible propagating trajectories. The red and orange stars represent the original and the perturbed source, respectively; the solid and dashed line segments represent the paths of the original and perturbed waveforms. This figure is a modified from Snieder and Vrijlandt (2005).

From here on, the theory in this chapter will focus on estimating inter-source separations, while the other two types of application of CWI will be introduced in Chapter 6. Now consider a case where two sources with identical mechanism occurring close to one another. The waveforms recorded at the same receiver should be of high level of similarity. However, if the magnitude of such two sources is different, so are their source spectra, which will have impact on the crosscorrelation of their waveforms. In reality, CWI should be applied to sources with similar magnitudes, so that the difference in frequencies of the recordings can be ignored when the waveforms have been filled with a narrow band pass filter.

As the sources are assumed to be apart by a small distance, the only segment that is different in each wave trajectory is the path from the source to the first scatterer, as shown in Figure 2-2. For trajectory T, the travel-time change τ_T due to the perturbation in source location δ is

$$\tau_T = -\frac{1}{v}(\hat{\boldsymbol{r}}_T \cdot \delta), \tag{2.16}$$

where the $\hat{\boldsymbol{r}}_T$ is the unit vector of the direction from which trajectory T leaves the source before the perturbation; v is the velocity as the wave leaves the source and is assumed to be constant in the source region. In elastic media, v denotes *P*-wave velocity if the wave starts off from the source as a *P*-wave, while it denotes *S*-wave velocity if the wave leaves as an *S*-wave.

Snieder and Vrijlandt (2005) derived the relation between the variance of the travel time changes ${\sigma_\tau}^2$ and source displacement δ for a range of types of sources. For an isotropic source in an acoustic medium with a source spectrum $S(\omega)$, assuming wave propagation from the source to the first scatterer in each wave trajectory can be described by the Green's function for a homogeneous medium, the waves travelling from the source to the first scatterer along each path are

$$u(r) = -\frac{e^{ikr}}{4\pi r} S(\omega). \tag{2.17}$$

where r is the distance to each the first scatterer in each path. Inserting the wave along each trajectory (equation 2.17) and their traveltime (equation 2.16) into equation 2.14, the averaged travetime of waves arriving within a time window given by

$$< \tau >= \frac{-\iint |-\frac{e^{ikr}}{4\pi r}|^2 \frac{1}{v}(\hat{\boldsymbol{r}}_T \cdot \delta)|S(\omega)|^2 d\Omega d\omega}{\iint |-\frac{e^{ikr}}{4\pi r}|^2 |S(\omega)|^2 d\Omega d\omega}, \tag{2.18}$$

where the integrals are over the angles of all outgoing directions in three dimensions and over all frequencies in the waveforms. As the scatterers are assumed to be distributed homogeneously, the distance r is on average the same for each direction, thus equation 2.18 can be rewritten as $< \tau >= \frac{-\int \frac{1}{v}(\hat{\boldsymbol{r}}_T \cdot \delta) d\Omega \int |S(\omega)|^2 d\omega}{4\pi \int |S(\omega)|^2 d\omega}$. The frequency integrals cancel, thus equation 2.18 becomes

$$< \tau >= -\frac{1}{4\pi v} \int (\hat{\boldsymbol{r}}_T \cdot \delta)\, d\Omega. \tag{2.19}$$

Integrating over the full unit sphere, the integral vanishes, i.e.

$$< \tau >= 0. \tag{2.20}$$

This is because in a medium where the scatterers are distributed homogeneously, when the source is displaced to a nearby location, some paths from the source to the first scatterer become longer and some shorter, and the change on average is zero.

Equation 2.20 leads to ${\sigma_\tau}^2 =< \tau^2 > -< \tau >^2 =< \tau^2 >$. Inserting the square of wave along each trajectory (equation 2.17) and their traveltime (equation 2.16), ${\sigma_\tau}^2 =< \tau^2 >$ becomes

$${\sigma_\tau}^2 = \frac{\iint |-\frac{e^{ikr}}{4\pi r}|^2 \frac{1}{v^2} (\hat{\boldsymbol{r}}_T \cdot \delta)^2 |S(\omega)|^2 d\Omega d\omega}{\iint |-\frac{e^{ikr}}{4\pi r}|^2 |S(\omega)|^2 d\Omega d\omega}. \tag{2.21}$$

Following the same reasoning as above, the travel time change variance ${\sigma_\tau}^2$ becomes

$${\sigma_\tau}^2 = \frac{1}{4\pi v^2} \int (\hat{\boldsymbol{r}}_T \cdot \delta)^2 \, d\Omega. \tag{2.22}$$

Using the representations of the unit vector $\hat{\boldsymbol{r}} = \begin{pmatrix} cos\varphi sin\theta \\ sin\varphi sin\theta \\ cos\theta \end{pmatrix}$, where φ and θ are the longitude and colatitude of a spherical coordinate system. Integrating along z-axis, the integral becomes $\delta^2 \int cos^2\theta \, d\Omega = 4\pi\delta^2/3$. Hence, the separation between a pair of isotropic sources in a 3D acoustic medium is given by

$${\sigma_\tau}^2 = \frac{\delta^2}{3v^2}. \tag{2.23}$$

In a 2D case, the waves that propagate from the source at origin to the first scatterers along each path is given by

$$u(r) = -\frac{1}{2\pi} \ln(r) \, S(\omega). \tag{2.24}$$

Inserting the wave along each trajectory (equation 2.24) and their traveltime (equation 2.16) into equation 2.14, the averaged travetime of waves arriving within a time window given by

$$< \tau >= \frac{-\iint |-\frac{\ln(r)}{2\pi}|^2 \frac{1}{v}(\hat{\boldsymbol{r}}_T \cdot \delta)|S(\omega)|^2 d\Omega d\omega}{\iint |-\frac{\ln(r)}{2\pi}|^2 |S(\omega)|^2 d\Omega d\omega}, \tag{2.25}$$

where the integrals are over the angles of all outgoing directions in two dimensions and over all frequencies in the waveforms. As the scatterers are assumed to be distributed homogeneously, the distance r is on average the same for each direction, thus equation 2.25 can be rewritten as $< \tau >= \frac{-\int(\hat{\boldsymbol{r}}_T \cdot \delta) d\Omega \int |S(\omega)|^2 d\omega}{2\pi v \int |S(\omega)|^2 d\omega}$. The frequency integrals cancel, thus equation 2.25 becomes

$$< \tau >= -\frac{1}{2\pi v} \int (\hat{\boldsymbol{r}}_T \cdot \delta)\, d\Omega. \tag{2.26}$$

Integrating over the full unit circle, the integral vanishes as in the 3D case, i.e.

$$< \tau >= 0. \tag{2.27}$$

Hence, the variance of the travetime chance ${\sigma_\tau}^2 =< \tau^2 >$ becomes

$${\sigma_\tau}^2 = \frac{\iint |-\frac{\ln(r)}{2\pi}|^2 \frac{1}{v^2}(\hat{\boldsymbol{r}}_T \cdot \delta)^2 |S(\omega)|^2 d\Omega d\omega}{\iint |-\frac{\ln(r)}{2\pi}|^2 |S(\omega)|^2 d\Omega d\omega}. \tag{2.28}$$

Following the same reasoning as above, the travel time change variance ${\sigma_\tau}^2$ becomes

$${\sigma_\tau}^2 = \frac{1}{2\pi v^2} \int (\hat{\boldsymbol{r}}_T \cdot \delta)^2\, d\Omega. \tag{2.29}$$

Using the representations of the unit vector $\hat{\boldsymbol{r}} = \begin{pmatrix} cos\varphi \\ sin\varphi \end{pmatrix}$, where φ is angular coordinate of a polar coordinate system. Integrating along z-axis, the integral becomes $\delta^2 \int_0^{2\pi} cos^2\varphi\, d\varphi = \pi\delta^2$. Hence, the separation between a pair of isotropic sources in a 2D acoustic medium is given by

$${\sigma_\tau}^2 = \frac{\delta^2}{2v^2}. \tag{2.30}$$

For earthquakes (double-couple sources), the relation is (Snieder and Vrijlandt, 2005)

$$\sigma_\tau{}^2 = \frac{\left(\frac{6}{\alpha^8} + \frac{7}{\beta^8}\right)\delta_{\parallel\text{Fault}}{}^2 + (\frac{1}{\alpha^8} + \frac{2}{\beta^8})\delta_{\perp\text{Fault}}{}^2}{7(\frac{2}{\alpha^6} + \frac{3}{\beta^6})}, \tag{2.31}$$

where $\delta_{\parallel\text{Fault}}$ and $\delta_{\perp\text{Fault}}$ are components of source displacement parallel and perpendicular to the fault, respectively, and α and β are the *P*- and *S*-wave velocity, respectively. This equation constrains the source separation to lie on an ellipsoid with a symmetry axis perpendicular to the fault plane. For two earthquakes located on the same fault plane, which is often the case for aftershork sequences, the perpendicular component vanishes and equation 2.31 simplifies to

$$\sigma_\tau{}^2 = \frac{\left(\frac{6}{\alpha^8} + \frac{7}{\beta^8}\right)\delta^2}{7\left(\frac{2}{\alpha^6} + \frac{3}{\beta^6}\right)}. \tag{2.32}$$

In equation 2.32, velocities of both P- and S-waves are raised to high powers. Hence, in cases for earthquakes in the same fault plane S-waves dominate, as $\beta < \alpha$. The dominance of S-wave energy has also been observed by Aki and Chouet (1975), Weaver (1982), and Snieder (2002b).

Equations 2.31 and 2.32 involve the quantitative magnitude (length) of the source displacement, while the orientation information is lost. This is because the derivations of the relationships between $\sigma_\tau{}^2$ and δ^2 all involve a weighted integration over all directions that the waves could leave the source. The direction of the perturbation therefore cannot be solved from these relations. In an earthquake cluster, the relative direction of the separations of event pairs can be retrieved by solving a multi-variable optimization problem (Robinson et al., 2013), which will be introduced in Chapter 4.

2.3 Foldy modeling

In the numerical example below I apply CWI to estimate inter-source separation between a pair of events. The waveforms used are generated with the modeling code developed by Galetti et al. (2013) – a simple and exact acoustic wavefield modeling method, based on the theory of multiple scattering introduced by Foldy (1945). The code calculates the signals in the frequency domain. Unlike the extensively used, grid-based modeling techniques, such as the finite difference (Moczo et al., 2007; Thorbecke and Draganov, 2011) and finite element (Komatitsch et al. 2010; Torabi and Rayhani, 2014) methods which allow different types of complexity to be included in the medium, the Foldy code simply applies isotropic point-scatterers as heterogeneities in the medium with a constant background velocity, which makes the simulation computation efficient, and it does not require large storage space. Besides, modeling methods like finite difference approximate the partial derivatives in the equations of motion with linear combinations of function values at grid points (Kelly et al., 1976). A coarse grid and a low order of derivatives can lead to numerical errors in the waveforms generated, and these may be transferred to the result of the subsequent processing or interpreting procedures. In that case, it may be difficult to distinguish errors produced by the algorithms being tested from those caused by the modeling method as shown by Galetti et al., (2013). Hence, I validate the theory of CWI with the waveforms generated using the Foldy code developed by Galetti et al. (2013) in a point-scatterer medium - as assumed in the derivation of CWI theory.

The Foldy code used simulates the acoustic wavefield excited by monopole or dipole sources and is recorded by monopole or dipole receivers. The impulse-response of a monopole source is estimated using the analytical Green's function in the frequency domain (Snieder, 2009), while that of a dipole source is analytically calculated from

the spatial derivative of the monopole Green's function. These analytical Green's functions constrain the velocity of the modeled direct and scattered waves to be constant, but also ensure that waveforms are exact and free from numerical errors which is desirable when testing new theories and algorithms. The isotropic point scatterers are treated as diffractors that scatter spherically symmetric acoustic waves. The scattered wavefield is modeled by computing all possible interactions between the scatterers in the model domain and using an exact solution to the infinite scattering series (Galetti et al., 2013). The remainder of this section provides a brief description of the Foldy method, using notation consistent with Galetti et al. (2013).

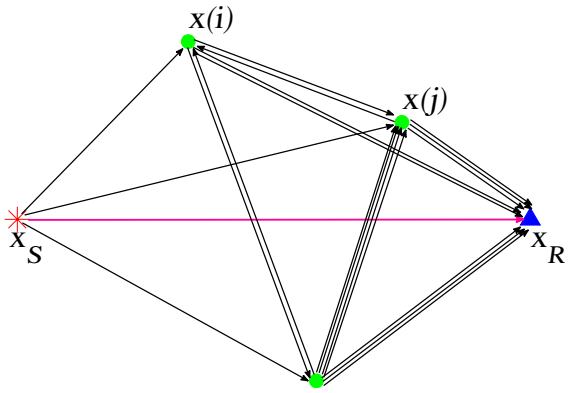

Figure 2-3: Sketch of the scattering theory assumed. The star, triangle, and dots represent the source, receiver and point-scatterers, respectively. Replicated from Galetti et al. (2013).

In a medium with N randomly distributed isotropic point scatterers and a constant background velocity, an impulsive source and a receiver are located at position x_S and x_R, as displayed in Figure 2-3. The total wavefield $\Psi(x_R)$ recorded at x_R is made up of two components - the direct wavefield $\Psi_0(x_R)$ from x_S to x_R, and the scattered wavefield:

$$\Psi(x_R) = \Psi_0(x_R) + \sum_{i=1}^{N} \Psi\left(x^{(i)}\right) A^{(i)} G\left(x_R, x^{(i)}\right), \tag{2.33}$$

where the summation term on the right-hand side gives the scattered wavefield arriving at x_R. $\Psi\left(x^{(i)}\right)$ denotes the total wavefield arriving at scatterer i located at $x^{(i)}$, $G\left(x_R, x^{(i)}\right)$ refers to the Green's function from $x^{(i)}$ to x_R, and $A^{(i)}$ is the scattering amplitude of scatter i. The code calculates the wavefields in the frequency domain. $A^{(i)}$ is a complex number, whose imaginary part must have a value that falls within a specific range to assure conservation of energy. Energy loss is assumed to be caused only by geometrical spreading. The direct wavefield $\Psi_0(x_R)$ can be expressed as the Green's function (impulse response) from x_S to x_R convolved with a source wavelet $s(\varpi)$:

$$\Psi_0(x_R) = s(\omega) G(x_R x_s). \tag{2.34}$$

By the same reasoning, the total wavefield $\Psi\left(x^{(i)}\right)$ arriving at scatterer i comprises the direct wavefield $\Psi_0\left(x^{(i)}\right)$ from the source x_S and the scattered wavefield from every other scatterers j $(j = 1,2, \dots, N;\ j \neq i)$:

$$\Psi\left(x^{(i)}\right) = \Psi_0\left(x^{(i)}\right) + \sum_{\substack{j=1 \\ j \neq i}}^{N} \Psi\left(x^{(j)}\right) A^{(j)}\, G\left(x^{(i)}, x^{(j)}\right), \tag{2.35}$$

Equations 2.35 represents a group of linear equations when there is more than one scatterer in the model domain. By moving the summation term on the right-hand side of the equal sign to the left, and arranging the terms $A^{(j)} G\left(x^{(i)}, x^{(j)}\right)$ into an N-dimensional square matrix $\mathbf{M}$, the linear equation system can be written in vector form:

$$-\mathbf{M}\boldsymbol{\Psi} = \boldsymbol{\Psi}_\mathbf{0}, \tag{2.36}$$

where vectors $\boldsymbol{\Psi}$ and $\boldsymbol{\Psi}_\mathbf{0}$ respectively contain the total and direct wavefields reaching each scatterer, and matrix $\mathbf{M}$ contains the interactive terms between the scatterers. The total wavefield $\Psi\left(x^{(i)}\right)$ arriving at each scatterer can thus be estimated by inverting equation (2.36), once $\boldsymbol{\Psi}_\mathbf{0}$ and $\mathbf{M}$ are estimated with

equation (2.34) using the Green's function formulae given in Snieder (2009)

$$\boldsymbol{\Psi} = -\mathbf{M}^{-1}\boldsymbol{\Psi}_{\mathbf{0}}. \tag{2.37}$$

Inserting the total wavefield arriving at each scatterer into equation (2.33), the exact total wavefield from a monopole source propagating through a homogeneous medium with randomly distributed point scatterers and recorded by a monopole receiver can be calculated. If a dipole source or receiver is used, as required for example in seismic interferometry (Wapenaar et al., 2010a, 2010b; Galetti et al., 2013), differentiation needs to be performed either at the terms "from" the source - $\Psi_0(x_R)$ and $\Psi\left(x^{(i)}\right)$ or at terms "to" the receiver $\Psi_0(x_R)$ and $G\left(x_R, x^{(i)}\right)$. The only other possible source of errors could be the finite length of a real number stored by the computer and inaccuracy in the inversion of matrix $\mathbf{M}$.

2.4 Synthetic examples

Generating waveforms

In this section, I validate CWI using synthetic waveforms generated with the Foldy code in a simple point-scatterer medium. In order to obtain multiply scattered waves, I used 150 randomly distributed point-scatterers in a $16km \times 16km$ model with a constant velocity of $350\, m/s$. The frequency of the dominant components in the waveform is $1.5\, Hz$, and the maximum frequency modeled is $20\, Hz$. Figure 2-4 shows the 2D model domain I use, where there are two identical isotropic sources (red and blue stars) in the center and a receiver (blue triangle) in the top left. The wavefields emitted from the two sources and recorded at the receiver are shown in Figure 2-5 a and b, respectively. The superposition of the two waveforms (Figure 2-5 c) shows their high level of similarity. This indicates that the assumption that in the pair of wave trajectories, only the path from source to the first scatterer differs and all the subsequent sections of the trajectory stay the same, is well satisfied. I then use

these waveforms to apply CWI to measure the separation between the two sources.

Applying CWI

A MATLAB script was written for estimating inter-source separations based on the theory of CWI. In the script, a sequence of non-overlapping time windows is applied along the two waveforms, which is followed by the calculation of the correlation coefficient for each window, leading to the standard deviation of the traveltime differences of waves arriving within each window. The separation between the two sources is then computed from equations 2.20 or 2.22 depending on source and medium type. Thus each time window produces its estimate of the source separation, and the estimates given by different windows provide a measure of uncertainty.

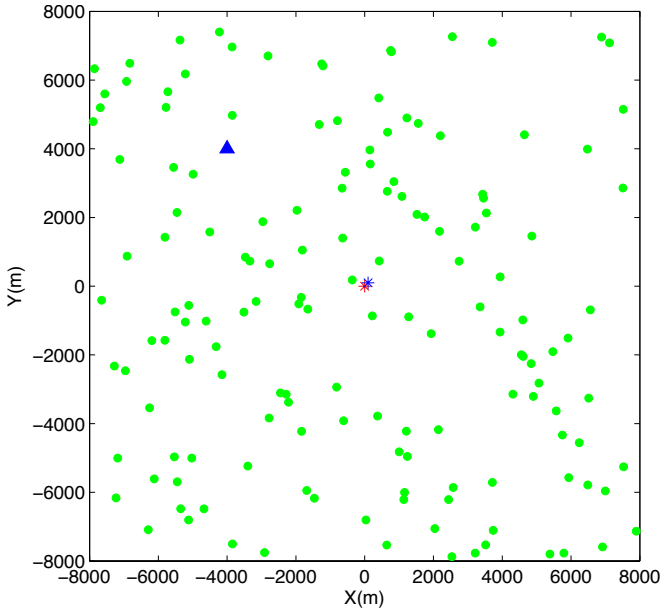

Figure 2-4: The 2D point-scatterer model. Blue and the red stars represent two sources with locations (0,0) and (40,40), respectively. The triangle represent the receiver. Green dots are 150 randomly distributed point scatterers.

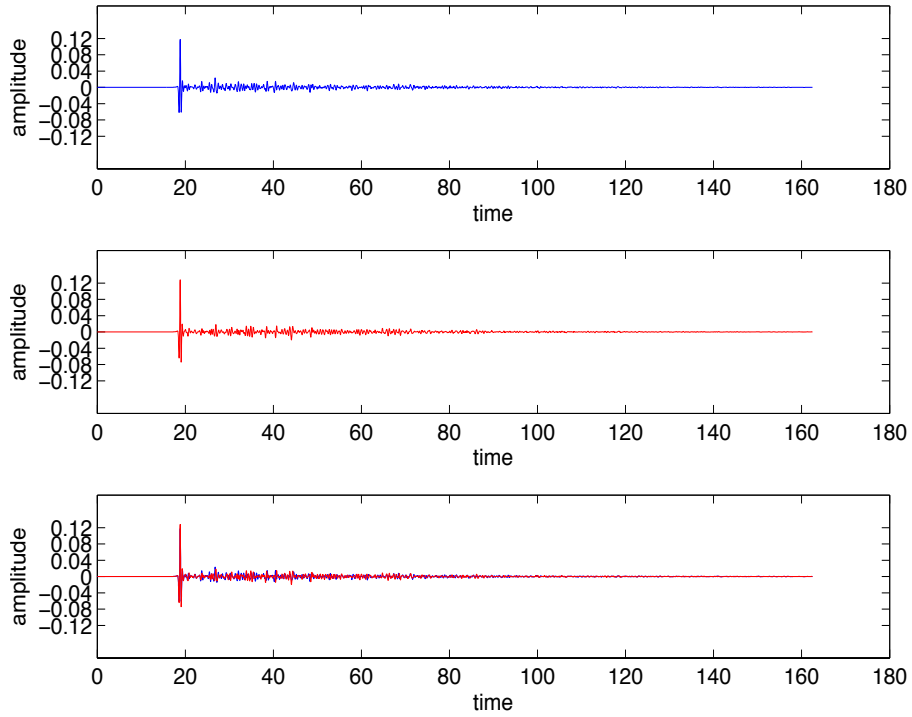

Figure 2-5: Scatterered waveforms. Panels (a) and (b) show the recorded waveforms from the two sources in Figure 2-4; panel (c) shows their superposition.

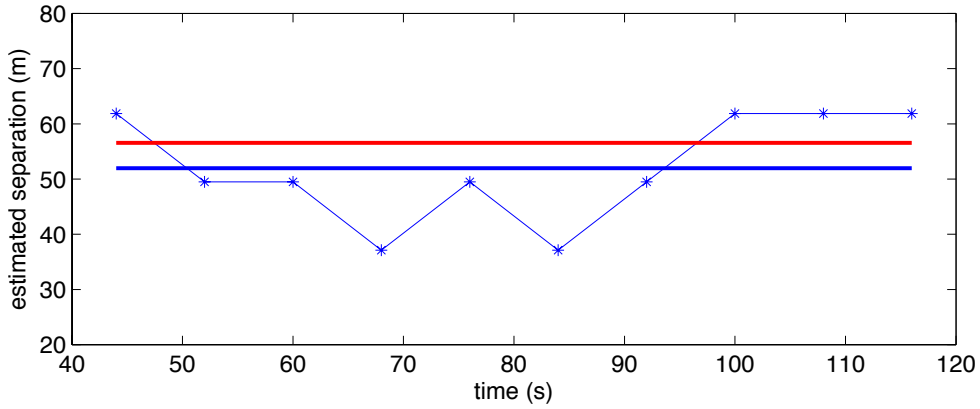

Figure 2-6: Source separation estimates derived from ten time windows along the coda of the waveforms. The blue stars and the thin line show the estimates of each time window, with the x-coordinates indicating the center of the windows. The bold line in blue and red are the mean of the estimated separation and the actual separation, respectively.

With the two modeled multiply scatterered waveforms, I take coda from 40s to 120s, divided into ten time windows with a length of 8s and apply CWI. Equation 2.20 is used as isotropic sources are applied in an acoustic medium in the experiment, and the factor 1/3 is replaced with 1/2 as the model is in 2D (Snieder and Vrijlantd, 2005). Figure 2-6 shows the estimated source separations from the 10 time windows. The estimated separations (blue stars) fluctuate about the actual value $56.57\,m$ (red bold line) with an average of $51.97\,m$ (blue bold line) over the 10 windows, underestimating the source separation by 8.13%. I repeat the experiment and find that, in general, the larger the true separation to be measured is, the more it is likely to be underestimated, given the true separation is less than the dominant wavelength. I do not expect exact estimation from every time window due to the probabilistic nature of the CWI method.

Examining consistency

It was suggested by Snieder (2006) and demonstrated by Robinson et al. (2011) that CWI does not require a large number of seismic stations. Here I test the stability of CWI estimation by comparing the estimates of source separation among multiple receivers at different locations. I use the same 2D model with point scatterers used in previous tests and generate multiply scattered waveforms with the Foldy code. I apply an array of 9 receivers in the medium, and the two sources in the center are 56.57m apart (Figure 2-7). The estimated separation between the two sources computed from waveforms recorded at each receiver is displayed in Figure 2-8 with uncertainties. The receivers give an overall average separation of 52.01m (blue bold line), underestimating the true source separation by 8.06%, which does not show much improvement from using a single receiver in the test shown above. The standard deviation of the estimates is $3.84m$, which is less than 7% of the actual source separation. These results show a level of consistency in the CWI estimates among individual receivers.

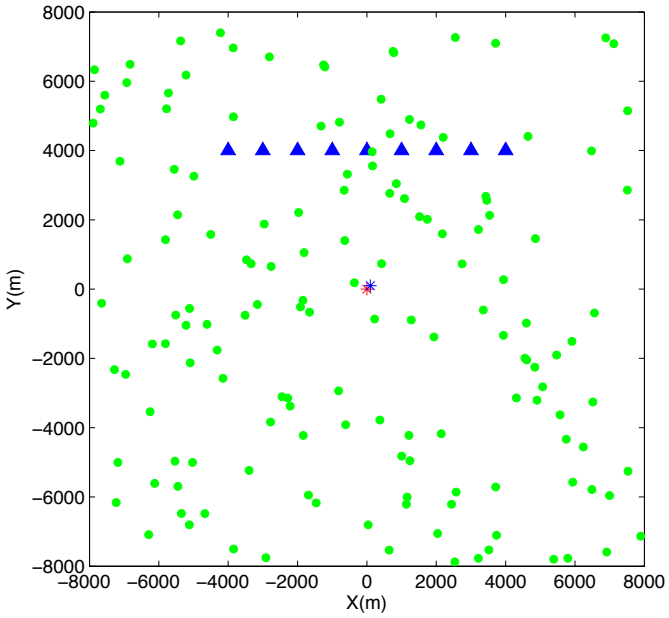

Figure 2-7: The 2D point-scatterer model. Blue and the red stars represent two sources with locations (0,0) and (40,40) , respectively. Triangles represent receivers. Green dots are 150 randomly distributed point scatterers.

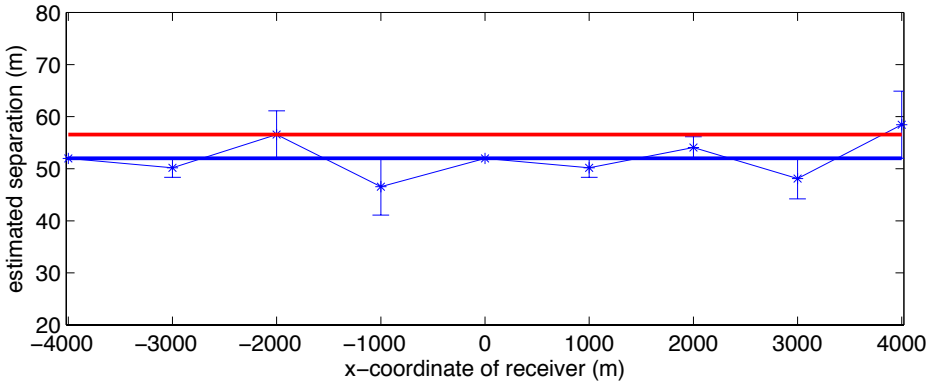

Figure 2-8: Source separation estimates given by receivers at different locations. Blue stars and error bars show the mean plus/minus one standard deviation of separation estimates from the 10 time windows of waveforms recorded by individual receivers. Blue bold line shows the overall average estimate among all receivers, and red bold line shows true separation.

2.5 Discussion and conclusion

In the synthetic example for validating my algorithm that applies CWI to estimate inter-source separations, I choose to use the Foldy method to model the multiply scattered wavefield, because unlike methods like finite difference, it uses analytically computed Green's functions and their derivatives and theoretically gives exact modeled waveforms. However, it is not absolutely error-free, and could even produce highly corrupted waveform, as shown in Figure 2-9. The cause of the corruption of modeled waveforms could be inaccuracy in calculation on the inverse of matrix $\mathbf{M}$, which contains the interactive terms of between point scatterers. In order to examine my hypothesis, I create two models with which corrupted and non-corrupted waveforms are created respectively, allowing us to analyse the corresponding $\mathbf{M}$ matrixes.

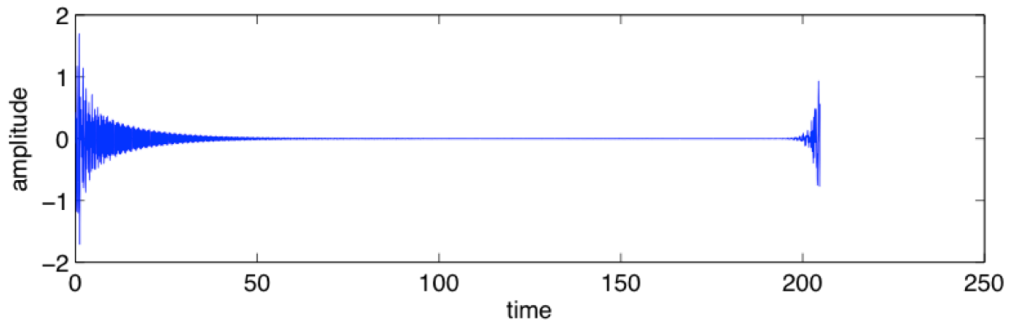

Figure 2-9: An example corrupted waveform generated using the Foldy code (Galetti et al., 2013).

The two models are of sizes of $200 \times 200m^2$ and $20000 \times 20000m^2$, respectively. They both contain 50 point scatterers whose positions are identical relative to the size of the two models. The deployment of source and receiver in both models is identical to of that shown in Figure 2-4. Both models have a constant

background velocity of 400m/s, the source has a central frequency of 2Hz hence a dominant wavelength of 200m, and the maximum frequency modeled is 20Hz. In both models I record the waveforms as shown in Figure 2-10. The larger model (bottom panel) produces a multiply-scattered waveform as used previously, however the waveform produced by the smaller model (top panel) is clearly affected artificially by abnormally high amplitude at the front and rear where the amplitude should be zero or rather small.

As mentioned, the modeling code of Galetti et al., (2013) calculates the signals in the frequency domain. Specifically, it computes matrix $\mathbf{M}$ and its inverse $\mathbf{M^{-1}}$ for each modelled frequency, and the waveform in the time domain is then obtained by applying an inverse Fourier transform to the signal computed in the frequency domain. I therefore investigate the frequency spectrum of the waveforms (Figure 2-11). The correct waveform (bottom panel) does have a central frequency at 2Hz as designed, while the corrupted waveform (top panel) does not seem to have a central frequency – some (many) frequencies are wrongly solved. This may by due to poor inverse estimate of $\mathbf{M^{-1}}$ at these frequencies, which is likely because their matrixes $\mathbf{M}$ are close to singular.

As the level of singularity of a matrix is measured by its condition number, I compute the condition number of matrix $\mathbf{M}$ for all modelled frequencies (Figure 2-12). The condition number spectrum of the correctly computed waveform (bottom panel) has a single peak at very low frequency (0.05 Hz), and the condition number of $\mathbf{M}$ is lower than 15 after 0.2Hz. On the contrary, the spectrum of the corrupted waveform (top panel) is multimodal, with condition number much larger at other frequencies than their counterpart for the correct waveform. Such condition number distributions of the two waveforms indicates that matrix $\mathbf{M}$ for most frequencies of

the corrupted waveform have much higher levels of singularity than those of the correct waveform. Recall that all elements of the two models are in proportion to the model sizes, except that they have identical dominant wavelength of 200m, which is equal to the side length in the smaller model, while it is equal to 1% of the side length in the larger model. In other words, the only differences in the two modelling runs is that their side length, hence the inter-scatterer distances relative to dominant wavelength, differs by 100 times. As matrix $\mathbf{M}$ contains all of the interactive terms between scatterers, the distances between scatterers relative to the dominant wavelength is the cause of ill-conditioning in matrixes $\mathbf{M}$, in turn causing poor inversion and poor solution of the waveform to be generated.

The purpose of using the Foldy code is to validate the algorithm and the implementation of CWI, which requires the inter-scatterer distances to be much larger than the dominant wavelength of the waveforms (Snieder and Vrijlandt, 2005). Therefore, in this case, I do not expect to get corrupted modelled waveforms, provided the aforementioned requirements of CWI are satisfied when designing the experiments. However, when the Foldy code is used to generate waveforms for the purpose involving other theories and methods, one is suggested to pay attention to the model size or inter-scatterer distances relative to the dominant wavelength of signals being modelled to avoid corrupted signals.

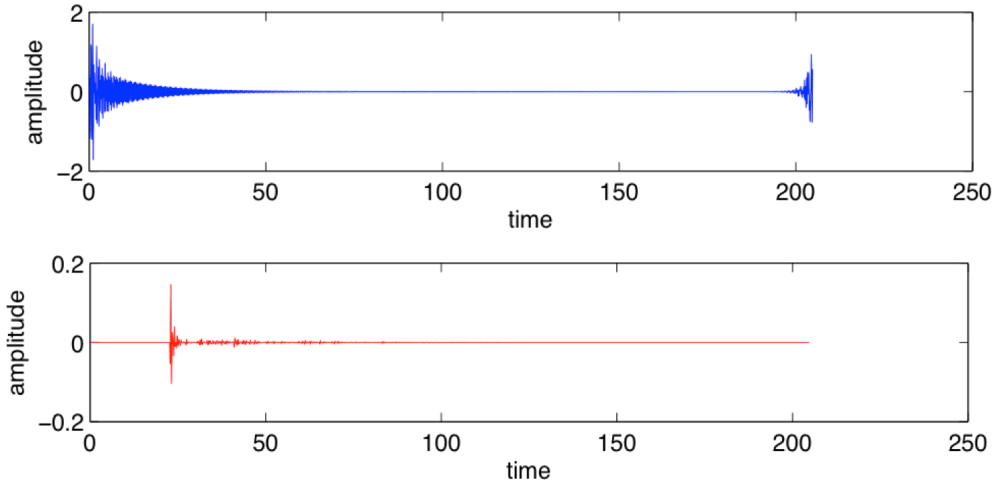

Figure 2-10: Waveforms in time domain. The top and bottom panels show the waveforms generated by the small and large model described in the main text, respectively.

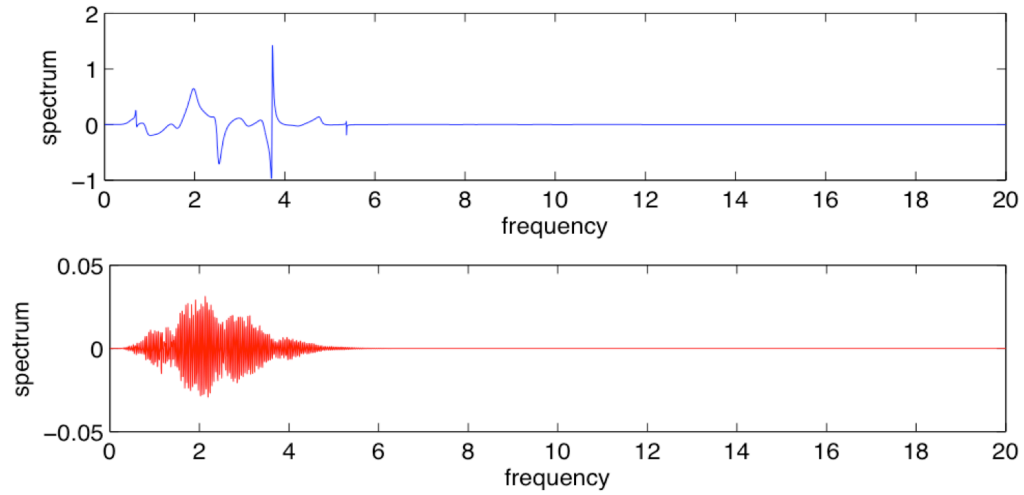

Figure 2-11: Frequency spectrum of waveforms generated in the small (top) and large (bottom) model described in the main text, respectively.

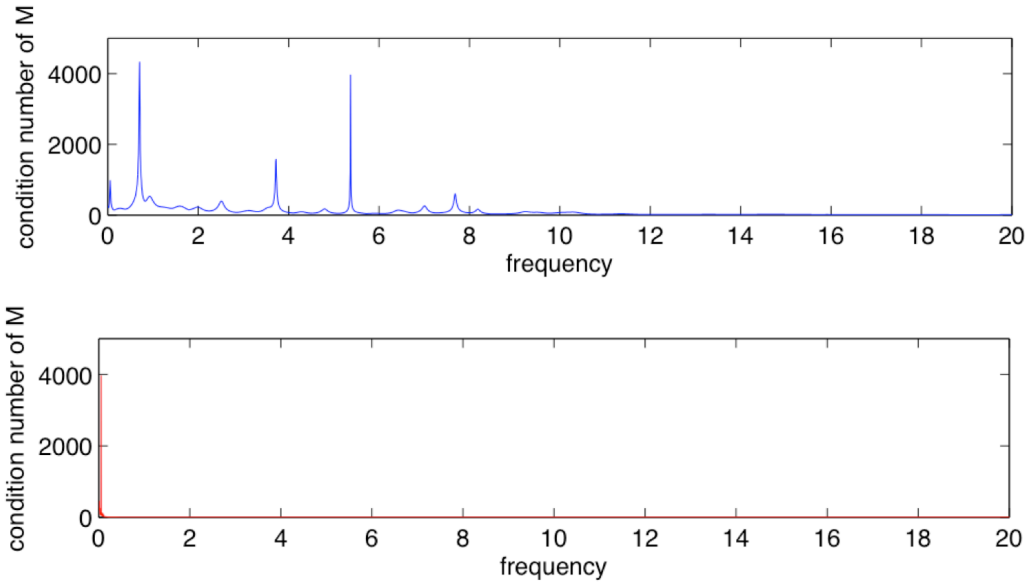

Figure 2-12: Condition number spectrum of matrix **M** of waveforms generated in the small (top) and large (bottom) model described in the main text, respectively.

In the synthetic experiments, I validate my implementation of the CWI method for estimating separation between a pair of sources in a point-scatterer medium where the distance between the sources is much smaller than the dominant wavelength of the waveforms. It is found that CWI estimates tend to be lower than the corresponding true values. Also, although individual receivers at different locations, to some extent, give consistent results, their estimates fluctuate about the true separation, and the uncertainty given by each receiver varies. This could be attributed to the minute difference in local scattering properties, which leads to inconsistent fulfillment of the assumptions in the theory. Therefore, more tests are needed in point-scatterer medium with different scattering properties, such as density of scatterers and scattering intensity. In addition, further tests are also needed in more complex types of velocity structures than point-scatterers with a constant background velocity, where more sophisticated modeling technique than Foldy is required.

3

ESTIMATING SOURCE SEPARATION USING CWI IN MODELS WITH VARYING COMPLEXITIES AND TYPES OF PRIOR INFORMATION

Estimating source separation is a relatively new type of application of CWI, it is therefore important that it is tested in synthetic experiments before being applied to real data. In this chapter, we test the performance of CWI with four series of experiments: in point-scatterer medium as presumed in the theory therefore used as reference for later tests; in media with horizontal layers, a fundamental structure type of the Earth subsurface; in media with different combinations of the two types of heterogeneities; and finally in the more realistic Marmousi model. It is found that in a point-scatterer medium with favorable properties, CWI gives accurate estimate of source separation for an event pair with a true separation up to a quarter of the dominant wavelength, after which it has an increasing tendency of underestimating until the true separation reaches 0.4 of the dominant wavelength where only an estimate of the lower bound of the source separation can be obtained. In media with parallel layers, although CWI shows limitations in estimating the source separations between events with some certain relative locations, it can be improved by including a small amount of point scatterers. In the Marmousi model, the accuracy of separation estimates obtained is very similar to the reference, when the assumptions in the theory does not adequately describe the data. The results of our tests will help understand and interpret the source separation estimates therefore relative locations using CWI in future applications.

3.1 Introduction

Seismic coda consists of the extended signals in the later part of seismograms that arise from multiple scattering. It is discarded in many seismological applications due to its complex appearance with few uniquely identifiable arrivals. However, coda is extremely sensitive to minute changes in seismic systems, therefore can be used to

measure changes between two seismic states that are too small to be identified from conventional techniques that use the first or early arrivals of the waveforms. Studies of coda were initiated by Aki (1969) who used the spectrum of coda from local earthquakes to estimate seismic moments. Later applications include attempts at earthquake forecasting from temporal change in coda attenuation intensity (Sato, 1986), measuring scattering coefficient from relative coda duration (Robinson, 1987), studying intrinsic and scattering attenuation (van Wijk et al., 2004), etc. The more recently developed technique coda wave interferometry (CWI) (Snieder et al., 2002; Snieder 2006), using phase information of individual waves in coda in a statistical manner, can be applied to determine minute relative changes of wave velocity, seismic (Pacheco & Snieder, 2005; 2006) or in laborotary (Snieder et al., 2002; Grêt et al., 2006); and to measure changes in scatterer displacements of the propagating medium, thus to monitor volcanoes (Grêt et al., 2005) and to study turbulent fluid with neutrally buoyant particles (Cowan et al., 2000; 2002; Page et al., 2000; Snieder, 2006). A third type of application of CWI is to estimate the separation between a pair of seismic events with identical source mechanism (Snieder & Vrijlandt, 2005; Robinson et al., 2011), which can be used for accurate relative source location (Robinson et al., 2013; Zhao et al., 2017).

The three types of CWI applications all rely on crosscorrelation of coda in waveforms recorded at the same seismic station. It extracts statistical characteristics of the changes in arrivals in coda from the crosscorrelations that can be used to estimate velocity change, scatterer displacement or difference in source locations. The three types of changes result in different statistical behavior in coda arrivals, hence in theory, could be distinguished and estimated separately, however it is beyond the scope of this study. This chapter focuses on estimating source separations between seismic events, which can be used to determine the relative locations of a

cluster of events. Unlike the widely-used travel or delay time source location methods that use the first or early arrivals of seismograms, such as the double difference location (Waldhauser and Ellsworth, 2000; Bai et al., 2006) and the master event location (Ito, 1985; Deichmann and Garcia-Fernandez, 1992), CWI does not require a dense seismic network with good source-stations azimuthal coverage, because it makes use of a much larger part of the seismogram. In fact, it is possible to locate a cluster of earthquakes using only a single-channel station (Zhao et al., 2017). This makes CWI a favorable alternative to the conventional methods in areas without a large number of seismic stations.

The theory of CWI assumes the propagating medium having a uniform background velocity, with heterogeneities being point scatterers (Snieder 2006). We test the CWI in media with pseudo-randomly distributed point scatterers with a range of physical properties, such as scatterer density and heterogeneity intensity, using seismic waves generated with finite-difference modeling. However, point-scatterer media are far from adequate in simulating the real Earth, which generally contains stratigraphic layers and heterogeneities of various sizes. Hence, it is essential to test CWI in more realistic Earth models before applying it to solve real-word problems. In this chapter, we first evaluate the performance of CWI in point-scatterer media with different properties, and use the results as a reference. We then test CWI in a medium consisting of parallel layers, which provides us with knowledge on how the performance of CWI is affected by layers alone. Next, we add point scatterers to the layered medium to examine CWI's behavior under the influence of the two types of basic heterogeneities that have been studied. Next, we apply CWI in the Marmousi model, in order to gain a better understanding of how effective the CWI technique would be in a more realistic Earth model. Finally, we also had an attempt in an elastic version of the Marmousi model.

As CWI uses waveform crosscorrelation to estimate source separations, the method is naturally subject to cycle skipping issues where the two events are too far apart from each other, and source separations tend to be underestimated, as observed in Chapter 2. For event pairs with even larger separations, CWI only gives an estimate of the lower bound of the separations. A rule of thumb of the applicable range of techniques relying on crosscorrelation to distinguish waveform differences is that the maximum event separation, after which local earthquake recordings become incoherent, is about a quarter of the wavelength of the highest frequency (Geller and Mueller, 1980). The reminder of this chapter uses synthetic tests to explore the applicable range and performance of CWI in point-scatterer media as assumed in the theory, as well as other media with different levels of resemblance to the real Earth.

In our synthetic experiments, the seismograms are generated by solving the acoustic wave equation with a staggered-grid finite-difference (FD) solver. The models for the point-scatterer media (Figure 3-1a), layered medium (Figure 3-5a), and the scatter-layer combined media (Figure 3-8) are created with 4000×4000 grid points, with grid spacing in both x and z directions being 10m and time step being 0.001s. The Marmousi model (Figure 3-10a) is created with 2400×10000 grid points, with grid spacing for depth and distance being 1.249m and time step being 0.0002s. A Ricker wavelet is used with a center frequency of 5Hz in all experiments. At least 45 samples per wavelength are taken in each simulation, numerical dispersion is thus minimized.

3.2 CWI in point-scatterer media

Here we use a series of point-scatterer media with different parameters to explore factors that have influence on the performance of the CWI technique. The point scatterers are not actually points that don't have a size, but circles with a radius of 8 grids, having a velocity distribution as a 2-D Gaussian function. Figure 3-1a shows the velocity model of a point-scatterer medium we use, with a uniform background velocity of 3000m/s. It contains 250 uniformly-distributed point scatterers with the maximum velocity difference Δv of 600m/s appearing in the center of each scatterer. 9 receivers are applied, and 16 sources are arranged in two geometries, a cluster and a straight line, as set1 and set2 (Figure 3-1b and c).

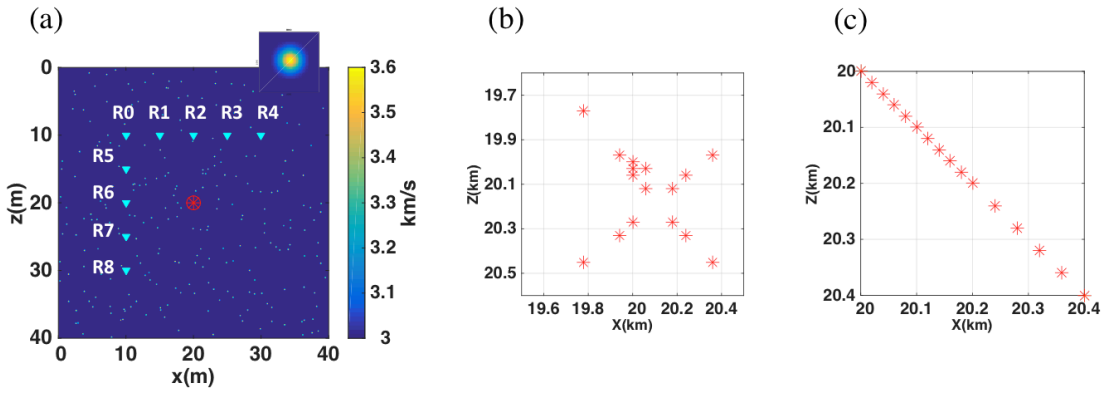

Figure 3-1: Synthetic tests with point-scatterer media. (a) shows the velocity model, where the circle with a star inside represents the source region, and the triangles represent receivers. The zoomed panel shows a point scatterer. (b) and (c) show the events of source set1 and set2, respectively.

CWI is applied with waveforms recorded by each receiver. For each pair of waveforms, four time-windows are taken from coda to estimate the source separations, and the average of the four estimates is plotted against their

corresponding true separations to assess the performance of CWI. Figure 3-2a and b show the estimate of source separation for the 120 event pairs made up of the 16 sources in set1 and set2, where both the estimated and the true separations are normalized by the dominant wavelength λ_d of the waveforms. The dashed line is $y = x$, representing the estimated source separation equals the true value. For both sets of sources recorded by most of receivers, the estimates are reasonably accurate for event pairs with true separations $\delta_{true} \leq 0.25\lambda_d$, after which there is a growing trend of underestimation, and for $\delta_{true} \geq 0.4\lambda_d$, CWI only gives an estimate of the lower bound of the separations. It can be summarized that in point-scatterer media, estimation of source separations are consistent among individual receivers, regardless of their locations. The highly similar separation patterns obtained from source set1 and set2 demonstrate that source geometry does not have impact on the performance of CWI in such media. The reason for this is that the scatterers are distributed uniformly, thus wherever the receivers are relative to the sources, and however the close-by sources are distributed, coda of recorded waveforms contain multiply scattered waves that originally leave the sources from all possible directions, satisfying the assumptions in the derivation of the theory (Snieder & Vrijlandt, 2005).

We also test the influence of the amount of scatterers and the velocity difference of the scatterers upon the background on CWI performance. Figure 3-3a-d show the estimation of source set1 using 10, 30, 50 and 600 point scatterers with a maximum velocity difference of $\Delta v = 600m/s$. Experiments with a medium containing as few as 10 point scatterers start to show a trend in the results recognizable as those obtained with much more scatterers, yet the separations are significantly underestimated with large uncertainties. Increasing the number of scatterers to 30 remarkably improves the estimation, while 50 scatterers leads to results with similar

accuracy as those derived with 250 scatterers (see Figure 3-2a), which is equally accurate with 600 scatterers with almost identical level of uncertainty. Hence, increasing the amount of heterogeneities would significantly improve the performance of CWI where scatterers are rare, while it no longer affects the results once the amount of scatterers reaches a certain level. This is because CWI relies on a time-window of a limit length in coda containing waves leaving the source from all directions, which becomes better satisfied as the number of scatterers increases from a very small number, until this requirement is met. These experiments are repeated with a higher maximum velocity difference of $\Delta v = 1800 m/s$. It is found that larger velocity difference of heterogeneities leads to lower estimation uncertainly in all cases, when compared panels e-h with panels a-d of Figure 3-3.

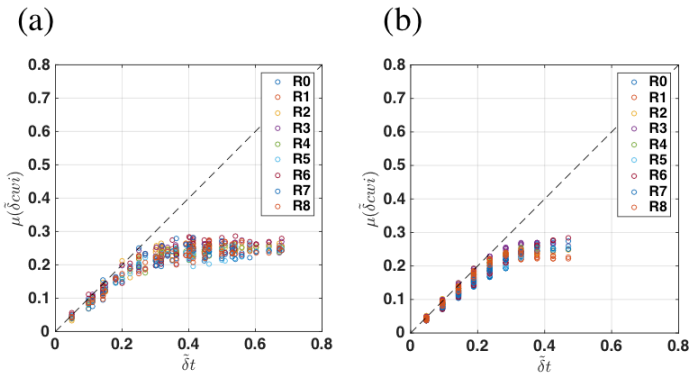

Figure 3-2: Source separation estimates calculated from recordings from individual receivers. (a) shows the results of source set1, (b) shows the results of source set2.

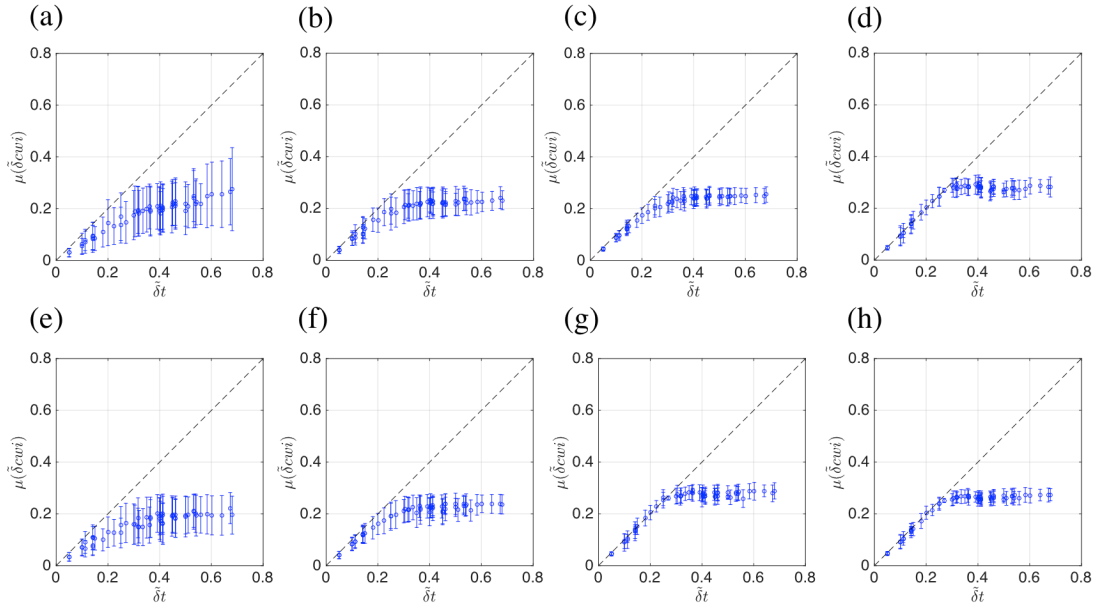

Figure 3-3: Source separation estimates calculated from recordings from all receivers, shown as mean ± standard deviation for each event pair. The top row (panels a-d) shows the results with point scatterers with a maximum velocity difference of $\Delta v = 600m/s$, and the bottom row (panels e-h) shows the results with point scatterers $\Delta v = 1800m/s$. The columns from left to right show the results of tests with 10 (panels a and e), 30 (panels b and f), 50 (panels c and g) and 600 (panels d and h) point scatterers.

3.3 CWI in layered medium

Stratigraphic layers are one of the most fundamental structures of the Earth's subsurface. To test the performance of CWI in layers, we create a synthetic model (Figure 3-4a) using the S-wave velocity, denoted as v_0, taken from the Continental Parametric Earth Model (PEM-C) (Dziewonski, et al. 1975), a 1-D reference Earth model that reflects different properties of the continental crust and upper mantle. The

$40km \times 40km$ model space is then divided into 400 horizontal layers of equal thickness, the velocity v of each layer is pseudo-randomly taken from a Gaussian distribution whose mean and standard deviation being v_0 and $0.15v_0$.

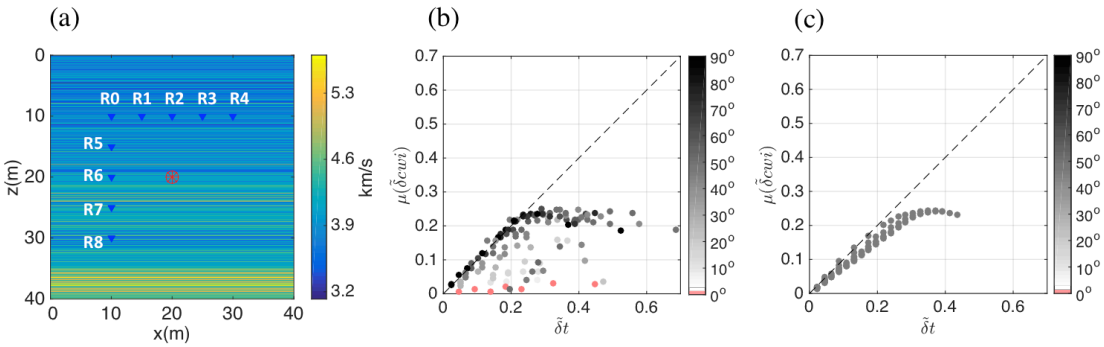

Figure 3-4: Synthetic tests with layered media. (a) shows the velocity model, where the circle with a star inside represents the source region, and the triangles represent receivers. (b) and (c) show the source separation estimates of events of set1 and set2, where the size angle θ of the event pairs are indicated with the colorbar.

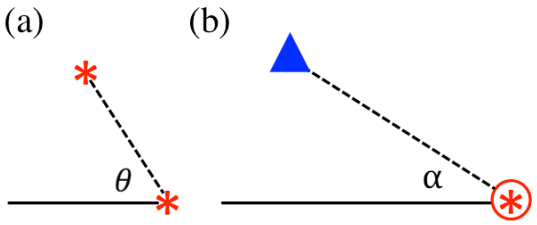

Figure 3-5: Definition of angle θ (panel a) and angle α (panel b). The circle with a star inside represents the source region, the stars represent individual sources, and the triangle represents a receiver.

CWI is applied to source set1 and set2 to estimate the source separations. Here we define two angles for easier referring when analyzing the results, that θ represents the acute or right angle ($\theta \leq 90^o$) formed by the straightly line linking a pair of sources and the orientation of the layers (Figure 3-5a); and that α represents the acute or right angle ($\alpha \leq 90^o$) formed by the straight line linking a receiver and the source region with the orientation of the layers (Figure 3-5b). Figure 3-4b displays the results given by receiver R1 in the horizontal array, where the source separation estimates of source set1 are shown with colored dots, whose colors represent the size of angle θ formed by the event pairs. Although the pattern formed with these dots as a whole seems erratic compared to those formed in the point-scatterer media, the dots for event pairs with $\theta \geq 30^o$ are close enough to the dashed line that represents exact separation estimates for us to conclude that CWI has produced reliable separation estimates for event pairs with $\theta \geq 30^o$ using receiver R1. In source set2, every event pairs has an angle θ of 45^o, i.e. $\theta \geq 30^o$, hence we should expect CWI to produce reasonably accurate results. Figure 3-4c shows the separation estimates of source set2 given by the same receiver, where, as expected, CWI performs at a similar level to what it does in the point-scatterer media.

We then explore the performance of CWI with different source-receiver positions relative to the layers, by looking into the estimates given by receivers at different locations. To this end, we use source set2 so that angle θ is fixed (at 45^o) for all event pairs. Figure 3-6 displays the results given by receivers R0, R2 and R4 from the horizontal array and receivers R6, R7 and R8 from the vertical array. CWI works approximately equally well for all receivers in the horizontal array (also see Figure 3-4c for R1) and receiver R8 in the vertical array, all of which have angle $\alpha \geq 30^o$; while less accurate results are produced by receivers R6 and R7, which have angle $\alpha < 30^o$. Here we summarize that CWI has produced reliable separation estimates

for receivers with $\alpha \geq 30^o$ for a favorable angle θ. Note that the relative position of angle θ and α doesn't have impact on CWI's estimation, because what matters to CWI results isn't the source-receiver path, but the scatterering path of waves in coda. For instance, angle θ of source set2 co-locates with angle $\alpha = 45^o$ formed by receiver R0 with the source region (Figure 3-6a), 90^o anticlockwise away from angle $\alpha = 45^o$ of receiver R4 (Figure 3-6c), and clockwise adjacent to angle $\alpha = 45^o$ of receiver R8 (Figure 3-6f), however, the estimating results given by receivers R0, R4 and R8 do not have systematic difference.

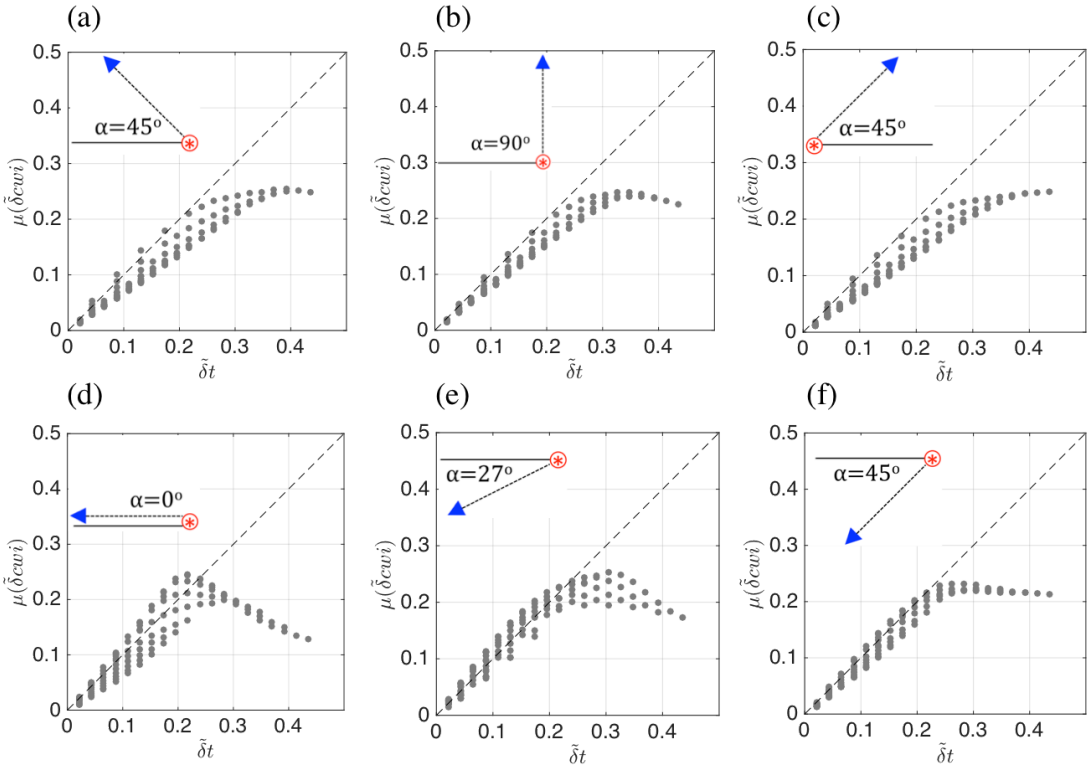

Figure 3-6: Source separation estimates of source set2 given by individual receivers in the layered medium. (a) to (c) shows results of receivers R0, R2 and R4 from the horizontal array, and (d) to (f) shows results of receivers R0, R2 and R4 from the vertical array. The angle pattern on the top-left of each panel shows angle α for the given receiver.

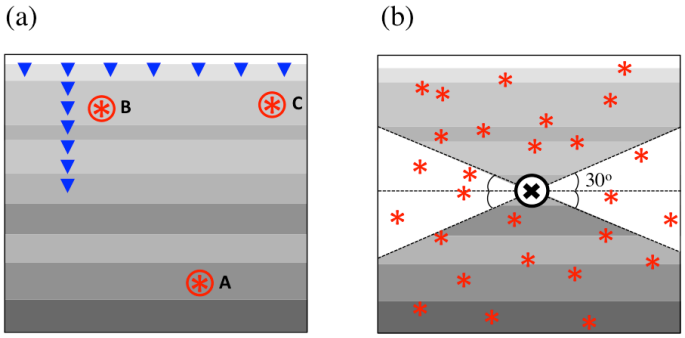

Figure 3-7: Schematic diagrams of a simplified Earth subsurface with layers. (a) shows the layered subsurface with receivers (triangles) in a surface array and in a borehole, and the circles with a star inside represent source regions with multiple events. (b) shows the layered subsurface with a cross-section of a horizontal well with receivers, and the stars represent individual sources.

The synthetic experiments conducted in the layered medium provide us with insights in predicting CWI performance in the Earth. Here we simplify the Earth by assuming the subsurface layer structures to be or close to horizontal. For naturally occurring earthquakes, if the sources are in depth as indicated by the source region A in Figure 3-7a, sensors both at surface and in the borehole have angle α large enough for CWI to produce reasonably accurate source separation estimates provided other factors being satisfactory ($\theta \geq 30^o$ for event pairs of interest, true source separations $\delta_{true} \leq 0.25\lambda_d$, reasonable signal-noise ratio in waveform coda). For shallower sources, we should expect reliable separation estimates from sensors that are not too far away in distance, as indicated by region B and C. Sensors in the borehole array could all fail for sources (in region C) horizontally distant from the borehole, while separations between events (in region B) that are very close to the borehole should be estimated accurately by most of the sensors, except for those at similar depth with the source region.

In hydrocarbon reservoir engineering and geothermal projects that involve induced events close to the sensors in the wells, knowledge learnt from our synthetic experiments can help assess the usability of CWI technique in different scenarios. Most of the sensors in vertical wells that are close to the induced events (indicated as source region B) should produce reliable source separation estimates as discussed above. Figure 3-7b shows the case where sensors in a horizontal well with induced events to all directions, where CWI should only work for events outside the white region with angle $\alpha \geq 30^o$. Moreover, in the layered medium in our experiments the performance of CWI deteriorates for event pairs with angle $\theta < 30^o$, and true separations $\delta_{true} > 0.25\lambda_d$.

3.4 CWI in scatterer-layer media

In this section, the performance of CWI is tested in media containing both types of heterogeneities, whose effects alone are tested in previous experiments. The media (Figure 3-8) are created by combining a range of numbers of point scatterers and the layers as used in the previous section. Figure 3-9 compares the CWI separation estimates of source set1 in media with 0, 30, 50 and 100 point scatterers using all receivers. Estimates of individual receivers are very consistent as expected, as all receivers form angle $\alpha \geq 30^o$ with the layers. Adding point scatterers doesn't have observable systematic influence on event pairs with angle $\theta \geq 30^o$, while the results for those with angle $\theta < 30^o$ are enhanced with the increasing amount of point scatterers. This shows that as the number of point scatterers increases, the effect of point scatterer becomes dominant over the layer structure. The real Earth contains more complicated structures than these simplified models. In the next section, CWI technique is applied in the more realistic Marmousi model.

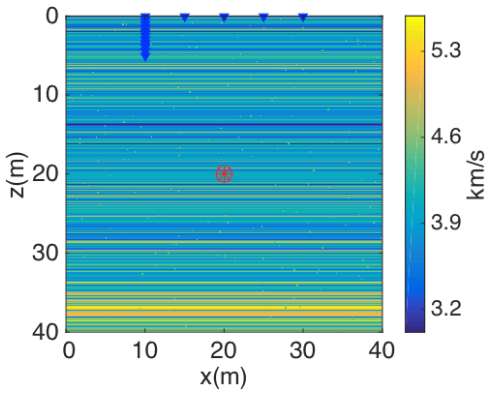

Figure 3-8: The velocity model of the scatterer-layer media, where the circle with a star inside represents the source region, and the triangles represent receivers.

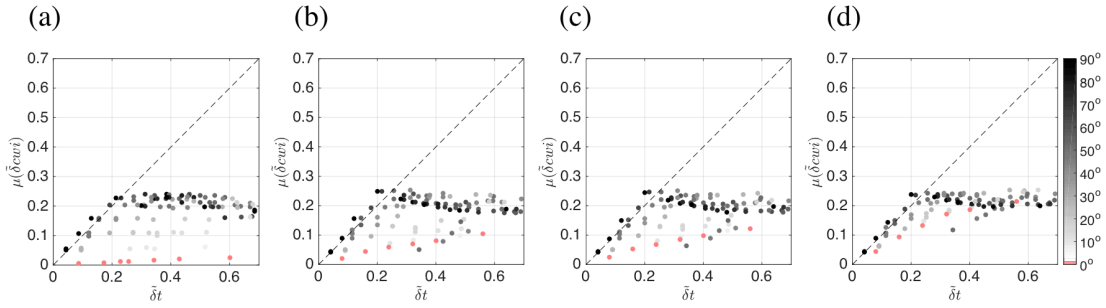

Figure 3-9: Source separation estimates of source set1 given by all receivers in: (a) the layered medium, (b-d) the scatterer-layer medium with 10, 30 and 50 scatterers.

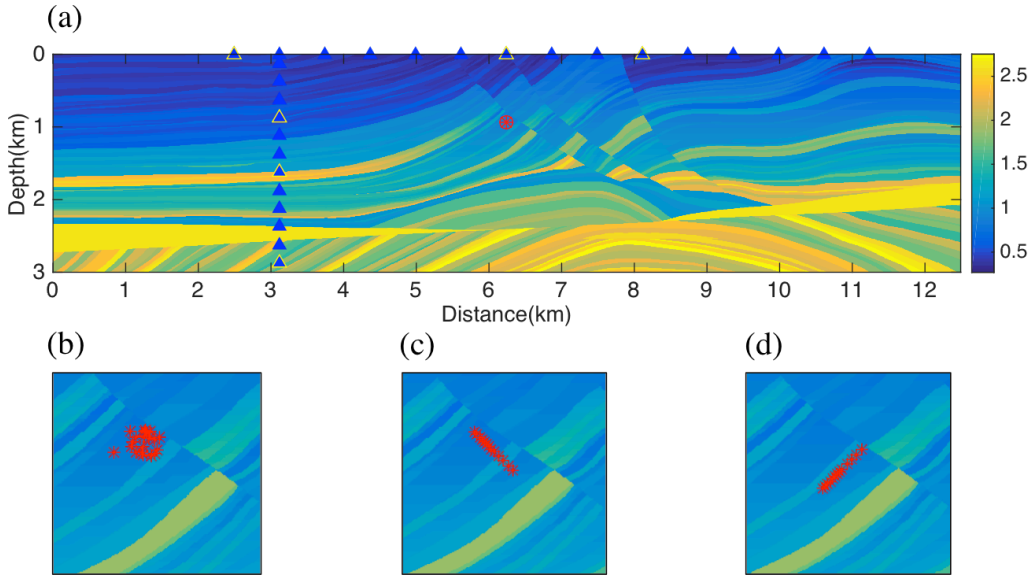

Figure 3-10: Synthetic tests with the Marmousi model. (a) shows the Marmousi model. The circle with a star inside represents the source region. The triangles represent the receivers, among which the results of those highlighted with lighter edges are displayed in Figure 3-11, 3-12, and 3-13. (b) shows source set1, containing 20 events randomly distributed as a cluster. (c) shows source set2, containing 13 events distributed in a straight line along the fault plane. (d) shows source set3, containing 13 events distributed in a straight line pseudo-parallel to the local layers and perpendicular to source set2.

3.5 CWI in Marmousi model

An acoustic case

A portion of the Marmousi model is used to test the performance of CWI in a complex Earth model. A horizontal array of 15 receivers and a borehole array of 12 receivers are applied to take recordings from three sets of sources, as shown in Figure 3-10. Source set1 contains a cluster of 20 randomly distributed events. Set2 and set3 each contains 13 events, distributing in two straight lines perpendicular to

one another. Source set1 and set2 simulate two possible scenarios of microearthquakes that could occur (inside a layer or along a fault plane). Set3 is applied here in order to investigate whether a complicated structure is able to compensate for the situation where all event pairs have angle $\theta \approx 0^o$ formed with the local layers.

The estimated results of the three source sets are shown in Figure 3-11 to 3-13, where typical results of individual receivers (R0, R6 and R9 from horizontal array, R18, R21 and R26 from the borehole array) and results obtained using all receivers in the horizontal array and in the borehole array are displayed. For all sets of sources, the estimates given by multiple receivers (Figure 3-11d, h; Figure 3-12d, h; Figure 3-13d, h) are consistent among different source geometries, and different receiver setups (horizontal array and borehole array) with similar levels of uncertainties. The estimating results of source set1 given by individual receivers (Figure 3-11a-c), colorcoded by the size of angle θ formed with the local layers, demonstrate that the complex heterogeneity combination in the Marmousi model is able to compensate for the limitation in CWI's ability to estimate source separation between event pairs with angle $\theta < 30^o$ in layered media (compared with Figure 3-4b). This is further proved with the results of source set3, where all event pairs have angle $\theta \approx 0^o$ (hence plotted in pink as shown in Figure 3-13).

All receivers in both arrays have produced similar patterns with very few outliers for the three source geometries, showing that the impact of source-receiver positions relative to the layers, described by angle α, on CWI performance in layered media are significantly reduced in a more realistic Earth model. In addition, as the estimated results are fairly consistent among individual receivers, CWI has the potential to estimate event source separations using only a single receiver, as

implemented by Robinson et al. (2013) and Zhao et al. (2017) with real data, making CWI a technique favorable in regions without dense seismic networks.

An elastic case

We also conduct a test in an elastic Marmousi model using source set1, with all the other settings unchanged. As in the acoustic experiment, individual receivers in both horizontal and borehole give consistent source separation estimates with low uncertainties, as shown in Figure 3-14 and 3-15. However, the results show a slightly lower applicable range of true separations ($0.2\lambda_d$ of the S waves) than that in the acoustic Marmousi model ($0.25\lambda_d$). In addition, the true separations in the elastic model are underestimated more than their counterparts in the acoustic case.

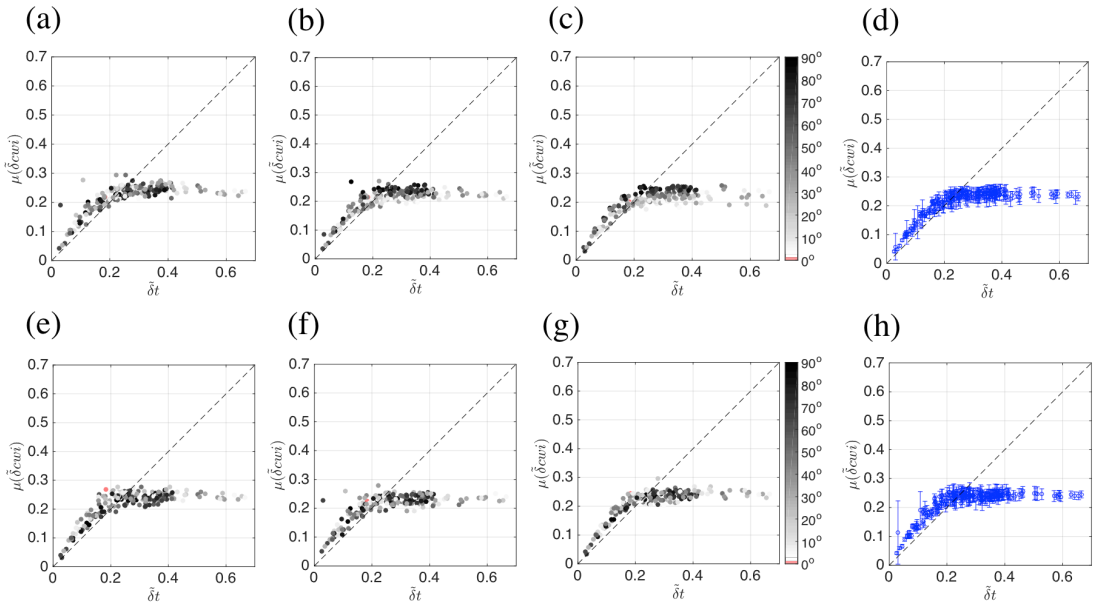

Figure 3-11: Source separation estimates of source set1. (a) to (c) shows results given by individual receivers R0, R6 and R9 from the horizontal array; (d) shows results given by all receivers from the horizontal array. (e) to (g) shows results given by individual receivers R18, R21 and R26 from the borehole array; (h) shows results given by all receivers from the borehole array.

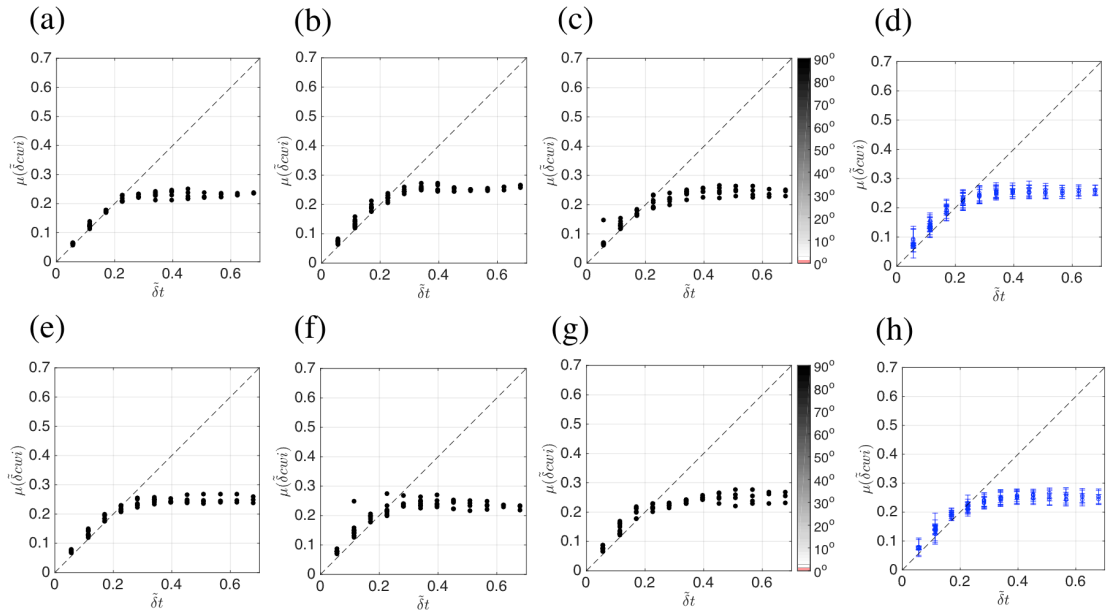

Figure 3-12: Source separation estimates of source set2.

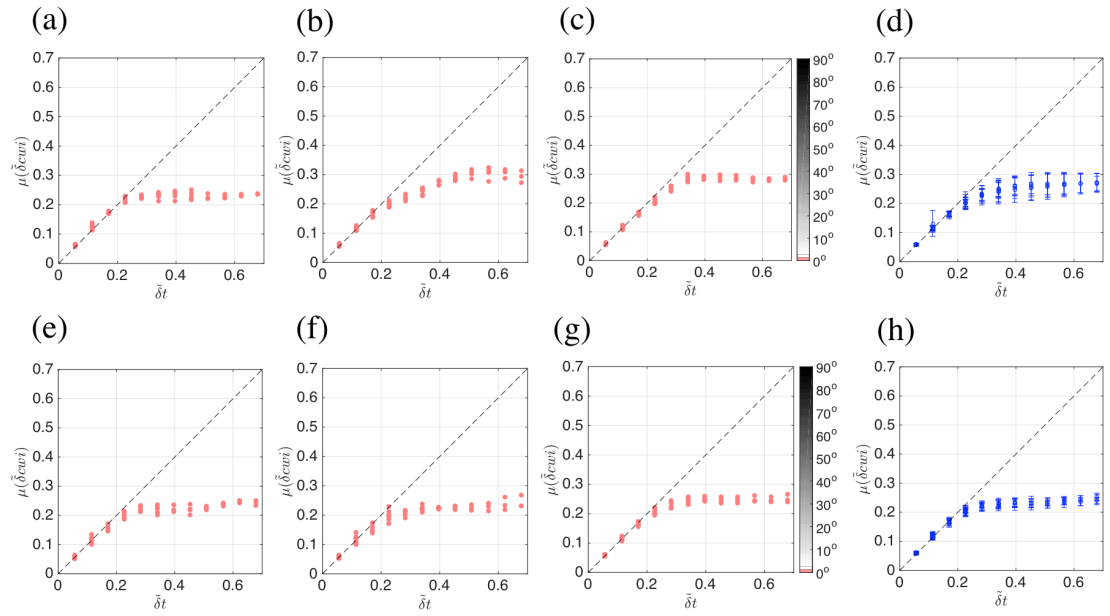

Figure 3-13: Source separation estimates of source set3.

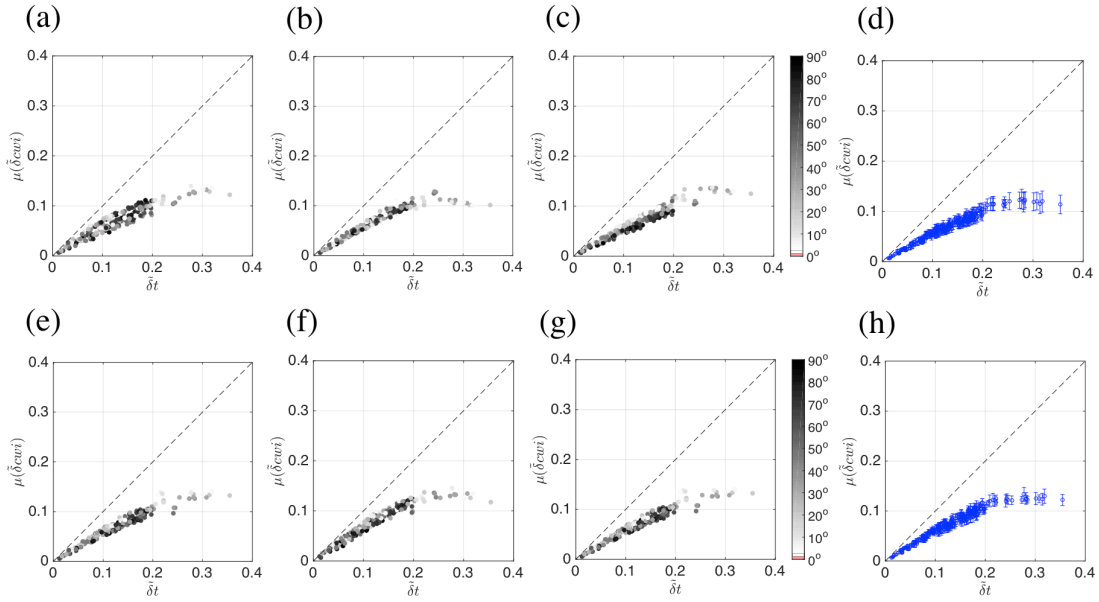

Figure 3-14: Source separation estimates of source set1 from vertical components in the elastic Marmousi medium.

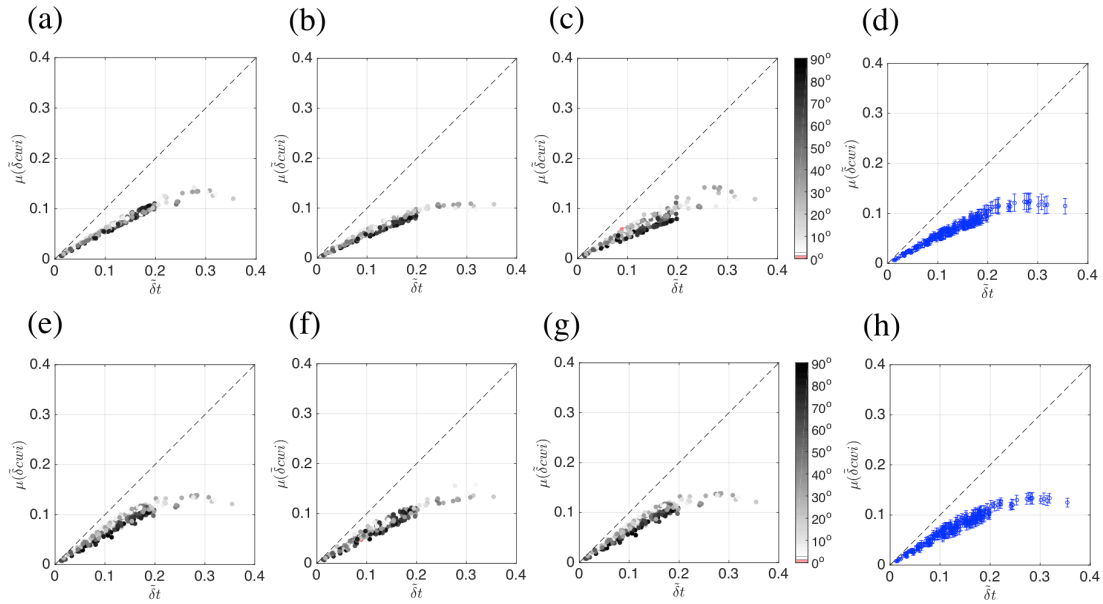

Figure 3-15: Source separation estimates of source set1 from horizontal components in the elastic Marmousi medium.

3.6 Discussion and Conclusion

We conduct synthetic experiments in four types of media, in order to test how different heterogeneities and their combinations influence the performance of the CWI technique. Source separation estimation in point-scatterer media is supposed to represent the standard of the CWI technique, as the theory of CWI presumes scattering to be caused by point scatterers (Snieder 2006), is therefore used as the reference throughout our work. It is demonstrated that CWI produces virtually exact estimate of the source separation between a pair of events with a true separation $\delta_{true} \leq 0.25\lambda_d$, after which it has an increasing trend of underestimation, and for $\delta_{true} \geq 0.4\lambda_d$ CWI only gives an estimate of the lower bond of the source separation. Therefore, in a given area where the events occur, using instruments with lower recording frequencies leads to larger dominant wavelength λ_d in the waveforms, which enables CWI to be applied to sources that are apart by a larger distance. In other words, using lower recording frequencies extends the applicable range of the CWI method to estimate inter-source separations, provided its effect on other aspects of the process is in a reasonable range.

It is observed that CWI is insensitive to the location of the receivers in point-scatterer media, provided the scatterers are uniformly distributed. An increasing amount of scatterers leads to more accurate estimates until a limit is reached, while larger difference in velocity of scatterers against the background lead to lower uncertainty in the estimates.

Specifically, in the point-scatterer media, a time window in the coda contains waves leaving the source from all possible directions, the integration in equation 2.21 (or equation 2.28) of CWI theory derivation is therefore conducted over all outgoing

directions in 3D (or 2D). However, in the layered media, only waves leaving the source from a maximum of half of the directions can arrive at a receiver, thus the integration in equation 2.21 (or equation 2.28) is no longer be over all outgoing directions, violating the CWI theory to an extent that is hard to specify. Therefore, the performance of CWI in a layered medium deteriorates. When point scatterers are added to the layered medium, the estimation of source separations improves quickly as the number of point-scatterers increases. This may be explained by an increasing number of directions from which waves leaving the source that arrive within a time window in the coda.

In our tests with the more realistic Marmousi model, the seemingly imperfect fulfillment of the assumption of the CWI theory is significantly compensated, and the result patterns similar to the point-scatterer reference are produced. The performance of CWI is almost unaffected by source geometry and receiver positions in both horizontal and borehole arrays. Our tests provide us with knowledge of how different types of heterogeneities affect the performance of CWI, which will be of help in understanding and interpreting source separation estimates hence relative location results in future application.

4

RELATIVE SOURCE LOCATION BASED ON CWI

A novel source location method based on coda wave interferometry (CWI) was applied to a micro-seismic dataset of mining induced events recorded in Nottinghamshire, England. CWI uses scattered waves in the coda of seismograms to estimate the differences between two seismic states. Here CWI is used to estimate the distances between pairs of earthquake locations, which are then used jointly to determine the relative location of a cluster of events using a probabilistic framework. We introduce two improvements to this location technique: these account for the impact of large difference in the dominant wavelength of recordings made on different instruments, and standardize the selection of parameters to be used when implementing the method. While the method has been shown to produce reasonable estimates on larger earthquakes, we test the method for microseismic events with shorter distinguishable codas in recorded waveforms, and hence fewer recorded scattered waves. The earthquake location results are highly consistent when using different individual seismometer channels, showing that it is possible to locate event clusters with a single-channel seismometer. We thus extend the potential applications of this cost-effective method to seismic events over a wider range of magnitudes.

4.1 Introduction

Finding relative locations of seismic events is essential for discriminating earthquake fault and auxiliary planes from the sequences of aftershocks or foreshocks (Got et al., 1994), studying earthquake interaction and recurrence (Chen et al., 2012), and monitoring stress state and induced (micro)seismicity (Ellsworth, 2013). Instead of obtaining the relative locations of a cluster of events from their absolute locations which are typically subject to inaccuracies in subsurface velocity models, they are preferably estimated directly from travel-time differences between early arriving

body waves, for example using joint hypocenter determination (Douglas, 1967; Dodge et al., 1995) or master event location (Deichmann and Garcia-Fernandez, 1992). The double-difference method of Waldhauser and Ellsworth (2000) locates clusters of earthquakes distributed over larger distances than the dominant recorded seismic wavelength when a dense seismic station network is available. However, in areas with fewer stations or unfavorable event-to-seismometer azimuthal coverage, the performance of the double-difference method deteriorates. In such circumstances, a recently developed source location method based on coda wave interferometry (Snieder et al., 2006) would be particularly useful if proven to be reliable over the range of earthquake magnitudes of interest.

Coda refers to the later part of a seismogram, generated by multiply scattered waves. Seismic coda is disregarded in many seismological applications due to its complex appearance with few uniquely identifiable arrivals. However, the coda is extremely sensitive to small changes in the seismic system. Aki (1969) used the spectrum of coda from local earthquakes to estimate seismic moments, and more recently Snieder et al. (2002) developed coda wave interferometry (CWI) to use phase information to infer differences between pairs of sources or changes in the medium. CWI has been used to determine the relative velocity changes in the Earth's subsurface (Poupinet et al., 1984) and other solid materials, and to monitor changes in the interior of volcanoes (Wegler et al., 2006). A third range of application of CWI is to estimate source separation between earthquakes with similar source mechanisms (Snieder and Vrijlandt, 2005; Robinson et al., 2011). The resulting source separations are used by Robinson et al. (2013) to determine the relative location of earthquakes, in which they demonstrate that CWI appears to outperform conventional location methods when the number of seismic stations is low.

CWI requires that the recorded coda contains waves that leave the source in many

directions, and which are then multiply scattered towards the seismometers by heterogeneities in the medium. Robinson et al. (2013) tested the method on events with long codas; hence on data that contained many scattered arrivals per event. In our implementation of this novel technique, we apply the method to a micro-earthquake dataset from a colliery in Nottinghamshire, England, for which the codas are relatively short. We thus test the location technique in a new region, and for sources for which the theoretical requirements of CWI are less obviously fulfilled. Additionally, the magnitude range is such that the method might have significant common industrial as well as academic and hazard-related applications. We find that source separation estimates are highly consistent and the earthquake location results agree to within estimated uncertainties when using different individual seismometer channels. Therefore, it is possible to locate these earthquakes with a single-channel seismometer. We also discuss two issues that arise during the implementation and provide solutions as they may be encountered by other authors in the future.

4.2 Data

The British Geological Survey (BGS) deployed a temporary seismic recording network of 4 three-component (NOLA, NOLD, NOLE and NOLF) and 3 Z-component (NOLB, NOLC and NOLG) stations from February 2014, after some small earthquakes were detected in and around New Ollerton, Nottinghamshire, since the middle of December 2013 (Figure 4-1a). This is a region where historical seismic activity is related to coal-mining. We selected 50 micro-earthquakes with the magnitudes 0.7-1.8 ML, with the criteria that 1) the signal-to-noise ratio is sufficiently high for the first arrivals to be identified, 2) recorded waveforms contain a distinguishable coda, and 3) the waveform of each event has a maximum

correlation coefficient larger than some threshold with waveforms of at least four other events. Dominant frequencies among the different seismic station channels vary between ~2.5-10 Hz. All waveforms were filtered to 2-20 Hz before processing.

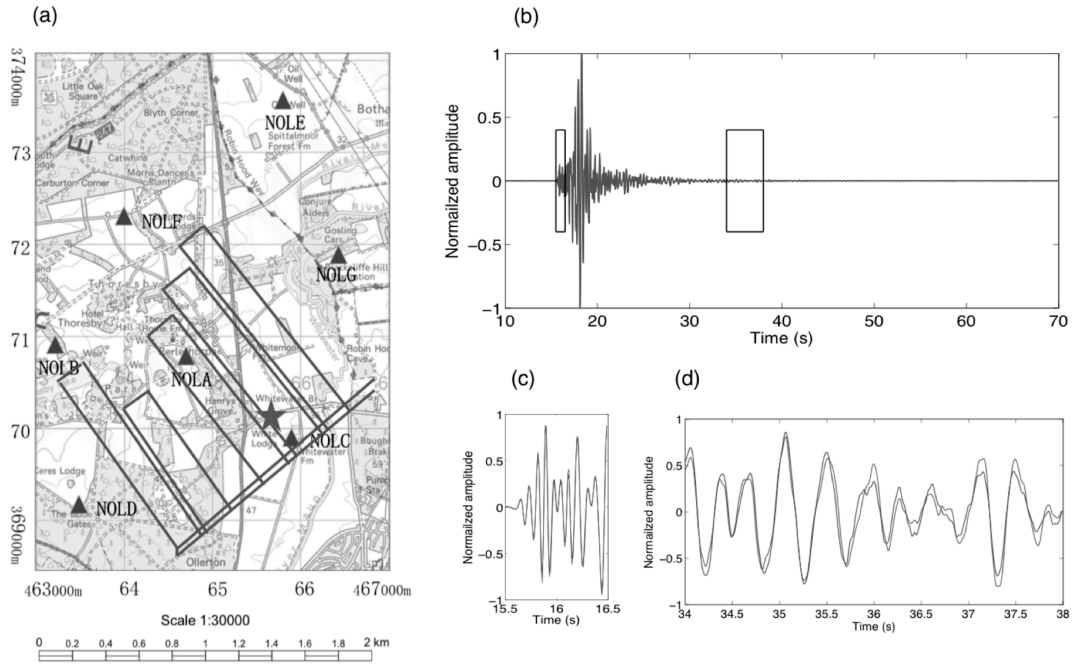

Figure 4-1: Map of the source region and typical waveforms. Panel (a) shows Thorsby colliery, New Ollerton, Nottinghamshire, England. The star shows the area around which the micro-earthquakes are likely to have occurred, triangles are temporary seismic stations, and the rectangles indicate locations of subsurface mining galleries. Panel (b)-(d) show the waveforms of two earthquakes in event Group 3 recorded by the N-channel of station NOLF, where (b) shows the whole waveforms, (c) and (d) show a 1-second window around the first arrival, and one of the time-windows (4 seconds) in the coda respectively, both indicated by boxes in (b). A comparison between panel (c) and (d) indicates that coda is more sensitive to source locations than early arrivals.

4.3 Estimating source separations with CWI

Coda wave interferometry constrains the separation between a pair of sources by comparing the two seismogram codas recorded at each station. The theory is based on scattering path summation (Snieder, 1999) whereby the total wavefield at a given location is written as the superposition of waves traveling along all possible trajectories,

$$u^1(t) = \sum_T A_T(t) \ , \tag{4.1}$$

where u^1 is the total wavefield from event 1, T represents a wave trajectory, and A_T is the contribution to the total wavefield of waves that travel along trajectory T. All scattered wave trajectories can be divided into the path from the source to the first scatterer, and the path followed thereafter. If two nearby and similar sources are compared, CWI assumes that the paths to the first scatterers change, but that subsequent paths do not, since they depend mainly on the medium rather than the source: the latter paths simply redistribute the small changes in energy arriving at the first scatterers over space and time throughout the coda. As a consequence, the dominant difference in recorded waveforms is in coda arrival times (Snieder, 2006). Equation 4.1 represents the waveform of one source recorded at an arbitrary station, so that of another closely-located source with identical mechanism recorded at the same station is $u^2(t) = \sum_T A_T(t - \tau_T)$, where τ_T is the travel-time difference of waves traveling along trajectory T due to the difference in source position. Since the two sources are located close together, the two waveforms will be similar, which can be quantified by the normalized cross-correlation of the two waveforms in a time-window defined with a central time t and a half-width t_ω, calculated for a sequence of time-windows in the coda

$$R(t_s) = \frac{\int_{t-t_\omega}^{t+t_\omega} u^{(1)}(t')u^{(2)}(t'+t_s)dt'}{\sqrt{\int_{t-t_\omega}^{t+t_\omega} {u^{(1)}}^2(t')dt' \int_{t-t_\omega}^{t+t_\omega} {u^{(2)}}^2(t')dt'}} \quad (4.2).$$

In each time window, the distribution of the travel-time differences τ_T contains information about the source separation δ (which can be in any direction). Snieder et al. (2006) estimate the standard deviation of the travel-time difference σ_τ from the maximum of the correlation coefficient R_{max}. σ_τ can then be related to the source separation δ by ${\sigma_\tau}^2 = \frac{1}{3}\frac{\delta^2}{v^2}$ for isotropic sources in an acoustic medium (where v is the velocity), or by ${\sigma_\tau}^2 = \frac{6/\alpha^8 + 7/\beta^8}{7(2/\alpha^6 + 3/\beta^6)}\delta^2$ (where α and β are P- and S-wave velocity) for double-couple sources on the same plane of the moment tensor (Snieder and Vrijlandt, 2005). As the waves arriving in different time windows have traveled along different paths, the separation results of each time window are independent and are used to estimate uncertainty.

We conducted a series of synthetic experiments using multiply-scattered waveforms generated with the acoustic Foldy method (Foldy 1945; Galetti et al., 2013) in a $16 \times 16\ km^2$ medium with 150 random point scatterers within a velocity of 3000 m/s, with receivers throughout. Twenty sources are located around the center of the medium with Ricker wavelet time functions of equal length, with small inter-source distances compared to the dominant wavelength, ensuring similarity in their synthetic waveforms. The results show that individual inter-source separations computed from different coda time-windows from any one receiver fluctuated by up to 12.8% of their mean across all time windows, and that mean estimates for any one receiver lie within the uncertainty bounds of any other single receiver. Such results provide confidence, but do not include real-world effects such as true heterogeneity, double-couple sources or elastic effects, for which we turn to the real data.

As the theory of CWI requires identical source mechanisms, we classified the 50 New Ollerton micro-earthquakes into three groups with 33, 10 and 7 events respectively. Source similarity in each group is assured by waveform similarity, assessed by cross-correlation. For each group, we picked the first arrivals of waveforms recorded by the same channels of seismic stations and aligned them. We assume differences in coda are due only to varying source locations; this is not true if seismic velocity also changes. While the two types of changes might be discriminated (Snieder et al. 2002), this is beyond our scope. Figure 4-1 shows the similarity of waveforms within one group, and compares early arrivals and coda of the same pair of waveforms.

We computed inter-source separations with data from each individual station. Coda windows begin at 26s, and assumed P- and S-wave velocities around the sources are 4088 m/s and 2298 m/s. Figure 4-2(a) shows the 21 inter-source separations from the 7 events in group 3. Each data point is the mean of results calculated for all available time-windows from each useable channel in each waveform pair, with the standard deviation of each mean displayed in panel (b). The results show that source separations and uncertainties are consistent between individual independent stations. Before passing the separation data to the location process, those pairs whose means were estimated to be smaller than their standard deviations were rejected.

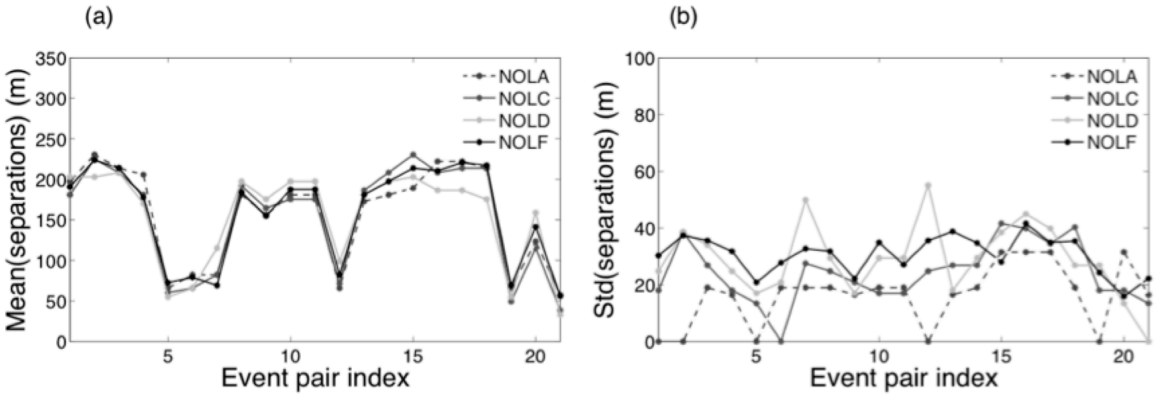

Figure 4-2: Source separations estimated with single station channels. Each point in panel (a) shows the mean of the five estimates; each corresponding point in panel (b) shows the standard deviation.

4.4 Source location

Our source location algorithm estimates relative location from the separation estimates and their uncertainties. It also accounts for a known bias – an increasing tendency towards underestimation of larger true source separations due to cycle-skipping in the correlation of coda in Equation 4.2. To quantify this bias, Robinson et al. (2011) apply a conditional probabilistic density function (pdf) $P(\widetilde{\delta_t}|\tilde{\delta}_{CWI})$, the probability of the true separation being $\widetilde{\delta_t}$ given that the estimate from CWI is $\tilde{\delta}_{CWI}$, where the tilde above the separations indicate that the quantities are normalised by the dominant wavelength λ_d in recorded data. The source separation estimates from CWI are always smaller than λ_d, so both $\widetilde{\delta_t}$ and $\tilde{\delta}_{CWI}$ are smaller than 1. According to Bayes' theorem, the posterior probability of $\widetilde{\delta_t}$ is proportional to the likelihood of observing $\tilde{\delta}_{CWI}$ given the true separation $\widetilde{\delta_t}$ multiplied by the prior on $\widetilde{\delta_t}$,

$$P(\widetilde{\delta_t}|\tilde{\delta}_{CWI}) \propto P(\tilde{\delta}_{CWI}|\widetilde{\delta_t}) \times P(\widetilde{\delta_t}) \quad (4.3).$$

The prior is used to incorporate information about source separation or event location known prior to the location process, which here is considered to be a uniform distribution with wide bounds. The likelihood function $P(\tilde{\delta}_{CWI}|\widetilde{\delta_t})$ is approximated by a positively bounded Gaussian pdf by establishing empirical functions for its mean $\mu = \mu(\widetilde{\delta_t})$ and standard deviation $\sigma = \sigma(\widetilde{\delta_t})$ given a true separation $\widetilde{\delta_t}$. These empirical functions are derived from a multitude of synthetic experiments with a large range of true separations in different Gaussian random media, by fitting the rational function forms (Robinson et al., 2011)

$$\mu(\widetilde{\delta_t}) = a_1 \frac{a_2 \widetilde{\delta_t}^{a_4} + a_3 \widetilde{\delta_t}^{a_5}}{a_2 \widetilde{\delta_t}^{a_4} + a_3 \widetilde{\delta_t}^{a_5} + 1},$$

$$\sigma(\widetilde{\delta_t}) = c + b_1 \frac{b_2 \widetilde{\delta_t}^{b_4} + b_3 \widetilde{\delta_t}^{b_5}}{b_2 \widetilde{\delta_t}^{b_4} + b_3 \widetilde{\delta_t}^{b_5} + 1}, \quad (4.4)$$

where a_1,…, a_5 are found to be 0.4661, 48.9697, 2.4693, 4.2467 and 1.1619, respectively; in $\sigma = \sigma(\widetilde{\delta_t})$, b_1,…, b_5, c are 0.1441, 101.0376, 120.3864, 2.8430, 6.0823 and 0.017, respectively, and location results do not change significantly with small changes in parameter values. Equation 4.3 holds for each earthquake pair, given the separation data from different time windows for each channel used. Robinson et al. (2013) incorporate the separations between multiple event pairs by multiplying the formulae for all available event pairs, assuming they are independent of each other

$$P(\boldsymbol{e}_1, \dots, \boldsymbol{e}_n|\tilde{\delta}_{CWI}) = c \prod_{i=1}^{n} P(\boldsymbol{e}_i) \times \prod_{i=1}^{n-1} \prod_{j=i+1}^{n} P(\tilde{\delta}_{CWI,ij}|\boldsymbol{e}_i, \boldsymbol{e}_j) \quad (4.5)$$

where c is a constant, n is the number of events, $\boldsymbol{e}_i = (x_i, y_i, z_i)$ is event i location, within the last term we use $\delta_{t,ij} = \|\boldsymbol{e}_i - \boldsymbol{e}_j\|_2$ for source separation $\delta_{t,ij}$ between the i'th and j'th earthquakes, and the prior $P(\boldsymbol{e}_i)$ only contains the relative event locations. The maximum of the joint posterior pdf occurs at the most probable combination of the events locations. Taking the negative logarithm of

equation 4.5, the multiplication is converted to summations, and the optimization is solved as a minimization problem using a conjugate gradient method.

We made two improvements to this location method. First, in each iteration of the minimization process, current event locations are used to compute the inter-event separations δ_t, which are then normalized to give the value of the joint posterior. However, the dominant frequency, hence dominant wavelength of micro-earthquakes, often extends over a large range, and is also subject to limitations of recording instruments. In this study, the dominant wavelength among different channels varies between 190m and 760m: using the average dominant wavelength over different channels/stations therefore introduces inaccuracy to the location process. To this end, when conducting multiple-channel locations we apply an individual likelihood for each channel, so that the inter-event separations computed during the iterations are normalized by the actual wavelengths. Thus when data from m channels are used, Equation 5 is modified to

$$P\left(\boldsymbol{e}_1, \dots, \boldsymbol{e}_n \middle| \tilde{\delta}_{CWI}\right) = c \prod_{i=1}^{n} P(\boldsymbol{e}_i) \times \prod_{k=1}^{m} \prod_{i=1}^{n-1} \prod_{j=i+1}^{n} P_k\left(\tilde{\delta}_{CWI,ij} \middle| \boldsymbol{e}_i, \boldsymbol{e}_j\right) \qquad (4.6)$$

where k is the index over m channels.

Second, when specifying the number and length of coda time windows for CWI, we want separation estimates to be consistent among different windows. Using data from different station channels, we find that the most consistent set of windows varies. Instead of using a trial-and-error method to fix these two fundamental parameters, we conduct a systematic search for an optimal combination that results in the lowest uncertainty of separations calculated between all events using CWI.

We compute a separation-uncertainty matrix for each channel (e.g. Figure 4-3): for each combination of parameters the matrix element is $\Omega_{i,j} = \sum_N \sigma_{i,j}/N$, where

$\sigma_{i,j} = \sqrt{\sum_l (\delta_{i,j,k} - \bar{\delta}_{i,j})^2 / l}$ is the standard deviation of separation estimates from l coda time windows for events i and j, $\delta_{i,j,k}$ is the separation estimate of the kth window and $\bar{\delta}_{i,j}$ is their mean, and N is the number of event pairs on that channel. The value of $\Omega_{i,j}$ reflects the uncertainty of separation estimates derived from one recording channel for each source pair. Averaging over multiple source pairs gives a final uncertainty estimate for that combination of parameters (we require at least four estimates to calculate a reasonable standard deviation). Figure 4-3 shows a typical matrix for the New Ollerton earthquakes, indicating that using four 4-second windows will give the most consistent separation estimates. The values of Ω appear to increase with the number of windows when windows are longer than 4.5s but this is due to micro-seismic codas being short: with more than three such windows, newly added windows are no longer suitable for CWI. This systematic approach thus frees us from the vagaries of trial-and-error methods and from using undefined or subjective quality metrics, and allows CWI technique to be automated.

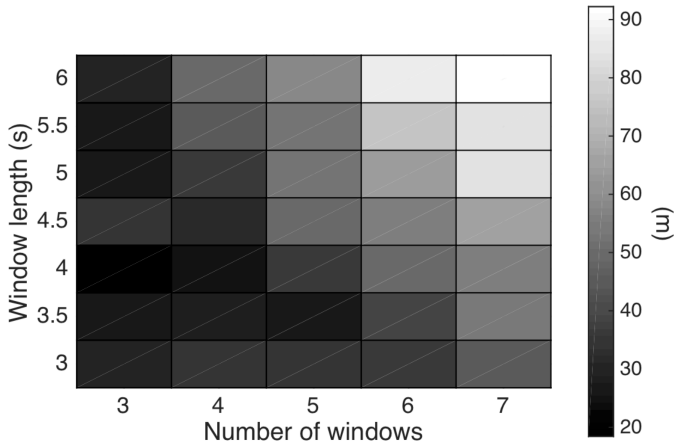

Figure 4-3: Separation-uncertainty matrix of the single-channel station NOLC. Colors indicate values of the average standard deviations resulting from the corresponding combination of number and length of time windows used to divide coda. As a minimum of four time windows is required for calculating standard deviations, the values for three windows are only shown here for illustration.

For each of the three groups, minimization of the negative logarithm of the joint location pdf is conducted 10 times with different randomly distributed initial locations. Figure 4-4(a) shows the location of group 3 with all available data from 11 seismic station channels, averaged over the results of the 10 experiments, and the variability between the 10 is indicated by 95% confidence ellipses. The average coordinate variability is only 12.7m and the minimizations therefore seem likely to have converged to the same (global) minimum, given the uncertainties in the source separation data. We located the events using data from each channel individually, and find that the estimated locations follow roughly consistent patterns. Figure 4-4(b)-(d) shows the estimated locations using single-channel stations NOLC, NOLD and NOLF; each gives similar results to those obtained using all available data. The other two groups exhibit similar levels of uncertainty. Some event pairs are more or less separated than their CWI estimates because the optimization attempts to satisfy all distances at once, which is generally impossible due to separation uncertainties. Nevertheless, location results of single channels or stations all share similar average patterns, even though the stations lie on very different azimuths from the event cluster (see Figure 4-1a). This is achieved because the coda in each time-window contains waves leaving the source from many directions; thus diminishing the sensitivity of the location result to the source-receiver azimuth. For comparison, the double-difference (DD) method with damping parameter 40 or 100 using data from all channels, gives results similar to CWI (c.f. right panel of Figure 4-4a with 4-4e and 4-4f). Across all three groups, locations from the two methods give fairly similar patterns with comparable spatial spreads using damping 40 (Figure 4-4g), and the DD cluster shrinks with damping 100 (Figure4- 4h).

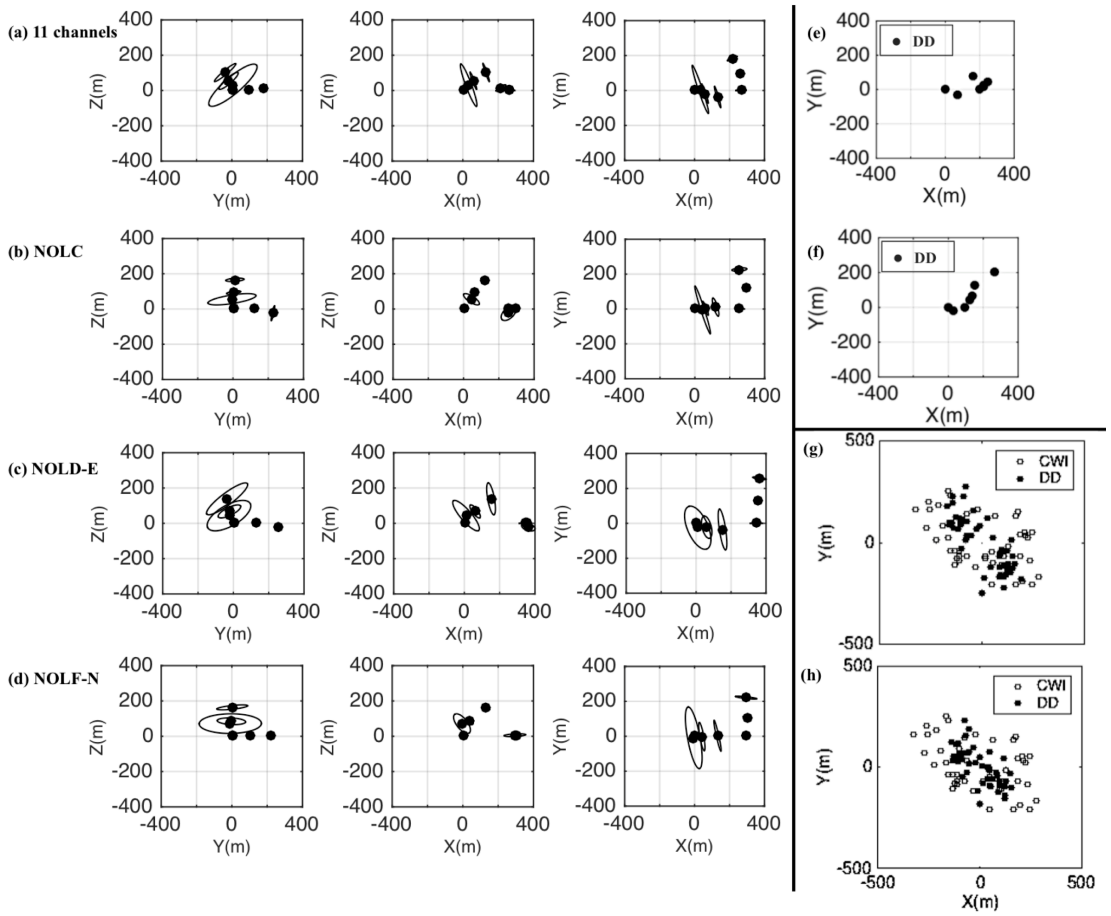

Figure 4-4: Planar projections of relative location results. Axes X, Y and Z point to three orthogonal directions. Panels (a-d) show the CWI results of group 3, where dots are the event mean locations averaged over 10 location optimizations; ellipses show 95% confidence intervals in the means. Panel (a) shows results obtained using all available data from 6 stations (11 channels). Panels (b) – (d) each shows the results from single channels from stations NOLC, NOLD and NOLF, respectively. Panels (e) and (f) show location results of the Double-Difference method with damping parameter 40 and 100, respectively. Panels (g) and (h) show comparisons of location results of CWI (hollow circles) and Double-Difference method (solid circles), with damping values in Double-Difference method of 40 and 100, respectively.

4.5 Conclusion

Our application of the CWI-based source location method to the New Ollerton earthquakes demonstrates that this method is applicable to micro-seismicity and to industrial as well as academic purposes. It also shows that the location results with individual stations are highly consistent, as long as recorded seismograms have a sufficient length of coda. This computationally inexpensive method therefore adds a new technique to the arsenal for seismological applications that require accurate locations of local earthquakes without dense seismometer arrays.

Acknowledgement

We thank British Geological Survey (BGS) for providing the seismic data of New Ollerton earthquakes. Youqian Zhao is grateful for funding provided by the School of GeoSciences, University of Edinburgh and BGS. We also thank Dr. Giovanni Meles for his help at early stage.

4 Relative source location based on CWI

5

CWIcluster – LOCATION CODE PACKAGE

5 *CWIcluster* –location code package

A wide range of applications requires relative locations of sources of energy to be known accurately. Most conventional location methods are either subject to errors that depend strongly on inaccuracy in the model of propagation velocity used, or demand a well-distributed network of surrounding seismic stations in order to produce reliable results. A new source location method based on coda wave interferometry (CWI) is relatively insensitive to the number of seismic stations and to the source-to-station azimuthal coverage. It therefore opens new avenues for research, for applications in areas with unfavourable recording geometries, and for applications which require a complementary method. This method uses CWI to estimate distances between pairs of seismic events with similar source mechanism recorded at the same station. These separation estimates are used to solve for the locations of clusters of events relative to one another within a probabilistic framework through optimization. It is even possible to find relative locations of clusters of events with one single-channel station. Given these advantages, it is likely that one reason that the method is not used more widely is the lack of reliable code that implements this multistage method. We therefore present a well-commented MATLAB code called *CWIcluster* that does so, and present examples of its applications. It can be used with seismic data from a single station channel, and enables data recorded by different channels and stations to be used simultaneously. It is therefore possible to combine data from permanent yet sparse networks, and from temporary arrays closer to the source region. We use the code to apply the location method to a selected data set of the New Ollerton earthquakes, England, to demonstrate the validity of the code. The worked example is provided within the package. A way to assess the quality of the location results is also provided.

5.1 Introduction

Finding accurate locations of seismic energy sources is essential for a wide range of seismological, industrial and other applications. Examples include the study of earthquake interaction and recurrence (Marzocchi and Lombardi, 2008; Chen et al., 2013), discriminating earthquake fault and auxiliary planes using aftershocks or foreshocks (Got et al., 1994), modeling earthquake hazards (Frankel et al., 2000), monitoring seismic activity during and after hydraulic fracturing (Kumar et al., 2017) or underground mining (Ge, 2005), and attempts to forecast earthquakes (Gerstenberger et al., 2005). In other areas of application, finding locations of different types of sources can be important, for example in ocean acoustic (Dosso and Wilmut, 2009; 2011; Verlinden et al., 2015), in disaster rescue (Mae et al., 2017; Kawaguchi and Fukuda, 2017), and in military applications (Sheng and Hu, 2005). The quality of absolute locations found in each case depends heavily on the velocity model used, the number of stations available, and source-to-receiver distances and azimuths. In seismological applications, earthquake location uncertainties are therefore usually of the order of kilometers (Shearer, 1999), and from here on we focus only on seismological applications.

To achieve higher precision, relative source location methods are often used. These typically ignore absolute locations and instead estimate the locations of multiple event positions relative to each other directly from the differences in their recorded arrival-times of their radiated energy at receivers which are obtained either from catalog (preprepared) data or from temporal crosscorrelation of their various recorded waveforms (Deichmann and Garcia-Fernandez, 1992; Waldhauser and Ellsworth, 2000; Sgattoni et al., 2016). Events located in this way are often clustered within a region smaller than a quarter of the wavelength of radiating energy at the

dominant frequency; the range of source-to-receiver distances, and velocity variations outside the source region therefore affect waveforms from all sources in a similar manner so that errors in their relative location associated with velocity variations are largely avoided.

Conventional relative location methods are often able to reduce seismic source relative location errors to less than ~100m provided that a well-designed seismic network with a large number of stations is available (Ito, 1985, 1990; Deichmann and Garcia-Fernandez, 1992; Waldhauser et al., 1999). The master event location method (Fremont and Malone, 1987; Deichmann and Garcia-Fernandez, 1992) takes one event in an event cluster as the master event, crosscorrelates its seismogram waveforms with those of the other events, and relocates each of them relative to their master event through their relative traveltime differences. Thus the spatial extension of the cluster is limited to about a quarter of a dominant wavelength as the waveforms of all other events need to be closely comparable to those of the master event to avoid circle skipping in their crosscorrelation. The popular double-difference (DD) location method (Waldhauser and Ellsworth, 2000; Bai et al., 2006) overcomes this limitation by linking different events and clusters using differential traveltimes obtained from catalog data, thus extending the feasible relative distance range. The DD method determines event locations by minimizing the double-difference (residual between observed and theoretical differential traveltimes of a pair of events recorded at a common station) of pair-wise events by adjusting the vector difference between their hypocenters. The system can easily become ill-conditioned, hence it is solved as a damped least squares problem. The solution is subject to the choice of the damping factor, which depends on the condition number of the system (Waldhauser, 2001; Zhao et al., 2017). The DD location results are also influenced by the number of seismic stations available:

results deteriorate when the number falls below seven, and the method fails to produce results when the number is smaller than four (Robinson et al., 2013).

A novel location method based on coda wave interferometry (CWI) (Snieder, 2006) is a feasible alternative to these conventional location methods when there are few seismic stations, or where the source-station azimuth range is unfavorable, where a different method is useful for a quality check of other methods. The CWI technique makes use of the multiply-scattered waves recorded in waveform codas which have travelled through a much larger volume of the medium, and hence contain more azimuthal information than the first or early arrivals used by conventional methods. As a result, the CWI-based location method is even able to locate a cluster of events with one single-channel station (Robinson et al., 2013; Zhao et al., 2017).

Coda refers to the multiply scattered waves comprising the later parts of recorded seismograms, and is extremely sensitive to differences in source position or changes in the medium of propagation. CWI measures the differences in the coda of waveforms recorded at the same station before and after some change occurs, to estimate the differences between the two seismic states. For example, it has been used in a laboratory to measure changes due to the nonlinear dependence of the seismic velocity structure of granite due to temperature variations that are too small for other methods to detect (Snieder et al., 2002); to monitor velocity changes associating volcano activities (Gret et al., 2005; Wegler et al., 2006; Brenguier et al., 2008a; Mordret et al., 2010; Baptie, 2010); to study changes in fault zones (Wang et al., 2008; Brenguier et al., 2008b; de Angelis, 2009); as well as in geoengineering to monitor stress changes in concrete structures, such as bridges (Stahler et al., 2011) and buildings (Larose et al., 2006).

By comparing pairs of similar earthquakes, the source location algorithm that we present here uses CWI to estimate the inter-source separations of a cluster of events with similar source mechanisms, and then uses the separation data as input to a location algorithm. Three types of changes of seismic states (velocity change, scatterer displacement and source displacement) leave different footprints on seismic coda when compared in a statistical manner (Snieder 2006). Although theoretically the three types of changes could therefore be discriminated, such tests and discussion are beyond the scope of this particular work: here we assume differences in coda are due only to differences in the source locations of different seismic events. In such case, clusters of events can even be located relative to one another in 3D using a single seismic receiver (Robinson et al., 2013; Zhao et al., 2017).

Despite the advantages of this method, it is curious to observe that uptake in its use has been limited to the above two papers. In part we suspect that this is because the relative location algorithm requires unfamiliar methods to be used, and is therefore also partly due to the lack of readily available, easily editable code with which practitioners can gain familiarity and confidence. We provide such a code - *CWIcluster*.

In this chapter, we present the CWI-based source location algorithm developed by Robinson et al. (2013) with the improvements proposed by Zhao et al. (2017). We then introduce a way to assess the location results obtained from the nonlinear optimization solution. We also describe the accompanying computer code, written in MATLAB, that combines these theories and methods and estimates relative source locations using a three step routine: 1) classifying events into clusters based on waveform similarity; 2) estimating inter-source separation distances with CWI; and 3) estimating the relative source locations from the separation data. The code package

can be downloaded at *www.geos.ed.ac.uk/eip/codes.html*. In what follows we first review the theory of CWI and the location algorithm in Section 5.2, and then give a brief description of the core functions and scripts of the code package in Section 5.3. The method used to classify events (Ottemoller et al., 2017) is also described in Section 5.3. Applications of the code to synthetic examples and to mining induced events are illustrated in Section 5.4 and Section 5.5, respectively, and these example data sets are included within the code package.

5.2 Theory overview

CWI estimates the inter-source separation between a pair of events by comparing the coda of the two seismograms recorded by each seismic station channel. The theory is based on path summation of scattered waves (Snieder, 1999) – the assumption that the total wavefield at a given location can be written as the superposition of waves traveling along all possible trajectories through the medium

$$u^1(t) = \sum_T A_T(t), \tag{5.1}$$

where $u^1(t)$ is the total wavefield from event 1, T represents a wave trajectory, and A_T is the contribution to the total wavefield of waves that travel along trajectory T. The trajectory of each scattered wave consists of the path from the source to the first scatterer encountered, and the path followed thereafter. For a second event that is close to event 1 and has very similar source mechanism, CWI assumes that the paths to the first scatterer on each trajectory change, but that the subsequent trajectory does not because it depends on the medium rather than on the sources. Since the subsequent scattering trajectories create a complex mixture of any differences in travel times to the first scatters, for small changes in source location the dominant differences in recorded waveforms at the same seismic station occur in

coda wave arrival times (Snieder, 2006). The wavefield of event 2 can be written as

$$u^2(t) = \sum_T A_T(t - \tau_T), \tag{5.2}$$

where τ_T is the travel-time difference of waves traveling along trajectory T to the first scatterer due to the difference in source position. If we assume proximity between the two source locations and similarity in source mechanisms, the amplitude A_T is assumed to be the same for both sources, and the two waveforms will be similar. Any differences can be quantified by the normalized crosscorrelation of the two waveforms in a time-window defined by a central time t and a half-width t_ω, computed for a sequence of time-windows in the coda

$$R(t_s) = \frac{\int_{t-t_\omega}^{t+t_\omega} u^{(1)}(t')u^{(2)}(t'+t_s)dt'}{\sqrt{\int_{t-t_\omega}^{t+t_\omega} {u^{(1)}}^2(t')dt' \int_{t-t_\omega}^{t+t_\omega} {u^{(2)}}^2(t')dt'}}. \tag{5.3}$$

The distribution of any traveltime differences τ_T in each time-window contains information about the source separation δ. Snieder (2006) estimate the standard deviation of the traveltime difference σ_τ from the maximum of the correlation coefficient R_{max}, and show that σ_τ is related to the source separation δ by

$${\sigma_\tau}^2 = \frac{1}{2}\frac{\delta^2}{v^2} \quad \text{for isotropic sources in 2D acoustic media} \tag{5.4a}$$

$${\sigma_\tau}^2 = \frac{1}{3}\frac{\delta^2}{v^2} \quad \text{for isotropic sources in 3D acoustic media} \tag{5.4b}$$

$${\sigma_\tau}^2 = \frac{6/\alpha^8 + 7/\beta^8}{7(2/\alpha^6 + 3/\beta^6)}\delta^2 \quad \text{for double couple sources on the same fault plane} \tag{5.4c}$$

where α and β are the P- and S-wave velocity in the vicinity of the two sources (Snieder and Vrijlandt, 2005). The waves arriving in different time-windows have traveled along different paths, so separation results derived from each time-window of the seismograms are therefore independent and their distribution can be used to estimate uncertainty. It has also been shown that estimates of inter-source separations from different station channels are highly consistent (Snieder and Vrijlandt, 2005;

Robinson et al., 2011; Zhao et al., 2017).

As we move through a seismogram towards later times, seismic coda becomes suitable for CWI where the waves are sufficiently scattered so that a time-window contains waves leaving the source from many different directions; the suitable section ends where the noise amplitude level exceeds that of the signal. There is therefore a limited length of coda that can be used. In turn, this constrains the choices of number and length of time windows used in equation 5.3, and clearly there is a trade-off between the two. From a theoretical point of view, if we insert wave representations 5.1 and 5.2 into equation 5.3, we can see that computation of $R(t_s)$ gives rise to double sums. CWI assumes the cross terms between the two summations are negligible compared to the diagonal terms, but their ratio is inversely proportional to the length of the time-windows (Snieder 2006). Hence, for this assumption to be reasonable, the time-windows need to have sufficient length. However, time windows cannot be unrestrictedly long as otherwise cycle skipping may occur in the crosscorrelation in equation 5.3. Also, in order to obtain usable standard deviations on separation estimates, at least four time-windows are needed for each pair of waveforms. Given all of these constraints, it is not a trivial task to select the number, length, and start time of windows used to implement CWI.

To avoid the vagaries of trial and error, the code package allows the separation-uncertainty matrix of Zhao et al. (2017) to be used to find the most suitable combination of the number, length and start time of windows systematically. For data from each station channel, a three-dimensional separation-uncertainty matrix is computed that includes a regularly-sampled subset of all possible combinations of the three parameters: number, length and start time of windows. Matrix elements are computed for one combination of the three parameters by first

calculating $\Omega_{i,j} = \sum_N \sigma_{i,j}/N$, where $\sigma_{i,j} = \sqrt{\sum_{k=1}^{l}(\delta_{i,j,k} - \bar{\delta}_{i,j})^2/l}$ is the standard deviation of separation estimates from l coda time windows for events i and j, $\delta_{i,j,k}$ is the separation estimate from the kth window and $\bar{\delta}_{i,j}$ is the mean separation over l windows, and N is the number of event pairs on that station channel. The value of $\Omega_{i,j}$ reflects the uncertainty of separation estimates derived from one recording channel for each source pair. Averaging over all source pairs gives a final uncertainty estimate for that combination of parameters. Thus, systematically searching for the combination of number, length, and start time of windows that gives the lowest estimate of separation uncertainties from CWI becomes an automated process.

It is essential to note that the CWI technique has a tendency to underestimate larger source separations due to cycle skipping in the correlation of coda in equation 5.3. This trend can be quantified by two empirical relations between the true separation $\widetilde{\delta_t}$ and the mean $\mu = \mu(\widetilde{\delta_t})$ and standard deviation $\sigma = \sigma(\widetilde{\delta_t})$ of CWI separation estimates (Figure 5-1 a, b), where the tilde above the separation indicates that the quantity is normalized by the dominant wavelength λ_d in the recorded data: $\widetilde{\delta_t} = \delta_t/\lambda_d$. The applicable range of CWI is visualized in Figure 5-1: CWI fails to identify any increase in length when the true separation is larger than $0.55\lambda_d$. The empirical functions that capture this behaviour are derived from a multitude of synthetic experiments with a large range true separations in different Gaussian random media, by fitting the rational functional forms

$$\mu(\widetilde{\delta_t}) = a_1 \frac{a_2 \widetilde{\delta_t}^{a_4} + a_3 \widetilde{\delta_t}^{a_5}}{a_2 \widetilde{\delta_t}^{a_4} + a_3 \widetilde{\delta_t}^{a_5} + 1}, \tag{5a}$$

$$\sigma(\widetilde{\delta_t}) = b_1 \frac{b_2 \widetilde{\delta_t}^{b_4} + b_3 \widetilde{\delta_t}^{b_5}}{b_2 \widetilde{\delta_t}^{b_4} + b_3 \widetilde{\delta_t}^{b_5} + 1} + c, \tag{5b}$$

where the values of the constants are listed in Table 1 (Robinson et al., 2011, 2013). The location algorithm introduced in the next section takes account of these known

biases of CWI-estimated source separations, and is able to correct for them to a significant extent in relative location results.

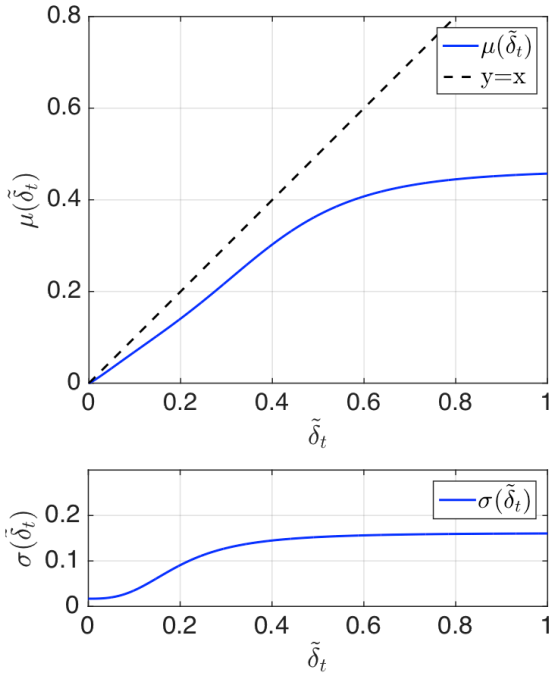

Figure 5-1: Empirical functions showing bias and uncertainties in separation estimates from the CWI technique. The upper panel shows the empirical relation between the mean of the source separation estimates $\mu = \mu(\widetilde{\delta_t})$ and the true separation $\widetilde{\delta_t}$. All separations are normalized by the dominant wavelengths of the coda waveforms. The dashed line $y = x$ shows the case where the mean of the CWI separation estimates are identical to the true separations. The lower panel shows the empirical relation between the standard deviation $\sigma(\widetilde{\delta_t})$ of the separation estimates and the true separation $\widetilde{\delta_t}$.

Constant in $\mu = \mu(\widetilde{\delta_t})$ and $\sigma = \sigma(\widetilde{\delta_t})$

$\mu = \mu(\widetilde{\delta_t})$	$\sigma = \sigma(\widetilde{\delta_t})$
$a_1 = 0.4661$	$b_1 = 0.1441$
$a_2 = 48.9697$	$b_2 = 101.0376$
$a_3 = 2.4693$	$b_3 = 120.3864$
$a_4 = 4.2467$	$b_4 = 2.8430$
$a_5 = 1.1619$	$b_5 = 6.0823$
	$c = 0.017$

Table 5-1: Constants in the empirical relations in equations 5.5a and 5.5b for $\mu = \mu(\widetilde{\delta_t})$ and $\sigma = \sigma(\widetilde{\delta_t})$ (Robinson et al., 2011).

The source location algorithm estimates relative locations from the separation estimates and their uncertainties using a probabilistic framework. Robinson et al. (2011) describe the probabilistic nature of CWI estimates using the conditional probability density function (pdf) $P(\widetilde{\delta_t}|\tilde{\delta}_{CWI})$, which is the probability of the true separation being $\widetilde{\delta_t}$ given that the estimate from CWI is $\tilde{\delta}_{CWI}$. According to Bayes' theorem, this so-called posterior probability of $\widetilde{\delta_t}$ is proportional to the likelihood of observing $\tilde{\delta}_{CWI}$ in the case that the true separation is $\widetilde{\delta_t}$, multiplied by the prior probability of $\widetilde{\delta_t}$ being true

$$P\left(\widetilde{\delta_t}\middle|\tilde{\delta}_{CWI}\right) \propto P\left(\tilde{\delta}_{CWI}\middle|\widetilde{\delta_t}\right) \times P\left(\widetilde{\delta_t}\right). \tag{5.6}$$

The prior pdf $P\left(\widetilde{\delta_t}\right)$ is used to describe information about source separation or event location known prior to and independently from the CWI location process, which here is considered to be a uniform distribution with wide bounds. The likelihood function $P\left(\tilde{\delta}_{CWI}\middle|\widetilde{\delta_t}\right)$ is approximated by a positively-bounded Gaussian pdf, whose mean and standard deviation are respectively represented by the

empirical functional relation $\mu(\widetilde{\delta_t})$ and $\sigma(\widetilde{\delta_t})$, given true separation $\widetilde{\delta_t}$.

For a cluster of events, equation 5.6 holds for each event pair. Robinson et al. (2013) incorporate the separations between multiple event pairs by multiplying the formulae for all available event pairs to establish their joint posterior pdf, assuming that they are independent of each other

$$P(\boldsymbol{e}_1, \ldots, \boldsymbol{e}_n | \tilde{\delta}_{CWI}) = c \prod_{i=1}^{n} P(\boldsymbol{e}_i) \times \prod_{i=1}^{n-1} \prod_{j=i+1}^{n} P(\tilde{\delta}_{CWI,ij} | \boldsymbol{e}_i, \boldsymbol{e}_j), \tag{5.7}$$

where c is a constant, n is the number of events, and $\boldsymbol{e}_i = (x_i, y_i, z_i)$ is the location of event i. Within the last term we use the Euclidean distance $\delta_{cwi,ij} = \|\boldsymbol{e}_i - \boldsymbol{e}_j\|_2$ for source separation between the i'th and j'th earthquakes. Throughout the evaluation of the joint pdf, the separation quantities are used in normalized form; that is, they are divided by the dominant wavelength λ_d. However, the dominant frequency, and hence the dominant wavelengths of the set of events, could extend over a large range, and is also subject to limitations of recording instruments. Using the average dominant wavelength over different station channels therefore introduces inaccuracy to the location process. To this end, our code package instead uses the joint pdf introduced by Zhao et al. (2017), which applies an individual likelihood for each channel when data from multiple channels are used, so that the separations computed during the evaluation of the joint pdf are normalized by the actual dominant wavelength from that channel

$$P(\boldsymbol{e}_1, \ldots, \boldsymbol{e}_n | \tilde{\delta}_{CWI}) = c \prod_{i=1}^{n} P(\boldsymbol{e}_i) \times \prod_{k=1}^{m} \prod_{i=1}^{n-1} \prod_{j=i+1}^{n} P_k(\tilde{\delta}^k{}_{CWI,ij} | \boldsymbol{e}_i, \boldsymbol{e}_j), \tag{5.8}$$

where m is the number of channels used, k is the index over m channels, and $P_k(\tilde{\delta}^k{}_{CWI,ij} | \boldsymbol{e}_i, \boldsymbol{e}_j)$ is the probability of observing $\tilde{\delta}^k{}_{CWI,ij}$ given source locations $\boldsymbol{e}_i$ and $\boldsymbol{e}_j$, where $\tilde{\delta}^k{}_{CWI,ij}$ is normalized by the dominant wavelength of the kth channel. The maximum of the joint posterior pdf (equation 5.8) occurs at the most probable combination of event locations. Hence, the event locations can be estimated

by solving an optimization problem. Taking the negative logarithm of equation 5.8, the multiplications are converted to summations that are more numerically stable

$$-\ln\left[P\left(\boldsymbol{e}_1,\ldots,\boldsymbol{e}_n\middle|\tilde{\delta}_{CWI}\right)\right] = -\ln[c] - \sum_{i=1}^{n}\ln[P(\boldsymbol{e}_i)] - \sum_{k=1}^{m}\sum_{i=1}^{n-1}\sum_{j=i+1}^{n}\ln\left[P_k\left(\tilde{\delta}_{CWI,ij}\middle|\boldsymbol{e}_i,\boldsymbol{e}_j\right)\right]. \quad (5.9)$$

Maximization of equation 5.8 is equivalent to minimizing equation 5.9, where $\ln[c]$ and $\ln\left[P(\boldsymbol{e}_i)\right]$ can be ignored as they are constant (for Uniform priors). Thus, the event locations $\boldsymbol{e}_1,\ldots,\boldsymbol{e}_n$ can be found by minimizing the objective function

$$L(\boldsymbol{e}_1,\ldots,\boldsymbol{e}_n) = -\sum_{k=1}^{m}\sum_{i=1}^{n-1}\sum_{j=i+1}^{n}\ln\left[P_k\left(\tilde{\delta}_{CWI,ij}\middle|\boldsymbol{e}_i,\boldsymbol{e}_j\right)\right]. \quad (5.10)$$

In the code package, objective function L is minimized using a conjugate gradient method, the Polak-Ribiere technique (Navon and Legler, 1987; Press et al. 1987). This uses the derivatives of function L, which are computed numerically to avoid calculating the integrals in their analytical forms given by Robinson et al. (2013).

5.3 Code description

The accompanying relative source location code is written in MATLAB with well-commented functions and scripts. These use seismic data recorded with single or multiple station channels to find relative source locations. The package consists of three parts, each of which contains codes conducting one step of the location method: clustering events, estimating inter-source separations, and estimating source locations. The entire process can be implemented by executing the script `main_running_script.m` sector by sector, with interactive operations involved occasionally. This section provides descriptions of the core functions and scripts used in each step. The sub- and auxiliary functions and scripts are explained in the user guide that is included within the package.

5.3.1 Clustering

The theory of CWI requires that events be constrained to have identical source mechanisms, so events first need to be classified into sets of similar mechanism. The similarity in pairs of sources is assessed by the similarity of their waveforms recorded by the same seismic station channel, which is measured by their crosscorrelation. The package classifies events in two steps, computing crosscorrelations then identifying clusters, with scripts `sort_cr.m` and `clustering.m`, respectively.

`sort_cr.m` reads in seismic data in SAC form (Helffrich et al., 2013). It first selects events and station channels for location according to criteria set by the user: `MIN_channel` is the minimum number of recording channels for an event to be considered, and `MIN_event_per_channel` is the minimum number of events recorded by a channel for that channel to be used. It then calculates the crosscorrelation cr of all available pairs of the selected events recorded by each selected station channel, and finds the maximum of each crosscorrelation cr_{max}. For each event pair, the values of cr_{max} are averaged over all selected station channels that have recorded both events, then for each channel these average maximum crosscorrelation $cravg_{max}$ are sorted in descending order.

`clustering.m` follows the method of Ottemoller et al. (2017) to identify clusters. It starts with the event pair with the highest $cravg_{max}$ value, making them the first two events of the first cluster. It then searches through the sorted list of $cravg_{max}$, adding events that are linked to the current cluster. A link to a cluster is defined as one of the events in the pair being correlated ($cravg_{max}$ higher than `MIN_corr`, the threshold of $cravg_{max}$ for an event pair to be included) with any event that is

already in the cluster. The search restarts from the first unclassified pair (the unclassified pair with the highest $cravg_{max}$) every time a new event is added to the cluster to avoid overlooking any linked events. The search loops until there is no event that can be added to the current cluster, after which it starts a new cluster from the two events of the first unclassified pair in the sorted list. The search ends when all events are classified. Clusters with fewer then `MIN_E_per_CLUSTER` events will not be identified as being part of a cluster.

5.3.2 Estimating inter-source separations

For each identified cluster, seismic data are processed in three sub-steps to estimate inter-source distances: picking waveform first arrivals; determining the combination of number, length, and start time of windows for implementing CWI; and estimating source separations with CWI. Users are free to conduct first arrival picking with their preferred method, however this package provides a user-friendly way for the task to be carried out in a graphical, interactive manner. The core functions and scripts are:

- `first_arrival_pick.m`: a script that allows users to pick the first arrivals of a series of waveforms interactively.
- `separation_parameters.m`: a script that finds the combination of number, length, and start time of windows to implement CWI with `CWI_sep.m` (see below) that gives the lowest separation uncertainties.
- `separations.m`: a function that estimates the inter-source separations of all event pairs in a given cluster recorded by a given station channel.
- `CWI_sep.m`: one of the core functions in the package called by multiple functions and scripts. It applies coda wave interferometry (Snieder, 2006) to estimate the separation between one pair of sources with similar mechanisms for isotropic sources in a 2D or 3D acoustic medium, or double-couple sources

in an elastic medium (Snieder and Vrijlandt, 2005). The two improvements introduced by Robinson et al. (2011) are applied: 1) removing the Taylor series approximation of the waveform autocorrelation, and 2) applying a restricted range when searching for the maximum correlation value `Rmax` to avoid cycle skipping.

The result of applying these functions is a data set of inter-source separations estimated by CWI, which are ready to be used to estimate relative source locations.

5.3.3 Estimating source locations

The relative locations of a cluster of events are solved by minimizing the objective function L (equation 5.10). To start the minimization, a set of initial event locations is needed, which can be generated either with function `initialize_locations.m` in the package, or be provided by user. The main location function `Source_Location.m` first evaluates L at the given initial event locations and computes its gradient, whose negative is the steepest descent direction and is used as the initial search direction. The function searches for the minimum along the search direction using a two-tier line search algorithm by calling `line_search.m`, First this routine conducts a brute force search by evaluating the objective function at regularly spaced points within a bracketed range to find bounds on a finer range search, and then conducts a second similar brute force search to find the approximate minimum within those bounds and finally sharpens the result by fitting a parabola using the approximate minimum and an adjacent point on each side. The event locations are then updated to the minimum found, and the value of L is reduced. The function then calculates the next search direction, a direction orthogonal to the gradient at the current position and conjugate to the last search direction, finds the minimum along the new search direction, and updates the event

locations. This process iterates until one of three conditions is met: 1) the value for any non-zero step length is larger than that obtained in the previous iteration; 2) the reduction in the value of L in an iteration is smaller than a threshold; or 3) the maximum allowed number of iterations is reached. Starting with a different set of initial locations is recommended if the iterations are terminated due to the third criterion, as some initializations may lead to convergence more rapidly than others.

For this part of the method, the core functions and scripts are:

- `Source_Location.m`: the main location function that estimates the relative location of a cluster of events using inter-source separation data (their mean and standard deviations) estimated with CWI.
- `ln_joint_likelihood.m`: a function that evaluates function L (equation 5.10) – the negative logarithm of the joint likelihood function for a cluster of events.
- `gradient.m`: a function that computes the gradient of function L numerically at a given set of event locations.
- `line_search.m`: a function that searches for the minimum of a one-dimensional function along a given direction.
- `initialize_locations.m`: a function that generates a set of initial locations for the minimization. It first randomly generates a set of locations, and then adjusts the order of these event locations to conform as well as possible to the input CWI separation estimates (so as to ensure the smallest sum of square residuals between the source separations given by the initial event locations and the mean of CWI separation estimates). This re-ordering procedure moves the initialization of optimization closer to the minimum, thus improving the speed of convergence.

- `rotate_cluster.m`: a function that rotates a cluster of points about its center in two orthogonal directions in the 3D space by given angles.

In a co-authored article (Singh et al., 2019) where changes in wave velocity and source locations are measured with the CWI method using laboratory rock physics data. I use code described above to estimate the relative locations of the acoustic emissions (sources) in Tivoli travertine. The estimated event locations form a pattern that is very similar to that formed by the actual locations of the sources applied in the experiment.

5.4 Synthetic examples

We use synthetic experiments to demonstrate the validity of the method and code; the data for these experiments is included in the code package so that users can verify their version of codes after editing to fit their specific needs. Applications of inter-source separation estimation and source location are shown separately in this section, to identify the abilities and limitations of each of the two successive steps. Whereas the theory of CWI assumes point scatterers (Snieder, 2006) with a constant background velocity, we use the Marmousi2 model (Irons, 2005) to test the method in a more realistic representation of Earth's velocity structure. We then demonstrate the performance of the optimization algorithm used to solve for event locations using CWI separation estimates. In the subsequent section we apply all three steps in the method (clustering, CWI and source location) to real earthquake data.

5.4.1 Estimating inter-source separations

We modeled the waveforms from two identical isotropic sources in the Marmousi2

model (Figure 5-2) which has an average velocity of 1250m/s. The recording network consists of a surface array with 15 receivers and two borehole arrays with 12 receivers each. The two sources are 64.7m apart with a dominant frequency of 5 Hz, and the dominant wavelength λ_d of the waveforms is 250m. We apply function `CWI_sep.m` to obtain estimates of the separation between the two sources. The estimates from different time-windows fluctuate around their mean at narrow distances as shown in Figure 5-2b for receiver R1, which gives a mean of 59.15m and a standard deviation of 6.40m. This result agrees with the empirical relations (Figure 5-1), that for a true separation $\delta_t = 64.7m$ (i.e., $\widetilde{\delta_t} = 0.259\lambda_d$) the separation mean $\mu(\delta_t)$ and standard deviation $\sigma(\delta_t)$ are estimated to be $0.237\lambda_d$ and $0.026\lambda_d$. The separation estimates are consistent among different receivers in both the surface array and borehole arrays, with uncertainties similar to that given by the empirical relations as shown in Figure 5-2c. For most receivers, the true separation is contained within one standard deviation of the mean of their associated separation estimates.

5.4.2 Estimating source locations

To demonstrate the ability of the code to solve for locations of a cluster of events using CWI separation estimates, we randomly distribute 50 sources in a cube with side length of 300m, shown as hollow circles in Figure 5-3. The dominant wavelength is $\lambda_d = 534m$, and the maximum source separation λ_{max} is $424m$ (i.e., $0.8\lambda_d$). For the purpose of this example, we create CWI separation data (separation mean and standard deviations) using the empirical relations (equation 5.5), where the true separations are computed as $\delta_t = \sqrt{(x'-x)^2 + (y'-y)^2 + (z'-z)^2}$ for events $e = (x, y, z)$ and $e' = (x', y', z')$. The separation data are thus exactly consistent with the known biases and level of

uncertainty of the CWI technique so that in this example we isolate the performance of the optimization algorithm that estimates source locations.

To implement the location process, initial locations for the 50 events are randomly distributed within the 3D cube using `initialize_locations.m`, as shown in Figure 5-3a. Thereafter the optimization took 27 iterations to converge with estimated locations shown as solid circles in Figure 5-3b. The improvement in event locations from the optimization is readily observed by comparing the result with their initial locations (red triangles in Figure 5-3a). The optimization does not lead the estimated locations to exactly the true event locations, due to the uncertainty $\sigma(\widetilde{\delta_t})$ in the separation data used. The average location error is 27m, corresponding to $0.05\lambda_d$. Figure 5-4 compares source separations calculated from the relocated event locations (red) to the separation data (blue) used as input to the optimization. This shows that although the input separation data deviate significantly from their actual value (the dashed line $y = x$) where the true separation is larger than $0.55\lambda_d$, the recovered source separations are only slightly underestimated. It is thus proven that the location algorithm is able to correct biases in the CWI estimates to a large extent.

Optimization techniques that guarantee convergence to the global minimum of a complicated nonlinear objective function do not currently exist. To this end, we implement the optimization multiple times with different random initializations of event locations. We illustrate the change of objective function value during the optimization process for all implementations in Figure 5-5. The 6 optimizations start with different objective function values because of their different random initial event locations. The value decreases rapidly for the first 10 iterations and then slows down as the algorithm approaches the various minima. All cases converge to the same minimum of 6738, except for the 4th, which gets stuck at a local minimum of

6753. For this synthetic example, the true (global) minimum of the objective function is known because the true event locations are known, and we find that the error in the minimum found is below 1, which is negligible. However, when applying the algorithm to real events where the correct minimum is unknown, using several optimizations from random event initializations can add confidence to the result to which most implementations converge.

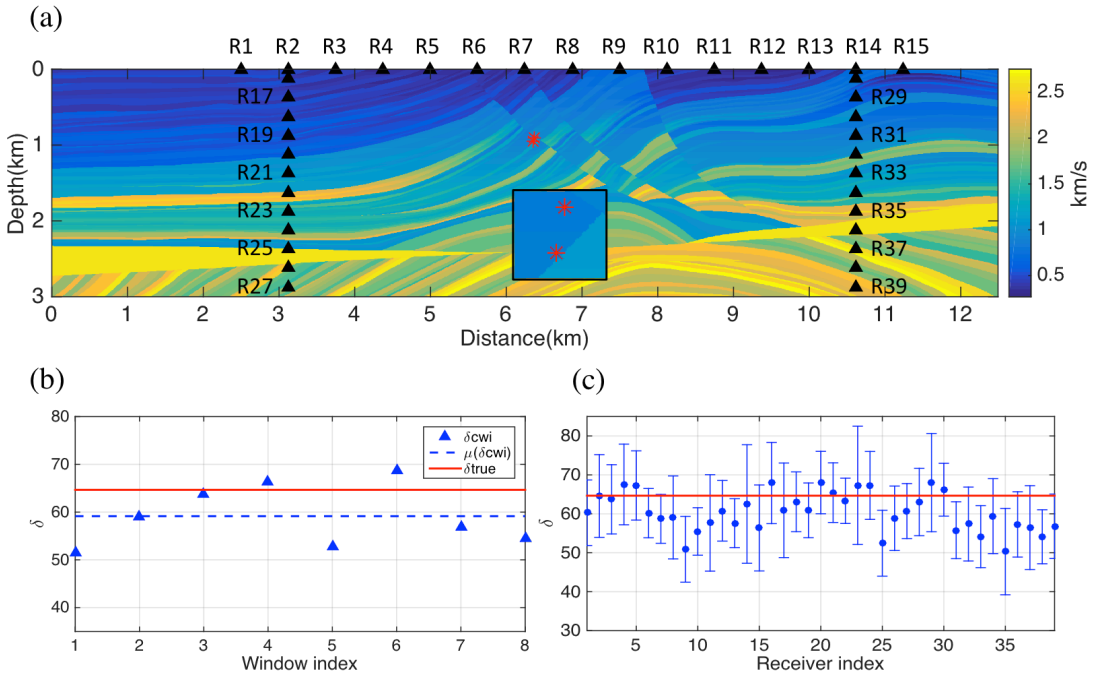

Figure 5-2: Panel (a) shows the Marmousi2 S-wave velocity model (Irons, 2005) used for the synthetic example. Triangles and stars are receivers and sources respectively; the small square panel shows the source region magnified. Panel (b) shows the separation estimates (triangles) of each time window from receiver R1 only, with the mean indicated by the dashed line and the true separation between the two sources by the solid line. Panel (c) shows separation estimates from all individual receivers with error bars showing the mean plus/minus one standard deviation; the red line is the true separation between the two events.

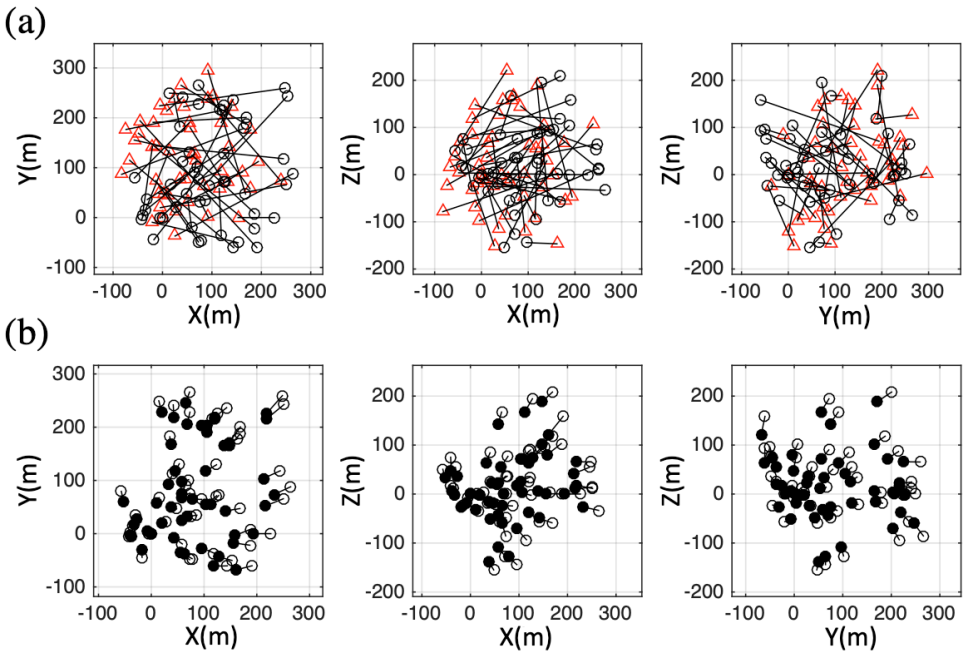

Figure 5-3: Planar projections of event locations, where axes X, Y and Z point in three orthogonal directions. Panels (a) compare the events' actual locations (circles) and their initial locations (triangles) before optimization, and the black bars show their differences. Panels (b) shows the events' actual locations (hollow circles) and the location results obtained (solid circles), with lines between the hollow and solid circles representing post-optimization location errors.

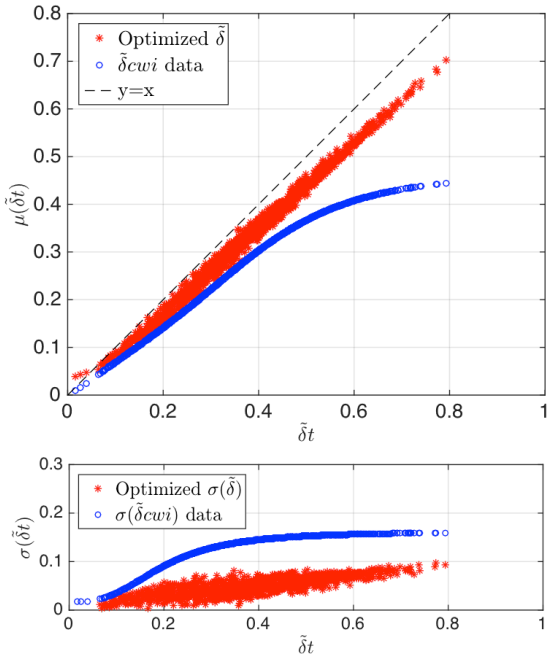

Figure 5-4: A comparison of input inter-source separations (blue circles) and separations calculated from the location result after optimization (red asterisks). The upper and lower panels show the separation data and their standard deviations, respectively.

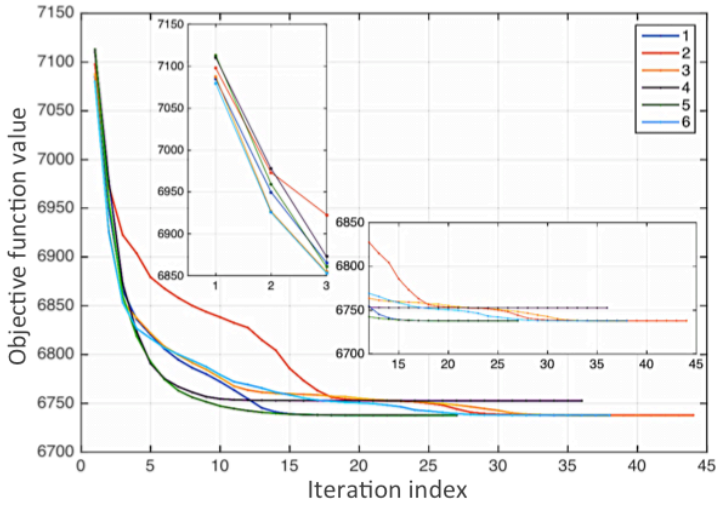

Figure 5-5: Illustration of the minimization process of each optimization from different initializations of random event locations using different colors to indicate each example optimization. The magnified panels show details of how the values of the objective function change with iteration number at the beginning and end of each optimization. The objective function is given in equation 5.10.

5.5 Application to New Ollerton earthquakes, England

New Ollerton, near Nottingham, England is a region where historical (micro-) seismic activity is related to coal mining. After some small earthquakes were detected, the British Geological Survey (BGS) deployed a temporary recording network in early 2014 to monitor further activity (Figure 5-6). These events have magnitude of 0.7-1.8ML, and the waveforms in standard SAC (Seismic Analysis Code) format (Helffrich et al., 2013) are filtered to 2-20Hz. Our dataset contains 118 SAC files, with 41 events recorded by 5 different channels of seismic stations. The code allows users to set customized criteria for selecting events and channels to be used to estimate locations. In this example, we required that events have been recorded by at least 2 station channels to be considered for clustering and then for location in the later steps. We also required that only station channels that have recorded at least 10 events contained in the total dataset (all 118 SAC files) should be used. These criteria are to ensure the robustness of data chosen for source location, presuming fewer data of higher quality gives more reliable results than more data of inconsistent quality. As a result, 34 events and 3 channels (channel NOLCZ, NOLFE, and NOLFN) are selected to be used for source location based on the above criteria.

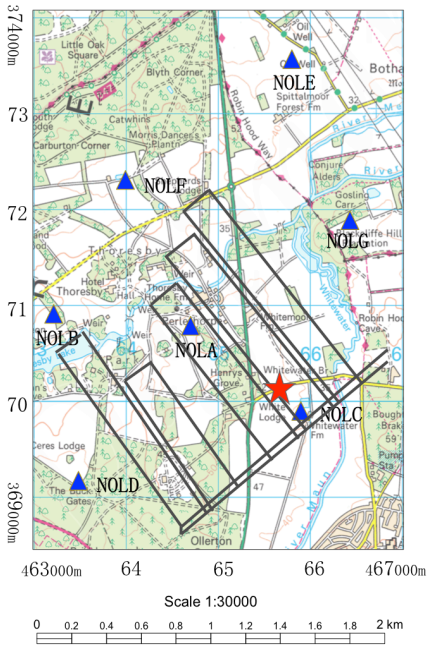

Figure 5-6: Map of the source region near Thorsby colliery, New Ollerton, Nottinghamshire, England. The rectangles indicate the locations of subsurface mining galleries, the star shows the area where the microearthquakes are likely to have occurred, and the triangles are temporary seismic stations.

With the threshold on the correlation coefficient of events set to `MIN_corr=0.9`, and the minimum number of events to form a cluster set to 5, the selected events are classified into two clusters with 11 and 23 events, respectively, with no unclassified events. Note that setting `MIN_corr` to 0.9 does not ensure that all events classified as being in the same cluster have an average maximum correlation coefficient $cravg_{max}$ over all station channels with one another, but rather it ensures that each event in a cluster has a $cravg_{max} \geq 0.9$ with at least *one* other event in the same cluster. Hence, it is recommended to set a high `MIN_corr` to ensure a sufficient level of waveform similarity, which ensures that the events have occurred on the same fault plane and that they have similar source mechanism as required by the

CWI theory.

For each cluster and each selected channel, we use the separation-uncertainty matrix to find the combination of number, length, and start time of windows that give the lowest uncertainties of CWI separation estimates. For example, for cluster 1 recorded by channel 1 (NOLCZ), the lowest average uncertainty of separation estimates is $\Omega = 11.08m$, when using 4 time windows with a length of 2.5s, starting from 19s, indicated by the darkest blue grid cell at the bottom-left of Figure 5-7. The separation-uncertainty matrix provides a guideline to choose an appropriate combination of parameters to use for CWI. Usually we find that when using other combinations of parameters, the results do not change significantly as long as we do not deviate too far from the optimal values found from the matrix.

We estimated source locations for each cluster using separation estimates obtained from all channels, and from individual channels. For each location optimization, 10 different random initializations are used to evaluate robustness of our location results. Figure 5-8a and 5-8b show the progress of each implementation of cluster 1 and 2 using data from channel NOLCZ, with the horizontal zoomed panels showing details of the eventual convergence. All cases converged to similar levels to within reasonable numerical errors. The convergence for cluster 2 seems less consistent than those for cluster 1. This is as expected: cluster 1 contains 55 event pairs from 11 events, hence its objective function L involves the sum of the logarithm of 55 pair-wise likelihood functions (equation 5.6), whereas cluster 2 comprises 23 events so function L involves the sum of the logarithm of 253 pair-wise likelihood functions. The consistent convergence level suggests that the minimum found using different random initializations should be close to the global minimum of function L, and therefore the relative source locations have been found.

The inter-source separations obtained from the optimizations are consistent among individual channels (red, blue and green) with small residuals, and they are very similar to the results obtained using all three channels (black) as shown in Figure 5-9a. The location process corrects for the underestimation bias of the CWI technique, as we see by comparing the recovered separations (red) and the original CWI separation data (black) used as input to the optimization (Figure 5-9b). Figure 5-10 illustrates the location results of cluster 2 using data from individual channels, and data from all three channels, projected onto three orthogonal planes. The patterns show a high level of consistency among single channels and multiple channels. All channel combinations predict a characteristic horseshoe type structure for the cluster. Thus, we show once again that the CWI source location technique is able to give reliable relative location estimates even from single recording channels.

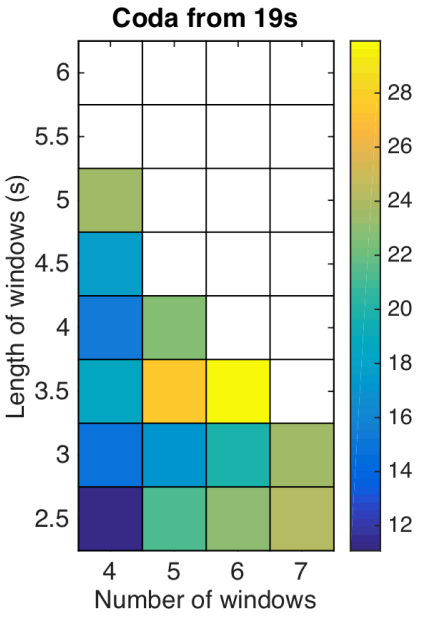

Figure 5-7: A slice of the 3D separation uncertainty matrix. Colors indicate the values of the average standard deviations resulting from the corresponding parameter combination of number of windows, window length and start time of windows, used to divide the coda. White cells indicate parameter combinations that are not supported by the available data. For all scenarios represented in this slice, the start of the time windows is 19s. The parameter combination giving the lowest average separation uncertainty is 4 windows with a length of 2.5s, starting from 19s.

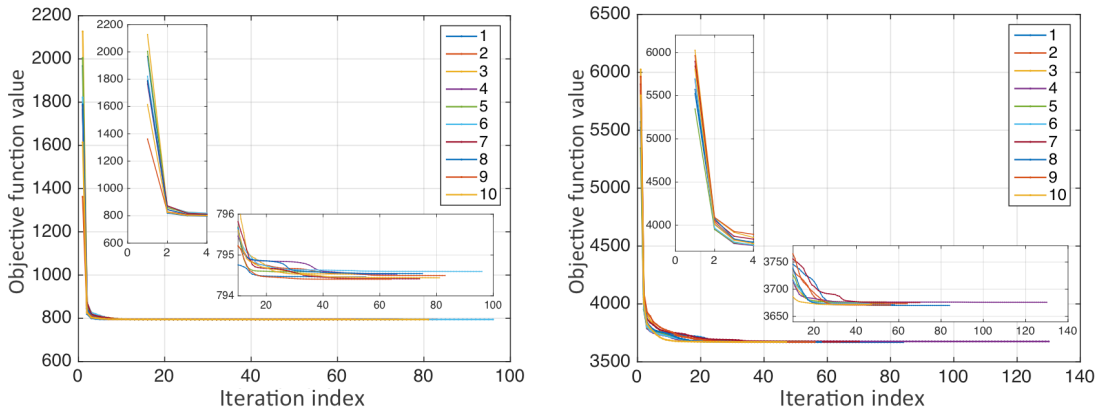

Figure 5-8: Illustrations of the minimization process using different colors for each optimization with different random initializations for cluster 1 (left) and cluster 2 (right) using data from channel NOLCZ. The magnified panels show details of how the values of the objective function change with iteration number at the beginning and end of each optimization. The objective function is given in equation 5.10.

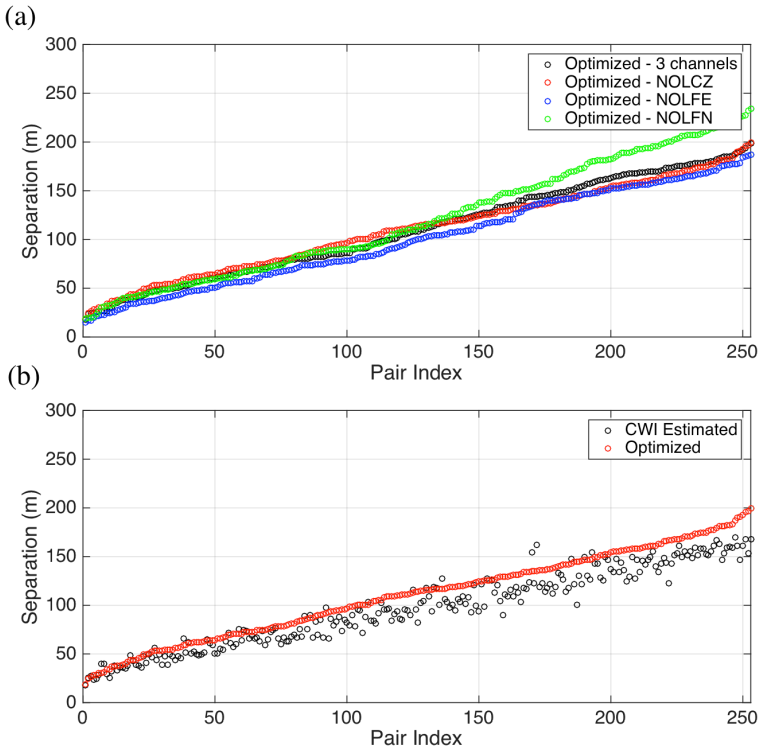

Figure 5-9: CWI estimates of source separations and their optimized counterparts (the latter calculated from the estimated event locations) of cluster 2. Panel (a) shows the optimized separations using all three channels (black), and using single channels NOLCZ, NOLFE and NOLFN (red, blue, and green). Panel (b) compares the optimized separations of channel NOLCZ (red) with the original CWI separation estimates (black).

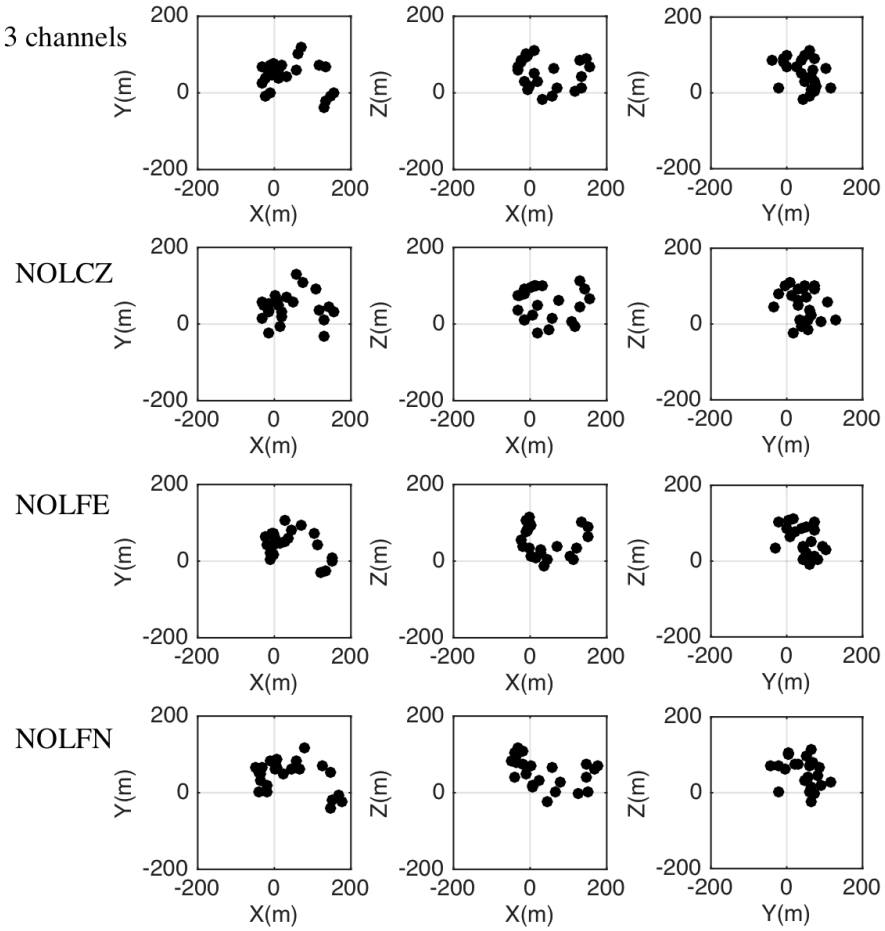

Figure 5-10: Planar projections of relative event location results of cluster 2, using all three channels (top row), and using single channels NOLCZ, NOLFE, and NOLFN (successive rows). Axes X, Y and Z point in orthogonal directions.

5.6 Discussion

A wide range of seismic applications requires accurate relative source locations. The popular double-difference method (Waldhauser and Ellsworth, 2000) produces high resolution location results when a large number of seismic stations is available, however its performance deteriorates when this requirement is not met, and results are subject to the choice of damping factor when solving the least squares problem. The novel location method based on coda wave interferometry opens a new avenue for research and applications in areas where a dense recording system with good source-station azimuthal coverage is unavailable, or where an independent method is useful to test compatibility of robustness of existing methods.

While we have developed and used the code package for seismic applications, there are numerous other areas in which energy source location estimates are useful or necessary as summarized in the Introduction. The CWI method could potentially be applied to any of them, provided that the medium of wave propagation scatters the wavefield strongly in many directions. This is necessary in order to ensure that the recording of coda at each receiver contains energy that left each source at a wide range of angles. This range of angles is the equivalent of the standard requirement of a wide aperture between each source and the set of receivers for conventional location methods.

The CWI based method was first developed ~10 years ago (Snieder and Vrijlandt, 2005; Robinson et al. 2011) but the uptake of the method has been slow, with only two known applications (Robinson et al., 2013; Zhao et al., 2017). This may partly be explained by the lack of a readily available code package to implement the method, a deficiency that we rectify herein. Harder is to change the attitude that

seismologists know the structure of the medium (Earth) well enough that deterministic methods can be used. Indeed, CWI as used here takes the opposite view: that we do not know the structure well, since the existence of strong coda in most recordings of crustal earthquakes shows that there must be strong scattering from unknown structure. The examples presented here show that even in such cases, relative locations can be found over length scales of a fraction of a wavelength, which should go some way towards convincing others that this point of view is both valid, and useful.

5.7 Conclusion

We present a MATLAB package that estimates relative source locations using source separations estimated with the CWI technique. The location method takes account of known biases in CWI separation estimates, and is capable of correcting them to a significant extent. It is able to locate events with a single station channel as demonstrated in our synthetic and real-data examples, but also to combine data from seismic arrays. The code package that accompanies this chapter provides a main script that allows users to conduct the three-step method (classifying events, estimating source separations, and estimating relative source locations) while maintaining the flexibility for users to edit the code based on their own needs. This computationally inexpensive code can be run on a standard laptop for the size of event cluster demonstrated herein.

6

DISCRIMINATING DIFFERENT TYPES OF PERTURBATIONS USING CWI

6.1 Introduction

In both seismic and laboratory rock physics settings, sometimes more than one type of perturbation can occur simultaneously. For instance, after a major earthquake, seismic velocity would change as aftershocks expanding along the fault plane would create new fractures which would change the properties of the medium in which seismic waves propagate (Baisch and Bokelmann, 2001; Schaff and Beroza, 2004; Peng and Ben-Zion, 2006); and in laboratory where repeated sources are needed to study physical properties of rocks or other materials, small changes in the location of sources could occur while the property of interest is being changed actively by experimenters, and this could have a significant impact on their measurements and hence their interpretations (Singh et al., 2018). To this end, it would be useful to identify all types of perturbations that have occurred in the system, and either to estimate all of the perturbations, or measure the perturbations of interest after removing the effect of others. CWI has the potential to distinguish among changes in propagating velocity, scatterer positions and source location, as the significant controlling data (travel-time differences of arrivals in coda) computed from the recorded signals have different distributions for different types of perturbations Snieder (2006). In this chapter, we explore this potential of the CWI methods though numerical experiments.

Section 6.2 focuses on estimating velocity change in the propagating medium with coexisting perturbations on source location or scatterer positions, where the conventional windowing technique to implement CWI is compared with the stretching technique. In Section 6.3, we study cases in which both velocity and the source location are changed, and show that both changes can be estimated with CWI separately. We show in Section 6.4 how to identity the changes when source location and scatterer positions are perturbed simultaneously, and that the estimation of changes in source location can be improved if the effect of scatterer positions displacement is removed. Section 6.5 shows our treatment for cases where all three types of perturbations exist.

6.2 Estimating velocity change dv/v

Conventional methods for measuring wave velocity often use the first or early arrivals of waveforms, assume a known source-receiver distance, and are strongly dominated by specific source-receiver paths (Molyneux and Schmitt, 1999; Zhou 2006; Jones 2010; Blias 2015). The result of these methods is therefore susceptible to the accuracy of source and receiver locations and can give erroneous results if used to represent the bulk velocity of the medium. Also, small perturbations in the medium can be hard to detect, especially if the change is not located along the specific source-receiver path followed by the first arriving waves. Coda waves, generated by multiple scatterering, travel across a much larger region of the medium, they may sample the regions multiple times, and are shown to be more sensitive to small velocity changes (Weaver and Lobkis, 2000; Snieder et al., 2002) and give more accurate and precise estimates of bulk velocity change of the medium (Singh et al., 2018).

Coda wave interferometry (CWI) estimates minute changes in velocity by using the crosscorrelation of the waveforms recorded by the same receiver before and after the perturbation. It has been used in the laboratory to measure small velocity changes in rocks due to changes in temperature (Snieder et al., 2002), stress (Gret et al., 2006), and water saturation (Tange et al., 2015); to monitor velocity changes in concrete (Larose and Hall, 2009; Masera et al., 2011; Planes and Larose, 2013); to detect velocity changes in fault planes before or after major earthquakes (Baisch and Bokelmann, 2001; Schaff and Beroza, 2004; Peng and Ben-Zion, 2006); to monitor temporal variations in volcanoes before, during or after eruption (Wegler et al., 2006; Gret et al., 2005; Hotovec-Ellis et al., 2014); and to study earthquake-volcano interaction (Battaglia et al., 2012).

The theory of CWI assumes that a medium with seismic velocity v is perturbed in a way that the relative velocity change dv/v is constant in the medium, and that heterogeneities in the medium and the source stay unchanged. Snieder et al. (2002a) show that the relative velocity change is related to the mean of the travel-time change of waves arriving in a time window with a central time t and a half-width t_ω by

$$\frac{dv}{v} = -\frac{\langle \tau_T \rangle_{(t,t_\omega)}}{t}. \tag{6.1}$$

The mean of travel-time differences $\langle \tau_T \rangle_{(t,t_\omega)}$ of waves arriving within window $[t - t_\omega, t + t_\omega]$ is found where the waveform correlation coefficient (equation 2.4) attains its maximum. Thus, the relative velocity change dv/v is readily computed as the negative ratio of $\langle \tau_T \rangle_{(t,t_\omega)}$ to the central time t. Note that the relative velocity change dv/v is considered to be constant in the medium, but not the velocity v. For elastic waves, the estimated relative velocity change is a weighted average of changes in P and S velocities Snieder et al. (2002b):

$$\frac{dv}{v} = \frac{\beta^3}{2\alpha^3 + \beta^3}\frac{d\alpha}{\alpha} + \frac{2\alpha^3}{2\alpha^3 + \beta^3}\frac{d\beta}{\beta}, \tag{6.2}$$

where α and β are P- and S-wave velocities, respectively. The weighted average is dominated by the S-wave component. For instance, for a Poisson medium $\frac{dv}{v} = 0.09\frac{d\alpha}{\alpha} + 0.91\frac{d\beta}{\beta}$. The relative velocity change dv/v is thus related to the mean travel-time differences in time window $[t - t_\omega, t + t_\omega]$, which can be obtained from correlation coefficient 2.4. Estimates from multiple time windows can be used to assess uncertainties.

There is another way of implementing CWI: the stretching interpolation technique (Sens-Schönfelder and Wegler, 2006). The stretching technique has been applied to study the variations of seismic velocities in volcanoes (Sens-Schönfelder and Wegler, 2006) and at fault zones (Wegler and Sens-Schönfelder, 2007), to assist forecasting volcano eruptions (Brenguier et al., 2008); and to monitor the weak changes in a gel

with scattering inclusions in laboratory experiments (Hadziioannou et al., 2009).

The stretching technique assumes a constant velocity change dv/v in the medium as the windowing technique does, so the relative travel-time difference $\frac{\tau_T}{t}$ is also a constant, which is determined as a factor by which the time axis of the perturbed waveform must be stretched (or compressed) to obtained the best correlation with the unperturbed waveform. The best stretching factor $\frac{\tau_T}{t}$ is found by interpolating the perturbed waveform at times $t(1-\varepsilon)$ with various constants ε and conducting a grid-search for ε_{max} that gives the maximum correlation coefficient with the unperturbed waveform. The relative velocity change is thus found to be $\frac{dv}{v} = \frac{\tau_T}{t} = \varepsilon_{max}$.

In the remainder of this section, we first compare the stretching and windowing techniques for implementing CWI with numerical experiments with velocity change being the only type of perturbation. We then introduce scatterer displacement and source displacement into the system, and test the ability of the two methods for measuring the velocity change. Waveforms are generated by solving the acoustic wave equation with a staggered-grid finite-difference (FD) solver. A point-scatterer medium (Figure 6-1) with 300 uniformly distributed scatterers is created with 3000×3000 grid points, with grid spacing in both x (horizontal) and z (depth) directions being 10m and a time step of 0.001s. A Ricker wavelet is used with a center frequency of 6Hz. Six isotropic sources are applied in the center of the medium, and they are recorded by six receivers as shown in Figure 6-1.

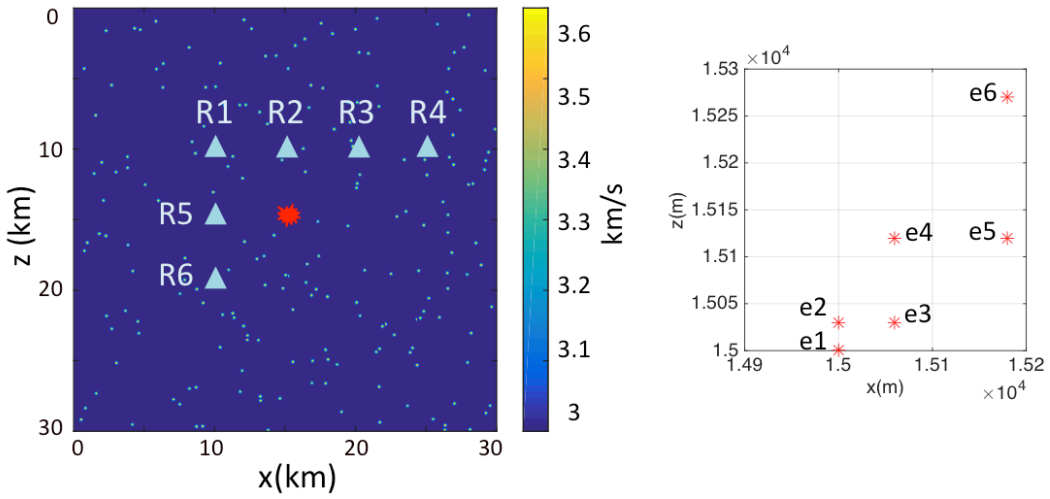

Figure 6-1: Point-scatterer medium used to conduct the experiments in this chapter. Color scheme indicates the velocity of the medium. Red stars in the center of the model show the source region, and the blue triangles are the receivers. The smaller panel is a zoomed source region.

6.2.1 Estimating dv/v as the only type of perturbation

The original velocity across the medium is $v_0 = 3000m/s$, and we use the six receivers to record wavefields emitted from each of the six sources. The velocity is then perturbed by a small uniform change of $15m/s$, i.e. $0.5\%v_0$, and waveforms are re-recorded. First, we use the stretching interpolation technique to measure this change. For each event and each receiver, we interpolate the perturbed waveform with stretching factors $\varepsilon = 0.00001$ to 0.01 in steps of 0.00001 (i.e. 0.001% to 1% in steps of 0.001%), calculate the crosscorrelation of the interpolated perturbed waveform with the unperturbed waveform, and find the relative velocity change dv/v as the factor that leads to the maximum correlation. Figure 6-2 shows an example of a perturbed waveform stretched by the best stretching factor ε_{max} and the unperturbed waveform recorded by the same receiver. With no added noise, the estimated dv/v using the stretching method for all sources and all receivers is 0.5% for the searching precision 0.001% used.

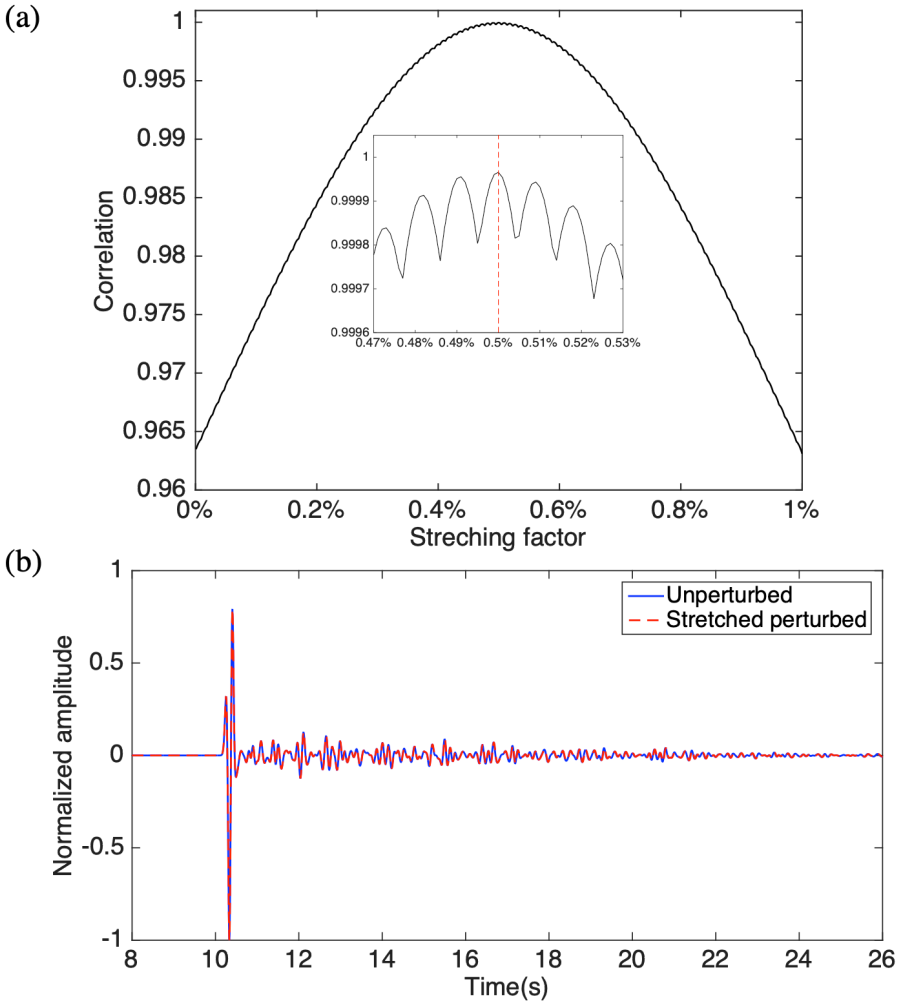

Figure 6-2: Example application of the stretch interpolation technique. Panel (a) shows the correlation of the original waveform and the perturbed waveform after stretching using different stretching factors. Panel (b) shows the comparison of the original (blue) and the perturbed (red) waveform after the detected velocity changed found removed.

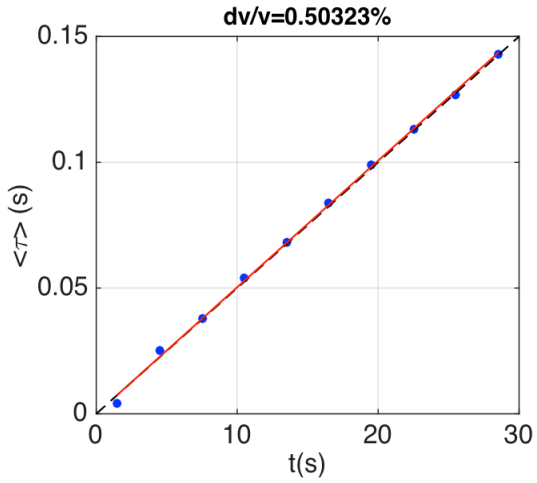

Figure 6-3: The mean of travel-time changes of each time window (dots) with the least-square fit (solid line) using the windowing CWI, and the reference for which the estimated velocity equals the true velocity (dashed line), using waveforms recorded from source e1 (see Figure 6-1) recorded by receiver R1.

We then use the windowing technique to measure the relative velocity change. For each event and each receiver, we take a segment 10s-40s from the unperturbed and the perturbed waveforms, align the first arrivals, and apply CWI with time windows of 3s. Each time window would give an estimate of the relative velocity change dv/v, however we take the average of the estimates from all time windows by fitting a line using doublets $[\langle\tau_T\rangle_{(t,t_\omega)},\ t]$ given by all windows in a least-squares sense, and take an estimate of dv/v as the slope of the fitted line. Figure 6-3 shows the case for source e1 using the waveforms recorded by receiver R1 before and after the perturbation, where the relative velocity change dv/v is estimated to be 0.5032%, resulting in an error of 0.0032%.

Figure 6-4 shows the estimates of dv/v using windowing technique for all events by each receiver. The mean of estimates of individual receivers fluctuates about the true dv/v (dashed line), distributing in a range of 0.4907%~0.5061% (blue dots),

giving an overall average estimate of dv/v of 0.4981% (solid line) with a small error of 0.0019%, and a standard deviation of 0.0068% (shade).

In order to understand the applicable range of the two methods, we conduct experiments with a wide range of true dv/v, varying over four orders of magnitude (i.e. 0.01% ~ 10%), and measure dv/v with the stretching and windowing method. Figure 6-5a shows the mean and standard deviation over all sources and receivers for each true dv/v, where true dv/v values are plotted on a logarithmic scale for display purpose. The dashed line shows the cases where the estimated dv/v is equal to its true value. For up to the true $dv/v = 2\%$, both methods lead to fairly accurate estimates, with low uncertainties, which are hardly observed in the plot. For true $dv/v \geq 2\%$ the stretching technique is able to give accurate estimates as expected, while the windowing technique fails to give correct estimates due to cycle skipping in the crosscorrelation of waveforms in the time windows applied. Figure 6-5b provides a clearer display of the uncertainties of estimates for each true dv/v using the two methods. The stretching technique gives lower standard deviations than the windowing technique for all cases, while the standard deviations of estimates given by the windowing technique are lower than 0.05 of the true values for all true dv/v. Hence, from the numerical experiments, we summarize that where velocity change is the only type of perturbation, the stretching technique works for a larger range of true dv/v than windowing, providing a lower uncertainty in the result.

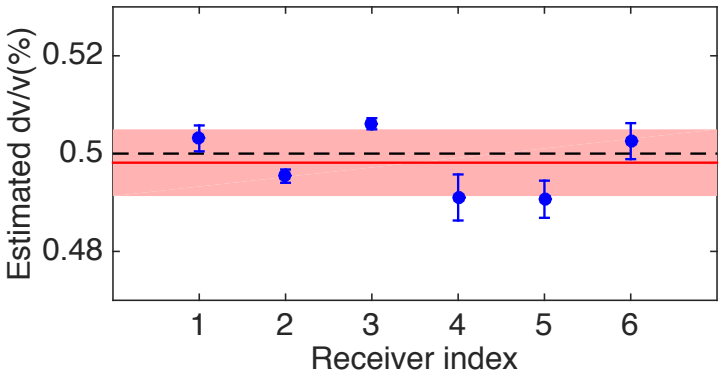

Figure 6-4: Estimated velocity change using windowing CWI. The dots and bars show the means and standard deviations of estimates over the six sources obtained from individual receivers; the solid line and the shade show the mean and standard deviations of the estimates over all receivers; and the dashed line shows the true velocity change.

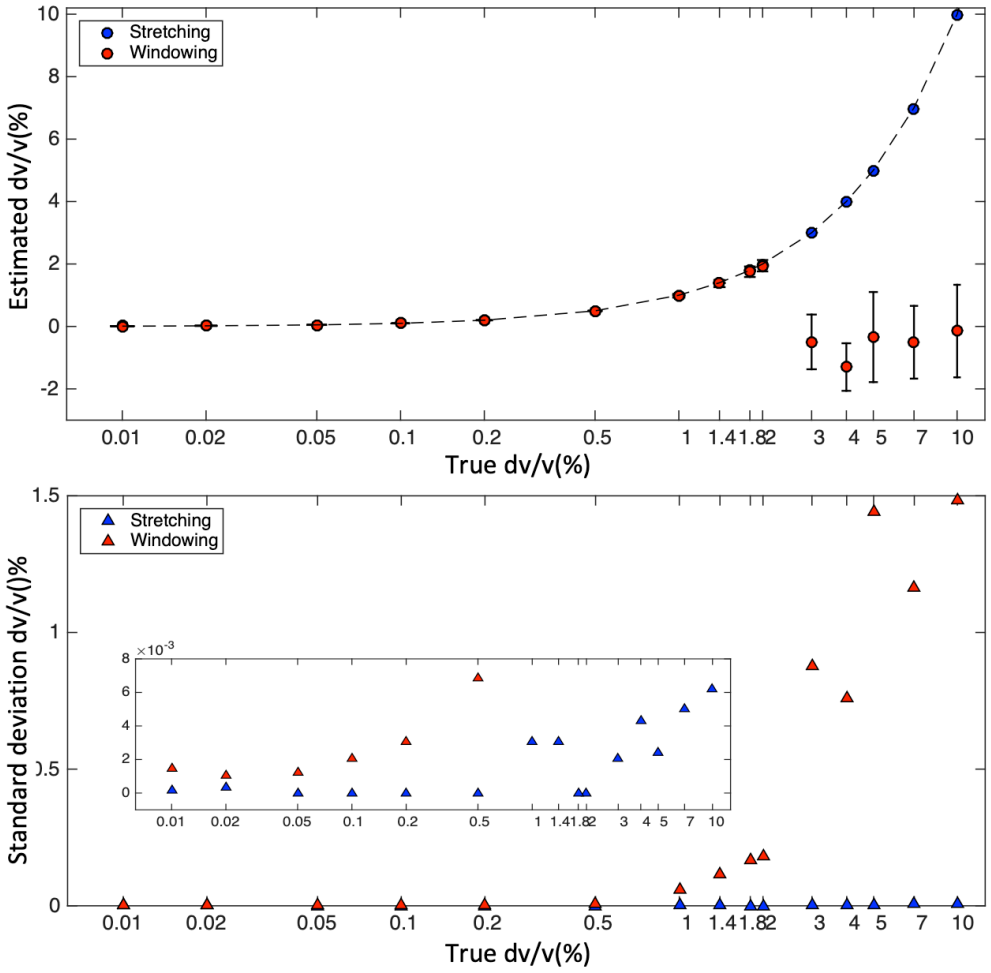

Figure 6-5: Estimated relative velocity change using the stretching (blue) and windowing technique (red), where true dv/v values are plotted on a logarithmic scale. Panel a shows the mean (dots) and standard deviations (bars) of the estimates over all sources and receivers, where the dashed line indicates where the estimate is equal to the true value. Panel b shows standard deviations of the estimates given by the two methods with a zoomed plot for the lower values observed.

6.2.2 Estimating dv/v with scatterer displacement

In some occasions, velocity change is accompanied by displacement of scatterers in the medium, for instance, in a turbulent fluid with bubbles or particle suspensions (Cowan et al., 2000; Page et al., 2000). In geophysics, wave velocity changes have been monitored for analyzing structural change in volcanoes before and after eruption (Wegler et al., 2006; Battaglia et al., 2012), while wave velocity changes could be accompanied by movement of heterogeneities. It would be intriguing and useful to know how each method would be affected by the existence of this other type of perturbation. Here we generate waveforms using a similar medium to that shown in Figure 6-1, with the introduction of a velocity change $dv/v = 0.5\%$, and an uncorrelated movement of the scatterers with a root mean square displacement $\delta_{scat} = 3\%\lambda_d$, where λ_d is the dominant wavelength of the waveforms. A root mean square displacement is a commonly used measurement of the spatial extent of a random motion, which can be thought of as a measure of the portion of the system explored by a random walker. A root mean square displacement of the scatterers is defined as (Daan and Berend, 2001):

$$\delta_{scat}(t) = \sqrt{\frac{1}{N}\sum_{n=1}^{N}\left(\boldsymbol{x_n}(t) - \boldsymbol{x_n}(0)\right)^2}, \tag{6.3}$$

where N is the number of scatterers, $\boldsymbol{x_n}(t)$ is the position of the nth scatterer at time t, and $\boldsymbol{x_n}(0)$ is the original position of the nth scatterer. In our experiment the equation is simplified by removing the time factor, as we only take one state other than the original state, i.e. the scatterers are only displaced once:

$$\delta_{scat} = \sqrt{\frac{1}{N}\sum_{n=1}^{N}(\boldsymbol{x'_n} - \boldsymbol{x_n})^2}, \tag{6.4}$$

where $\boldsymbol{x_n}$ and $\boldsymbol{x'_n}$ are the position of the nth scatterer before and after being

perturbed. This is implemented by moving the scatterers by a distance r to the direction forming an angle of θ from negative depth axis, where r follows a Gaussian distribution with a mean of $3\%\lambda_d$ and a standard deviation of $1\%\lambda_d$, and θ follows a uniform distribution from 0 to 2π.

We estimated dv/v of the perturbed medium using the two methods. Figure 6-6 shows the estimates given by each individual receiver. Both methods lead to estimates with errors smaller than 0.01%, however estimates of the windowing CWI are clearly more accurate and precise than those of stretching CWI. Estimates of windowing technique are also more consistent among different receivers than those from stretching.

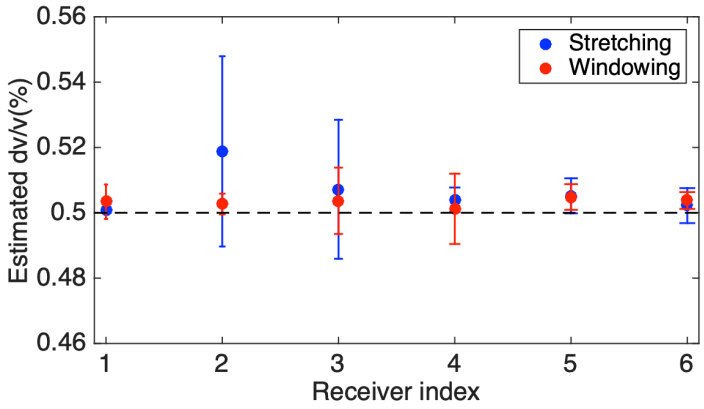

Figure 6-6: Estimates of relative velocity change dv/v using the stretching (blue) and windowing (red) technique when scatterer displacement also occurs. The dots and bars show the mean and standard deviations over all sources obtained from individual receivers. The dashed line shows the true relative velocity change.

6.2.3 Estimating dv/v with source location displacement

We now consider cases where a velocity change and a source displacement occur simultaneously. A displacement in source location is modeled by using multiple

identical sources in the medium at different locations as shown in Figure 6-1. We record waveforms in the original medium and then in the perturbed medium with true $dv/v = 0.5\%$. First, we take waveforms from source e1 propagating in the original medium ($v_0 = 3000m/s$) and those from source e2 propagating in the perturbed medium ($v = 3015m/s$) and use both techniques to measure the velocity change with a source displacement of $\delta_{source} = 30m$, i.e. $6\%\lambda_d$. Figure 6-7 shows the results obtained using individual receivers. The stretching technique leads to estimates of dv/v with a mean of 0.5458% (error=0.0458%) and a standard deviation of 0.0748% over individual receivers, and the estimates of windowing technique have a mean of 0.4996% (error=0.0004%) and a standard deviation of 0.0122%. In this experiment, windowing CWI measures velocity change 2 orders of magnitude more accurately than stretching, and reduces the uncertainties in the estimates by ~80%. Hence, we summarize that for a small source displacement, windowing technique gives more reliable estimates of velocity change than the stretching technique.

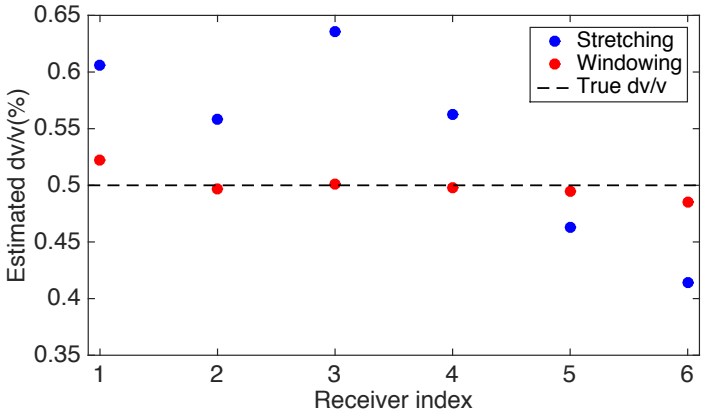

Figure 6-7: Estimates of relative velocity change dv/v using the stretching (blue) and windowing (red) technique when a simultaneous perturbation in source location occurs. The dots show estimates obtained from individual receivers. The dashed line shows the true relative velocity change.

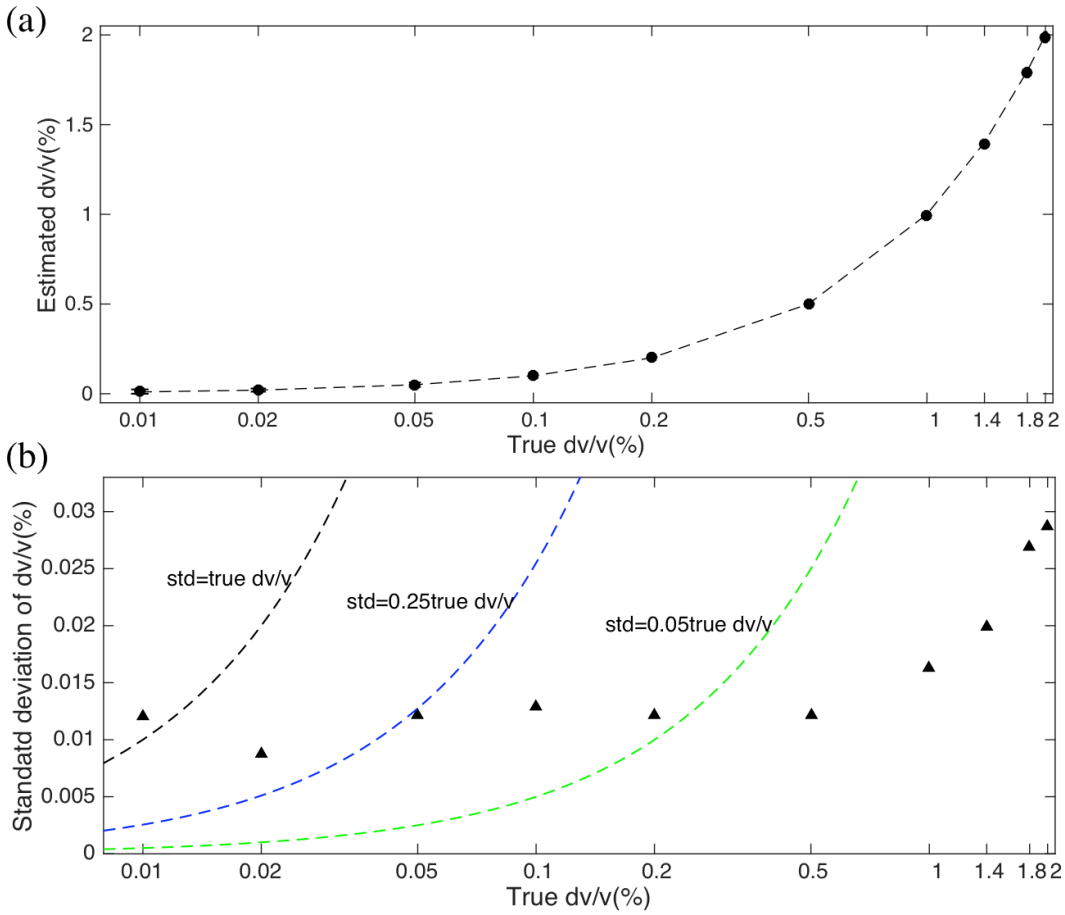

Figure 6-8: Estimated relative velocity change using windowing CWI, where a simultaneous source perturbation of 30m occurs and true dv/v values are plotted on a logarithmic scale. Panel a shows the mean (dots) and standard deviations (bars) of the estimates over all sources and receivers, where the dashed line indicates where the estimate equals to the true value. Panel b shows the standard deviations of the estimates. The black line shows where the standard deviation (std) of the estimate equals the value of true dv/v, hence the area above shows std is greater than the true dv/v and the area below shows std is lower than the true dv/v. The blue and green line show where std equals to $0.25dv/v$ and $0.05dv/v$, respectively.

To further explore the capability of CWI for estimating velocity change under the influence of displacement in source location, we conduct experiments with a series

of true dv/v within the working range ($\leq 2\%$) of windowing CWI found previously, and a source displacement $\delta_{source} = 30m$. Figure 6-8 shows the mean (top panel) and standard deviation (bottom panel) over all receivers for each true dv/v, where true dv/v values (horizontal axis) are plotted in their logarithm scale for displaying purpose. The dashed line indicates where the estimated dv/v is equal to the true value, which is the case for all true dv/v in our experiments. The standard deviations of the estimates are too small to be observed in the same plot with the means, hence are displayed separately, where the dashed lines indicate where the standard deviations of dv/v estimates equal 1 (black), 0.25 (blue) and 0.05 (green) times dv/v. In all cases except for true dv/v=0.01%, the standard deviation of the estimated true dv/v are lower than true dv/v. For true $dv/v \geq 0.05\%$, the standard deviation are lower than 0.25 of the true values. Windowing CWI achieves standard deviations lower than 0.05 of true dv/v when the true dv/v are above 0.2%. Therefore, with a source displacement of 30m ($6\%\lambda_d$), windowing CWI gives reliable estimates of velocity change for true dv/v in a range of 0.05%~2%, with standard deviations lower than 0.25 of the true dv/v.

As shown above, a source displacement over $25\%\lambda_d$ can lead to cycle skipping in waveform crosscorrelation so that the windowing technique would fail to give an accurate estimate of source displacement. We wondered whether the method would also fail to give an accurate estimate of velocity change with a source displacement $\delta_{source} > 25\%\lambda_d$. To investigate this, we use windowing CWI to measure the velocity change with a range of source displacements, using the six sources as shown in Figure 6-1. The velocity change is fixed at true $dv/v = 0.5\%$, and source displacement varies from 30m to 325m, i.e. 6%~65%λ_d. For each test, we take an unperturbed waveform with $v_0 = 3000m/s$ and a perturbed waveform from a different source with $v_1 = 3015m/s$. We repeat this process 15 times for all

waveform pairs from the 6 sources. Figure 6-9 shows the estimated dv/v for each source displacement, which indicates that for up to $\delta_{source} = 120m$ (i.e. $24\%\lambda_d$), windowing CWI method gives measurements of dv/v with errors within acceptable range. The results of this experiment demonstrate that a small velocity change can be measured using the windowing CWI method with a source displacement not larger than a quarter of a dominant wavelength.

In this section, we used numerical experiments to test the reliability and applicable range of the stretching interpolation technique and the windowing technique to implement CWI to measure a velocity change in the propagating medium. The stretching technique has a larger working range than windowing when only a change in velocity occurs: windowing technique works for true $dv/v \leq 2\%$, while in our experiment the stretching technique works up to $dv/v = 10\%$, which theoretically has an unlimited upper limits as it uses the whole waveforms as one time window. Within the working range of both techniques, in general, stretching leads to lower uncertainties.

However, the windowing technique outperforms stretching when other types of perturbation accompany the velocity change. If a small scatterer displacement or a source displacement occurs simultaneously with the velocity perturbation, estimates of dv/v using windowing technique are more accurate and more precise than those using stretching in all cases. In our experiments, windowing technique gives reliable dv/v measurements for true dv/v in a range of 0.05% to 2% for a small separation. It is also found to give correct measurement of velocity change with acceptable uncertainties with the existence of a source placement of up to a quarter of a dominant wavelength.

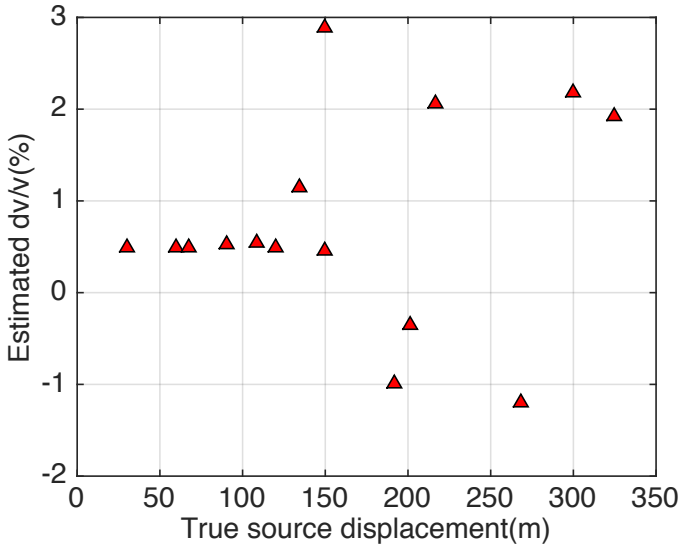

Figure 6-9: Estimated relative velocity change dv/v measured with a range of source displacements.

6.3 Estimating source location displacement with velocity change

We consider cases where perturbations in source location and velocity of the propagating medium occur simultaneously, and measure the perturbation in source location. Usually, when distances between sources are measured for relative source location, velocity change is not taken into consideration. This can lead to impact on the estimation of inter-source distances and the error will be passed on to source locations. To this end, it would be desirable to detect and remove any velocity change before measuring the inter-source distances. Here we show how this can be achieved using windowing CWI and the stretching technique together for sources of similar mechanism, and how the implementation improves the inter-source separation estimation.

The experimental settings used are shown in Figure 6-1. Taking source e1 and e3 as

an example, Figure 6-10 shows a 3s time window of the unperturbed waveform of e1 ($v_0 = 3000m/s$) and the perturbed waveform of e3 ($v = 3015m/s$) recorded by receiver R1, which contains the early arrivals and a part of coda, respectively. Event e1 and e3 are separated by $\delta_{source} = 67m$ (i.e. $13.4\%\lambda_d$). First, we use CWI to detect the velocity change. A segment of 10s-40s from the pair of waveforms is taken, and ten time windows of 3s are used. Figure 6-11 shows that the bulk velocity of the medium has changed by 0.4978% when the waveform of e3 is recorded. When all receivers are considered, the velocity change is estimated to be $dv/v = 0.4921\%$, with a standard deviation of 0.0079% (Figure 6-12).

Next, we use the idea of the stretching interpolation technique to remove the effect of the velocity change from the perturbed waveform. The detected velocity change $dv/v = 0.4921\%$ is considered as the factor by which if the time axis of the perturbed waveform is stretched, it will become the waveform that would have been recorded if there were no velocity change in the medium, with the only perturbation being the source displaced from the location of e1 to that of e3. This is done by interpolating the perturbed waveform at times $t(1 - dv/v)$, and the stretched perturbed waveform and the unperturbed waveform of e1 and e3 recorded by receiver R1 is displayed in Figure 6-13. The differences in the two waveforms are now only due to the difference in source location, assuming that the velocity change measurement is correct to within acceptable errors.

Finally, we use the unperturbed waveform of e1 and the stretched perturbed waveform of e3 to estimate the source displacement (i.e. the distance between sources e1 and e3) using CWI. Six time windows of 3.5s starting from 15s of the waveforms are used. Figure 6-14 shows the results given by all individual receivers with an average of 62.43m, underestimating the source displacement by 4.57m.

Estimates from individual receivers for both velocity change dv/v and source displacement δ_{source} are consistent, indicating that CWI is able to give reliable results using very few receivers in scattering medium.

For all events, we repeat the test to measure a range of source displacements by taking one source from the unperturbed medium ($v_0 = 3000m/s$) and another from the perturbed medium ($v = 3015m/s$). Figure 6-15 shows a comparison of the source displacement estimates of 15 event pairs estimated with dv/v (red) and estimated after dv/v is removed (blue). Both the estimated and true source displacements are normalized by the dominant wavelength of the waveforms. It is found that removing the effect of velocity change can significantly improve the estimation of source displacement for the whole working range of CWI, i.e. true $\delta_{source} \leq 25\%\lambda_d$, in that both the accuracy and precision of the estimates are increased.

In this section, we proposed a treatment for cases where both medium velocity and source location are perturbed. As shown in Section 6.2, windowing CWI is able to measure small changes in velocity (0.05%-2% in our numerical experiments), so we first use the windowing CWI method to determine the velocity change with a high accuracy. We then use the stretching technique to remove the effect of the velocity change from the perturbed waveform, and finally use windowing CWI to estimate the source displacement. It is demonstrated that this "estimation-compensation" treatment of dv/v can significantly improve the estimation of source displacement. Note that this treatment can also be used as a pre-processing step when other methods for estimating inter-source distances are used, as it removes the influence of the velocity change and leaves the differences in the waveforms only attributed to differences between sources.

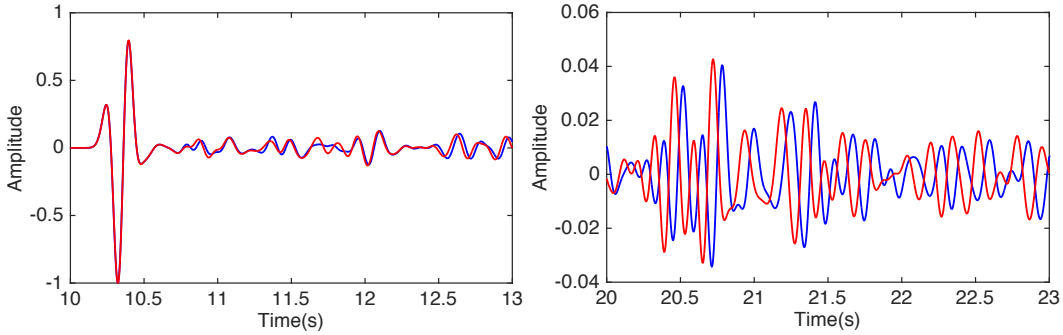

Figure 6-10: Comparison of the original (blue) and perturbed (red) waveforms recorded by receiver R1. Panel a and b show the early arrivals and a part of the coda of the two waveforms, respectively.

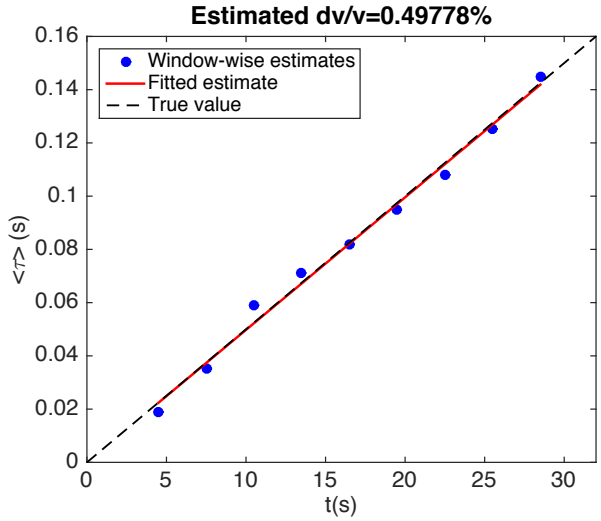

Figure 6-11: The mean of the travel time changes of each time window. Dots show the estimates from each time window, the solid line shows the least squares fit to those dots, and the dashed line indicates the case where the estimate equals the true travel time change.

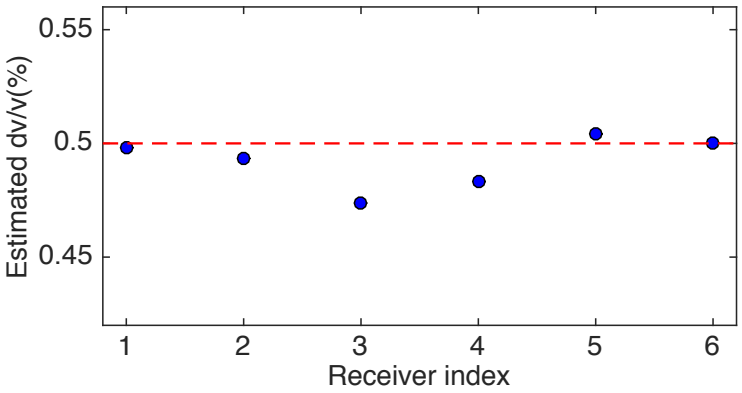

Figure 6-12: Estimated relative velocity change dv/v. Dots show the estimate of each receiver, with a mean of 0.4921%, and the dashed line shows the true velocity change.

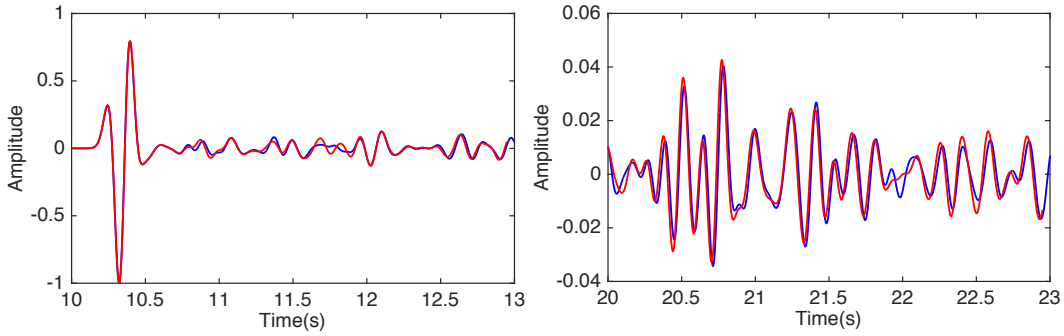

Figure 6-13: Comparison of the original (blue) and perturbed (red) waveforms recorded by receiver R1 after the effect of velocity change is removed from the perturbed waveform using the stretching technique. Panel a and b show the early arrivals and a part of the coda of the two waveforms, respectively.

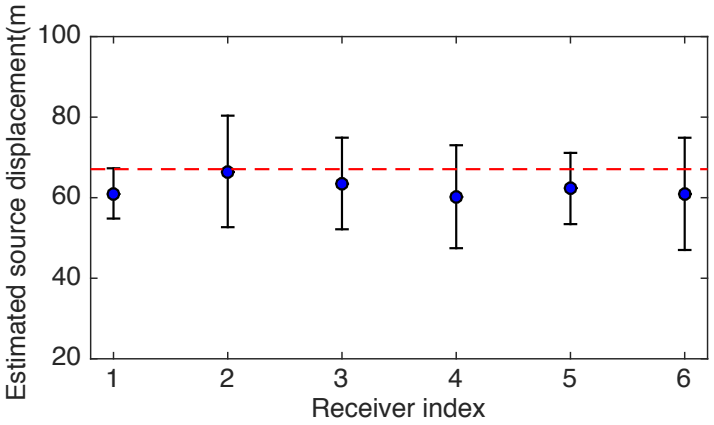

Figure 6-14: Estimated source displacement made using by each receiver individually. The dots and bars show the mean and standard deviation over all time windows used, and the dashed line shows the true source displacement.

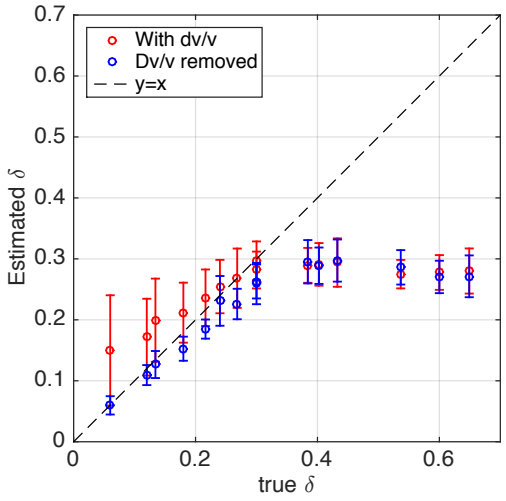

Figure 6-15: Comparison of the estimated source displacement obtained without compensating for the velocity change in the perturbed waveforms (red), and that obtained with effect of the velocity change removed from the perturbed waveform (blue). The circle and bars show the means and standard deviations over all time windows and receivers, and the dashed line shows where the estimated and true displacements are identical. All displacement values are normalized by the dominate wavelength of the waveforms.

6.4 Estimating source location displacement with scatterer displacement

We now consider cases where the perturbation in source location is accompanied by scatterer displacement. In order to obtain accurate estimates of source displacement, we attempt to use CWI to distinguish the scatterer displacement in the system and remove its effect. In a medium with point scatterers which are displaced independently, the mean-squared displacement δ^2 of the scatterers can be resolved by relating it to the variance ${\sigma_\tau}^2$ of the travel-time change of waves arriving within a time window. Due to the displacement of the scatterers, some scattering trajectories become longer and others shorter, while the average does not change provided the movement of the scatterers is uncorrelated. Hence, the mean of the travel-time change $\langle \tau_T \rangle$ vanishes. The variance of the travel-time change ${\sigma_\tau}^2$ is related to the variance of trajectory-length change ${\sigma_L}^2$. Snieder (2006) derived the relationship between ${\sigma_L}^2$ and the mean-squared displacement δ^2:

$$ {\sigma_L}^2 = \frac{2vt\delta^2}{l^*}, \tag{6.5} $$

where t is the center time of the time window employed, and l^* is the transport mean free path. The transport mean free path of a scattering medium is the mean distance of wave propagation over which the scattered wave has lost all information of direction of propagation. It is defined as $l^* = l/(1 - \overline{cos\theta})$, where $\overline{cos\theta}$ is the average of cosine of the scattering angle over all paths in a certain time window, and l is the scattering mean free path (van Rossum and Nieuwenhuizen, 1999). The scattering mean free path l of a scattering medium refers to the characteristic distance between scatterers, which has a different definition with the transport mean free path l^*.

For a constant velocity, $\sigma_\tau = \frac{\sigma_L}{v}$, the mean-squared displacement δ^2 is therefore related to the ${\sigma_\tau}^2$, i.e.

$$\sigma_\tau{}^2 = \frac{2t\delta^2}{vl^*}. \tag{6.6}$$

The variance of the travel-time changes $\sigma_\tau{}^2$ can be obtained from a series of non-overlapping time windows from correlation coefficient 2.4, and the root mean squared displacement δ of scatterers can then be obtained if the velocity v and the transport mean free path l^* are known.

The numerical models used in this section contain 300 point-scatterers with a background velocity of 3000m/s, as shown in Figure 6-1. Six identical isotropic sources and six receivers are applied. We first introduce an uncorrelated movement of the scatterers with a root mean square displacement $\delta_{scat} = 3\%\lambda_d$ (using the moving method described in Section 6.2). From now on, in this section, root mean square displacement of scatterers is denoted as δ_{scat}, and source displacement as δ_{source}. Thus, the expression of the variance of travel-time changes due to scatterer displacement is written as (Snieder, 2006)

$$\sigma_\tau{}^2 = \frac{2\delta_{scat}{}^2}{vl^*}t, \tag{6.7}$$

and that due to source displacement (for an isotropic source in a 2D acoustic medium) is (Snieder and Vrijlandt, 2005)

$$\sigma_\tau{}^2 = \frac{\delta_{source}{}^2}{2v^2}. \tag{6.8}$$

As is readily observed from the two equations above, the variance of the travel-time changes $\sigma_\tau{}^2$ is proportional to time t (central time of the time window applied) for scatterer displacement, while it is invariant with time for a source displacement. As source displacement and scatterer displacement control $\sigma_\tau{}^2$ independently, their joint influence on $\sigma_\tau{}^2$ should be represented by a simple summation of the two:

$$\sigma_\tau{}^2 = \frac{2\delta_{scat}{}^2}{vl^*}t + \frac{\delta_{source}{}^2}{2v^2} \tag{6.9}$$

Thus, theoretically, the features of how $\sigma_\tau{}^2$ changes with t can be used to

discriminate among three scenarios: source location being perturbed, scatterers being displaced, and both source and scatterers being displaced.

We take source e1 and e2 (30m, i.e. $6\%\lambda_d$ apart) for example. Figure 6-16a shows the ${\sigma_\tau}^2$- t relation of waveforms of source e1 in the original medium and in the perturbed the medium (with $\delta_{scat} = 3\%\lambda_d$) recorded by the same receiver R3, where each point indicates a time window used. We fit a straight line using ${\sigma_\tau}^2$ estimated for each time window in a least-squares sense, which shows that the travel-time variance ${\sigma_\tau}^2$ does change proportionally with time t, taking a form of $y = Ax$, where A is a constant. Figure 6-16b shows ${\sigma_\tau}^2$ from each time window estimated with waveforms of source e1 and e2 in the original medium (without scatterer displacement) recorded by receiver R3. The travel-time changes are due to the difference in source location (source displacement), and their variance ${\sigma_\tau}^2$ estimated from each time window fluctuation about their average (red line), and are invariant with time t, taking a form of $y = B$, where B is a constant. Figure 6-16c shows the case where both source location and scatterer positions are perturbed, i.e. waveform of source e1 in the original medium and that of e2 in the perturbed medium are used. The ${\sigma_\tau}^2$-t relation is described by equation 6.9, which takes a form of $y = A'x + B'$. We found that the slope of the fitted straight line (black solid line) is 3.91e-6, which is close to the slope of the line in Figure 6-16a which is 3.56e-6; also the y-intercept (black dashed line) is 4.83e-5, which is close to that in Figure 6-16b which is 4.79e-5: that is, $A \approx A'$ and $B \approx B'$. This verifies equation 6.9 that scatterer displacement δ_{scat} and source displacement δ_{source} influence ${\sigma_\tau}^2$ in an independent sense when they occur simultaneously in the system. Thus source displacement can be extracted from

$$\frac{{\delta_{source}}^2}{2v^2} = B', \tag{6.10}$$

given the propagating velocity v.

The black dashed line in Figure 6-16c marks the level of the y-intercept of the fitted $\sigma_\tau{}^2$-t relation, which is used to estimate source displacement for the scenario with perturbations in both source location and scatterer positions; while the red line represents the $\sigma_\tau{}^2$-t relation of a reference scenario with source displacement being the only perturbation in the system. The similarity in the level of the two lines means that the source displacements calculated for the two scenarios will be very similar, which demonstrates that the level of accuracy of source displacement estimates achieved in a system accommodating two types of perturbations is similar to that for a system in which only source location is perturbed.

Figure 6-17 shows the $\sigma_\tau{}^2$-t relation fitting for six pairs of waveforms recorded by receiver R3, one of which is from a source in the original medium and the other is from another source in the medium within which scatterers are displaced by $3\%\lambda_d$. The true source displacements of the six pairs are 30m, 60m, 67m, 90m, 108m, and 120m, i.e. 6%, 12%, 13.4%, 18%, 21.6% and 24% of λ_d. The value used for estimating source displacement is marked by a black dashed line in each panel, and that for each reference case (with no scatterer displacement) is marked by a red line. For most cases, the two lines are located closely, indicating similar estimates for source displacements with no scatterer displacement occurring, and for the case where scatterer displacement occurs but its effect is removed. As a result, the estimated source displacements δ_{source} are 28.2m, 53.6m, 54.6m, 81.7m, 90m and 98.9m, with the largest error being 18% of the true source displacement.

We repeat the experiment by increasing the scatterer displacement to $6\%\lambda_d$, and fitted the $\sigma_\tau{}^2$-t relation of the six cases are shown in Figure 6-18. The estimated source displacements are 35.9m, 48.9m, 56.3m, 93.6m, 90.8m and 93.0m. It appears that the estimation of some source displacements have improved (cases 3, 4 and 5)

and some have deteriorated (cases 1, 2 and 6) due to larger scatterer displacements.

The slope and y-intercept of the fitted line reflect the value of $\frac{2{\delta_{scat}}^2}{vl^*}$ and $\frac{{\delta_{source}}^2}{2v^2}$ respectively, and we are able to use equation 6.10 to compute the source displacement δ_{source}. It appears that the root mean square displacement of scatterers δ_{scat} is also readily obtained from $\frac{2{\delta_{scat}}^2}{vl^*} = A'$, given velocity v and transport mean free path l^*. However, the value of A' (the slope of the fitted of ${\sigma_\tau}^2$-t relation) is unstable with different source displacements, as shown in Figure 6-17 and Figure 6-18. Therefore, it would be extremely difficult to obtain reliable estimates of the root mean square displacement of the scatterers δ_{scat} this way.

Figure 6-19 shows the estimates of source displacements over a wider range of true source displacements with scatterers displaced by $3\%\lambda_d$ and $6\%\lambda_d$ in panels (a) and (b), respectively. Each value in the plots shows the mean and the standard deviation of the estimates over all receivers. The estimates of source displacement for each reference case (no scatterer displacement) using standard CWI are shown in black. Blue shows the estimates obtained using the method described in this section, which discriminates the perturbations in source location and scatterer positions by fitting $y = A'x + B'$ to obtain the ${\sigma_\tau}^2$-t relation. Red shows the estimates using the standard CWI that does not separate the contributions of the two types of perturbation by assuming ${\sigma_\tau}^2$ being time-invariant and obeys $y = B$. It is found that within the applicable range of CWI (true source displacement δ_{source} below a quarter of dominant wavelength), for larger scatterer displacement (panel b), discriminating the contribution of the two types of perturbation improves the estimation of source displacement by significantly reducing overestimation. This is because both types of perturbation are recognized as source displacement by the standard CWI method, so the estimated source displacements are much larger than

their true values. For smaller scatterer displacements (panel a), using standard CWI appears to have improved the estimation in some cases. However, we do not recommend it because this 'improvement' is not real: since we know that CWI has a tendency to underestimate source displacements, counting the contribution of scatterer displacement as part of source displacement seems to compensate for this tendency in the result, however with erroneous (entirely unrelated) physics, and the size of the compensation is unclear.

In this section we proposed a treatment for estimating source displacement in cases where both source location and scatterer positions are perturbed. Standard CWI assumes a single type of perturbation occurring in the system and tends to over estimate source perturbation when scatterer displacement also occurs. Our treatment removes this assumption by discriminating the contribution of the two types of perturbations and thus improves the estimation of source displacement.

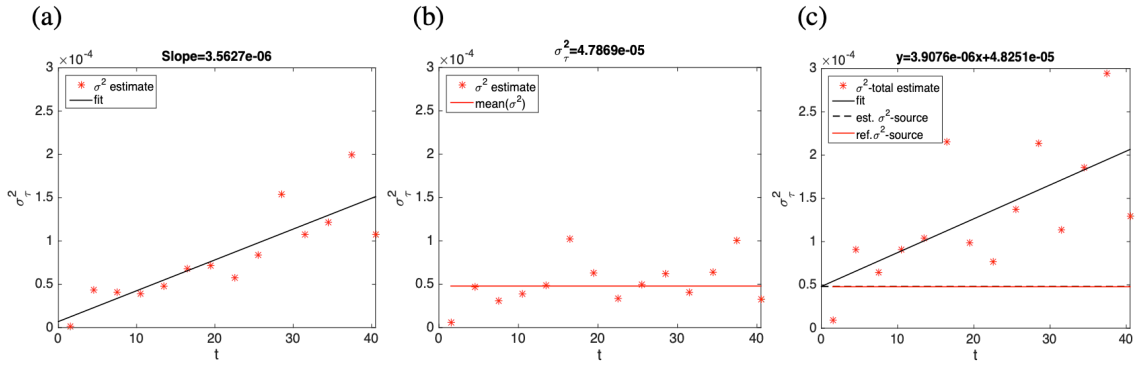

Figure 6-16: Plots of the $\sigma_\tau{}^2$-t relation of the original and perturbed waveforms, where stars show the variance of the travel-time changes $\sigma_\tau{}^2$ of each time window in the waveforms. Panel a shows the case for scatterer displacement being the only perturbation in the system, where the line shows the lease squares fit; panel b shows the case for source displacement being the only perturbation in the system where the line shows the level of the average over all time windows applied; and panel c shows the case where scatterer displacement and source displacement both exist, where the black solid line shows the lease squares fit, the dashed black line marks the level of the y-intercept of the fit, and the red line shows the mean of the reference case without scatterer displacement shown in panel b.

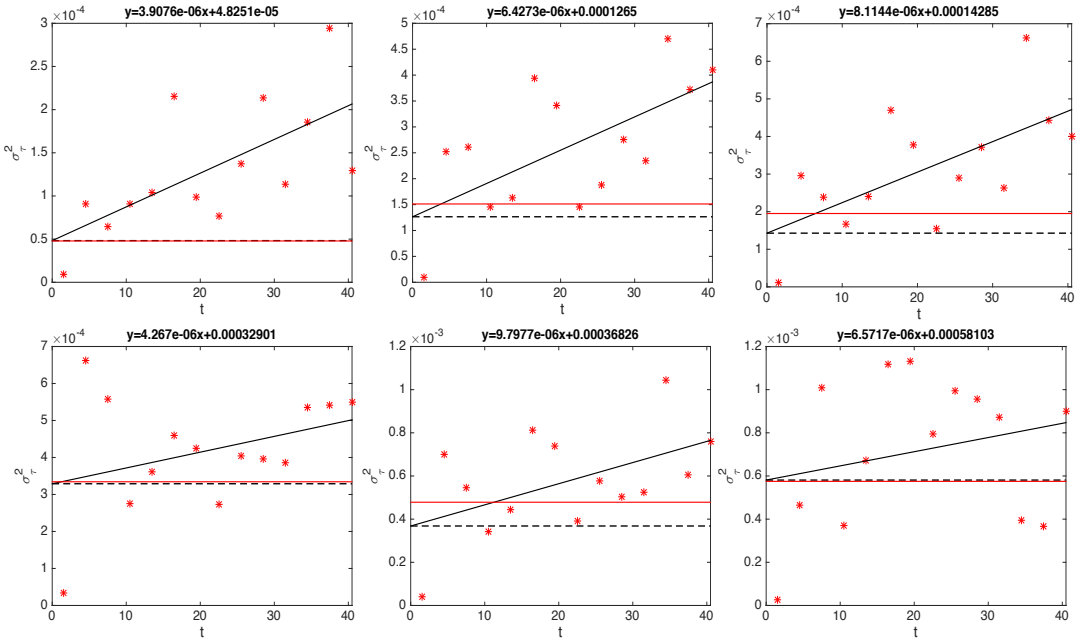

Figure 6-17: Plots of the $\sigma_\tau{}^2$-t relation and least squares fits for cases with a scatterer displacement of $3\%\lambda_d$. Panel a-f shows the case where the true source displacements are 30m, 60m, 67m, 90m, 108m and 120m.

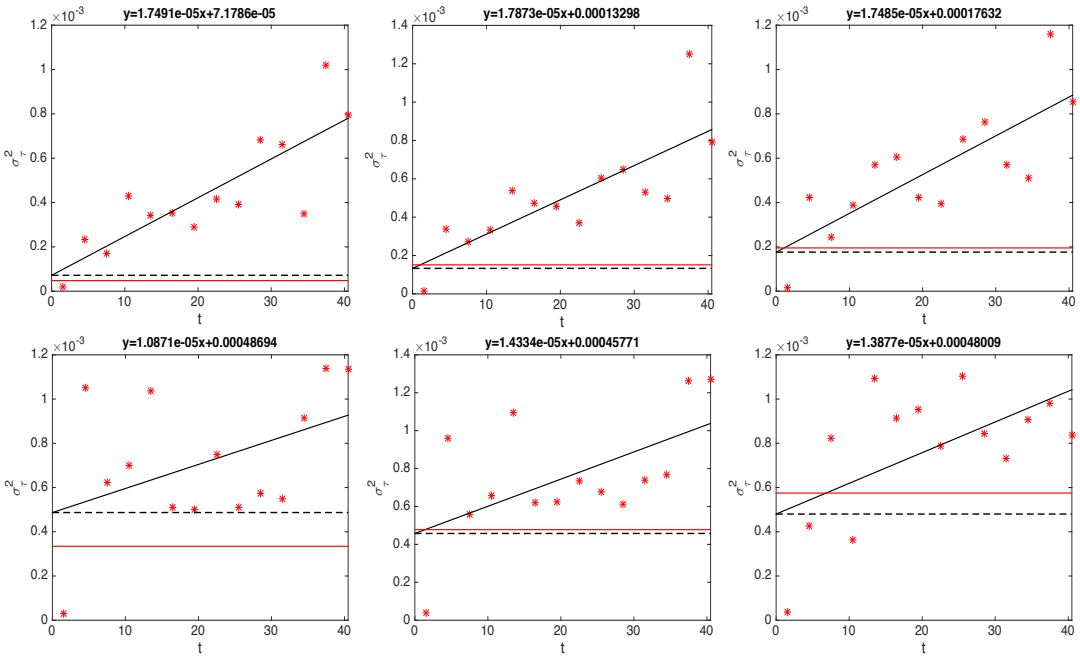

Figure 6-18: Plots of the $\sigma_\tau{}^2$-t relation and least squares fits for cases with a scatterer displacement of $6\%\lambda_d$. Panel a-f shows the case where the true source displacements are 30m, 60m, 67m, 90m, 108m and 120m.

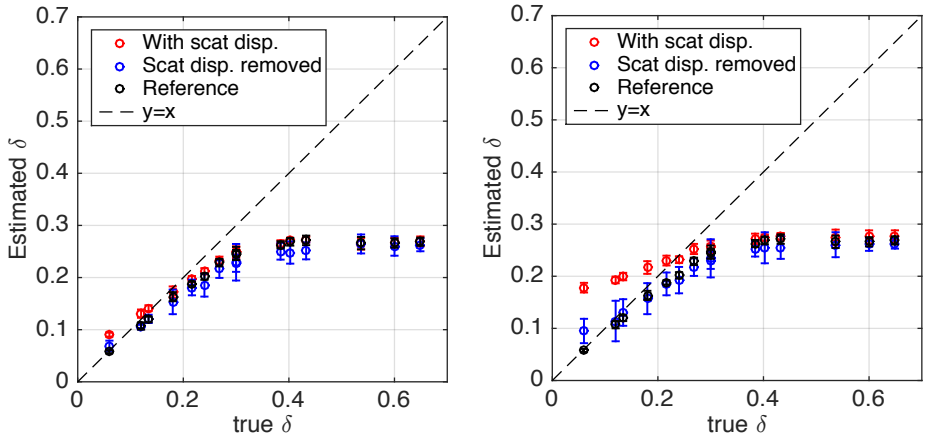

Figure 6-19: Comparison of the estimated source displacement obtained using the standard CWI method (red), CWI after scatterer displacement is removed (blue), and reference cases in which source displacement is the only type of perturbation (black). All displacement values are normalized by the dominant wavelength of the waveforms. Panels a and b show the case for $\delta_{scat} = 3\%\lambda_d$ and $\delta_{scat} = 6\%\lambda_d$, respectively.

6.5 A general treatment for small perturbations with CWI

In both seismic and laboratory rock physics settings, sometimes more than one type of change occur simultaneously. Most existing methods that measure these changes contain underlying assumption that the change being measured is the only type of change that occurred. Standard CWI, which can be used to estimate bulk velocity change, scatterer displacement or source location displacement, is one such method. In former sections we discussed how CWI can be used to discriminate different perturbations in the system where there are two types of perturbations whose existence is known. In this section, we propose a general treatment to detect and estimate small perturbations using CWI when the types of perturbations which have occurred are not known.

Assuming all perturbations are small and non-destructive, we use two simple plots to detect and measure, which are computed from a pair of waveforms recorded by the same receiver before and after the perturbations. The numerical models shown in Figure 6-1 are used to demonstrate the treatment. The original medium contains 300 point scatterers and has a velocity of $v_0 = 3000m/s$. The scatterers are perturbed with a root mean square of $\delta_{scat} = 3\%\lambda_d$, and the velocity is changed to $v = 3015m/s$ (true $dv/v = 0.5\%$). A displacement in source location is also modeled by using multiple identical sources at different locations. The two plots we use to detect perturbation types are plots of the $<\tau>$-t relation and ${\sigma_\tau}^2$-t relation, where $<\tau>$ and ${\sigma_\tau}^2$ are the mean and variance of the travel-time difference of waves arriving in the time windows applied.

Here we show how the two plots are used with an example in which all three types of perturbations occur. Figure 6-20a shows the plot showing the $<\tau>$-t relation, computed with the unperturbed waveform of source e1 (source location at e1, $v_0 = 3000m/s$, scatterers at their original positions) and the perturbed waveform of e1 (source displaced to the location of e2, $v = 3015m/s$, scatterers perturbed with $\delta_{scat} = 3\%\lambda_d$) recorded by receiver R1. The plot (Figure 6-20a) shows that $<\tau>$ increases proportionally with t. This feature can only be explained as a change in bulk velocity, as $<\tau>$ would be approximately zero for all time windows for uncorrelated scatterer displacement or source displacement in a scattering medium (Snieder 2006), as shown in Figure 6-20b for comparison, which is computed with the waveform of source e1 in the original medium and that of e2 in a perturbed medium with a source displacement of $\delta_{scat} = 3\%\lambda_d$ and no velocity change. Thus, the velocity change is readily deduced from the slope of the fitted straight line in the $<\tau>$-t plot (Figure 6-21). In this example, the velocity change is estimated to be $dv/v = 0.51\%$.

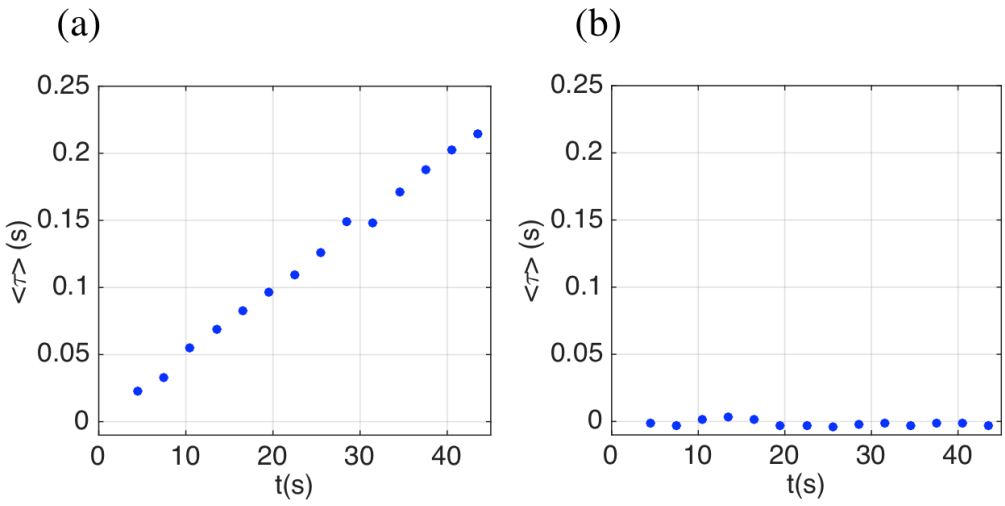

Figure 6-20: Plot of $<\tau>$-t relation. Panel a shows the $<\tau>$-t relation when all three types of perturbation occur, obtained using the original waveform (source location at e1, $v_0 = 3000m/s$) and the perturbed waveform (source location at e2, $dv/v = 0.5\%$, scatter displacement $\delta_{scat} = 3\%\lambda_d$) recorded by receiver R1. Panel b shows the counterpart of Panel (a) with no velocity change in the perturbed waveform.

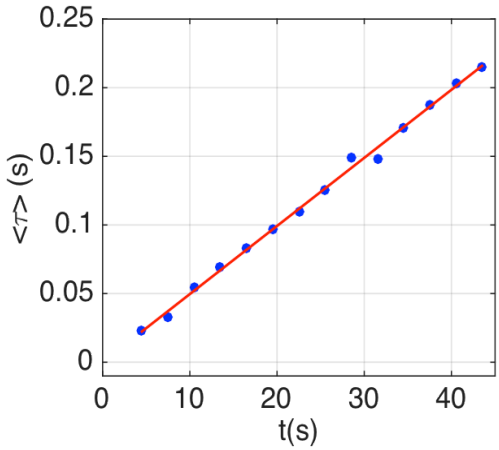

Figure 6-21: Least squares fit of the $<\tau>$-t relation.

The velocity change found is then removed using the stretching interpolation technique as in Section 6.2. Figure 6-22 shows a comparison of the unperturbed and perturbed waveforms before and after the velocity change is removed. To determine the existence of perturbations in source location and scatterer positions, we plot the $\sigma_\tau{}^2$-t relation computed with the unperturbed waveform of e1 and the perturbed waveform of e2 with dv/v removed (Figure 6-23). The window-wise travel-time variance $\sigma_\tau{}^2$ seems to increase with time t, indicating a scatterer displacement, however it is unclear whether the source location has also been perturbed. We fit a straight line and found the y-intercept is non-zero, indicating that a source displacement has also occurred. Using the value of the y-intercept, the source displacement can be calculated from equation 6.10. In this example, the source displacement is estimated to be $\delta_{source} = 28.16m$, giving an error of 1.84m compared to the true value of $30m$.

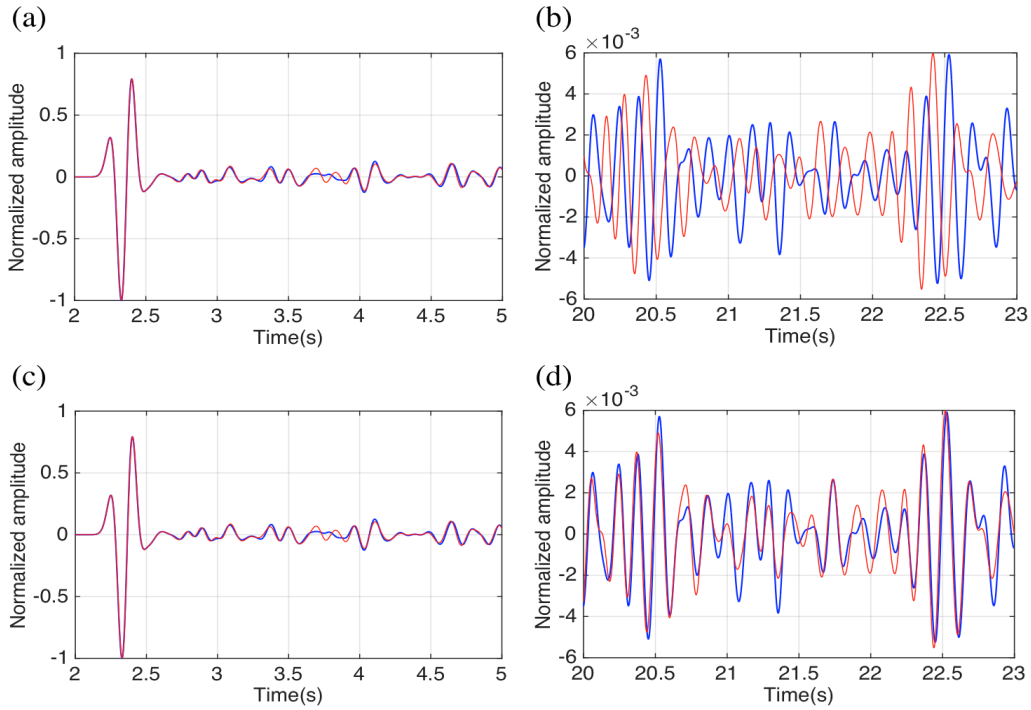

Figure 6-22: Comparison of waveforms before and after removing the measured effect of velocity change. Panel a and b show the early arrivals and a part from coda, respectively of the original (blue) and perturbed (red) waveforms; Panel c and d show the early arrivals and a part from coda of the original (blue) and perturbed (red) waveforms with the velocity change removed.

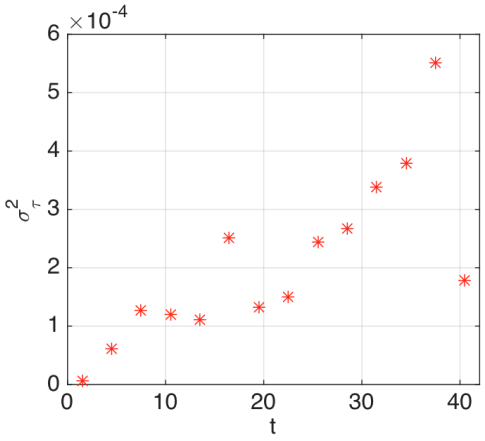

Figure 6-23: Plot of the $\sigma_\tau{}^2$-t relation after the effect of the velocity change is removed from the perturbed waveform.

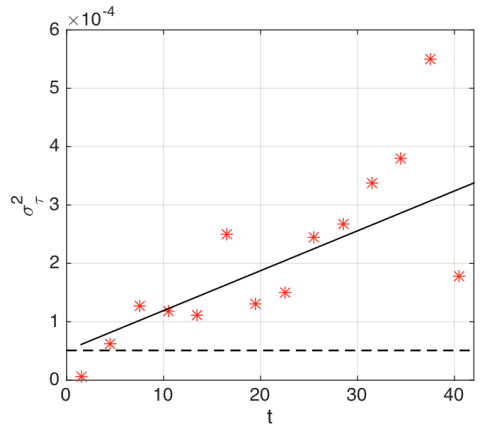

Figure 6-24: Least squares fit of the $\sigma_\tau{}^2$-t relation in Figure 6-23 (solid line), where the dashed line marks the level of y-intercept.

We repeat the experiment with true source displacements of 60m, 67m, 90m, 108m and 120m, i.e. 12%, 13.4%, 18%, 21.6% and 24% of the dominant wavelength λ_d. Figure 6-25 shows the two plots used to detect and measure velocity change and source displacement in each case, and that of the example shown above is also included. The estimated dv/v and δ_{source} are listed in Table 6-1. For all cases, we obtain a relative velocity change estimate dv/v with an error smaller than 0.01%.

6 Discriminating different types of perturbations using CWI

As we separate the contribution of scatterer displacement and source displacement, the estimated source displacement shows an increasing tendency of underestimation as the true source displacement increases, without the artificial compensation from the scatterer displacement discussed above.

We thus propose a general treatment for small non-destructive perturbations occurring in a multiply scattering medium using CWI methods. Instead of assuming a single type of change, we first detect the types of changes that have occurred and then measure the perturbations separately.

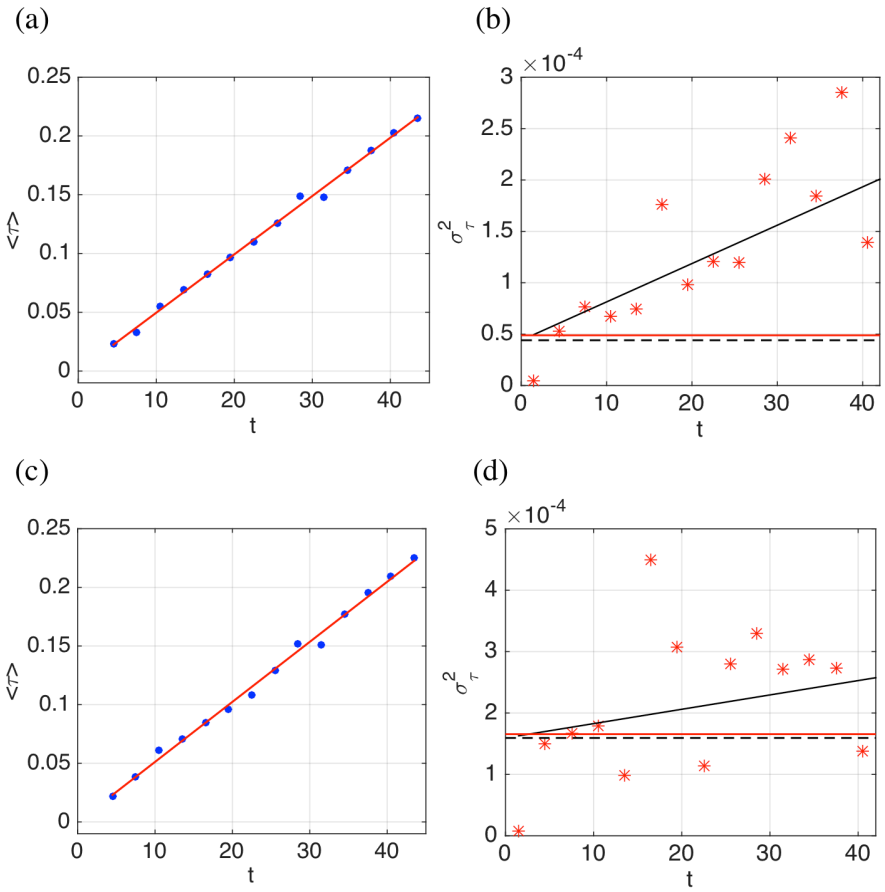

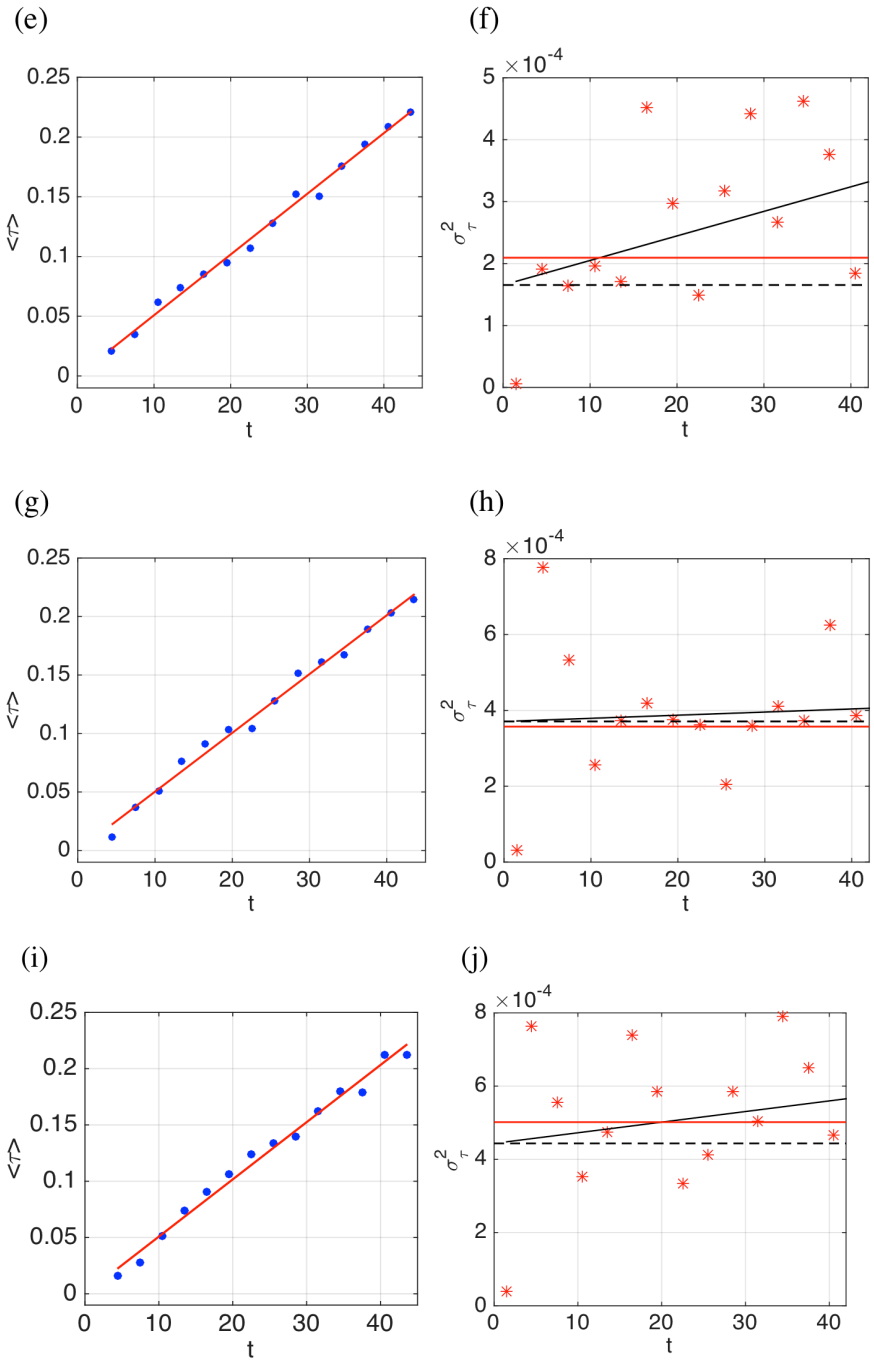
(e)
(f)
(g)
(h)
(i)
(j)
<τ>
σ^2_τ
×10^-4
t

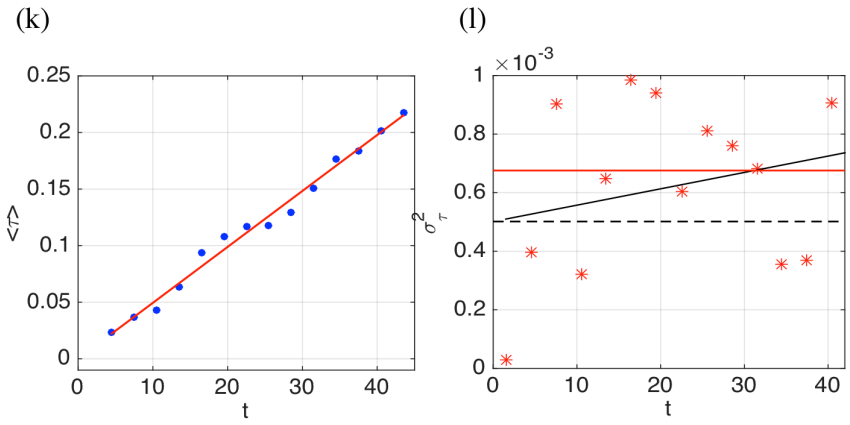

Figure 25: Plots of the $<\tau>$-t (left column) and $\sigma_\tau{}^2$-t (right column) relation and the least-square fits. Panel pairs a-b, c-d, e-f, f-g, i-j and k-l show plots for cases with true source displacement of 30m, 60m, 67m, 90m, 108m and 120m. In the left panels, dots show the mean of the travel-time changes $<\tau>$ of each time window, and the line shows the least squares fit. In the right panels, stars show the variance of the travel-time changes $\sigma_\tau{}^2$ of each time window, the solid line (black) shows the least-square fit, and dashed line marks the level of the y-intercept of the fit.

Index	True δsource	Estimated δsource	Estimated dv/v
1	30m	28.16m	0.4963%
2	60m	53.56m	0.5119%
3	67m	54.57m	0.5083%
4	90m	81.71m	0.5027%
5	108m	89.35m	0.5082%
6	120m	95.01m	0.4903%

Table 6-1: Estimated relative velocity change dv/v and source displacement δ_{source} for each true source displacement where the true dv/v is 0.5% and with a scatterer displacement of $\delta_{scat} = 3\%\lambda_d$.

6.6 Discussion

When using windowing CWI to measure changes in bulk velocity of a medium, according to Figure 6-4, although in general the standard deviation of estimates among different sources given by individual receivers (blue bars) is small, for some receivers (R2, R3, R4 and R5), the true value of dv/v (dashed line) does not lie within one standard deviation of the mean of estimates among the sources (although for most it lies within three standard deviations). Also, it is noticeable that the dv/v estimates fluctuate more across receivers than across sources. This could be attributed to the medium being imperfectly diffusive: the scattering properties in different areas therefore vary to some extent. As the receivers distribute much more dispersedly in the medium than the sources do, waveforms travelling between one source and multiple receivers have been affected by the difference in local scattering properties more than those travelling between multiple sources and one receiver.

To verify this hypothesis, we repeat the experiment using a medium with twice the number of scatterers, and show the estimates in Figure 6-26. A comparison of Figure 6-4 and Figure 6-26 shows that the overall standard deviation of dv/v estimates (shade) is reduced from 0.0068% to 0.0052%, and the overall average of dv/v estimates becomes more accurate, changed from 0.4981% to 0.5003%, with error reduced from 0.0019% to 0.0003% when a more diffusive medium is used. We find that both the accuracy and precision of the estimates from most individual receivers are also improved due to the more diffusive medium. This result also indicates that the ability of CWI to measure medium velocity change with few or even a single receiver is associated with the scattering properties of the medium.

The methods used in this chapter are based on standard CWI. Apart from maintaining a single type of perturbation at a time, all other assumptions made in the theory of CWI were adopted in our experiments. When measuring the velocity change, CWI assumes a constant relative velocity change dv/v. This does not require the absolute velocity change to be the same across the medium, rather its ratio to the original velocity is assumed to be uniform in all locations. This assumption is also made in the stretching technique to implement CWI. However it is not necessarily the case in reality. Pacheco and Snieder (2005; 2006) extend the theory to measure localized velocity changes using a mean of travel-time changes $< \tau >$ that depends on location.

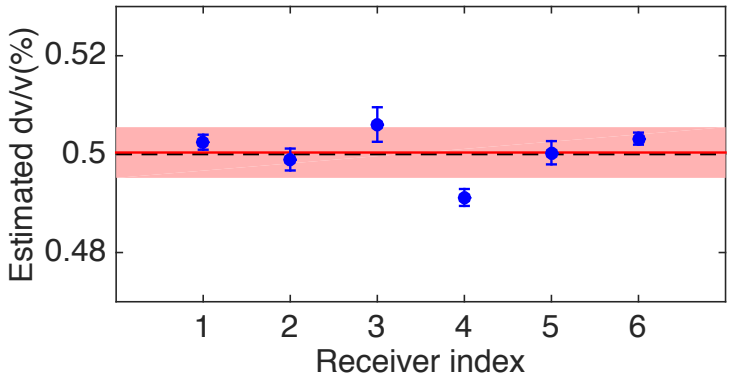

Figure 6-26: Estimated velocity change using windowing CWI in a medium with 600 point-scatterers. The dots and bars show the means and standard deviations of estimates over the six sources obtained from individual receivers; the solid line and the shade show the mean and standard deviations of the estimates over all receivers; and the dashed line shows the true velocity change.

6.7 Conclusion

In this chapter, we explore the potential of CWI to separate the effects of perturbations in bulk velocity, scatterer position, and source location in the system. The windowing and stretching interpolation techniques for implementing CWI to measure velocity change are compared, and it is found that the stretching technique outperforms the windowing technique when the velocity change is the only type of change occurring in the system. However, within the working range of windowing CWI ($dv/v < 2\%$), it gives much more accurate and precise estimates of dv/v than stretching when a small change in source location or in scatterer positions also exists.

Nevertheless, the idea of time-axis stretching in waveforms can be used to remove the effect of velocity change in the perturbed waveform, so that its differences from the unperturbed waveform is only due to other perturbations which can be measured using CWI or other suitable methods. We show in our experiments that removing the effect of dv/v can significantly improve the estimation of source displacement. We recommend this simple estimation-compensation treatment of dv/v to be applied as a pre-processing step for any methods using time-lapse signals.

In a strongly scattering medium where a perturbation in source location is accompanied with scatterer displacements, we separate the contribution of the two by fitting a line of the form $y = Ax + B$ for the $\sigma_\tau{}^2$- t relation, instead of $y = B'$. This implementation is shown to improve the estimation of source displacement, especially for larger scatterer displacements. Although perturbations in scatterer positions can also be recognized in most cases, the term used for determining their magnitude amount is unstable, and therefore estimating scatterer displacement in this

way is not recommended.

In more realistic scenarios where the types of perturbations are unclear, instead of assuming a single type as in standard CWI, we propose a general treatment to recognize different types of changes that have occurred. Two plots, of the σ_τ^2- t relation and the $<\tau>$-t relation, are used, and they are shown to be able to correctly detect and measure velocity change and source displacement within the applicable range of CWI methods.

7

DISCUSSION

The novel location method based on coda wave interferometry opens a new avenue for research and applications in areas without favorable recording conditions. CWI can only be used to estimate inter-source separations of events whose true separations are below about half of a dominant wavelength of seismic waves. Specifically, CWI can only produce accurate estimate of source separations for true source separations of up to a quarter of a dominant wavelength, and after that CWI tend to underestimate the separations. The reason for this is that CWI uses waveform correlation to extract differences in source locations, hence any differences that cause the traveltime difference of the same wave trajectory in the two waveforms to be larger than a quarter of a period of the waves could lead to cycle skipping in the correlation. This leads to an erroneously high R_{max}, hence a lower estimate of source separation than its true value. The chance of the occurrence of cycle skipping increases with larger true source separations, and when the true separation reaches about half of a dominant wavelength, the estimates deteriorates to a point where CWI is no longer applicable.

It has been shown that the CWI-based location algorithm can correct for the underestimation bias of the CWI method to some extent, however it is unable to determine the relative locations of events distributed in a cluster expanding over one wavelength in diameter. Indeed, the theory of CWI does not allow changes with a typical length over half of a dominant wavelength to be estimated, the applicable range of the CWI-based location method could be extended in a similar way Waldhauser and Ellsworth (2000) used to extend the working range of the double difference method by linking different event clusters using traveltimes from catalog data.

We have shown that the performance of CWI to estimate inter-source separations deteriorates in layered media. This is because in the current theory of CWI, scattering

occurs at point-scatterers that distribute uniformly in the medium, hence in each time window traveltime differences τ are averaged over all directions from which waves leaving the source. However, in a layered medium, weights should be applied when averaging over the take-off directions in each time window. A future work could be to extend the CWI theory to layered media by working out a way to determine these weights. A guideline on such a work is that for later windows the waves have bounced up and down in the near-vertical direction during propagation, while for earlier windows they have propagated more horizontally. Unlike in point-scatterer media where the orientation information of the two sources is lost when averaging over all take-off directions, the orientation of the two sources may be retrievable using those weights.

The methods proposed for separating the effects of different types of perturbations using CWI were validated with synthetic data. However, as it is the first known study of its kind, and estimating displacement in source location and estimating scatterer displacement using CWI on their own both lack abundance of research as more widely used methods do, the methods shown in this thesis are in need of more tests both numerically and in laboratory.

While in this thesis we have discussed and applied the methods for seismic applications, there are numerous other areas in which energy source location estimates are useful or necessary, such as in medical sciences and even military applications. The CWI method could potentially be applied to any of them, provided that the medium of wave propagation scatters the wavefield strongly in many directions. This is necessary in order to ensure that the recording of coda at each receiver contains energy that left each source at a wide range of angles. This range of angles is the equivalent of the standard requirement of a wide aperture between each source and the set of receivers for conventional location methods. However, the equivalence is not direct since all of the latter methods use deterministic physics to optimize locations by matching synthetic and real data, whereas CWI uses statistical

relations to estimate source separations. This difference means that CWI can also be used to provide an independent test of the efficiency of other source location methods, and also that CWI uses far more parts of recorded data.

8

CONCLUSION

8 Conclusion

Seismic coda, the later part of a seismogram, is disregarded in many seismological applications due to its complex appearance with few uniquely identifiable arrivals. However, consisting of multiply scattered waves, coda is extremely sensitive to small changes in the seismic system (medium velocity change, source location perturbation and scatterer displacement), hence can be used to measure perturbations occurring in the system that are too small to measure for conventional methods that use early arrivals of seismograms. In recent years, the methods of coda wave interferometry (CWI), that uses the sensitivity of coda to estimate minute differences between seismic states, has become appealing to geophysicists, and has been used in many applications through measuring the time-lapse changes in bulk velocity of the medium. In the first part of this thesis, I focused on a less studied type of CWI application: estimating change in source location. This is equivalent to estimating the separation between a pair of sources with similar mechanism. For a cluster of similar sources, pairwise separations can lead to their relative locations. The second part of this thesis focuses on an algorithm that uses the inter-source separation data to estimate relative source locations of a cluster of events. In the third part of this thesis, I returned to the basic CWI methods and discussed scenarios where multiple types of changes occur simultaneously in a system.

In Chapter 2, I briefly presented the theory of CWI and showed how it can be used to estimate inter-source separations. I then validated this type of CWI application using synthetic waveforms generated with Foldy code, an exact modeling code using point-scatterer media, as assumed in the derivation of the theory of CWI. It is observed that the source separation estimates of CWI tend to be lower than the true values due to cycle skipping, and estimates from individual receivers at different locations vary to some extent. The deficiency observed in these synthetic tests could be caused by underlying biases of the method.

To address this question, and also to explore this relatively new type of CWI application given various conditions, in Chapter 3 I tested the performance of CWI to estimate source separations in media with varying complexities and types in synthetic experiment. In point-scatterer medium with favorable parameters, CWI produces virtually exact estimate of the source separation between a pair of events with a true separation $\delta_{true} \leq 0.25\lambda_d$, after which it has an increasing trend of underestimation, and for $\delta_{true} \geq 0.4\lambda_d$ CWI only gives an estimate of the lower bound of the separation. Layer structure is found to disrupt the estimation to an extent depending on the event pair locations relative to the orientation of the layers, however the estimation is remarkably improved when a small number of point-scatterers is included. Tests in the Marmousi model reveals that in more complex media, CWI is able to produce reliable estimates even when the assumptions in the theory does not adequately describe the data. This study contributes to better understand and interpret the source separation estimates and therefore relative locations using CWI.

In Chapter 4, I validated the relative location algorithm with both synthetic and microearthquake data. I provided two improvements to this location method: to account for the impact of large difference in the dominant wavelength of recording made on different instruments, I introduced a new formulation for the optimization problem; to avoid the vagaries of trial-and-error method in parameter selection when applying CWI, I presented a systematic approach which helps standardize the method, and also allow CWI techniques to be automated. The microearthquake location results in our experiments are highly consistent when using different individual seismometer channels, showing that it is possible to locate event clusters with a single-channel seismometer. It is also shown in Chapter 5 that the location algorithm is able to correct bias (underestimation) in the CWI separation estimates to

some extent. This application presented is the second known application to real data, which have shorter distinguishable codas in recorded waveforms, and hence fewer recorded scattered waves than those that have been used to test this method previously. Thus, the potential applications of this non-demanding method are extended to seismic events over a wider range of magnitudes.

Given the advantages of this location method, it is likely that it has not been used more widely is in part because the algorithm requires unfamiliar methods to be used, and is therefore also partly due to the lack of a readily available, easily editable code with which practitioners can gain familiarity and confidence. To this end, in Chapter 5 I developed such a code called *CWIcluster* in MATLAB that implements the method, accompanied by replicable examples with both synthetic and real data, and a user manual. The code implements the location method in three steps: classifying events into clusters based on waveform similarity, computing inter-source separations using CWI, and estimating their relative locations. Each step can be implemented in an automated sense given criteria chosen by the user.

In Chapter 6, I returned to the three basic types of applications of CWI: estimating bulk velocity change, scatterer displacement, and source location perturbation. Standard CWI methods require an assumption that a single type of perturbation has taken place, so does most other methods that measure changes in a seismic system. However, in reality more than one type of perturbation can occur simultaneously. I studied a series of scenarios with numerical experiments where one type of change is accompanied by another, explored their applicable range, and how the effect of the undesired type of perturbation can be compensated. It is found that within its applicable range, the windowing technique for implementing CWI outperforms the stretching interpolation technique to measure velocity change with coexisting

perturbations on source location or scatterer positions in all cases. However, the latter technique is shown to be useful to compensate for the effect of velocity change (measured with CWI) when other types of perturbations are to be measured. I discovered that the effect of source location perturbation and scatterer displacement can be separated from the σ_τ^2 - t relation (relation between the variance of travel-time perturbation of scattered waves arriving within each time window and the central time of the window), from which source location perturbation can be obtained to an accuracy comparable to scenarios where it is the only type of perturbation in the system. Although scatterer displacement can also be recognized in most cases, their magnitude amount tend to be unstable, and therefore estimating scatterer displacement in this way is not recommended. With these observations, finally, I proposed a general treatment to account for multiple types of perturbations, allowing each type to be recognized, velocity change and source location perturbation to be measured with the effects of others being compensated.

In Chapter 7, I discussed issues lie in this work and future research potentials.

References

Ake, J., K. Mahrer, D. O'Connell, and L. Block, 2005, Deep-injection and closely monitered induced seismicity at Paradox Valley, Colorado: Bulletin of the Seismological Society of America, **95**, 664-683.

Aki, K., 1969, Analysis of seismic coda of local earthquakes as scattered waves: Journal of Geophysical Research, **74**, 615-631.

Aki, K., and B. Chouet, 1975, Origin of coda waves - source, attenuation, and scattering effects: Journal of Geophysical Research, **80**, 3322-3342.

Bai, L., I. Kawasaki, T. Zhang, and Y. Ishikawa, 2006, An improved double-difference earthquake location algorithm using *s P* phases: application to the foreshock and aftershock sequences of the 2004 earthquake offshore of the Kii peninsula, Japan (M_W=7.5): Earth, Planets and Space, **58**, 823-830.

Baisch, S., and G. H. R. Bokelmann, 2001, Seismic waveform attributes before and after the Loma Prieta earthquake: Scattering change near the earthquake and temporal recovery, Journal of Geophysical Research, **106**, 16323– 16337.

Baptie, B. J., 2010, Lava dome collapse detected using passive seismic interferometry: Geophysical Research Letter, **37**, L00E10.

Battaglia, J., J. Metaxian, and E. Garaebiti, 2012, Earthquake-volcano interaction imaged by coda wave interferometry: Geophysical Research Letters, **39**, L11309.

Bhattacharya, P. M., J. Pujol, R. K. Majumdar, and J. R. Kayal, 2005, Relocation of earthquakes in the Northeast Indian region using joint hypocentre determination method: Current Science, **89**, 1404-1413.

Blias, E., 2015, Non-first-break solutions for shallow velocity anomaly problem: CSPG/CSEG 2015 GeoConvention, Extended Abstracts, No. 41602.

Brenguier F., N. M. Shapiro, M. Campillo, V. Ferrazzini, Z. Duputel, O. Coutant, and A. Nercessian, 2008, Towards forecasting volcanic eruptions using seismic noise: Natrue Geoscience, **1**, 126–130.

References

Brenguier, F., M. Campillo, C. Hadziioannou, N. M. Shapiro, R. M. Nadeau, and E. Larose, 2008b, Postseismic Relaxation Along the San Andreas Fault at Parkfield from Continuous Seismological Observations: Science, **321**, 1478-1481.

Chen, K. H., R. Bürgmann, and R. M. M. Nadeau, 2013, Do earthquakes talk to each other: Triggering and interaction of repeating sequences at Parkfield: Journal of Geophysical Research - Solid Earth, **118**, 165-182.

Chouet, B., 1976, Source, Scattering and attenuation effects on high frequency seismic waves: Doctoral thesis, Massachusetts Institute of Technology.

Cleaty, J. R., and A. L. Hales, 1966, An analysis of the travel times of P waves to North American stations, in the distance range 32 ° to 100 °: Bulletin of the Seismological Society of America, **56**, 467-489.

Cowan, M. L., I. P. Jones, J. H. Page, and D. A. Weitz, 2002, Diffusing acoustic wave spectroscopy: Physical Review E, **65**, 066605.

Cowan, M. L., J. H. Page, and D. A. Weitz, 2000, Velocity Fluctuations in Fluidized Suspensions Probed by Ultrasonic Correlation Spectroscopy: Physical Review Letters, **85**, 453-456.

Daan, F., and S. Berend, 2002, Understanding molecular simulation: from algorithms to applications (2nd edition): Academic Press.

de Angelis, S., 2009, Seismic source displacement by coda wave interferometry at Soufrière Hills Volcano, Montserrat, WI: Natural Hazards and Earth System Science, **9**, 1341-1347.

Deichmann, N., and M. Garcia-Fernandez, 1992, Rupture geometry from high-precision relative hypocenter locations of microearthquake clusters: Geophysical Journal International, **110**, 501-517.

Deichmann, N., and D. Giardini, 2009, Earthquakes induced by the stimulation of an enhanced geothermal system below Basel (Switzerland): Seismology Research Letters, **80**, 784-798.

Dodge, D. A., G. C. Beroza, and W. L. Ellsworth, 1995, Foreshock sequence of the 1992 landers, California, earthquake and its implications for earthquake nucleation: Journal of Geophysical Research - Solid Earth, **100**, 9865-9880.

Douglas, A., 1967, Joint epicenter determination: Nature, **215**, 47-48.

Dosso, S. E., and M. J. Wilmut, 2009, Bayesian ocean acoustic source track with environmental uncertainty: Journal of the Canadian Acoustical Association, **37**, No 3.

Dosso, S. E., and M. J. Wilmut, 2011, Bayesian localization of multiple ocean acoustic sources with environmental uncertainties: Journal of the Canadian Acoustical Association, **39**, No 3.

Dziewonski, A. M., A. L. Hales, and E. R. Lapwood, 1975, Parametrically simple earth models consistent with geophysical data, Physics of the Earth and Planetary Interiors, **10**, 12-48.

Ellsworth, W. L., 2013, Injection-induced earthquakes: Science, **341**, 1225942(1-7).

Foldy, L. L., 1945, The multiple scattering of waves. 1. General theory of isotropic scattering by randomly distributed scatterers: Physical Review, **67**, 107-119.

Frankel, A., and R. W. Clayton, 1986, Finite-difference simulations of seismic scattering: implications for the propagation of short-period seismic-waves in the crust and models of crustal heterogeneity: Journal of Geophysical Research, **91**, 6465-6489.

Frankel, A. D., C. S. Mueller, T. P. Barnhard, E. V. Leyendecker, R. L. Wesson, S. C. Harmsen, F. W. Klein, D. M. Perkins, N. C. Dickman, S. L. Hanson and M. G. Hopper, 2000, USGS National seismic hazard maps: Earthquake Spectra, Professional Journal of the Earthquake Engineering Research Institute, **16**, 1–19.

Fremont, M., and S. D. Malone, 1987, High precision Relative locations of earthquakes at Mount St. Helens, Washington: Journal of Geophysical Research, **92,** 10223–10236.

Frohlich, C, and M. Brunt, 2013, Two-year survey of earthquakes and injection/production wells in the Eagle Ford Shale, Texas, prior to the Mw 4.8 420 October 2011 earthquake: Earth and Planetary Science Letters, **379,** 56-63.

Galetti, E., D. Halliday, and A. Cutis, 2013, A simple and exact acoustic wavefield modeling code for data processing, imaging, and interferometry applications: Geophysics, **78**, F17-F27.

Ge, M. C., 2005, Efficient mine microseismic monitoring: International Journal of Coal Geology, **64**, 44-56.

Geller, R. J., and C. S. Mueller, 1980, Four similar earthquakes in central California,

Geophysical Research Letters, **7,** 821–824.

Gerstenberger, M.C., S. Wiemer, L. M. Jones, and P. Reasenberg, 2005, Real-time forecasts of tomorrow's earthquakes in California: Nature, **435**, 328-331.

Gnyp, A., 2013, Recovering relative locations of the 2005-2006 Mukacheve Earthquakes from similarity of their waveforms at a single station: Acta Geophysica, **61**, 1074-1087.

Got, J. L., J. Frechet, and F. W. Klein, 1994, Deep fault plane geometry inferred from multiplet relative relocation beneath the south flank of Kilauea: Journal of Geophysical Research - Solid Earth, **99**, 15375-15386.

Grêt, A., R. Snieder, R. Aster, and P. Kyle, 2005, Monitoring rapid temporal change in a volcano with coda wave interferometry: Geophysical Research Letters, **32**, L06304.

Grêt, A., R. Snieder, and J. Scales, 2006, Time-lapse monitoring of rock properties with coda wave interferometry, Journal of Geophysical Research, **111**, B03305.

Hadziioannou, C., E. Larose, O. Coutant, P. Roux, and M. Campillo, 2009, Stability of monitoring weak changes in multiply scattering media with ambient noise correction: laboratory experiments: The Journal of the Acoustical Society of America, **125**, 3688-3695.

Groenenboom, J., and R. Snieder, 1995, Attenuation, dispersion, and anisotropy by multiple scattering of transmitted waves through distribution of scatterers: Journal of the Acoustical Society of America, **98**, 3482-3492.

Harris, D., 1987, A master event strategy for location with seismic array data: IEEE International Conference on Acoustics, Speech, and Signal Processing, ICASSP'87, Extended Abstracts, 2217-2220.

Helffrich, G., J. Wookey, and I. Bastow, 2013, The seismic analysis code: a primer and user's guide: Cambridge University Press.

Hotovec-Ellis, A. J., J. Gomberg, J. E. Vidale, and K. C. Creager, 2014, A continuous record of interruption velocity change at Mount St. Helens from coda wave interferometry, Journal of Geophysical Research - Solid Earth, **119**, 2199–2214.

Irons, T., 2005, Marmousi2 Model, http://www.reproducibility.org/RSF/book/data/marmousi2/paper.pdf, accessed 15 May 2017.

Ito, A., 1985, High resolution relative hypocenters of similar earthquakes by cross-spectral analysis method: Journal of Physics of the Earth, **33**, 279–294.

Jones, I. F., 2010, Tutorial: velocity estimation via ray-based tomography: First Break, **28**, 45-52.

Kawaguchi, E., and N. Fukuda, 2017, "Listening" drone helps find victims needing rescue in disasters, https://www.titech.ac.jp/english/news/2017/040159.html, accessed 15 January 2018.

Kelner, S., M. Bouchon, and O. Coutant, 1999, Numerical simulation of the propagation of P waves in fractured media: Geophysical Journal International, **137**, 197-206.

Kumar, A., E. Zorn, R. Hammack, and W. Harbert, 2017, Seismic Monitoring of Hydraulic Fracturing Activity at the Marcellus Shale Energy and Environment Laboratory (MSEEL) Site, West Virginia: unconventional Resources Technology Conference, DOI: 10.15530/urtec-2017-2670481.

Larose, E., J. de Rosny, L. Margerin, D. Anache, P. Gouedard, M. Campillo, and B. van Tiggelen, 2006, Observation of multiple scattering of kHz vibrations in a concrete structure and application to monitoring weak changes: Physical Review E, **73**, 016609.

Larose, E., and S. Hall, 2009, Monitoring stress related velocity variation in concrete with a 2.10–5 relative resolution using diffuse ultrasound: Journal of the Acoustical Society of America, **125**, 1853-1856.

Lombaert, G., S. Pouillon, D. Clouteau, 2007, A probabilistic evaluation of the multiple wave scattering in the seismic response of a city: 7eme Colloque National AFPS 2007 – Ecole Centrale Paris.

Mae, N., Y. Mitsui, S. Makino, D. Kitamura, N. Ono, T. Yamada, H. Saruwatari, 2017, Sound source localization using binaural difference for hose-shaped rescue robot: 2017 Asia-Pacific signal and information processing association annual summit and conference, Conference Paper, 1621-1627.

References

Marzocchi, W., and A. M. Marzocchi, 2008, A double branching model for earthquake occurrence: Journal of Geophysical Research, **113**, B08317.

Masera, D., P. Bocca, and A. Grazzini, 2011, Coda wave interferometry method applied in structural monitoring to assess damage evolution in masonry and concrete structures: Journal of Physics Conference Series, **305**, 012108.

Molyneux, J. B., and D. R. Schmitt, 1999, First-break timing: Arrival onset times by direct correlation: Geophysics, **64**, 1492-1501.

Mordret, A., A. D. Jolly, Z. Duputel, N. Fournier, 2010, Monitoring of phreatic eruptions using interferometry on retrieved cross-correlation function from ambient seismic noise: results from Mt. Ruapehu, New Zealand: Journal of Volcanology and Geothermal Research, **191**, 46–59.

Nagaoka, Y., K. Nishida, Y. Aoki, and M. Takeo, 2010, Temporal change of phase velocity beneath Mt. Asama, Japan, inferred from coda wave interferometry: Geophysical Research Letters, **37**, L22311.

Navon, I. M., and D. M. Legler, 1987, Conjugate-Gradient methods for Large-scale minimization in meteorology: Monthly Weather Reviews, **115**, 1479-1502.

Ottemoller, L., P. Voss, and J. Havskov, Seisan: Earthquake Analysis Software for Windows, Solaris and Macosx, 2017, http://seisan.info, accessed 20 December 2017.

Pacheco, C., and R. Snieder, 2005, Time-lapse travel time change of multiple scattered acoustic waves, Acoustical Society of America, **118 (3)**, 1300-1310.

Pacheco, C., and R. Snieder, 2006, Time-lapse traveltime change of singly scattered acoustic waves, Geophysical Journal International, **165**, 485-500.

Page, J. H., M. L. Cowan, and D. A. Weitz, 2000, Diffusing acoustic wave spectroscopy of fluidized suspensions: Physica B: Condensed Matter, **279**, 130-133.

Pavlis, G. L., 1992, Appraising relative earthquake location errors: Bulletin of the Seismological Society of America, **82**, 836-859.

Peng, Z., 2013, Introduction to seismic analysis code (SAC), http://geophysics.eas.gatech.edu/classes/SAC/, accessed 20 March 2017.

Peng, Z., and Y. Ben-Zion, 2006, Temporal changes of shallow seismic velocity around the Karadere-Duzce branch of the North Anatolian Fault and strong ground motion: Pure Applied Geophysics, **163**, 567–600.

Planes, T., and E. Larose, 2013, A review of ultrasonic coda wave interferometry in concrete: Cement and Concrete Research, **53**, 248-255.

Poupinet, G., W. L. Ellsworth, and J. Frechet, 1984, Monitoring velocity variations in the crust using earthquake doublets: An application to the Calaveras Fault, California: Journal of Geophysical Research, **89**, 5719–5731.

Press, W. H., B. P. Flannery, S. A. Teukolsky, and W. T. Vetterling, 1987, Numerical Recipes: The Art of Scientific Computing: Cambridge University Press.

Ratdomopurbo, A., and Poupinet, G., 1995, Monitoring a temporal change of seismic velocity in a volcano - application to the 1992 eruption of Mt-Merapi (Indonesia): Geophysical Research Letters, **22**, 775-778.

Roberts, P. M., W. S. Phillips, and M. C. Fehler, 1992, Development of the active doublet method for measuring small velocity and attenuation changes in solids: Journal of the Acoustical Society of America, **91**, 3291-3302.

Robinson, R., 1987, Temporal variations in coda duration of local earthquakes in the Wellington region, New Zealand, Pure and Applied Geophysics, **125**, 579–596.

Robinson, D. J., M. Sambridge, and R. Snieder, 2007a, Constraints on coda wave interferometry estimates of source separations: the acoustic case: Exploration Geophysics, **38**, 189-199.

Robinson, D. J., R. Snieder, and M. Sambridge, 2007b, Using coda wave interferometry for estimating the variation in source mechanism between double couple events: Journal of Geophysical Research - Solid Earth, **112**, B12302.

Robinson, D. J., M. Sambridge, and R. Snieder, 2011, A probabilistic approach for estimating the separation between a pair of earthquakes directly from their coda waves: Journal of Geophysical Research, **116**,1-14.

Robinson, D. J., M. Sambridge, R. Snieder, and J. Hauser, 2013, Relocating a Cluster of Earthquakes Using a Single Seismic Station: Bulletin of the Seismological Society of America, **103**, 3057-3072.

Sato, H. (1986), Temporal change in attenuation intensity before and after the eastern Yamanashi earthquake of 1983 in central Japan, Journal of Geophysical Research, **91**, 2049–2061.

Schaff, D. P., and G. C. Beroza, 2004, Coseismic and postseismic velocity changes measured by repeating earthquakes: Journal of Geophysical Research, **109**, B10302.

Sens-Schonfelder, C., and U. Wegler, 2006, Passive image interferometry and seasonal variations of seismic velocities at Merapi Volcano, Indonesia: Geophysical Research Letters, **33**, L21302.

Sgattoni, G., O. Gudmundsson, P. Einarsson, and F. Lucchi, 2016, Joint relative relocation of earthquakes without a predefined velocity model: an example from a peculiar seismic cluster on Katla volcano's south-flank (Iceland): Geophysical Journal International, **207**, 1244-1257.

Shearer, P. M., 1999, Introduction to Seismology: Cambridge University Press.

Shearer, P. M., 2005, Deep Earth structure: seismic scattering in the deep Earth, *in* Schubert, G., B. Romanowicz, and A. Dziewonski, eds., Treatise on Geophysics: Elsevier Academic Press, 11, 759-785.

Singh, J., A. Curtis, Y. Zhao, A. Cartwright-Taylor, and I. Main, 2018, Coda wave interferometry for experimental rock physics and rock mechanics applications: Journal of Geophysical Research - Solid Earth, submitted.

Snieder, R., 1999, Imaging and averaging in complex media in diffuse waves in complex media: Springer Netherlands.

Snieder, R., 2002, Coda wave interferometry and the equilibration of energy in elastic media: Physical Review E, **66**, 046615.

Snieder, R., 2004, Extracting the Green's function from the correlation of coda waves: A derivation based on stationary phase. Physical Review E, **69**, 046610.

Snieder, R., 2006, The theory of coda wave interferometry: Pure and Applied Geophysics, **163**, 455-473.

Snieder, R., A. Gret, H. Douma, and J. Scales, 2002, Coda wave interferometry for estimating nonlinear behavior in seismic velocity: Science, **295**, 2253.

Snieder, R., and M. Vrijlandt, 2005, Constraining the source separation with coda wave interferometry: Theory and application to earthquake doublets in the Hayward fault, California: Journal of Geophysical Researc, **110**, B04301.

Stahler, S. C., C. Sens-Schonfelder, and E. Niederleithinger, 2011, Monitoring stress changes in a concrete bridge with coda wave interferometry: The Journal of the

Acoustical Society of America, **129**, 1945-1952.

Stam, J., 1995, Multiple scattering as a diffusion process: Rendering Techniques '95 - Proceedings of the Eurographics Workshop, 41-50.

Tang, J., J. Li, Z. Yao, J. Shao, and C. Sun, 2015, Reservoir time-lapse variations and coda wave interferometry: Applied Geophysics, **12**, 244-254.

Van Rossum, M. C. W., and Th. M. Nieuwenhuizen, 1999, Multiple scattering of classical waves: microscopy, mesoscopy, and diffusion: Reviews of Modern Physics, **71**, 313-371.

Vandecar, J. C., and R. S. Crosson, 1990, determination of teleseismic relative phase arrival times using multi-channel cross-correlation and least-squares: Bulletin of the Seismological Society of America, **80**, 150-169.

van der Woerd, J., C. Dorbath, F. Ousadou, L. Dorbath, B. Delouis, E. Jacques, P. Tapponnier, Y. Hahou, M. Frogneux, and H. Haessler, 2014, The Al Hoceima Mw 6.4 earthquake of 24 February 2004 and its aftershocks sequence. Journal of Geodynamics, **77**, 89-109.

van Wijk, K., D. Komatitsch, J. Scales, and J. Tromp, 2004, Analysis of strong scattering at the micro-scale, J. Acoustical Society of America, **3**, 1006–1011.

Verlinden, C. M. A., J. Hodgkiss, and W. A. Kuperman, 2015, Passive acoustic source localization using sources of opportunity: The Journal of the Acoustical Society of America, **138**, EL54.

Waldhauser, F., 2001, hypoDD – a program to compute Double-Difference Hypocenter Locations: U.S. Geological Survey, https://nehrpsearch.nist.gov/static/files/USGS/PB2006105370.pdf, accessed 10 April 2016.

Waldhauser, F., W. L. Ellsworth, and A. Cole, 1999, Slip-parallel lineations on the Northern Hayward Fault, California: Geophysical Research Letters, **26**, 3525–3528.

Waldhauser, F., and W. L. Ellsworth, 2000, A double-difference earthquake location algorithm: Method and application to the northern Hayward fault, California: Bulletin of the Seismological Society of America, **90**, 1353-1368.

Waldhauser, F. and W. L. Ellsworth, 2002, Fault structure and mechanics of the Hayward Fault, California, from double-difference earthquake locations: Journal of

Geophysical Research - Solid Earth, **107**, 1-15.

Wang, B., P. Zhu, Y. Chen, F. Niu, and B. Wang, 2008, Continuous subsurface velocity measurement with coda wave interferometry: Journal of Geophysical Research, **113**, B12313.

Wapenaar, K., D. Draganov, R. Snieder, X. Campman, and A. Verdel, 2010a, Tutorial on seismic interferometry: Part 1 – Basic principles and application: Geophysics, **75**, A195-A209.

Wapenaar, K., E. Slob, R. Snieder, and A. Curtis, 2010b, Tutorial on seismic interferometry: Part 2 – Underlying theory and new advances: Geophysics, **75**, A211-A227.

Weaver, R. L., 1982, On diffuse waves in solid media: Journal of the Acoustical Society of America, **71**, 1608-1609.

Weaver, R. L., and O. I. Lobkis, 2000, Temperature dependence of diffuse field phase: Ultrasonics, **38**, 491–494.

Wegler, U., B. G. Luhr, and A. Ratdomopurbo, 1999, A repeatable seismic source for tomography at volcanoes: Annali Di Geofisica, **42**, 565-571.

Wegler, U., B. G. Luhr, R. Snieder, and A. Ratdomopurbo, 2006, Increase of shear wave velocity before the 1998 eruption of Merapi volcano (Indonesia): Geophysical Research Letters, **33**, L09303.

Wegler and Sens-Schonfelder, 2007, Fault zone monitoring with passive image interferometry: Geophysical International Journal, **168**, 1029-1033.

Zhao, Y., A. Curtis, B. Baptie, 2017, Locating micro-seismic sources with a single seismometer channel using coda wave interferometry: Geophysics, **82**, A19-A24.

Zhou H., 2006, First-break vertical seismic profiling tomography for Vinton Salt Dome: Geophysics, **71**, U29-U36.

Appendix 1

Relative source location based on coda wave interferometry (CWI)

MATLAB code *CWIcluster* user manual with examples

Youqian Zhao[1] and Andrew Curtis[1,2], 2018

[1] School of Geosciences, University of Edinburgh, Edinburgh

[2]Department of Earth Sciences, ETH Zurich, Switzerland

Summary:

This user manual accompanies the coda wave interferometry (CWI) relative source location MATLAB code package *CWIcluster*. The code estimates the relative location of a cluster of events of similar source mechanisms using inter-source separations estimated with CWI (Snieder, 2006). The advantage of this location technique is that the location result is insensitive to the number and distribution of seismic stations. The method is particularly useful where there are not a large number of seismic stations with a good event-sensor azimuthal coverage so that the performance of the conventional double-difference relative source location method of Waldhauser & Ellsworth (2000) deteriorates. It also provides an alternative, entirely independent method with which conventional methods can be compared in order to assess relative location uncertainties.

This manual provides a brief introduction of CWI and the location algorithm. This is sufficient to run the code. More details are given in the accompanying paper. The package consists of three sections, each of which contains codes that conduct one step of the location method: 1) classifying events into different clusters with given

waveforms recorded by one or multiple seismic station channels, 2) estimating inter-source separations with the CWI method, and 3) estimating the relative event locations from the separation data. The code solves for the event locations as an optimization problem, where the most likely set of event locations are found where an objective function attains its minimum. This algorithm takes account of the known biases of CWI-estimated source separations, and is able to correct for them to a significant extent in location results. Examples on synthetic and real data are presented in this manual to demonstrate how to use the codes, and test-data is included in the package. For real Earth problems where the actual event locations are unknown, we propose a way to assess the quality of location results.

Contents:

Appendix I

1. Introduction

This manual accompanies the *coda wave interferometry (CWI) relative source location MATLAB code package*. The package implements source location estimation in three steps. First, the events are classified into different clusters based on recorded waveform similarity. Second, for each cluster, inter-source separations between all available event pairs are estimated with CWI. Finally, the relative event locations are obtained from an optimization problem. Using the code to estimate event locations does not require a thorough understanding of the technique, however users are recommended to refer to Snieder (2006), Robinson et al. (2013), and the accompanying paper Zhao and Curtis (2018) to gain a full understanding. The remainder of this section provides an introduction to the technique used in each step. For a quick start, users can implement the whole process by running a single script `Main_running_script.m` in directory `codes` using the test-date set provided, or after editing to use their own data.

1.1 Clustering

CWI uses scattered waves in seismograms to estimate the separations between pairs of source locations, which are then used jointly to determine the relative locations between all events. It has been proved that the location results of CWI-based technique are insensitive to the number and distribution of seismic stations, and it is even possible to estimate event locations with data from a single station channel (Robinson et al., 2013; Zhao et al., 2017). In order to estimate inter-source separations with CWI, it is required that the sources have identical source mechanism (Snieder, 2006). Therefore, it is essential to classify the events into clusters, within each of which, all the events have very similar source mechanisms so that CWI can be applied. The similarity in source mechanism can be assessed by waveform similarity, which is measured by crosscorrelation between pairs of waveforms. The package classifies events in two steps: computing crosscorrelations and identifying clusters. `sort_cr.m` computes the crosscorrelation of all available

waveforms recorded by the same seismic station channel, and sorts the event pairs in a descending order of their correlation coefficients. `clustering.m` then classifies the events into clusters using the sorted crosscorrelations, following the method used by Ottemoller et al. (2017), so that each cluster contains events of similar source mechanisms.

1.2 Estimating inter-source separation with CWI

Coda refers to later part of a seismogram, generated by multiply scattered waves. In spite of its complex appearance with few uniquely identifiable arrivals, coda is extremely sensitive to minute changes in the seismic system. It therefore has the potential to be used for applications involving distinguishing and monitoring small perturbations in seismic systems that are difficult for methods that only use early arrivals of seismograms. Aki (1969) uses the spectrum of coda from local earthquakes to evaluate seismic moments, and more recently Snieder et al. (2002) developed CWI that uses phase information to identify differences between pairs of sources or changes in the propagating medium. The location technique of this package uses inter-source separations between all available event pairs in a cluster as data to estimate the relative locations of the events. This subsection focuses on how CWI estimates inter-source separations.

CWI estimates the inter-source separation between a pair of events by comparing coda of the two seismograms recorded by the same seismic station channel. The theory is based on path summation of scattering waves (Snieder, 1999) - that the total wavefield at a given location can be written as the superposition of waves traveling along all possible trajectories

$$u^1(t) = \sum_T A_T(t), \qquad (1)$$

where u^1 is the total wavefield from event 1, T represents a wave trajectory, and A_T is the contribution to the total wavefield of waves that travel along trajectory T. The trajectory of each scattered wave consists of the path from the source to the first

scatterer encountered, and the path followed thereafter. For event 2 that is close to event 1 and with very similar source mechanisms, CWI assumes that the paths to the first scatterer change, but that subsequent paths do not because they depend mainly on the medium rather than on the source location. Thus the dominant difference of the recorded waveforms at the same seismic station is in coda arrival times (Snieder, 2006). The wavefield of event 2 can then be written as

$$u^2(t) = \sum_T A_T(t - \tau_T), \tag{2}$$

where τ_T is the travel-time difference of waves traveling along trajectory T due to the difference in source position. Due to the proximity in source locations and the similarity in source mechanisms, the two waveforms will be similar, which can be quantified by the normalized cross-correlation of the two waveforms in a time-window defined with a central time t and a half-width t_ω, computed for a sequence of time-windows in the coda

$$R(t_s) = \frac{\int_{t-t_\omega}^{t+t_\omega} u^{(1)}(t')u^{(2)}(t'+t_s)dt'}{\sqrt{\int_{t-t_\omega}^{t+t_\omega} {u^{(1)}}^2(t')dt' \int_{t-t_\omega}^{t+t_\omega} {u^{(2)}}^2(t')dt'}} \tag{3}.$$

In each time-window, the distribution of the travel-time differences τ_T contains information about the source separation δ. Snieder et al. (2006) estimates the standard deviation of the travel-time difference σ_τ from the maximum of the correlation coefficient R_{max}. σ_τ can then be related to the source separation δ by

$${\sigma_\tau}^2 = \frac{1}{2}\frac{\delta^2}{v^2} \quad \text{for isotropic sources in a 2D scoustic medium,} \tag{4a}$$

$$\text{or} \quad {\sigma_\tau}^2 = \frac{1}{2}\frac{\delta^2}{v^2} \quad \text{for isotropic sources in a 3D scoustic medium,} \tag{4b}$$

$$\text{or } {\sigma_\tau}^2 = \frac{6/\alpha^8 + 7/\beta^8}{7(2/\alpha^6 + 3/\beta^6)}\delta^2$$

$$\text{for double} - \text{couple sources in an elastic medium,} \tag{4c}$$

where α and β are P- and S-wave velocity (Snieder and Vrijlandt, 2005). Since the waves arriving in different time-windows have traveled along different paths, the separation results of each time-window are independent and their variation can be

used to estimate uncertainty. It has been proved that inter-source separation estimates are often highly consistent among different station channels (Snieder and Vrijlandt, 2005; Robinson et al., 2011; Zhao et al., 2017).

It is essential to be aware that the CWI technique has an increasing tendency toward underestimation of larger source separation due to the cycle-skipping effect in the correlation of coda in equation 3. This trend can be quantified by two empirical relations between the mean $\mu = \mu(\widetilde{\delta_t})$ and the standard deviation $\sigma = \sigma(\widetilde{\delta_t})$ of CWI separation estimates with the true separations $\widetilde{\delta_t}$ (Figure 1 a, b), where the tilde above separation δ_t indicates that the quantity has been normalized by the dominant wavelength λ_d in the recorded data. The applicable range of CWI is visualized in Figure 1: CWI fails to identify any increase in inter-source separation when the true separation is larger than $0.55\lambda_d$. The empirical functions are derived from a multitude of synthetic experiments with a large range true separations in different Gaussian random media, by fitting the rational function forms

$$\mu(\widetilde{\delta_t}) = a_1 \frac{a_2 \widetilde{\delta_t}^{a_4} + a_3 \widetilde{\delta_t}^{a_5}}{a_2 \widetilde{\delta_t}^{a_4} + a_3 \widetilde{\delta_t}^{a_5} + 1}, \tag{5a}$$

$$\sigma(\widetilde{\delta_t}) = b_1 \frac{b_2 \widetilde{\delta_t}^{b_4} + b_3 \widetilde{\delta_t}^{b_5}}{b_2 \widetilde{\delta_t}^{b_4} + b_3 \widetilde{\delta_t}^{b_5} + 1} + c, \tag{5b}$$

(Robinson et al., 2011) where the value of the constants are listed in Table 1.

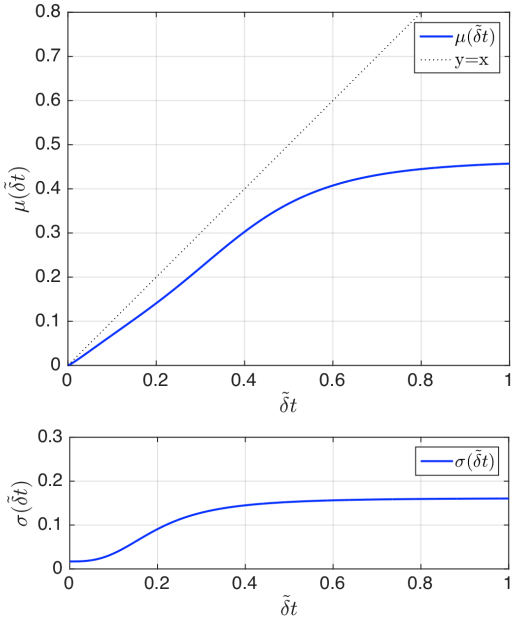

Figure 1: Empirical functions showing the bias and uncertainties of separation estimates of the CWI technique. The upper panel shows the empirical relation between the mean of the source separation $\mu = \mu(\widetilde{\delta_t})$ and the true separation $\widetilde{\delta_t}$. All separations are normalized by their dominant wavelengths. The dotted line labelled $y = x$ shows the case where the mean of the CWI separation estimates are identical to the true separations. The lower panel shows the empirical relation between the standard deviation $\sigma(\widetilde{\delta_t})$ of the separation estimates and the true separation $\widetilde{\delta_t}$.

$\mu = \mu(\widetilde{\delta_t})$	$\sigma = \sigma(\widetilde{\delta_t})$
$a_1 = 0.4661$	$b_1 = 0.1441$
$a_2 = 48.9697$	$b_2 = 101.0376$
$a_3 = 2.4693$	$b_3 = 120.3864$
$a_4 = 4.2467$	$b_4 = 2.8430$
$a_5 = 1.1619$	$b_5 = 6.0823$
	$c = 0.017$

Table 1: Constants used in the empirical relations $\mu = \mu(\widetilde{\delta_t})$ and $\sigma = \sigma(\widetilde{\delta_t})$ in equation 5 (Robinson et al., 2013).

o incorporate information about source separation or event location known prior to the location process, which here is considered to be a uniform distribution with wide bounds. The likelihood function $P\left(\tilde{\delta}_{CWI}\middle|\widetilde{\delta_t}\right)$ is approximated by a positively bounded Gaussian pdf, whose mean and standard deviation are represented by the empirical relations $\mu = \mu(\widetilde{\delta_t})$ and $\sigma = \sigma\left(\widetilde{\delta_t}\right)$ given true separation $\widetilde{\delta_t}$.

For a cluster of events, equation 6 holds for each event pair. Robinson et al. (2013) incorporate the separations between multiple event pairs by multiplying the formulae for all available event pairs to establish the joint posterior pdf, assuming they are independent of each other:

$$P\left(e_1, \dots, e_n\middle|\tilde{\delta}_{CWI}\right) = c\prod_{i=1}^{n} P(e_i) \times \prod_{i=1}^{n-1}\prod_{j=i+1}^{n} P\left(\tilde{\delta}_{CWI,ij}\middle|e_i, e_j\right), \qquad (7)$$

where c is a constant, n is the number of events, $\boldsymbol{e}_i = (x_i, y_i, z_i)$ is event i location, within the last term we use $\delta_{t,ij} = \left\|\boldsymbol{e}_i - \boldsymbol{e}_j\right\|_2$ for source separation $\delta_{t,ij}$ between the i'th and j'th earthquakes, and the prior $P(\boldsymbol{e}_i)$ only contains the relative event locations. Throughout the evaluation of the joint pdf, the separation quantities are used as their normalizations (divided by dominant wavelength λ_d). However, the dominant frequency, hence dominant wavelength of the events can extend over a large range, and is also subject to limitations of recording instruments; using the average dominant wavelength over different station channels therefore introduces inaccuracy to the location process. To this end, this package uses the joint pdf introduced by Zhao et al. (2017), which applies an individual likelihood for each channel when data from multiple channels are used, so that the separations computed during the evaluation of the joint pdf are normalized by the actual dominant wavelengths recorded on that channel

$$P\left(\boldsymbol{e}_1, \dots, \boldsymbol{e}_n\middle|\tilde{\delta}_{CWI}\right) = c\prod_{i=1}^{n} P(\boldsymbol{e}_i) \times \prod_{k=1}^{m}\prod_{i=1}^{n-1}\prod_{j=i+1}^{n} P_k\left(\tilde{\delta}_{CWI,ij}\middle|\boldsymbol{e}_i, \boldsymbol{e}_j\right), \qquad (8)$$

where m is the number of channels used and k is the index over m channels.

The maximum of the joint posterior pdf (equation 8) occurs at the most probable combination of the events locations. Hence, the event locations can be found by

solving an optimization problem. Taking the negative logarithm of equation 8, the multiplications are then converted to summations that are more numerically stable:

$$-\ln\left[P\left(\boldsymbol{e}_1,\ldots,\boldsymbol{e}_n\middle|\tilde{\delta}_{CWI}\right)\right] = -\ln[c] - \sum_{i=1}^{n}\ln[P(\boldsymbol{e}_i)] - \sum_{k=1}^{m}\sum_{i=1}^{n-1}\sum_{j=i+1}^{n}\ln\left[P_k\left(\tilde{\delta}_{CWI,ij}\middle|\boldsymbol{e}_i,\boldsymbol{e}_j\right)\right]. \quad (9)$$

Optimization of equation 8 is equivalent to minimizing equation 9, where $\ln[c]$ and $\ln[P(\boldsymbol{e}_i)]$ (for uniform priors) can be ignored as they are constant. Thus, the event locations $(\boldsymbol{e}_1,\ldots,\boldsymbol{e}_n)$ can be solved by minimizing the objective function

$$L(\boldsymbol{e}_1,\ldots,\boldsymbol{e}_n) = -\sum_{k=1}^{m}\sum_{i=1}^{n-1}\sum_{j=i+1}^{n}\ln\left[P_k\left(\tilde{\delta}_{CWI,ij}\middle|\boldsymbol{e}_i,\boldsymbol{e}_j\right)\right]. \quad (10)$$

The objective function L is minimized using a conjugate gradient method, Polak-Ribiere technique (Navon and Legler, 1987; Press et al. 1987).

2. Package contents

The package include the following files and directories:

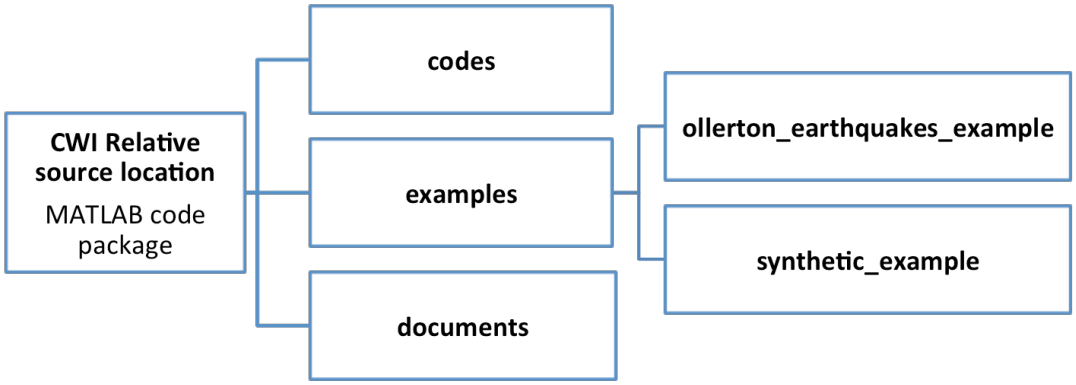

Directory `codes` contains the following scripts and functions that conduct clustering, estimating inter-source separations, and estimating relative event locations. The entire process can be implemented by running a single script `Main_running_script.m` in the directory step-by-step. The files generated will be stored in directory `codes` as the working directory. However, files generated when the authors implemented the example are stored in directories `examples/synthetic_example` and `examples/ollerton_earthquakes_example/` for the real-data example and synthetic data, respectively.

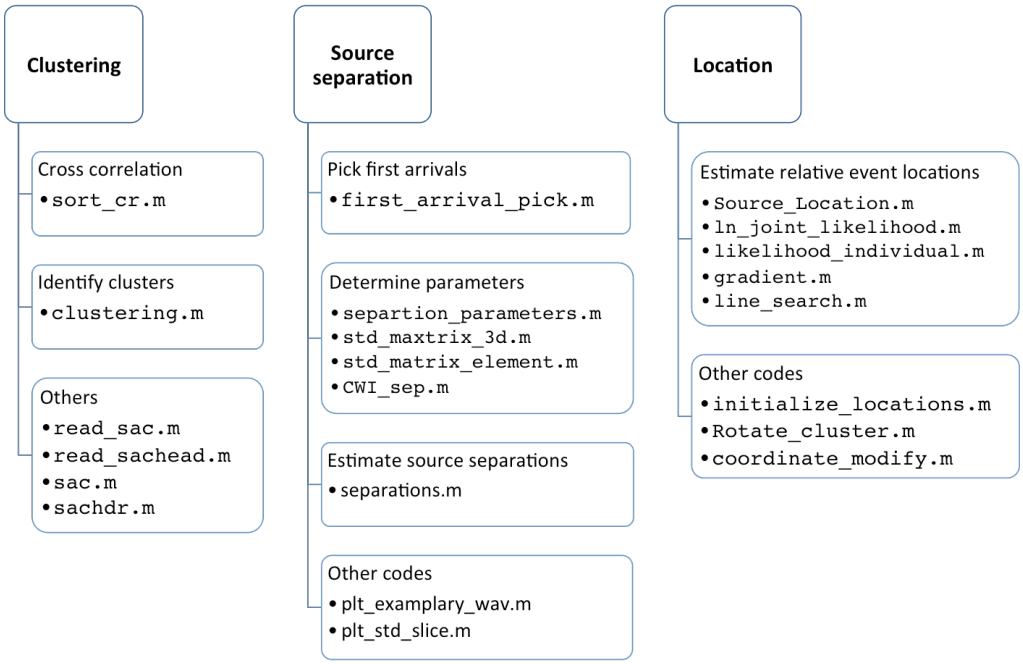

3. Codes

This section introduces the usage of the codes listed in section 2 in three subsections, Clustering, Estimating inter-source separations, and Location. A working example using microearthquake data from New Ollerton, Nottinghamshire, England is presented to demonstrate how to use the code package to process seismic data to solve for source locations.

3.1 Clustering

The theory of CWI requires the events to have identical source mechanisms, so the events need to be classified into clusters of similar source mechanisms. The similarity in sources is assessed by the similarity in waveforms recorded by the same seismic station channel, which is measured by their correlation coefficients.

The package classifies events in two steps, computing crosscorrelations and identifying clusters, with scripts `sort_cr.m` and `clustering.m`, respectively. `sort_cr.m` reads in seismic data in SAC form. It first selects events and station channels for location according to criteria set by user: `MIN_channel` is the minimum number of recording channels for an event to be considered, and `MIN_event_per_channel` is the minimum number of events that a channel records for the channel to be used. It then calculates the correlation coefficient cr of all available pairs consisting of the selected events recorded by each selected station channel, and finds the maximum of each correlation coefficient cr_{max}. For each event pair, cr_{max} are then averaged over all selected station channels that have recorded both events, and these average maximum correlation coefficient $cravg_{max}$ are then sorted in descending order.

`clustering.m` implements the method of Ottemoller et al. (2017) to identify clusters. It starts with the event pair with the highest $cravg_{max}$, making them the first two events of the first cluster. It then searches through the sorted list of

$cravg_{max}$, and adds events that are linked to the current cluster. A link to a cluster is defined as one of the events in the pair is correlated with any event that is already in the cluster (event pairs are defined to be correlated if $cravg_{max}$ is higher than `MIN_corr`, the threshold of $cravg_{max}$ for an event pair to be considered part of a cluster). The search restarts from the first unclassified pair (unclassified pair with the highest $cravg_{max}$) every time a new event is added to the cluster to avoid overlooking any linked event. The search loops until there is no event that can be added to the current cluster, after which it starts a new cluster by adding the two events of the first unclassified pair. The search ends when all events are classified. Any clusters with fewer then `MIN_E_per_CLUSTER` events will be removed from the list of clusters.

3.1.1 Code description

This subsection contains a short description of each script or function for event clustering. A thorough explanation of inputs and outputs is included in Appendix 1(a).

Crosscorrelation

- `sort_cr.m`:

`sort_cr.m` selects events and station channels using the SAC files according to the given criteria `MIN_channel` and `MIN_event_per_channel`. For each station channel, the correlation coefficient of all available event pairs are computed and the maximum correlation coefficient of each pair are found. The maximum correlation coefficient is then averaged over all channels that have recorded the given event pair. The average maximum correlation coefficients are then sorted in a descending order and sorted in `max_cr.xls` or `max_cr.csv` depending on the availability of Excel.

Identify clusters

- `clustering.m`:

`clustering.m` classifies the selected events into clusters according to waveform

similarity, which is reflected by maximum correlation coefficient.

3.1.2 Example

In order to demonstrate how to use the codes in the package, we use the New Ollerton microearthquake data recorded by a temporary recording network deployed by British Geological Survey (BGS) in early 2014. The events have magnitudes of 0.7-1.8ML, and the waveforms are filtered to 2-20Hz. In order to show the capability of the codes, we used 118 SAC files, with 41 events recorded by 5 different channels of seismic stations. Specifically, 8 events were recorded by station channel NOLA_E, 35 by NOLC_Z, 34 by NOLF_E, 34 by NOLF_N, and 7 by NOLF_Z.

Crosscorrelation

The SAC files are stored in directory `example_data`. To acquire the sorted crosscorrelation file `max_cr.xls` (or `.csv`) using `sort_cr.m`, the following lines are executed (Session 1.1 in `Main_running_script.m`):

```
data_location='../examples/ollerton_earthquakes_example/exampl
e_data/';
MIN_channel=2;
MIN_event_per_channel=10;
xcorr_range=[10 30];
max_time_lag=10;
sort_cr
```

For these waveforms, we set the selection criteria that only events that have been recorded by at least 2 station channels should be considered for clustering and hence for location in later steps; and that only station channels that have recorded at least 10 events should be used. These criteria are to ensure the robustness of data chosen for source location, presuming fewer data of higher quality gives more reliable results than more data of inconsistent quality. We only compute the crosscorrelation of the part between 10-30 seconds of waveforms to save computation time, as most of the energy of a waveform is contained in the early arrivals which contribute most

to the crosscorrelation. As all of the events are located very close to each other compared to event-station distances, the first arrival time in each waveform should not differ very much, and a search range can be set to shorten the time used searching for the maximum crosscorrelation: it is set to 10 seconds this case. The results are shown in the MATLAB workspace:

```
There are 41 events and 5 channels found.
There are 34 events and 3 channels selected.
Files generated:
events_channels_selected.txt
file_indices.csv
max_cr.csv
```

The code identified 41 events and 5 station channels from the SAC files, among which 34 events and 3 station channels were selected (not rejected), based on the criteria above. The files generated by executing `sort_cr.m` are also listed. The selected events and station channels are stored in file `events_channels_selected.txt`, as shown below:

```
1    NOLCEHZ
2    NOLFHHE
3    NOLFHHN

01    2014-02-07-04-06-05
02    2014-02-07-15-13-54
03    2014-02-09-05-33-27
04    2014-02-09-13-56-42
        …
```

The first three lines are the names of the selected station channels, and the following lines show the selected events, represented by their occurrence time. For example,

`"01 2014-02-07-04-06-05"` means the first selected event occurred at year 2014, month February, day 07, hour 04, minute 06, and second 05.

`file_indices.csv` keeps a record of the indices of the SAC files of the waveforms from the selected events recorded by the selected station channels. For instance the panel below shows the first few lines of `file_indices.csv`, where in the first line `"2 3 4"` refers to the indices of SAC files of waveforms from the first selected event `2014-02-07-04-06-05` recorded by the selected channels NOLCEHZ, NOLFHHE, and NOLFHHN, respectively, which is used by `clustering.m` in later steps:

```
2 3 4
6 7 8
11 12 13
15 16 17
  …
```

The third file generated by `sort_cr.m` is `max_cr.csv`, which stores the maximum crosscorrelations of all available pairs consisting of the selected events in descending order. The panel below shows the first few lines:

```
33 34 0.99682 0.99331 0.99816 0.999
28 29 0.99527 0.98852 0.99812 0.99918
27 28 0.99525 0.99552 0.99397 0.99627
12 13 0.9921  0.98366 0.99608 0.99657
…
```

The first line `"33 34 0.99682 0.99331 0.99816 0.999"` shows the highest average maximum crosscorrelations $cravg_{max}$ among the available channels. `"33 34"` are the indices of the selected events with highest $cravg_{max}$, `"0.99682"` is their $cravg_{max}$, and each of the following figures is the maximum crosscorrelation

cr_{max} of the waveforms of these two events recorded by one selected channel.

Identify clusters

With the sorted crosscorrelations, the events are classified into clusters with similar source mechanisms by running the following lines (Session 1.2 in `Main_running_script.m`):

```
data_location='../examples/ollerton_earthquakes_example/example_data/';
max_cr_pair=load('Max_cr.csv');
load('file_indices.csv');
MIN_corr=0.9;
MIN_E_per_CLUSTER=5;
clustering
```

We choose to only consider event pairs with a high similarity in source mechanisms, hence set the threshold `MIN_corr` at 0.9, so that the event pairs in `max_cr.csv` whose $cravg_{max}$ is below 0.9 will not be searched by `clustering.m`. In the location algorithm, up to $n(n-1)$ separation data (a mean and a standard deviation for each event pair out of up to $n(n-1)/2$ pairs for n events) are used to invert for $3n$ variables (x, y and z coordinate for each event location) for the locations of n events. Therefore, the more events are contained in a cluster, the denser information we have to solve the locations. However,since only 34 events were selected, the lower threshold to form a cluster should be relatively wide, therefore `MIN_E_per_CLUSTER` is set to 5 in this example. The following results are shown in the MATLAB workspace:

```
34 events classified into 2 clusters.
cluster1: 11 events
cluster2: 23 events

Files generated:
```

```
files_cluster1_channel1.txt
files_cluster1_channel2.txt
files_cluster1_channel3.txt
files_cluster2_channel1.txt
files_cluster2_channel2.txt
files_cluster2_channel3.txt
```

All selected events are classified into 2 clusters, with 11 and 23 events, respectively, and there are no unclassified events. The generated files store the filenames of the SAC files of waveforms of events in each cluster recorded by each station channels. For instance, files_cluster1_channel1.txt lists the SAC files of waveforms of the 11 events in cluster 1 recorded by channel 1 (NOLCEHZ):

```
2014-04-17-1750-40S.BGS___015_NOLC__EH_Z.SAC
2014-04-18-0453-16S.BGS___015_NOLC__EH_Z.SAC
2014-04-13-2058-38S.BGS___015_NOLC__EH_Z.SAC
2014-04-10-0653-33S.BGS___015_NOLC__EH_Z.SAC
                        …
```

Thus, events in each cluster have very similar source mechanism, with $cravg_{max} \geq 0.9$, and are suitable for source separation estimation using CWI.

3.2 Estimating inter-source separations

For each cluster, we pick the first arrivals of waveforms recorded by the same station channel and align them. We assume that the differences in the coda are only due to the difference in source locations, as we have ensured that the source mechanisms are similar. This is not true if seismic velocity changes between the different event occurring times. Although theoretically, the two types of changes could be discriminated (Snieder et al., 2002), this is beyond our scope. This package allows

users to manually pick waveform first arrivals in an interactive graphical manner.

To apply CWI to estimate inter-source separations, waveform coda needs to be divided into non-overlapping time-windows with equal length. Seismic coda starts to become suitable for CWI where the waves are sufficiently scattered so that a time-window contains waves leaving the source from many possible directions; and it ends where the background noise level exceeds the amplitude of the signal from the events. Therefore, there is a limited length of coda that can be used. In order to obtain reliable separation standard deviations, at least four time-windows are needed for each pair of waveforms. Deciding the lengths of time-windows involves a trade-off: the computation of equation 3 using wave representations 1 and 2 gives rise to double sums, and CWI assumes the cross term is negligible compared to the diagonal terms, whose ratio is inversely proportional to the length of time-windows (Snieder 2006); for it to be reasonable to ignore the cross terms, the time-windows need to have sufficient length. On the other hand, the time-windows cannot be too long to avoid cycle skipping in the crosscorrelation (equation 3). It is therefore not a trivial task to decide the number, length, and start of time-windows applied to implement CWI.

To avoid the vagaries of trial and error, this package applies the separation-uncertainty matrix introduced by Zhao et al. (2017) to systematically find the most suitable combination of [number, length, start-time] of time-windows. Script `separation_parameters.m` allows users to set a time `coda_start` in the waveform, a time shortly after which coda should be taken; and a time `coda_end`, at which coda is no longer suitable for CWI. At each time, the [start-time] of time-windows is given by `coda_start+n*dl_coda_start`, where `dl_coda_start` is the increment of the starting time of windowing, and `n=0,1,2…`. The script then takes the part of the aligned waveforms starting from the [start-time] of time-windows, and ending at `coda_end`. For each taken length of waveform coda, the script is able to work out all the possible combinations of [number, length] of time-window allowed, given the minimum number and length of

time-window (`min_num_win` and `min_l_win`), the maximum time-window needed (`max_num_win_limit`) if the total length of coda taken is sufficiently long, and the increment of window length (`dl_win`). It then computes the uncertainty of separation estimates using each possible [number, length] parameter combination for the current selected coda.

For data from each station channel, the script computes a separation-uncertainty matrix, with elements $\Omega_{i,j} = \sum_N \sigma_{i,j}/N$, where $\sigma_{i,j} = \sqrt{\sum_l (\delta_{i,j,k} - \bar{\delta}_{i,j})^2/l}$ is the standard deviation of separation estimates from l coda time windows for events i and j, $\delta_{i,j,k}$ is the separation estimate of the kth window and $\bar{\delta}_{i,j}$ is their mean, and N is the number of event pairs on that channel. The value of $\Omega_{i,j}$ reflects the uncertainty of separation estimates derived from one recording channel for each source pair. Averaging over multiple source pairs gives a final uncertainty estimate for that combination of parameters. Thus, the script searches for the combination of time-window [number, length, start-time] parameters that gives the lowest uncertainties for separation estimates.

With the number, length and start-time of time-windows systematically determined by `separation_parameters.m`, or set by the users for their specific needs, inter-source separations between all possible event pairs in a cluster recorded by the same station channel can be estimated with script `separations.m`. The script generates files storing the mean and standard deviations of separation estimates that are used in the location algorithm. For each cluster and channel combination, a file `seps_clusteri_channelj.xls (or .csv)` is generated, which contains two columns of N elements, where N is the number of event pairs. The first and second column store the means and standard deviations of the separation estimates from all time-windows used. In each column, the event pairs are ordered as $[e_1\ e_2]$, $[e_1\ e_3]$,…, $[e_1\ e_n]$, $[e_2\ e_3]$, $[e_2\ e_4]$,…, $[e_2\ e_n]$, $[e_3\ e_4]$, $[e_3\ e_5]$,… $[e_{n-1}\ e_n]$, where n is the number of events. If practitioners use their own separation data to estimate relative event locations, the separation data files should be organized in the same way.

The remainder of this subsection introduces the scripts and functions used for first arrival picking, determining separation parameters, and estimating source separations. It is then shown how they are used with the example of the New Ollerton microearthquake data.

3.2.1 Code description

This subsection contains a short description for each script or function for estimating inter-source separations. Thorough explanation of inputs and outputs are included in Appendix 1(b).

Pick first arrival of waveforms

- `first_arrival_pick.m`

`first_arrival_pick.m` allows users to interactively pick the first arrival of the waveforms listed in a .txt file in three simple steps:

1) On an exemple waveform of events in the cluster recorded by the same station channel (listed in the given .txt file), select a rough (initial) range containing the early arrivals, including a small interval before the first arrival.

2) The script then allows the user to pick the first arrival of each waveform within the initial searching range selected in step 1. For each waveform, two plots are generated. The first plot shows the part of waveform inside the initial range, and allows the user to select a narrower range that contains the first arrival and only a few subsequent arrivals of the waveform.

3) For each event, the second plot shows the part of waveform inside the narrow range selected in step 2, which should be narrow enough for the user to location the center of the first arrival with a high accuracy. The user then picks the first arrival at its center. If in step 2, the part of the waveform selected is found to be inconvenient for selecting the narrow range and picking the first arrival, end the process by closing any plotted figure and rerun the script.

Determine parameters for estimating source separations

- `separation_parameters.m`

`separtion_parameters.m` finds the combination of [number, length, start-time] of time-windows for running `CWI_sep.m`. A 3D std-matrix is generated. Each element is the average standard deviation of inter-source separations over all available pairs in the given cluster recorded by the given station channel(s).

- `CWI_sep.m`

`CWI_sep.m` is one of the core functions in this package, called by multiple scripts and functions. It applies coda wave interferometry (CWI) (Snieder, 2006) to estimate the separation between one pair of sources with similar mechanisms for isotropic sources in a 2D or 3D acoustic medium, or double-couple sources in an elastic medium, assuming both sources are on the same fault plane (Snieder and Vijlandt, 2005). The two improvements introduced by Robinson et al. (2011) are applied: 1) they remove the Taylor series approximation of the autocorrelation of waveforms of the two events, and 2) appliey a restricted searching range when searching for the maximum of the correlation coefficient `Rmax` to avoid cycle skipping.

- `std_maxtrix_3d.m`

`std_maxtrix_3d.m` is called by `separation_parameters.m` generates a three-dimensional matrix. Each element is the average standard deviation of inter-source separations over all available pairs in the given cluster recorded by the given station channel(s).

- `std_matrix_element.m`

`std_matrix_element.m` is called by `std_maxtrix_3d.m`. It calculates elements of `STD_matrix_3D`, with given [number, length, start-time] of time-windows.

Estimate inter-source separations

- `Separations.m`

`separations.m` estimates the inter-source separations of all available event pairs in the given cluster recorded by the given station channel. It generates `.xls` (or `.csv`) files containing the means and standard deviations of all event pairs from the cluster. For event pairs whose waveforms do not all exist, the results are marked with `-1`.

3.2.2 Example

The 34 selected events have been classified into 2 clusters, with 11 in cluster 1 and 23 in cluster 2. Waveforms recorded by the selected station channels NOLCZ, NOLFE and NOLFN (short for NOLCEHZ, NOLFHHE, and NOLFHHN) will be used to estimate inter-source separations. For each cluster recorded by each channel, the routine consisting of first arrival picking, parameter determining, and separation estimation are conducted.

Pick first arrival of waveforms

To use `first_arrival_pick.m` to pick the first arrival of waveforms in cluster 1 recorded by channel 1 (NOLC), the following lines are executed (Session 2.1 in `Main_running_script.m`):

```
data_location='../examples/ollerton_earthquakes_example/example_data/';
txtfilename='files_cluster1_channel1.txt';
first_arrival_pick
```

A plot (Figure 2) of an exemple waveform is generated for the user to select an initial range containing the early part of the waveform. Click twice to select the two boundaries of the initial range, each indicated by the center of the cross as shown in Figure 2. Only the horizontal coordinate of the clicked positions will be recorded, as

the boundaries are defined on the time axis. This range should contain the first and the early arrivals for all waveforms in the cluster recorded by the same channel.

Two plots are then generated for each waveform listed in the .txt file used above. The first plot shows the part of the waveform inside the initial range for event 1 of cluster 1 recorded by channel 1, as shown in Figure 3a. Click twice on the plot to select a narrower range that contains the first arrival and only a few subsequent arrivals (3 to 5 is suggested). The second plot is then generated, containing the part of the waveform in the narrow range, as shown in Figure 3b. Pick the first arrival of event 1 by clicking at its center. Plots for subsequent events in the cluster will then be generated for the user to pick their first arrivals. The index of the sample at which the first arrival is picked for each waveform is stored in `first_arrivals_clusteri_channelj.xls` (or `.csv`) for cluster i recorded by channel j, which can be used to align the waveforms by their first arrivals at the same position. Figure 4a and 4b show exemples of aligned waveforms of cluster 1 and cluster 2 recorded by channel 2 (NOLFE).

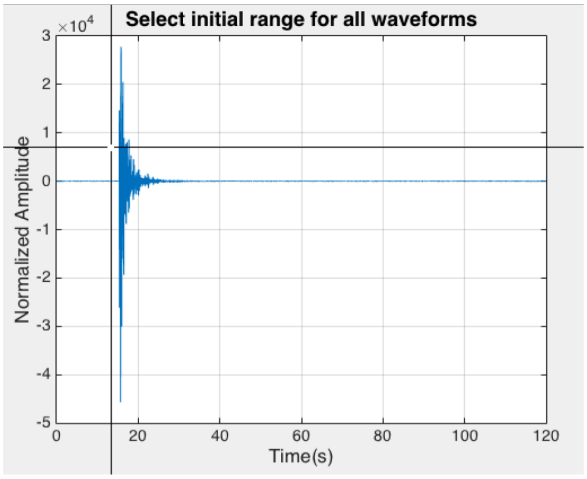

Figure 2: An exemple waveform in the first cluster displayed for the user to select the initial range that contains the first arrival.

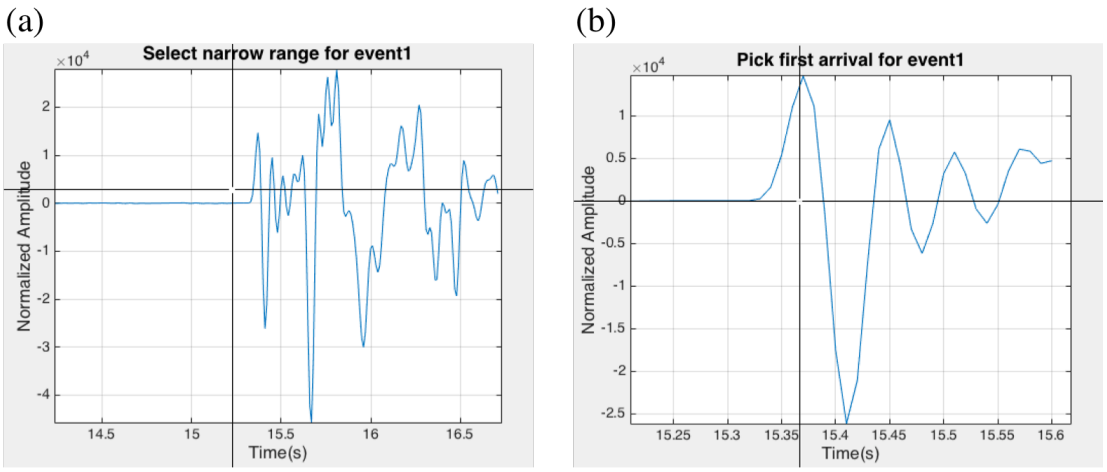

Figure 3: Two plots created for each waveform in the cluster. Panel (a) is the part of waveform in the selected initial range for the user to pick a narrower range that contains the first arrival. Panel (b) is the part of waveform in the selected narrow range, where the user picks the center of the first arrival of the waveform.

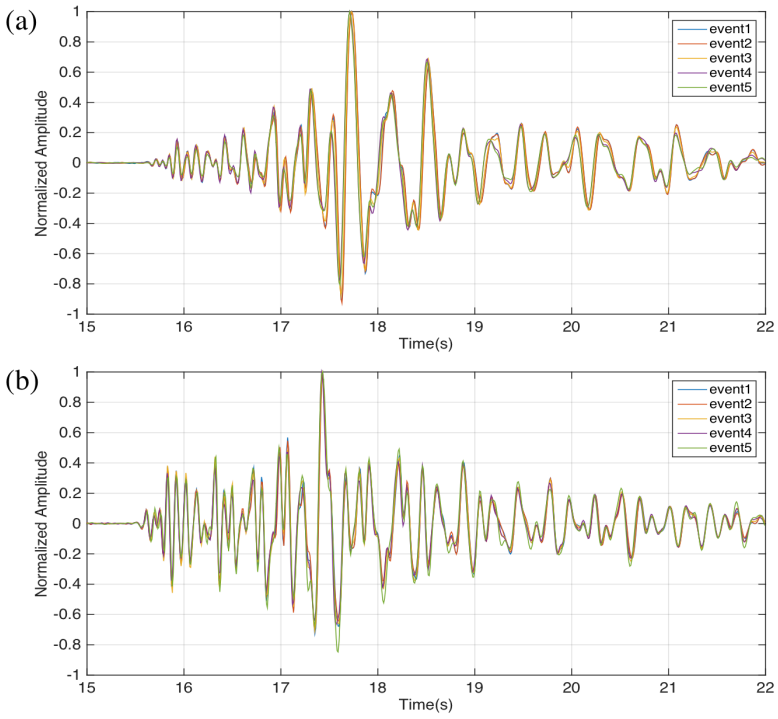

Figure 4: Exemplary waveforms with first arrivals aligned together. Panel (a) and (b)

are waveforms from cluster 1 and 2, recorded by channel 2 (NOLFE), respectively.

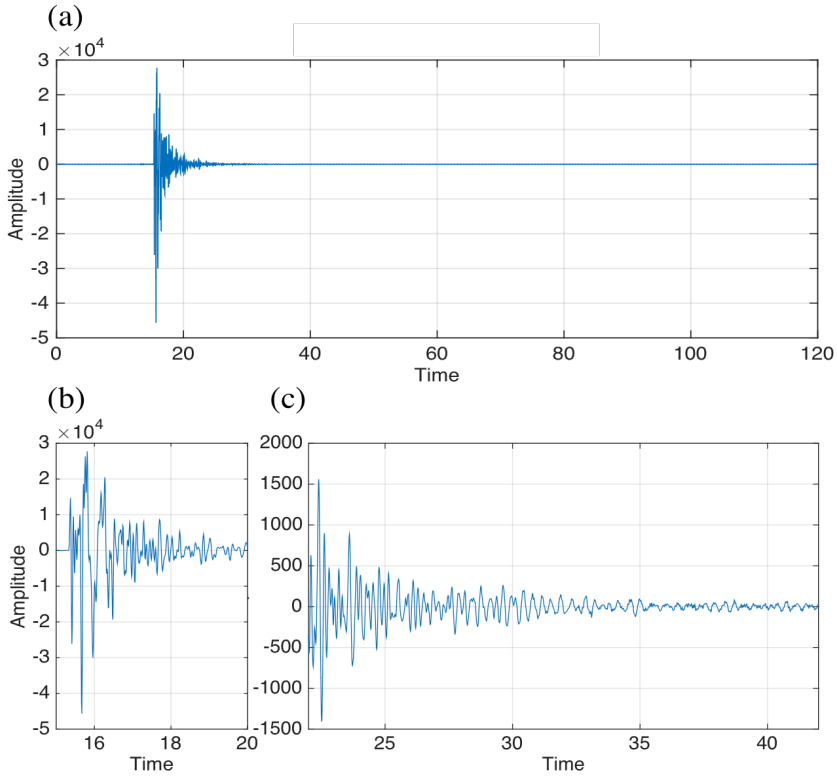

Figure 5: An exemple waveform in the cluster. Panel (a) is the full waveform; panel (b) contains the early arrivals and a small part of coda, within which the user chooses where to start searching for the start of windowing; and panel (c) contains a large part of the coda where the amplitude of coda falls significantly.

Determine parameters for estimating source separations

Before using CWI to estimate inter-source separations, we use the separation-uncertainty matrix to determine the parameters [number, length, start-time] of time-windows. First, execute the following lines (Session 2.2 in `Main_running_script.m`) to acquire the plot of an exemple waveform (Figure 5) to determine the remaining inputs of `separation_parameters.m` (unless determined otherwise):

```
first_arrival_ind=load('first_arrivals_cluster1_channel1.csv')
txtfilename='files_cluster1_channel1.txt';
data_location='../examples/ollerton_earthquakes_example/exampl
```

```
e_data/';
plt_examplary_wav
```

The exemple waveform is shown as Figure 5a, with its zoomed panels that contain the interval where the potential start for windowing lies (Figure 5b) and the interval where the amplitude of coda falls significantly, indicating the end of the search (Figure 5c). We decide to start the search from 16s (`coda_start`) when the multiply scattered waves started to be recorded, and to end the search at 40s (`coda_end`) when the amplitude of coda has fallen to noise level. We set the increment of the [start-time] of windowing to be 1s (`dl_coda_start`), the minimum length of windows `min_l_win` to 2.5s, which can increase at an increment of 0.5s (`dl_win`). We also set the minimum number of windows `min_num_win` to 4 to ensure some robustness of uncertainty estimation, and the maximum number of windows `max_num_win_limit` to 7. `max_num_win_limit` is not necessarily the maximum number of time-windows being searched, but an upper limit of the number of windows examined if the available coda is so long that the maximum number of windows allowed for some given [start-time, length] is more than that the user desires. If there isn't a limit on the number of time-windows, `max_num_win_limit` can be set to a number that is guaranteed to be larger than the maximum number of windows allowed by the length of available coda. We want the case represented by coda [start-time] to be displayed, and the running result to be saved, so `plt_flag` and `save_flag` are both set to '`y`'.

`separation_parameters.m` calls for function `CWI_seps.m`. Some of its inputs are generated inside `separation_parameters.m`, and the remainder need to be provided. The following lines are executed (Session 2.2 in `Main_running_script.m`):

```
coda_start=16;
coda_end=40;
```

Appendix I

```
dl_coda_start=1;
min_num_win=4;
min_l_win=2.5;
max_num_win_limit=7;
dl_win=0.5;
plt_flag='y';
save_flag='y';
% Inputs for running CWI_sep.m
veloc=[4200 2360];
source_type='doublecouple';
search_range=40;
num_interpo_point=10;
separtion_parameters
```

The MATLAB workspace shows the combination of parameters found that gives the lowest separation estimation uncertainty:

```
The smallest average standard deviation 11.08m is obtained when
using:
4 2.500s time-windows, starting from 19s.
```

It is found that using 4 time-windows with a length of 2.5s starting from 19s of the waveforms to conduct source separation estimation gives the lowest average standard deviation of 11.08m, indicated by the darkest blue grid at the bottom left of Figure 6a. The separation-uncertainty matrix provides a guideline to enable us to determine the combination of parameters for CWI. However, when using other combinations of parameters, the results should not change significantly if we do not move far from those found with the matrix. For instance, using 4 time-windows with a length of 3s starting from 19s leads to an average standard deviation of 15.64 (Figure 6a), and using 5 time-windows with a length of 2.5s starting from 21s leads to an average standard deviation of 17.22 (Figure 6b). We can thus determine the [number, length, start-time] of time-windows for each cluster recorded by each channel and estimate

the source separations.

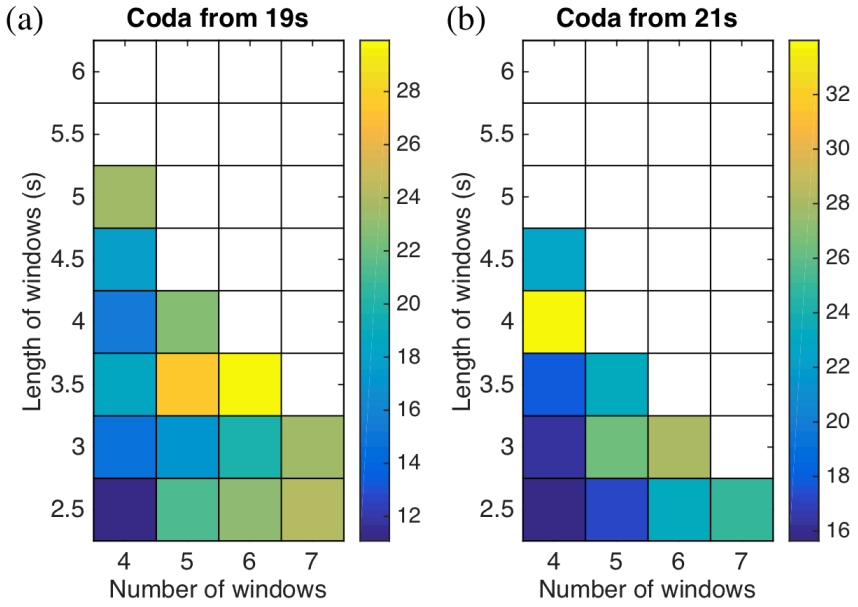

Figure 6: Slices of the 3D separation uncertainty matrix. Colors indicate the values of the average standard deviations resulting from the corresponding parameter combination of number of windows, window length and start-time of windows, used to divide the coda. White cells indicate parameter combinations that are not supported by the available data. Panel (a) is the slice of the matrix where all parameter combinations have a start time of windowing at 19s. Panel (b) is the slice where all combinations have a start time of windowing at 21s.

Estimate inter-source separations

With the combination of parameters found with the separation-uncertainty matrix, we estimate the inter-source separations for each cluster recorded by each channel separately. For cluster 1 channel 1, the following lines are executed (Session 2.3 in `Main_running_script.m`):

```
first_arrival_ind=load('first_arrivals_cluster1_channel1.csv')
txtfilename='files_cluster1_channel1.txt';
data_location=' ../examples/ollerton_earthquakes_example/example_data/';
```

```
veloc=[4200 2360];
source_type='doublecouple';
search_range=40;
num_interpo_point=10;
plt_aligned='y';
win_length=2.5;
win_start=21;
win_num=5;
separations
```

There are 55 event pairs made up of 11 events in cluster 1. For each event pair, there are 4 estimates of source separations given by the 4 time-windows. The generated file `seps_cluster1_channel1.csv` stores the mean and standard deviation of the 4 separation estimates for each event pair, which are then used for source location.

3.3 Location

The relative source locations of events in a cluster are solved by minimizing the objective function L in equation 10. The most likely set of event locations are obtained where the function L attains its minimum. The main function in the package for source location is `Source_Location.m`, which estimates the relative source locations of a cluster of events with the mean and standard deviations of the inter-source separations estimated with CWI. To start the minimization, a set of initial locations of the events are needed; these can be generated with function `initialize_locations.m` given in the package, or provided by the user. Function `Source_Location.m` first evaluates the objective function L (the negative logarithm of the joint likelihood function) at the given initial event locations (by calling `ln_joint_likelihood.m`) and computed the gradient (by calling `gradient.m`). The function searches along the star searching direction `-Gradient0` for the minimum in the given direction (by calling

`line_search.m`). The event locations are thus updated to the minimum found, and the value of L is reduced. The function then calculates the next searching direction that is orthogonal to the gradient at the current position and conjugate to the last searching direction, conducts a line search along the new searching direction, and updates the event locations to the new minimum found. Such iterations continues until one of the three conditions is met: 1) the value for any non-zero step length is larger then that obtained in the later iteration; 2) the reduction in the value of L in an iteration is trivial (smaller than `L_tolerance`); or 3) the maximum number of allowed iterations `max_iteration` is reached. Starting with a different set of initial location is recommended if the iterations are terminated due to the third condition, as some initializations can lead to convergence quicker than others.

Inter-source separations estimated with CWI are required to estimate the relative locations using function `Source_Location.m`. If users are using their own separation data, the separation files for each cluster and channel combination should be generated in the format described in the introduction of section 2.2.

3.3.1 Code Description

This subsection contains a short description for each script or function for source location. Thorough explanations of inputs and outputs are included in Appendix 1(c).

- `Source_Location.m`

`Source_Location.m` estimates the relative location of a cluster of events, using inter-source separation data (their mean and standard deviations) estimated with CWI. The location is solved as a minimization problem, where the most probable set of event locations are found where the objective function L attains its minimum.

Parameters of the empirical relations (equation 5) between the true separation and the mean and standard deviation of the CWI estimates are given inside function `Source_Location.m`. Here we use the ones derived by Robinson et al. (2011), however, users can change them to those derived from their own experiments.

- `ln_joint_likelihood.m`

`ln_joint_likelihood.m` estimates the negative logarithm of the joint likelihood function L for a cluster of events. For each station channel, all available event pairs are considered, except for those instructed to be discarded in the input of the function.

- `likelihood_individual.m`

`likelihood_individual.m` estimates the likelihood function for an individual pair of events.

- `gradient.m`

`gradient.m` computes the gradient of L at a given set of event locations

- `line_search.m`

`line_search.m` conducts searches for the minimum of an objective function L over a given direction in three steps:

1) along the given direction, evaluate L in a large range with increments of `delta_lambda_coarse`, and find the (coarse) minimum among these values of L.

2) define a smaller range around the minimum found, evaluate L in the smaller range with increments of `delta_lamba_dense`, and find a new (dense) minimum among these values of L.

3) adjust the dense minimum by fitting a parabola using the minimum point found and two of its adjacent points, and take the vertex of the parabola as the final minimum of L along the given direction.

- `initialize_locations.m`

`initialize_locations.m` generates a set of initial locations for the minimization problem solved by `Source_Location.m`. It first creates a set of locations for the given event number, uniformly distributed in the given range. It then reorders the created events to ensure the least squares residuals of inter-source

separations (residuals being the difference in separation of each event pair between that calculated from the created initial locations and that estimated with CWI from seismic data).

3.3.2 Synthetic example

Here we use a synthetic example to show that optimization conducted by function `Source_Location.m` is able to solve the relative location of a cluster of events using CWI separation estimates. We randomly distribute 50 sources in a homogeneous cube with side length of 300m, shown as the hollow circles in Figure 7. Dominant wavelength is $\lambda_d = 534m$, and the maximum source separation is λ_{max} is $424m$, i.e. $0.8\lambda_d$. The purpose of this synthetic experiment is to demonstrate the location of a cluster of events with CWI separation data, we therefore start by generating CWI separation with the features of CWI estimates given by equation 5. With the locations of the 50 events, we calculate their true separations δ_t, and create the CWI separation data (separation mean and standard deviation) using the empirical relations $\mu(\widetilde{\delta_t}) = a_1 \frac{a_2\widetilde{\delta_t}^{a_4} + a_3\widetilde{\delta_t}^{a_5}}{a_2\widetilde{\delta_t}^{a_4} + a_3\widetilde{\delta_t}^{a_5} + 1}$, and $\sigma(\widetilde{\delta_t}) = b_1 \frac{b_2\widetilde{\delta_t}^{b_4} + b_3\widetilde{\delta_t}^{b_5}}{b_2\widetilde{\delta_t}^{b_4} + b_3\widetilde{\delta_t}^{b_5} + 1} + c$ (equation 5). The separation data are thus consistent with the known biases and level of uncertainty from the CWI technique.

To implement the location process, initial locations of the 50 events are randomly distributed within a cube of the same size of that of the true locations of the events using `initialize_locations.m`, shown as red triangles in Figure 7a. The spread (the volume in the medium over which the sources extend) of the initial locations are not necessarily similar to that of the true locations, however in most cases doing so can lead to faster convergence to the global minimum of the objective function, and significantly reduce the chance of converging to a local minimum. Hence, when applying the location codes to real data, users are recommended to make an estimation of the spread of the event cluster for initializing the optimization.

The optimization with the given true and initial locations in this example took 27

iterations to converge, with max_iteration set to 300, L_tolerance to 10^{-5}, and no discarded pairs. The estimated locations are shown as solid circles in Figure 7b, where the improvement in event locations from optimization is readily observed by comparing with their initial locations (red triangles in Figure 7a). The optimization does not lead the estimated locations to exactly the true event locations, due to the uncertainty $\sigma(\widetilde{\delta_t})$ added. The average location error is 27m, amounting to 6.4% of δ_{max}, or 5% of λ_d. Figure 8 compares source separations calculated from the relocated event locations (red) to the separation data (blue) used as input to the optimization. Figure 8a shows that although the input separation data deviate significantly from their actual value (dashed line $y = x$) where the true separation is larger than $0.55\lambda_d$, the recovered source separations are only slightly underestimated. It is therefore proved that the location algorithm is able to correct the biases of CWI estimates to a large extent.

As optimization techniques that guarantee converge to the global minimum of a complicated non-linear objective function do not currently exist, it is suggested to implement the optimization multiple times with different random initializations. In order to examine the location results, we illustrate the change of objective function value in the optimization process for all implementations, as shown in Figure 9. The two zoomed panels show details of the start and end of the processes. The 6 implementations start with different objective function values because of different initial locations. The value decreases rapidly for the first 10 iterations following different paths, and then slows down towards the minima. All optimizations converged to the same minimum of 6738, except for the 4th, which was stuck at a local minimum at 6753. For this synthetic example, the true (global) minimum of the objective function is known as the true event locations are known, hence we can conclude that the minimum 6738 found is correct within a small numerical error. However, when applying this technique to real events where the correct minimum is unknown, using this method can add confidence to the result at which most implementations converge. This will be shown in the next part of this subsection where the location codes are applied to New Ollerton data.

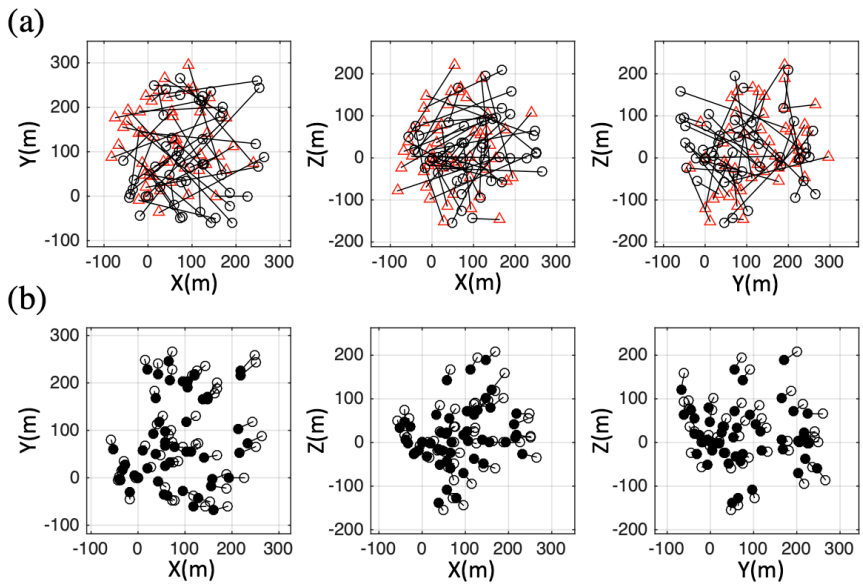

Figure 7: Planar projections of event locations, where axes X, Y and Z point in three orthogonal directions. Panels (a) compare the events' actual locations (circles) and their initial locations (triangles) before optimization, and the black bars show their differences. Panels (b) shows the events' actual locations (hollow circles) and the location results obtained (solid circles), with lines between the hollow and solid circles representing post-optimization location errors.

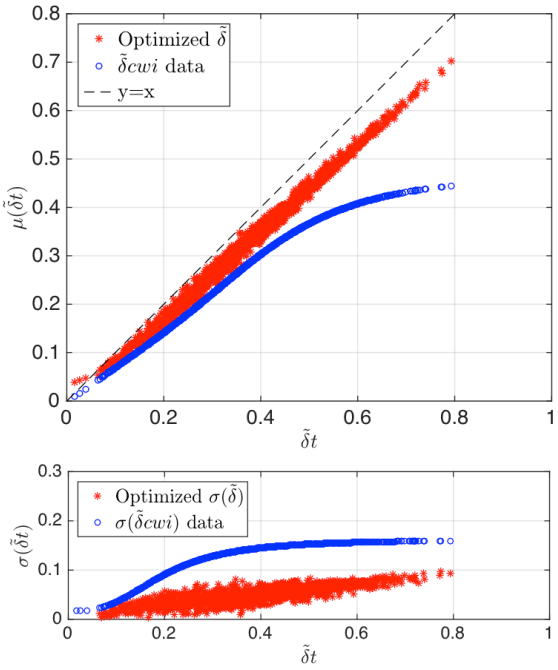

Figure 8: A comparison of input inter-source separations (blue circles) and separations calculated from the location result after optimization (red asterisks). The upper and lower panels show the separation data and their standard deviations, respectively.

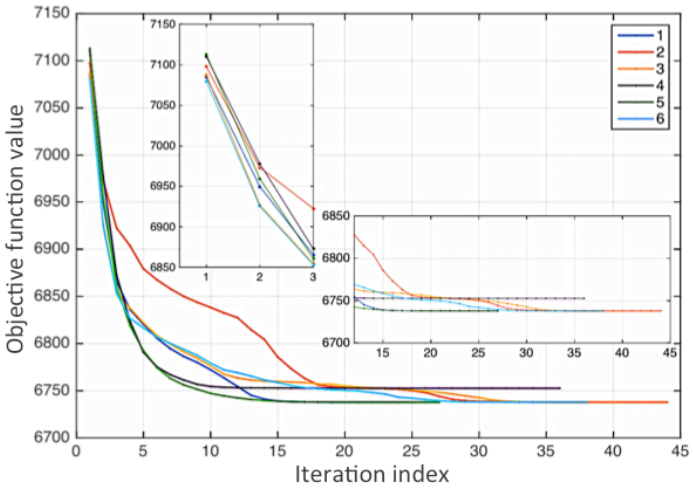

Figure 9: An illustration of the minimization process of each of 6 optimizations from different initializations of random event locations using different colors to indicate each example optimization. The magnified panels show details of how the values of the objective function change with iteration number at the beginning and end of each optimization.

3.3.3 Example with New Ollerton earthquake

With the CWI separation data obtained in 3.2.2, we conduct relative source location for each cluster using data from single station channels (NOLCZ, NOLFE, and NOLFN) and data from all three channels. The followings show the example of estimating source locations of cluster 1 with data from all three channels (Session 3 in `Main_running_script.m`):

```
% Basic parameters
veloc=[4200 2360];
domin_freq=[2.6 2.7 3.2];
domin_wavelength=veloc(2)./domin_freq;
nevent=11;
num_channel=3;
num_pair=(1+(nevent-1))*(nevent-1)/2;
max_iteration=240;
L_tolerance=1e-5;
% Separation data
seps1=load('seps_cluster1_channel1.csv');
seps2=load('seps_cluster1_channel2.csv');
seps3=load('seps_cluster1_channel3.csv');
MU_n=[seps1(:,1) seps2(:,1) seps3(:,1)];
SIGMA_n=[seps1(:,2) seps2(:,2) seps3(:,2)];
select_e_pair
% Initialization
initial_loc=load('../examples/ollerton_earthquakes_example/generated_files/initial_location_cluster1.csv');

% Location
[              optm_loc,              Func_L_add]              =
Source_Location( initial_loc,MU_n,SIGMA_n,...
```

```
domin_wavelength,discarded_pairs,max_iteration,L_tolerance);
% Save location results
xlswrite('location_cluster1_3channels',optm_loc);
```

`discarded_pairs` are selected with script `select_e_pair.m` with criteria that 1) the mean of the source separation of all event pairs used as input is lower than $0.5\delta_d$ because of the known bias of the CWI technique, as suggested in Figure 1(a); and that 2) the standard deviations of all pairs are lower than $0.17\delta_d$, in order to avoid the impact of event pairs whose data uncertainty is larger than the largest that any CWI estimates should have empirically. Users should apply their own criteria to selected data for input, however they are suggested to include at least these two in order to obtain reliable results. The number of pairs that are discarded can also be used as a rough measurement of data quality. In this example, any standard deviations that are smaller than a certain value, conservative_std, are replaced with conservative_std to avoid including data with falsely estimated very small uncertainties.

The initial locations of 11 events were randomly distributed in a cube with a side-length of 80m using function `initialize_locations.m` as:

```
[initial_loc] = initialize_locations([0 80],[0 80],[0 80], ...
    nevent, MU_n);
```

The initial locations created were stored in file `initial_location_cluster1_1.csv`.

The optimization converged to `optm_loc` with 56 iterations, where the value of function L is reduced to 794.4637. We then repeated the location 9 times with different initializations. Figure 10 shows the progress of each implementation, with the horizontal zoomed panel showing details of convergence. All cases converged to the same level, with reasonable numerical errors. This adds to our confidence that the minimum found with different random initializations is the global minimum of function L, and therefore the relative locations of these 11 events are found.

We conduct source location for both clusters with 1) each single channel, and 2) all three channels. The recovered sources separations are consistent among individual channels (red, green, and cyan) with small residuals, and they are very similar to the result obtained using all three channels (blue), as shown in Figure 11a. The location process also corrects for the underestimation bias of the CWI technique, as illustrated in Figure 11b, which compares the recovered separations (red) and the CWI separation data (black) as input of the optimization. Figure 12 shows the location results of cluster 2 using data from single channels and all three channels, projected onto three orthogonal planes. The patterns show a high level of consistency among single channels and multiple channels. Hence, we proved once again that CWI source location technique is able to give reliable relative locations of a cluster of events using only a single recording channel.

It is worth noting that Figure 12 merely shows one way to present these relative locations, and the patterns would be different when projected to other planes. In some cases, the plotted patterns of location results of different initializations or different channels can appear different, but they can be adjusted to look the same with some rotation operations of the cluster. However, with the criteria discussed above and shown with Figure 10 and 11, it is unnecessary to obtained similar projected patterns to assess the consistency of the location results.

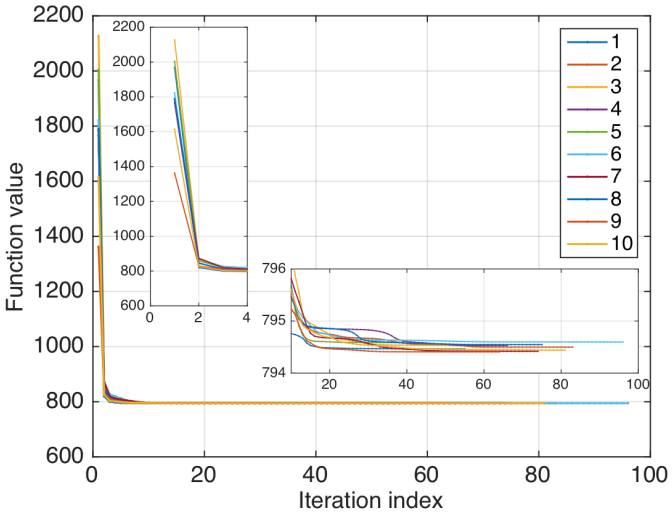

Figure10: An illustration of the minimization process of each optimization from different initializations of random event locations using different colors to indicate each example optimization for cluster 1 using data from all three channels. The magnified panels show details of how the values of the objective function change with iterations at the beginning and end of each optimization.

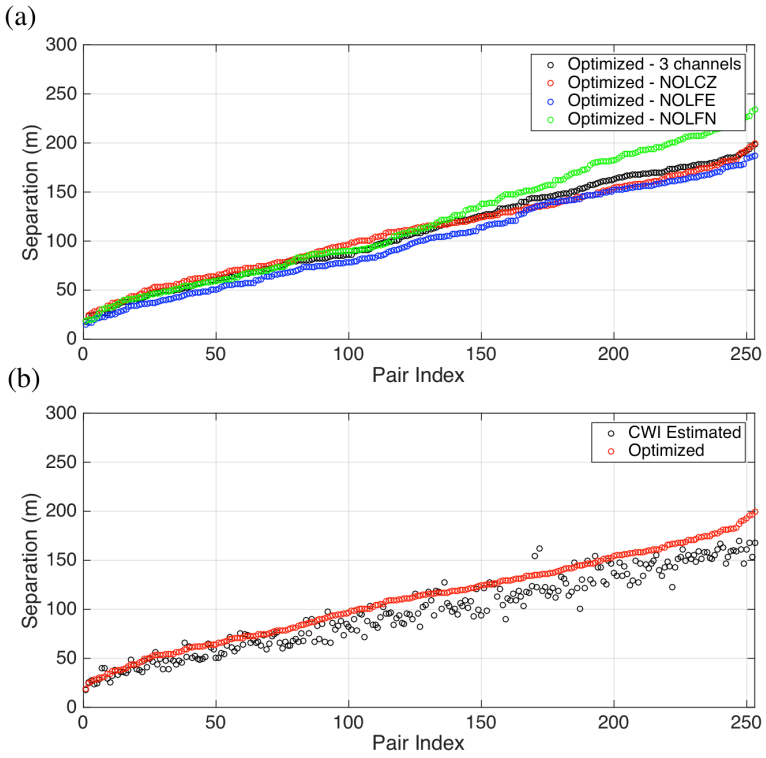

Figure 11: CWI estimates of source separations and their optimized counterparts (the latter calculated from the estimated event locations) of cluster 2. Panel (a) shows the optimized separations using all three channels (black), and using single channels NOLCZ, NOLFE and NOLFN (red, blue, and green). Panel (b) compares the optimized separations of channel NOLCZ (red) with the original CWI separation estimates (black).

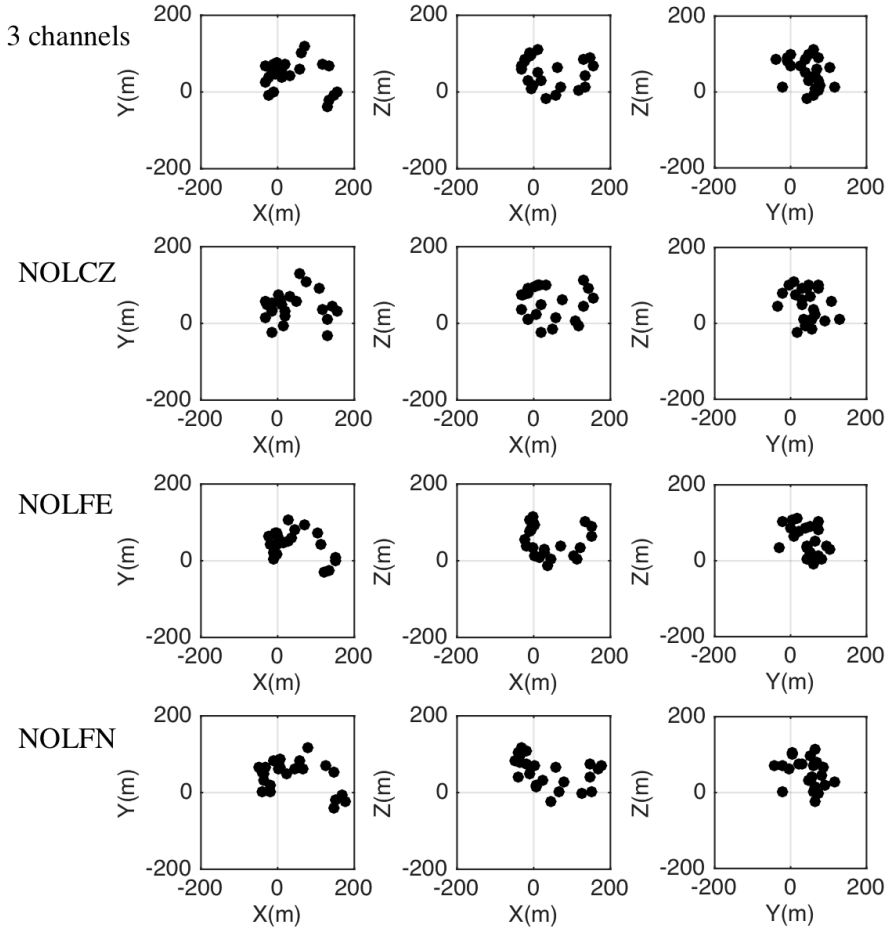

Figure 12: Planar projections of relative event location results of cluster 2, using all three channels (top row), and using single channels NOLCZ, NOLFE, and NOLFN (successive rows). Axes X, Y and Z point in orthogonal directions.

Acknowledgements

We thank Jonathan Singh (University of Edinburgh) for his constructive reviews of this document and code usability. We also thank Brian Baptie (British Geological Survey) for providing the seismic data of the New Ollerton earthquakes used in the real-data example.

References:

Aki, K., 1969, Analysis of seismic coda of local earthquake as scattered waves: Journal of Geophysics Research, **74**, 615-631.

Navon, I. M., D. M. Legler, 1987, Conjugate-Gradient methods for Large-scale minimization in meteorology: Monthly Weather Reviews, **115**, 1479-1502.

Ottemoller, Voss, and Havskov, Seisan: Earthquake Analysis Software for Windows, Solaris and Macosx, 2017, http://seisan.info, accessed 20 December 2017.

Press, W. H., B. P. Flannery, S. A. Teukolsky, and W. T. Vetterling, 1987, Numerical Recipes: The Art of Scientific Computing: Cambridge University Press, U.S.A.

Robinson, D. J., M. Sambridge, and R. Snieder, 2011, A probabilistic approach for estimating the separation between a pair of earthquakes directly from their coda waves: Journal of Geophysical Research, **116**,1-14.

Robinson, D. J., M. Sambridge, R. Snieder, and J. Hauser, 2013, Relocating a Cluster of Earthquakes Using a Single Seismic Station: Bulletin of the Seismological Society of America, **103**, 3057-3072.

Snieder, R., 1999, Imaging and averaging in complex media in diffuse waves in complex media: Springer Netherlands.

Snieder, R., 2006, The theory of coda wave interferometry: Pure and Applied Geophysics, **163**, 455-473.

Snieder R., A. Gret, H. Douma, and J. Scales (2002), Coda wave interferometry for estimating

nonlinear behavior in seismic velocity, Science, **295**, 2253-2255.

Waldhauser, F., and W. L. Ellsworth, 2000, A double-difference earthquake location algorithm: Method and application to the northern Hayward fault, California: Bulletin of the Seismology Socioty of America, **90**, 1353-1368.

Zhao, Y., A. Curtis, B. Baptie, 2017, Locating micro-seismic sources with a single seismometer channel using coda wave interferometry: Geophysics, **82**, A19-A24.

Appendix 1(a) Descriptions of codes and variables for clustering

Crosscorrelation

- `sort_cr.m`:

`sort_cr.m` selects events and station channels using the SAC files according to the given criteria. For each station channel, correlation coefficient of all available event pairs are computed and the maximum correlation coefficient of each pair is found. The maximum correlation coefficient is then averaged over all channels that have recorded the given event pair. The average maximum correlation coefficients are then sorted in a descending order and sorted in `max_cr.xls` or `max_cr.csv` depending on the availability of Excel.

The following inputs are required:

- `data_location`: directory storing the .SAC files
- `MIN_channel`: minimum number of recording channels for an event to be considered
- `MIN_event_per_channel`: minimum number of events a channel records for the channel to be used
- `xcorr_range`: part of waveform (in seconds) to compute crosscorrelation
- `max_time_lag`: expected largest time-lag (in seconds) of waveforms from each other.

The following files are generated:

- `events_channels_selected.txt`: a list of the selected station channels and the selected events
- `max_cr.xls` (or `.csv`): average maximum crosscorrelation coefficients in descending order
- `file_indices.xls` (or `.csv`): the indices of the SAC files of the selected events and station channels.

Whether the generated files are in `.xls` or `.csv` depends on the availability of Excel.

Identify clusters

- `clustering.m`:

`clustering.m` classifies the selected events into clusters according to waveform similarity, which is reflected by maximum crosscorrelation coefficient.

The following inputs are required:

- `data_location`: directory storing the SAC file
- `MIN_corr`: threshold of maximum crosscorrelation coefficient to be considered for clustering
- MIN_E_per_CLUSTER: the minimum number of event for a cluster
- max_cr_pair: the maximum crosscorrelation coefficients used for clustering, can be read from file `max_cr.xls` (or `.csv`)
- `file_indices`: indices of the SAC files of the selected events and station channels, can be read from file `file_indices.xls` (or `.csv`).

The following files are required (generated by `sort_cr.m`):

- `max_cr.xls` (or `.csv`)
- `file_indices.xls` (or `.csv`).

The following files are generated:

- `files_clusteri_channelj.txt`: a list of SAC file names of waveforms of events in cluster i recorded by channel j.

Appendix 1(b) Descriptions of codes and variables for estimating inter-source separations

Pick first arrival of waveforms

- `first_arrival_pick.m`

`first_arrival_pick.m` follows the clustering method used by Ottemoller et al. (2017). It allows users to interactively pick the first arrival of the waveforms listed in a .txt file in three simple steps:

1) On an exemple waveform of events in the cluster recorded by the same station channel (listed in the given .txt file), select a rough (initial) range containing the early arrivals and with a small period before the first arrival.

2) The script then allows the user to pick first arrival of each waveform within the initial searching range selected in setp 1. For each waveform, two plots are generated. The first plot shows the part of waveform inside the initial range, and allows the user to select a narrower range that contains the first arrive and only a few subsequent arrivals of the waveform.

3) For each event, the second plot shows the part of waveform inside the narrow range selected in step 2, which should be narrow enough for the user to location the center of the first arrival with a high accuracy. Pick the first arrival at its center.

If in step 2, the part of waveform selected is found inconvenient for selecting the narrow range and picking the first arrival, end the process by closing any plotted figure and rerun the script.

The following inputs are required:

- `data_location`: directory storing the SAC files
- `txtfilename`: name of the .txt file that lists SAC filenames of waveforms for first arrival picking

The following files are required (generated by `clustering.m`):

- `files_clusteri_channelj.txt`

The following files are generated:

- `first_arrivals_clusteri_channelj.xls` (or `.csv`): sample indices of first arrival of waveforms listed in `files_clusteri_channelj.txt`

Determine parameters for estimating source separations

- `separation_parameters.m`

`separtion_parameters.m` finds the combination of [number, length, start] of time-windows for running `CWI_sep.m`. A 3D std-matrix is generated. Each element is the average standard deviation of inter-source separations over all available pairs in the given cluster recorded by the given station channel(s).

The following inputs are required:

- `coda_start`: start of the searching range of windowing (in seconds)
- `coda_end`: end of the searching range of windowing (in seconds)
- `dl_coda_start`: increment of the start of windowing
- `min_num_win`: minimum number of time-windows allowed
- `min_l_win`: minimum length of time-windows allowed
- `max_num_win_limit`: maximum number of time-windows allowed, regardless the number of time-windows contained within the searching range
- `dl_win`: increment of the length of time-windows to be searched
- `plt_flag`: plot the slice of the 3D std-matrix containing the lowest value?
  - 'y' for plotting
  - 'n' for not plotting
- `save_flag`: save the workspace?
  - 'y' for saving
  - 'n' for not saving

The following inputs are required to call `CWI_seps.m`, for details see code description for `CWI_seps.m`: `veloc`, `source_type`, `search_range`, and `num_interpo_point`.

The following files are required (generated by `first_arrival_pick.m`):

- `first_arrivals_clusteri_channelj.xls (or .csv)`

Appendix I

The following scripts/functions are required:

- `std_maxtrix_3d.m`
- `std_matrix_element.m`
- `CWI_sep.m`

The following files are generated on request (`save_flag` set to '`y`'):

- `seps_param_clusteri_channelj.mat`: stores the workspace after running `separtion_parameters.m` for cluster i channel j.

- `CWI_sep.m`

`CWI_sep.m` is one of the core functions in this package, called by multiple scripts and functions. It applies coda wave interferometry (CWI) to estimate the separation between a pair of sources with similar mechanisms for isotropic sources in a 2D or 3D acoustic medium, or double-couple sources in an elastic medium, assuming both sources are on the same fault plane.

The following inputs are required:

- `S1`, `S2`: waveforms of the event pair
- `time`: time series of waveforms
- `dt`: length of interval between two samples in seconds
- veloc: seismic velocity in the source region

  - for acoustic media veloc is a scaler;

  - for elastic media, veloc is a 1x2 vector consisting of [P-wave-velocity S-wave-velocity]

- `source_type`: ype of source mechanism and propagating medium

  - '`2d`' for isotropic sources in 2D an acoustic medium

  - '`3d`' for isotropic sources in 3D an acoustic medium

  - '`doublecouple`' for double-couple sources in an elastic medium

- `win_length`: length of each time-window in coda
- `win_start`: starting time of windowing
- `win_end`: ending time of windowing

- search_range: number of data to search on each side of the point where time-shift is zero when searching for the maximum of the correlation coefficient (Rmax) for each time-window
- num_interpo_point: number of data to interpolate between adjacent samples when looking for Rmax for each time-window.

The following output are generated:

- source_sep: an array containing estimated source separation from all time-windows
- sep_mean: the mean of the estimated source separations
- sep_std: the standard deviation of the estimated source separations.

- std_maxtrix_3d.m

std_maxtrix_3d.m is called by separation_parameters.m generates a three-dimensional matrix. Each element is the average standard deviation of inter-source separations over all available pairs in the given cluster recorded by the given station channel(s).

The inputs required are provided in separation_parameters.m.

The following scripts/functions are required:

- std_matrix_element.m
- CWI_sep.m

The following output are given:

STD_matrix_3D: a three-dimensional matrix. Each element is the average standard deviation of inter-source separations over all available pairs in the given cluster recorded by the given station channel(s), calculated with one possible combination of [number, length, start] of time-windows

- dimension 1: possible number of time-windows
- dimension 2: possible length of time-windows
- dimension 3: possible starting time of windowing

- `std_matrix_element.m`

`std_matrix_element.m` is called by `std_maxtrix_3d.m`. It calculates elements of `STD_matrix_3D`, with given [number, length, starting time] of time-windows.

The inputs required are provided in `std_maxtrix_3d.m`.

The following scripts/functions are required:

- `CWI_sep.m`

The following output are generated:

- `STD_mean`: an element of `STD_matrix_3D`, for the given parameter combination.

Estimate inter-source separations

- `separations.m`

`separations.m` estimates the inter-source separations of all available event pairs in the given cluster recorded by the given station channel. It generates a `.xls` (or `.csv`) files containing the means and standard deviations of all event pairs from the cluster. For event pairs whose waveforms do not all exist, the results are marked with `-1`.

The following inputs are required:

- `first_arrival_ind`: sample index of the first arrival for all given waveforms
- `txtfilename`: name of the .txt file listing SAC filenames, for which the waveform first arrival to be picked
- `data_location`: directory storing the SAC files.

The following inputs are required to call `CWI_seps.m`, for details see code description for `CWI_seps.m`: `velocity`, `source_type`, `win_length`, `win_start`, `win_end`, `search_range`, and `num_interpo_point`.

The following files are required:

- `files_clusteri_channelj.txt` (generated by `clustering.m`)

- `first_arrivals_clusteri_channelj.xls` (or `.csv`) (generated by `first_arrival_pick.m`).

The following scripts/functions are required:

- `CWI_seps.m`

The following files are generated:

- `seps_clusteri_channelj.xls` (or .csv): stores the means and standard deviations of source separation estimates of all time-windows for each available waveform pairs. The mean and standard deviation is marked with "`-1`" for pairs where at least one waveform does not exist.

  - column 1: means of source separation estimates
  - column 2: standard deviations of source separation estimates.

Appendix 1(c) Descriptions of codes and variables for location

- **`Source_Location.m`**

`Source_Location.m` estimates the relative location of a cluster of events, using inter-source separation data (their mean and standard deviations) estimated with CWI. The location is solved as a minimization problem, where the most probable set of event locations are found where the objective function L attains its minimum.

The following inputs are required:

- `initial_loc`: an N x 3 array storing the initial locations are minimization
  - column 1 - x-coordinates of the initial event locations
  - column 2 - y-coordinates of the initial event locations
  - column 3 - z-coordinates of the initial event locations
- `MU_n`: an $N(N-1)/2 \times K$ array, each column storing the means of the CWI separation estimates for all available event pairs, with N being the number of events, K being the number of channels
- `SIGMA_n`: an $N(N-1)/2 \times K$ array, each column storing the standard deviations of the CWI separation estimates for all available event pairs
- `discarded_pairs`: indices of event pairs to be discarded

  an $0 \times K$ array - no pair to be discarded, with K being the number of channels

  an $n \times 1$ array - single channel case with n pair(s) to be discarded

  an $n \times K$ array - K channle case, with n being the largest number of pairs to be discarded for any individual channel
- `max_iteration`: maximum number of iterations allowed
- `L_tolerance`: a trivial constant, the threshold for the iterations to terminate when the reduction in the value of L is smaller than.

The following outputs are generated:

- optm_loc: an $N \times 3$ array, storing the location results found by optimization
  - column 1 - x-coordinates of the final event locations
  - column 2 - y-coordinates of the final event locations

- column 3 - z-coordinates of the final event locations

- Func_L_add: an $m \times 1$ array, storing the value of L of after each iteration, with m being the number of iterations.

The following scripts/functions are required:

- `line_search.m`
- `gradient.m`
- `ln_joint_likelihood.m`
- `likelihood_individual.m`.

Parameters of the empirical relations (equation 5) between the true separation and the mean and standard deviation of the CWI estimates are given inside function `Source_Location.m`. Here we use the ones derived by Robinson et al. (2011), however, users can change them to those derived from their own experiments.

- **`ln_joint_likelihood.m`**

`ln_joint_likelihood.m` estimates the negative logarithm of the joint likelihood function L for a cluster of events. For each station channel, all available event pairs are considered, except for those instructed to be discarded in the input of the function.

The following inputs are required:

- `X (Y,Z)`: x (y, z)-axis coordinates of the event locations in the cluster
- `domin_wavelength`: dominate wavelength of the propagating waves
- `a_mu1`: parameters of the empirical relation between true separation and the mean of the CWI estimates
- `a_sigma1,c`: parameters of the empirical relation between true separation and the standard deviation of the CWI estimates
- `MU_n`: an $N(N-1)/2 \times K$ array, each column stores the means of the CWI separation estimates for all available event pairs, with N being the number of events, K being the number of channels
- SIGMA_n: an $N(N-1)/2 \times K$ array, each column stores the standard deviations of the CWI separation estimates for all available event pairs
- `discarded_pairs`: indices of event pairs to be discarded

an $0 \times K$ array - no pair to be discarded, with K being the number of channels

an $n \times 1$ array - single channel case with n pair(s) to be discarded

an $n \times K$ array - K channle case, with n being the largest number of pairs to be discarded for any individual channel.

The following outputs are generated:

- `Ln_prob_joint`: negative logarithm of the joint likelihood function for data from single or multiple station channels.

The following scripts/functions are required:

- `likelihood_individual.m`

- **`likelihood_individual.m`**

`likelihood_individual.m` estimates the likelihood function for an individual pair of events.

The following inputs are required:

- `x (y, z)`: x (y, z)-axis coordinates of the location of the two events
- `domin_wavelength`: dominate wavelength of the propagating waves
- `a_mu1`: parameters of the empirical relation between true separation and the mean of the CWI estimates
- `a_sigma1,c`: parameters of the empirical relation between true separation and the standard deviation of the CWI estimates
- `mu_n`: the mean of the CWI separation estimates
- `sigma_n`: the standard deviation of the CWI separation estimates.

The following outputs are generated:

- `prob_indiviudal`: the likelihood function of an individual pair of events.

- **`gradient.m`**

`gradient.m` computes the gradient of L at a given set of event locations

The following inputs are required:

- `Xc (Yc,Zc)`: x (y, z)-axis coordinates of the current event locations

- `domin_wavelength`: dominate wavelength of the propagating waves
- `a_mu1`: parameters of the empirical relation between true separation and the mean of the CWI estimates
- `a_sigma1,c`: parameters of the empirical relation between true separation and the standard deviation of the CWI estimates
- `MU_n`: an $N(N-1)/2 \times K$ array, each column stores the means of the CWI separation estimates for all available event pairs, with N being the number of events, K being the number of channels
- SIGMA_n: an $N(N-1)/2 \times K$ array, each column stores the standard deviations of the CWI separation estimates for all available event pairs
- `discarded_pairs`: indices of event pairs to be discarded

an $0 \times K$ array - no pair to be discarded, with K being the number of channels

an $n \times 1$ array - single channel case with n pair(s) to be discarded

an $n \times K$ array - K channle case, with n being the largest number of pairs to be discarded for any individual channel.

The following outputs are generated:

`gradient`: gradient of L at the given point (`Xc, Yc, Zc`). An $N \times 3$ matrix, with the 1st, 2nd, and 3rd column storing the partial derivatives in terms of x, y and z-coordinates of the event locations.

The following scripts/functions are required:

- `ln_joint_likelihood.m`
- `likelihood_individual.m`.

- **`line_search.m`**

`line_search.m` conducts searches for the minimum of an objective function L in a given direction in three steps:

1) along the given direction, evaluate L in a large range with increments of `delta_lambda_coarse`, and find the (coarse) minimum among these values of L.

2) define a smaller range around the minimum found, evaluate L in the smaller range with increments of `delta_lamba_dense`, and find a new (dense) minimum among these values of L.

3) adjust the dense minimum by fitting a parabola using the minimum point found and two of its adjacent points, and take the vertex of the parabola as the final minimum of L along the given direction.

The following inputs are required:

- `Xc (Yc,Zc)`: x (y, z)-axis coordinates of the current event locations
- `dc`: current searching direction
- `domin_wavelength`: dominate wavelength of the propagating waves
- `min_lambda_coarse`: lower bound of the large (coarse) searching range
- `max_lambda_coarse`: upper bound of the large (coarse) searching range
- `delta_lambda_coarse`: increment of the large (coarse) searching range
- `delta_lambda_dense`: increment of the small (dense) searching range
- `a_mu1`: parameters of the empirical relation between true separation and the mean of the CWI estimates
- `a_sigma1,c`: parameters of the empirical relation between true separation and the standard deviation of the CWI estimates
- `MU_n`: an $N(N-1)/2 \times K$ array, each column stores the means of the CWI separation estimates for all available event pairs, with N being the number of events, K being the number of channels
- SIGMA_n: an $N(N-1)/2 \times K$ array, each column stores the standard deviations of the CWI separation estimates for all available event pairs
- `discarded_pairs`: indices of event pairs to be discarded

  an $0 \times K$ array - no pair to be discarded, with K being the number of channels

  an $n \times 1$ array - single channel case with n pair(s) to be discarded

  an $n \times K$ array - K channle case, with n being the largest number of pairs to be discarded for any individual channel.

The following outputs are generated:

lambda_step: step length the current iteration should take to attain the minimum in the given searching direction

fvalue_new: value of L at the minimum found in the given searching direction.

The following scripts/functions are needed:

- `ln_joint_likelihood.m`
- `likelihood_individual.m`.

- **`initialize_locations.m`**

`initialize_locations.m` generates a set of initial locations for the minimization problem solved by `Source_Location.m`. It first creates a set of locations for the given event number, uniformly distributing in the given range. It then reorders the created events to ensure the least square residuals of inter-source separations (residuals being the difference in separation of each event pair between that calculated from the created initial locations and that estimated with CWI from seismic data).

The following inputs are required:

- `x_range (y_range,z_range)`: an 1×2 array, storing the range for x (y, z) -coordinates
- `num_event`: number of events in the given cluster
- `MU_n`: an $N(N-1)/2 \times 1$ array, storing the means of the CWI separation estimates for all available event pairs, averaged over all channels if data from multiple channels are used, with N being the number of events.

The following outputs are generated:

- initial_position: an $N \times 3$ array, storing the locations to be used as initialization of the minimization problem
  - column 1 - x-coordinates
  - column 2 - y-coordinates
  - column 3 - z-coordinates

- **`rotate_cluster.m`**

`rotate_cluster.m` rotates a cluster of points about its center in two orthogonal

directions in the 3D space by given angles.

The following inputs are required:

- `P0`: an $n \times 3$ array, storing the original point coordinates, where n is the number of events.
- `alpha`: angle by which the cluster rotates anticlockwise when observed from above about a line passing the cluster center and parallel to z-axis.
- `theta`: angle by which the cluster rotates anticlockwise about a line passing the cluster center and parallel to x-axis.

The following outputs are generated:

- `P_rotate:` an $n \times 3$ array, storing the rotated point coordinates,where n is the number of events.

- **`coordinate_modify.m`**

`coordinate_modify.m` adjusts the coordinate system of event cluster to remove the ambiguity, following four steps (Robinson et al., 2013):

1) Move the cluster so that event 1 is at the origin, i.e. $e_1 = (0,0,0)$;

2) Rotate the cluster so that event 2 lies on positive x-axis, i.e. $e_2 = (x2, 0,0)$, where $x2 > 0$;

3) Rotate the cluster so that event 3 lies in x-y plane, and the y-coordinate is positive, i.e. $e_3 = (x3, y3,0)$, where $y3 > 0$;

4) Make sure z-coordinate of event 4 is positive, i.e. $e_4 = (x4, y4, z4)$, where $z4 > 0$.

The following inputs are required:

- `X (Y,Z):` $N \times 1$ array, storing the x (y,z)-coordinate of event locations to be adjusted
- `num_event`: number of events in the cluster

The following outputs are generated:

- `X4 (Y4,Z4)`: $N \times 1$ array, storing the x (y,z)-coordinate of the adjusted event locations

Coda Wave Interferometry for Accurate Velocity Monitoring and Acoustic Source Location in Experimental Rock Physics

J. Singh[1], A. Curtis[1,2], Y. Zhao[1], A. Cartwright-Taylor[1], I. Main[1]

[1]University of Edinburgh, School of GeoSciences, Edinburgh, UK

[2]ETH Zurich, Switzerland

Key Points:

- Conventional laboratory methods for measuring changes in seismic velocity and source locations are inaccurate
- Coda Wave Interferometry provides far greater accuracy, even with high levels of background noise
- Method to estimate both P and S velocity changes from coda wave interferometry

Corresponding author: Jonathan Singh, jonathan.singh@ed.ac.uk

Abstract

Estimating the bulk seismic velocity of materials is of great importance in many applications in geoscience, material science and engineering. It is necessary for the interpretation of industrial seismic and earthquake seismological data, for monitoring structural materials, and as an input to rock physics models that predict other parameters of interest. Bulk velocity is commonly estimated in laboratories from ultrasonic first-arrival times between a source and a receiver, assuming a linear ray path. In heterogeneous media, that method provides biased estimates of the bulk velocity, and of derived parameters such as velocity changes over time or locations of acoustic emissions. We show that Coda Wave Interferometry (CWI) characterizes changes in the bulk properties of a scattering medium far more effectively on the scale of laboratory rock samples. Compared to conventional methods, CWI provides significant improvements in both accuracy and precision of estimates of velocity changes, and of acoustic source separation distances within a sample. The method remains more accurate in the presence of substantial background noise, and when source location and velocity perturbations occur simultaneously. We demonstrate that CWI allows relative locations of a cluster of acoustic emissions to be estimated using a single sensor. We also provide a method to use CWI to infer changes in both P and S wave velocities individually. These results represent a significant improvement in our ability to characterize the evolution of properties of media, and of acoustic emissions in laboratory experiments, for a variety of applications in geoscience and engineering.

1 Introduction

Experimental studies of wave propagation in rock cores are performed across many disciplines within geosciences: to develop relationships between changes in external conditions and seismic properties such as seismic velocity (Wang, 2001), anisotropy (Christensen, 1966; Sayers & Kachanov, 1995) and attenuation (Sams, Neep, Worthington, & King, 1997; Toksöz, Johnston, & Timur, 1979), and to examine the process of rock fracturing (Pyrak-Nolte, Myer, & Cook, 1990) and acoustic emissions (Lockner, 1993; Lockner, Byerlee, Kuksenko, Ponomarev, & Sidorin, 1992). Established relationships between seismic attributes and underlying rock physical properties are particularly important for monitoring purposes in the hydrocarbon industry and in subsurface CO_2 storage projects, notably for relating effective stress changes during subsurface injection or production to changes that maybe observed in the seismic velocity (Arts et al., 2004; Brown, 2002; Guil-

bot & Smith, 2002; Herwanger & Horne, 2009; Stork, Allmark, Curtis, Kendall, & White, 2018). It is therefore of great importance that models developed from laboratory experiments accurately represent the response of in-situ rocks.

Commonly used methods for measuring changes in the velocity of a medium involve picking of first-break arrival times of seismic waves traveling between a fixed source and receiver pair. The velocity of the medium is then estimated using the known straight-line distance between the source and receiver. There are obvious problems associated with such methods: 1) the measured velocity is not sensitive to the bulk properties of a medium, but rather to properties along a very specific (fastest) ray path between the source and receiver, resulting in a bias towards higher velocities. 2) The path followed by the first-arriving energy is unlikely to be straight, so that velocity estimates made using the straight-line path are biased towards lower values. 3) Biases in points 1 and 2 are generally unrelated so are not expected to cancel out. 4) The effects of small perturbations in the medium, not located along the specific source-receiver path cannot be detected. 5) Such errors in velocity estimation are carried forward to any subsequent calculations (e.g., in locating acoustic source position with unrepresentative velocity estimates, source locations will also be biased).

Coda waves are the multiply-scattered waves that are recorded towards the tail of a seismogram. Recordings of coda waves are far more sensitive than first arrivals to changes in pore-pressure, fracture density and temperature (Snieder, Grêt, Douma, & Scales, 2002; Vlastos et al., 2006; Vlastos, Liu, Main, & Narteau, 2007), due to the fact that coda waves follow much longer and more complex paths, eventually sampling the entire medium, and sampling any sub-volume of the medium multiple times. There are also established methods called coda wave interferometry (CWI) that estimate changing properties of the medium, or changes in the locations of sources or receivers (Snieder, 2006). There have been several field and laboratory applications of CWI to date, including the monitoring of velocity changes in ice sheets (James, Knox, Abbott, & Screaton, 2017; Mordret, Mikesell, Harig, Lipovsky, & Prieto, 2016), concrete (Larose & Hall, 2009; Planès & Larose, 2013), mining environments (Grêt, Snieder, & Özbay, 2006), and volcanic regions (Sens-Schönfelder & Wegler, 2006). CWI has also been used to study earthquake focal mechanisms (D. Robinson, Snieder, & Sambridge, 2007), earthquake separation (D. Robinson, Sambridge, & Snieder, 2011; Snieder & Vrijlandt, 2005), and source network locations of induced microseismic events (Zhao & Curtis, 2018; Zhao, Curtis, & Baptie, 2017).

In this paper we test the hypothesis that Coda Wave Interferometry (CWI) can provide an improvement in accuracy and precision when inferring and quantifying the changes in bulk velocity and relative source locations in laboratory settings. The method takes advantage of the multiple sampling of a medium's properties by the multiply-scattered coda waves, as opposed to sampling along a single ray path as in standard methods. Thus CWI could provide more representative measures of bulk properties. Accordingly, we test CWI against commonly used methods in numerical and experimental core-scale examples.

In what follows we first outline the theory of Coda Wave Interferometry and how it can be used in an experimental setting. Then we examine multiple samples of varying rock type and heterogeneity using both numerical simulations and laboratory experiments, where changes in source location and velocity are estimated using both CWI and standard methods. We show how changes in source position and velocity can be jointly estimated when both perturbations occur simultaneously. We then demonstrate an optimization algorithm for estimating the relative locations of sources within a cluster, given the source separations estimated from CWI. Following this, we test the sensitivity of CWI as well as conventional methods to increasing contamination of noise. In all cases CWI is shown to out-perform conventional methods.

Accompanying this manuscript, we provide a well-commented set of MATLAB functions for implementing the CWI method to estimate velocity changes, and for the joint estimation of velocity change and source separation. These codes use a form of CWI that estimates changes relative to a moving reference seismogram, which is particularly important for longer deformation experiments in which scattering paths may change significantly, which contravenes the assumptions of standard CWI theory. Together with the suite of CWI codes made available by Zhao and Curtis (2018) this allows all techniques used in this paper to be implemented.

2 Coda Wave Interferometry

CWI allows small changes in velocity, the displacement of source or receiver locations, or movement of scatterers to be monitored (Sens-Schönfelder & Wegler, 2006; Snieder, 2006; Snieder et al., 2002). These different perturbations and their effect on recorded signals are illustrated in Figure 1. First we consider the effect of a velocity perturbation

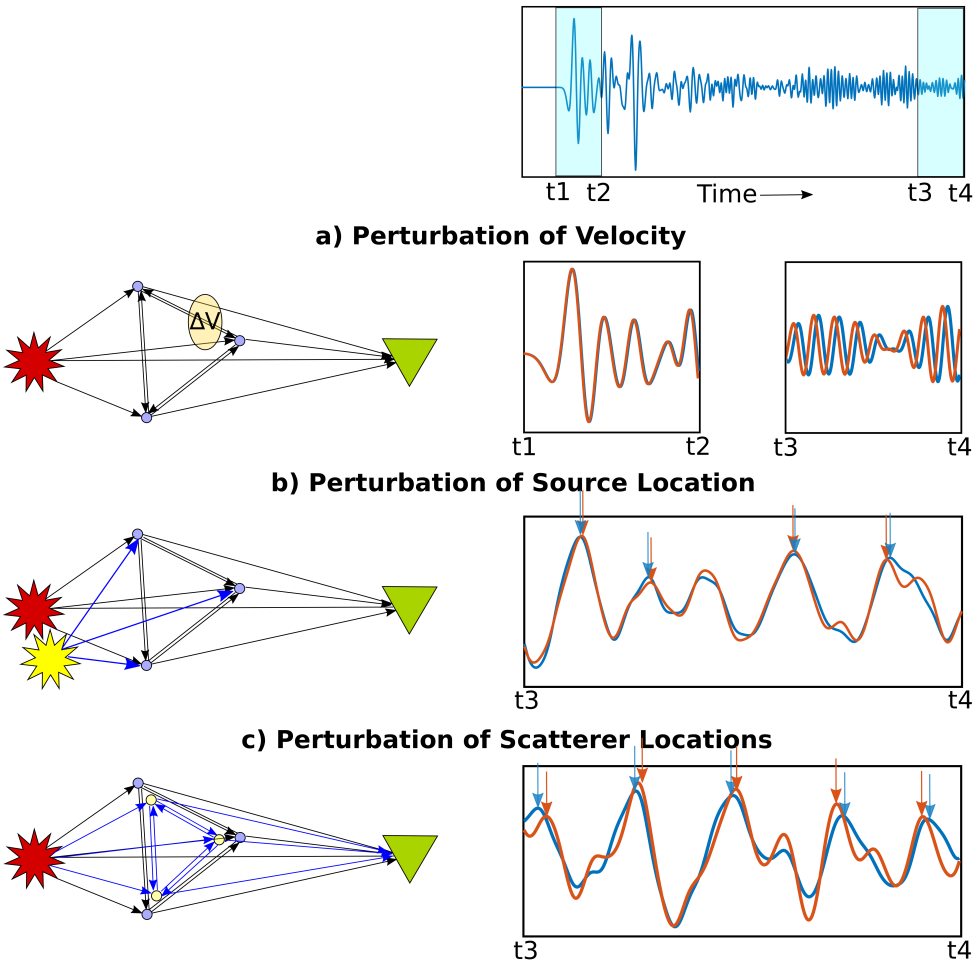

Figure 1. Illustrations of different perturbation types and their effects on coda waves. The cartoons (left) represent a scattering medium, with a source (star), receiver (triangle), and point scatterers (circles). Ray paths between the source and receiver, including multiple reverberations, are represented as black arrows. A velocity perturbation (a) is represented as a yellow ellipse, which has a velocity different to the background medium. New ray paths that are introduced due to source location (b) and scatterer location (c) perturbations are represented as blue arrows. Example recorded signals (right) at early (t1,t2) and late (t3,t4) time windows for each perturbation type are shown before and after each perturbation takes place (blue and red, respectively). Differences in travel times of arriving energy for b) and c) are highlighted with vertical arrows.

(ΔV in Figure 1a), where the direct arriving wave between a source and receiver would only sample the perturbation once (or not at all), whereas the multiply reflected waves sample the perturbation many times. Therefore the change in arrival times for later arriving waves (t3,t4) is much larger than for the first arrival (t1,t2). The second perturbation type is a displacement of the source or receiver location (source displacement in Figure 1b): in this case, the difference in ray paths before and after the perturbation is the path between the source and the first scattering point (blue arrows in Figure 1b). Paths would be both shortened and lengthened depending on the location of the first scatterer, which is reflected by the advancement and retardation of peaks highlighted by red and blue arrows. The extent to which these travel times are perturbed (their variance) is directly proportional to the (small) displacement of the source. The third perturbation type is the displacement of all scattering points (yellow circles in Figure 1c): in this case, all paths between scattering points are perturbed (both shortened and lengthened) and similarly to the previous case, the statistics of travel time perturbations are related to the displacement of scattering points. All three perturbation types can be monitored by using a cross correlation of the unperturbed (u_{unp}) and perturbed (u_{per}) waveforms - the waveforms from the source recorded by the receiver before and after the change or displacement takes place.

One method to estimate the change in velocity is known as trace stretching (Sens-Schönfelder & Wegler, 2006), where the perturbed waveform is assumed to be a time-stretched version of a reference waveform; this follows if one assumes that a velocity perturbation is uniform across the entire medium, so all arriving energy is perturbed at the same temporal rate. We stretch the time axis of the perturbed signal by a range of stretching factors (ϵ) and compute the correlation coefficient R between $u_{unp}(t)$ and the stretched version of the perturbed waveform $u_{per}(t[1+\epsilon])$ over a given time window (t_1, t_2):

$$R^{(t_1,t_2)}(\epsilon) = \frac{\int_{t_1}^{t_2} u_{unp}(t) u_{per}(t[1+\epsilon])dt}{\sqrt{\int_{t_1}^{t_2} u_{unp}^2(t)dt \int_{t_1}^{t_2} u_{per}^2(t[1+\epsilon])dt'}} \quad (1)$$

The optimum stretching factor ϵ_{max} that maximizes the correlation coefficient (for which $R = R_{max}$), is related to the ratio of the change in velocity ΔV to the original velocity V) by

$$\epsilon_{max} = -\frac{\Delta V}{V} \quad (2)$$

(Sens-Schönfelder & Wegler, 2006). That method also assumes that the velocity changes are small to avoid cycle skipping in the calculation of R in equation 1. In cases where

the medium changes significantly, such as during material deformation where new scattering paths are introduced due to fracturing, it may not be appropriate to use a constant reference trace (u_{unp}) for all recorded waveforms during deformation. We propose the use of a moving reference trace, where the optimum stretching factor from the initial reference trace (u_0) to any other recorded waveform during deformation (u_n) can be calculated as

$$\epsilon_{u_0 u_n} = \epsilon_{u_0 u_s} + \epsilon_{u_s u_n} \tag{3}$$

where $s = k\lfloor n/k \rfloor$, n is the trace number, k is the user-selected step size of the moving reference trace, and $\lfloor \ldots \rfloor$ denotes a floor function, which outputs the greatest integer less than or equal to the input. Accompanying this manuscript are a suite of MATLAB functions for implementing the moving-reference stretching CWI method. Snieder (2002) derived the relationship between the inferred medium velocity change from CWI, and changes in P-wave and S-wave velocities:

$$\frac{\Delta V}{V} = \frac{\beta^3}{2\alpha^3 + \beta^3}\frac{\Delta \alpha}{\alpha} + \frac{2\alpha^3}{2\alpha^3 + \beta^3}\frac{\Delta \beta}{\beta} \tag{4}$$

where α and β are the velocities of P and S waves, respectively. In a Poisson medium where $\alpha = \sqrt{3}\beta$, if either or both of the P or S wave velocity changes then the relation simplifies to

$$\frac{\Delta V}{V} = 0.09\frac{\Delta \alpha}{\alpha} + 0.91\frac{\Delta \beta}{\beta} \tag{5}$$

and if α and β change such that the Poisson medium is preserved then

$$\frac{\Delta V}{V} = \frac{\Delta \alpha}{\alpha} = \frac{\Delta \beta}{\beta} \tag{6}$$

The strengths of the CWI technique lie in the ability to resolve very small changes in velocity compared to standard methods. If we take the sampling interval of a recorded signal to be dt and the duration of the signal to be t_{max}, and make the conservative assumption that one sample interval is the smallest resolvable time difference between waveforms in the two recordings, then the maximum resolution of CWI (the smallest resolvable change in velocity that can be measured) is

$$\left[\frac{\Delta V}{V}\right]_{min} = \frac{dt}{t_{max}} \tag{7}$$

The maximum resolution for measuring $\Delta V/V$ from the standard first-break method would be

$$\left[\frac{\Delta V}{V}\right]_{min} = \frac{dt}{(t_0 + dt)} \tag{8}$$

where t_0 is the first-break arrival time. Both equations 7 and 8 assume no background noise and hence no uncertainty in the recorded waveforms. Inserting typical values for laboratory core scale measurements, such as those used in the experiments in the following section (sampling interval = 0.04μs, signal duration = $0.64m$s, and arrival time = 65μs), the smallest perturbations that can theoretically be detected are 0.00625% for CWI and 0.062% for the standard first break method. Hence, CWI offers an order of magnitude improvement in precision in the absence of noise. The standard method is also much more sensitive to noise in the data due to the difficulty of measuring the small signal amplitude in the first break; hence intuitively we would expect to require larger perturbations to occur for the *change* to be resolved above the noise (as shown below). The CWI method computes the cross-correlation function using many more data points, making it less susceptible to the effects of noise. We test this hypothesis in the experiments outlined in section 3.3.

Another advantage of using CWI is that it allows a joint estimate of both a velocity perturbation and the displacement r of the source/receiver location to be made from a single receiver. This is because velocity perturbation information is retrieved from the consistent phase information along the waveforms, whereas the source or receiver separation is related to the variance of inconsistent phase perturbations and hence to the maximum value of the cross correlation value (R_{max}) in equation 1 (Figure 1). Snieder (2006) derives the relationship between the maximum cross-correlation and the variance of the travel time perturbation (σ_τ^2) as

$$R_{max} = 1 - \frac{1}{2}\bar{\omega}^2\sigma_\tau^2 \tag{9}$$

where $\bar{\omega}^2$ is the dominant mean squared frequency in the recorded waveform. When a source or receiver is displaced by distance r, one can estimate separation r from the variance of the travel time perturbation

$$\sigma_\tau^2 = \frac{(\frac{6}{\alpha^8} + \frac{7}{\beta^8})}{7(\frac{2}{\alpha^6} + \frac{3}{\beta^6})} r^2 \tag{10}$$

where α and β are estimates of the representative P- and S-wave velocities of the medium. In a two-dimensional acoustic medium this relationship simplifies to:

$$\sigma_\tau^2 = \frac{1}{2\alpha^2} r^2. \tag{11}$$

To summarize, the main advantages of using CWI in an experimental setting are that: 1) CWI is more representative of changes in the bulk properties of a medium be-

cause coda waves sample the entire medium. 2) Coda waves sample the same area multiple times, so CWI is capable of resolving smaller changes in the medium giving a theoretical order of magnitude increase in precision for typical laboratory experiments. 3) CWI is generally less susceptible to the presence of noise as it uses many more data points at higher amplitude, providing more robust estimates. 4) CWI allows for the calculation of source separation between nearby events from a single receiver, even in cases where velocity changes occur simultaneously, as the two estimates utilize different measurements extracted from the correlation function in equation 1.

3 Results

3.1 Conventional Methods for Estimating Velocity and Source Locations: Synthetic Tests

Rock cores typically used for geomechanics and rock physics experiments are on the scale of 3 mm to 100 mm in diameter, and seismic wave frequencies studied are on the order of kHz - MHz. At these frequencies most rock samples act as strongly scattering media, where most recorded waves take very complex, long paths and experience multiple reflections, diffractions and reflections (Sato, Fehler, & Maeda, 2012). The complex nature of wave propagation through highly scattering media, such as the Tivoli Travertine sample shown in Figure 2, can be studied using methods of digital rock physics (Madonna, Almqvist, & Saenger, 2012). First a reconstructed micro-tomography (μCT) cross-section is segmented into appropriate mineral and pore phases, and converted into velocity and density models (wave physics parameters used for different phases are shown in Table 1). Using finite difference methods (Moczo, Robertsson, & Eisner, 2007), wave propagation through the medium can be simulated so that full waveforms can be generated, as though they have been recorded at any point within the medium. These methods are increasingly used for estimating the acoustic or elastic properties of rocks based on μCT images (Saenger, Madonna, Osorno, Uribe, & Steeb, 2014; Saxena & Mavko, 2016; Sell et al., 2016).

We simulate wave propagation through three different digital rock samples: Tivoli Travertine, Westerly Granite and Copp-Crag Sandstone. These rock types have been selected to represent a range of types of heterogeneity, where Tivoli Travertine has high porosity with complex pore shapes and pore size distribution, Copp-Crag is a relatively

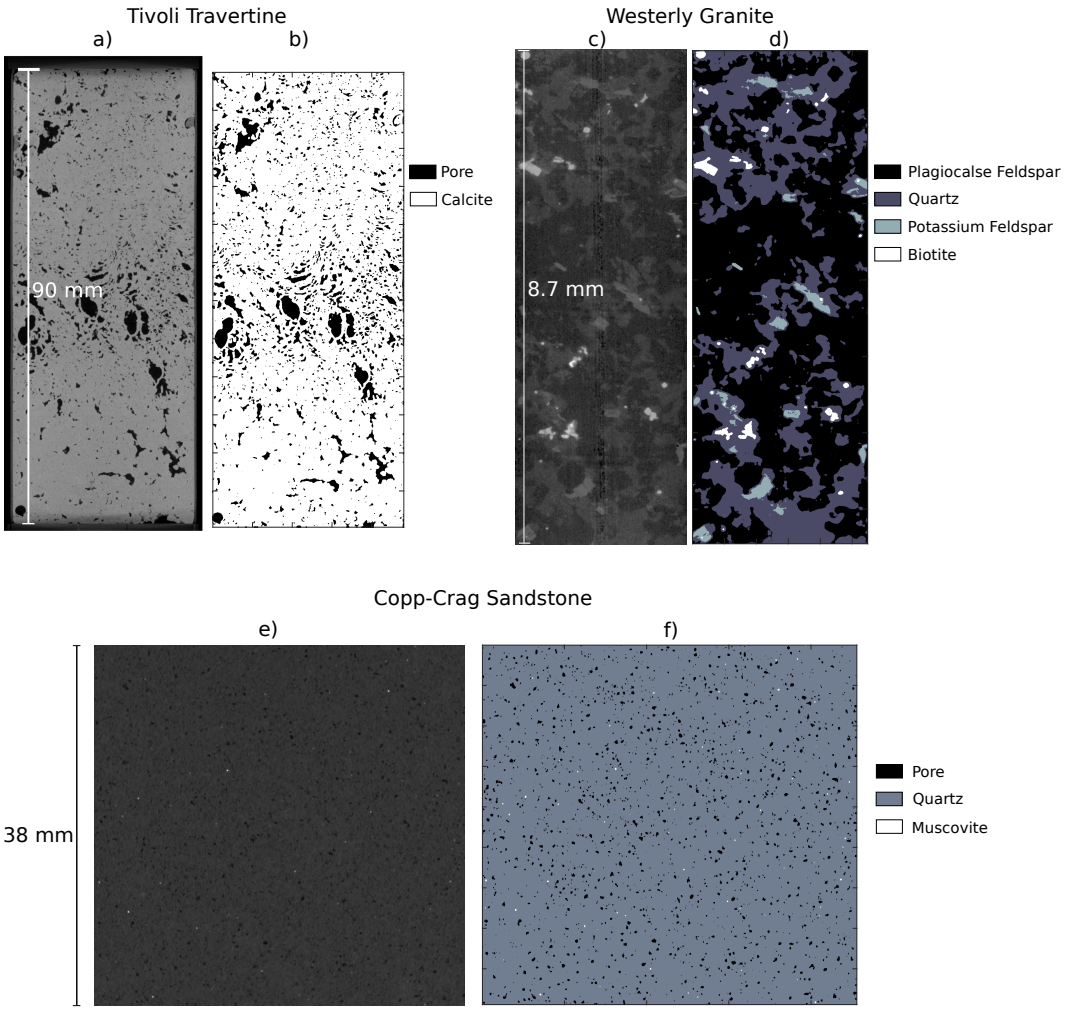

223 **Figure 2.** Set of X-ray μCT slices (left images) and equivalent models of segmented phases
224 (right images) for three rock cores with varying heterogeneity and rock type: a) and b) Tivoli
225 Travertine, c) and d) Westerly Granite, e) and f) Copp-Crag Sandstone. The properties assigned
226 to each material phase for wavefield simulation can be found in Table 1.

Table 1. Parameters used for finite difference wavefield simulation through the samples shown in Figure 2. Values are from Mavko et al. (2009).

Phase	**Density (kg/m^3)**	**Velocity (m/s)**
Pore Fluid	1000	1500
Calcite	2710	6500
Plagioclase	2620	6500
Quartz	2650	5800
Potassium Feldspar	2560	6300
Biotite	3090	5260
Muscovite	2790	6460

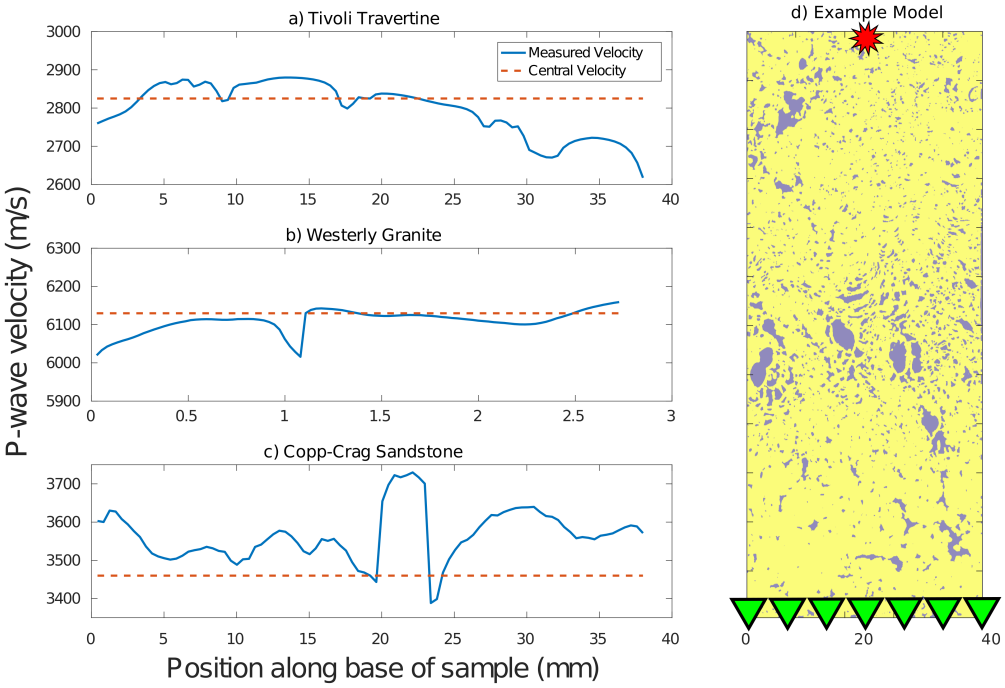

Figure 3. Estimated seismic velocity obtained from simulated waveforms through a μCT digital rock sample in a model shown (d) for the Tivoli Travertine. The source (star) is fixed at the top and the receivers (triangles) are distributed along the bottom. The blue curve shows velocity estimates made using first-break arrival times and straight-line source-to-receiver distances as a function of receiver location. The dashed red line represents the conventional estimate of velocity using a single receiver at the center of the core. Results are for a) Tivoli Travertine, b) Westerly Granite, and c) Copp-Crag Sandstone.

homogeneous sandstone with more uniform pore shapes and pore size distribution, and Westerly Granite is the most homogeneous and exhibits little porosity. The μCT slices and corresponding models of segmented phases for each rock type are shown in Figure 2 and are converted to wave physics models using the parameters stated in Table 1. First, we simulate a single source located at the top of the samples and a row of receivers along the bottom (Figure 3d). The resulting velocities estimated at each receiver from manually picked first arrivals assuming straight ray paths are shown in Figure 3a, b and c. For the three samples, the estimated velocities at each receiver show considerable variation depending only on where the receiver is located. This response is concerning as in many cases a single receiver and hence a simple, non-representative velocity may be used to characterize an entire sample - from a receiver at the center of the core in conventional experimental configurations (shown as dashed red lines in Figure 3). To explore this variation further, a similar experiment was carried out on the three velocity models in which eikonal ray tracing was implemented from Margrave (2007). This gives an estimated arrival time ($t[\boldsymbol{x}]$) for every point $\boldsymbol{x}$ in the model for a fixed source location (in this case the source is located at the center-top of each sample). Using these arrival times, we can imagine a receiver placed at every point within and on the boundary of a model, and an estimate of the velocity for that source-to-receiver path can be calculated using the standard travel time method. Figure 4 shows the calculated velocity $v[\boldsymbol{x}]$ for all model points $\boldsymbol{x}$ in each sample, again showing that measured velocity may be strongly dependent on source and/or receiver locations. We see that for Tivoli Travetine (Figure 4a) the variation in velocity estimates are greater than for Copp-Crag Sandstone (Figure 4c), and that Westerly Granite (Figure 4b) has the smoothest image, reflecting the smallest variation in estimated velocity $v[\boldsymbol{x}]$. In all cases the longer the source-to-receiver distance, the more stable is the result.

There are therefore several concerning implications of characterizing a medium with velocities calculated from standard methods: 1) a measured cross-core velocity is not sensitive to the bulk properties of a medium, but rather to the velocities along a specific ray path between the source and receiver, as demonstrated by the variation of estimated velocity with receiver position in Figures 3 and 4. Therefore, 2) the effects of small perturbations in a medium that are not located on the specific source-to-receiver path will not be detectable using these methods.

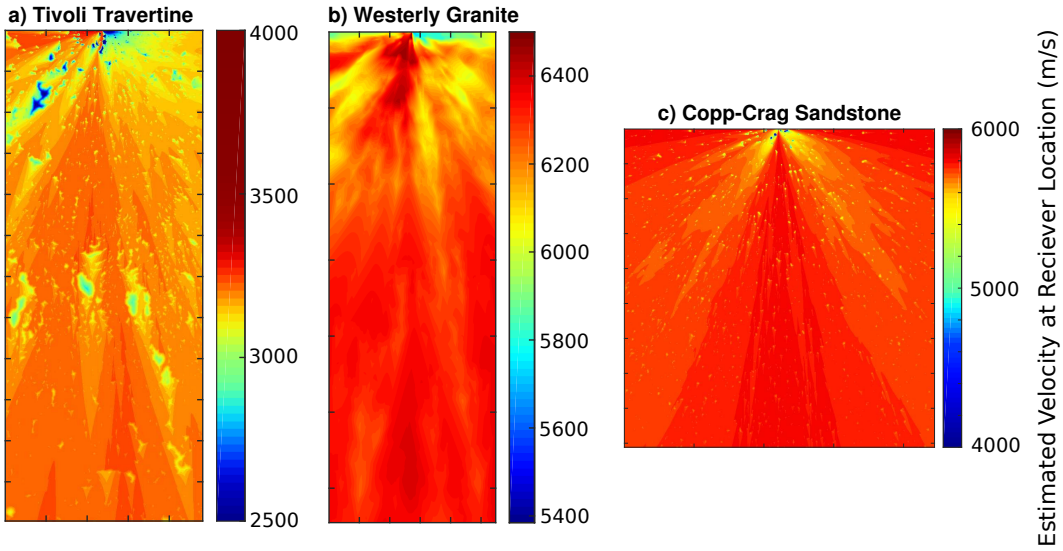

Figure 4. The estimated velocity between a constant source location (centre of the top of the sample) and every position in the model $\boldsymbol{x}$. To emulate estimates from the standard method, an eikonal ray tracing method from Margrave (2007) was used to calculate travel times while a straight ray path was used to calculate velocity $v[\boldsymbol{x}]$. Results are for a) Tivoli Travertine, b) Westerly Granite, and c) Copp-Crag Sandstone.

The assumption that a medium is represented by a single constant velocity also introduces errors into subsequent calculations, such as in the estimation of source locations. This effect can be examined using a further experiment. We simulate a series of regularly spaced sources placed on a rectilinear grid throughout each of the three media, representing acoustic emissions occurring throughout the sample. We measure the arrival times for each source (S) at a set of receivers (i) as t_S^i using the first-break method, and use a single measured velocity through each sample (V_{med}), which is assumed to be representative of the entire medium. In our implementation the exact value of this velocity does not affect source locations - it only affects the estimates of the source origin time (t_0). In this particular case, it is therefore not inaccuracy in the velocity estimate, but rather the very assumption that there is a single representative medium velocity that will affect locations. We estimate source locations (S_{est}) using trilateration (actually multilateration), by implementing a grid-search through all model positions ($\boldsymbol{x}$) and through a range of source origin times (t_0), to find values of $\boldsymbol{x}$, and t_0 that minimize the objec-

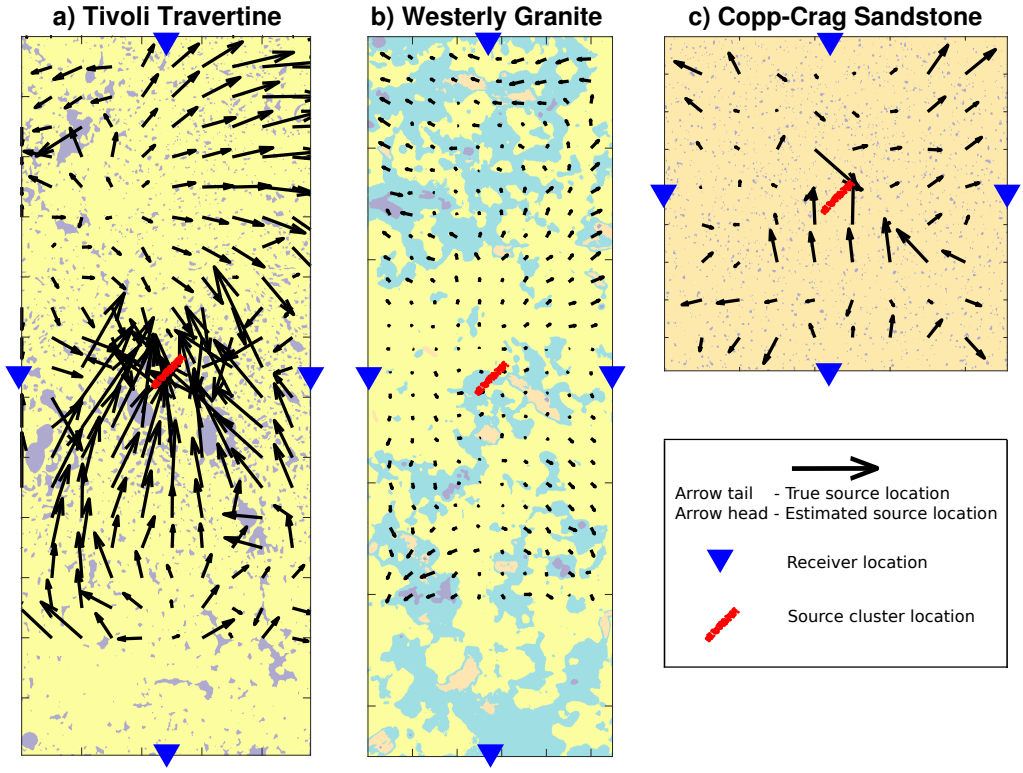

Figure 5. The resulting systematic errors in source location, represented as black arrows, using standard phase picking methods that assume a single representative velocity for each sample, for a) Tivoli Travertine, b) Westerly Granite, and c) Copp-Crag Sandstone. The base of each arrow is located at the true source positions (S_j), and estimated locations (S_{est}) are displayed at arrow tips. The red points represent the source cluster used for the source relocation experiment, with results shown in Figure 7.

tive function

$$\varphi(\boldsymbol{x}, t_0) = \sum_{i=1}^{N^i} [V_{med} \times (t_S^i - t_0) - (i - \boldsymbol{x})] \tag{12}$$

The estimated source location S_{est} is the location $\boldsymbol{x}$ that minimizes φ. Figure 5 displays the error in estimated source locations S_{est} (arrowheads) compared to true locations (arrow tails) for each of the three samples. For the majority of sources in Tivoli Travertine (5a) and Copp-Crag Sandstone (5c), the resulting systematic error in source location is significant in both amplitude and direction. In Westerly Granite (5b), errors have much smaller amplitudes. It is therefore clear that in more heterogeneous media, a single velocity is not appropriate and estimated source locations in many areas are highly inaccurate when estimated using conventional methods of trilateration.

3.2 CWI and Conventional Estimates of Changes in Velocity and Source Location: Synthetic Tests

We now test CWI against conventional methods for measuring a change in the bulk velocity of a medium, using finite difference numerical wavefield simulations through the three μCT slices in Figure 2. Two slightly different velocity models for each sample are generated: one is the unperturbed medium and the other has a perturbed velocity equivalent to a -1% velocity change throughout the medium. The simulated signals are obtained from an array of receiver positions along the bottom of the sample as used in Figure 3. The change in velocity between each pair of models are estimated from these signals by CWI (using equation 1) and using the conventional method of phase-picking of first-break arrivals and assuming straight rays. Figure 6 compares the estimates for each sample. For all samples, CWI gives more accurate (closer to the true value in the model) and more precise (lower standard deviation) estimates of $\Delta V/V$, and shows significantly less variation between different receiver locations when compared to the first-break method. This effect is clearly dependent on the complexity of the medium: the first-break estimates for Tivoli Travertine (Figure 6a) show much stronger variation than those for Westerly Granite (Figure 6b). The CWI estimates for $\Delta V/V$, however, do not vary between samples of differing complexity. This consistency of estimates shows that CWI is less dependent on sample complexity, and on receiver location, and suggests that the multiply reflected waves used in CWI effectively sample the entire medium, providing more representative measures of velocity changes from any source and receiver pair.

We also test CWI and conventional methods for estimating *changes* in source locations. For this test, waveforms were simulated for a cluster of sources along a fracture plane in the middle of each of the three samples, and with receivers located at the bottom and at either side of the model (experimental configuration and source cluster locations shown in Figure 5). The standard method of trilateration (minimizing Eqn. 12) is used to locate source positions for each source in the cluster, assuming a constant bulk velocity which is measured with a single source and receiver placed at the top-center and bottom-center of the sample respectively. CWI provides the separation between pairs of sources (it does not provide absolute source locations), so Figure 7 compares separations between the estimated source locations from trilateration with source separations estimated from CWI, which uses equations 9 and 10, and an estimate of the bulk velocity of the medium (the same measured velocity used in trilateration) for each sample.

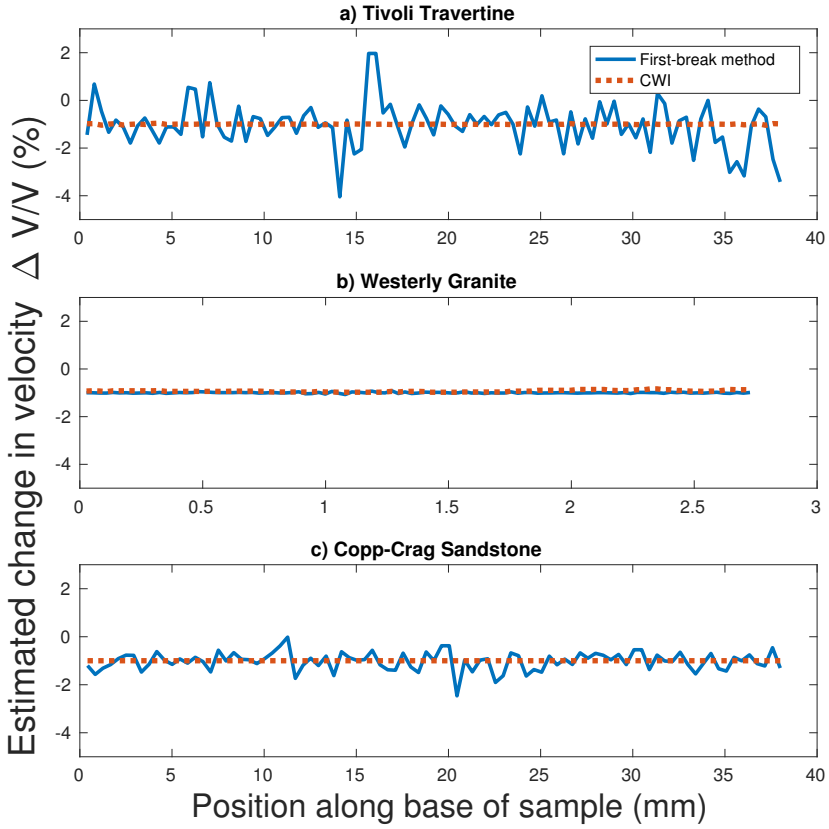

Figure 6. The estimation of a relative velocity change ΔV/V for a true change in velocity of -1%, i.e., ΔV/V = -0.01. Results for a) Tivoli Travertine, b) Westerly Granite, and c) Copp-Crag Sandstone. ΔV/V is estimated using the standard phase-picking method and Coda Wave Interferometry using each of 100 receiver locations along the base of each sample and a single source location at the center-top of each sample.

For all three media, the trilateration-method estimates are quite scattered, particularly for Tivoli Travertine and Copp-Crag Sandstone, and show a far weaker response to changing source separations. CWI estimates are more precise, and are more accurate up to approximately 0.2-0.4λ, where λ is the dominant wavelength. At larger separations cycle-skipping in the cross-correlation is likely to interfere with the signals that we seek in the maximum of the correlation function, causing estimates to tend to a constant value at larger source separations. We demonstrate in section 3.5 below how relative locations of sources can be obtained using separation data from even only a single receiver, and how the working-range of source separations can be increased beyond 0.4λ.

3.3 Experimental Examples

In experimental rock physics, trends in velocity are often measured to model the response of seismic velocity to changes in external conditions (e.g., temperature, effective and differential stresses, fluid properties, etc.), conferring particular importance to interpretation of dynamic changes. This is of importance to a range of geophysical scenarios on a larger scale, such as monitoring subsurface fluid reservoirs or rock changes using time-lapse (4D) seismic methods. Here we show results of two laboratory experiments of changes in external conditions: temperature and stress. In the first experiment a 10 cm^3 block of Halldale Sandstone was heated from room temperature to a temperature of 54°C. A thermocouple and velocity transducers were attached to the sample for continuous temperature measurements and ultrasonic surveys were undertaken during the cooling phase back down to room temperature.

The P-wave sensors are Glaser-type conical piezoelectric sensors (McLaskey & Glaser, 2012). These laboratory-standard, wide-band sensors are calibrated against theoretical displacement time history and have an almost flat displacement response spectrum in the 20 kHz to 1 MHz frequency band. This means that, in this frequency band, they are essentially displacement sensors and their voltage output is linearly proportional to the surface normal displacement. Aperture effects are negligible due to the 0.5 mm sensor contact area (which is even higher than the resolution used in Figure 3). We used an Itasca Image pulser-amplifier system with frequency range 100 kHz to 1 MHz and pre-amp gain of 40 dB, which switches between all transducers in an ultrasonic array, allowing each to act as both a transmitter and a receiver. The amplitude of the pulse spike is 500 V with approximate signal rise time of 0.3 μs and total duration of 2.8 μs. The output recorded

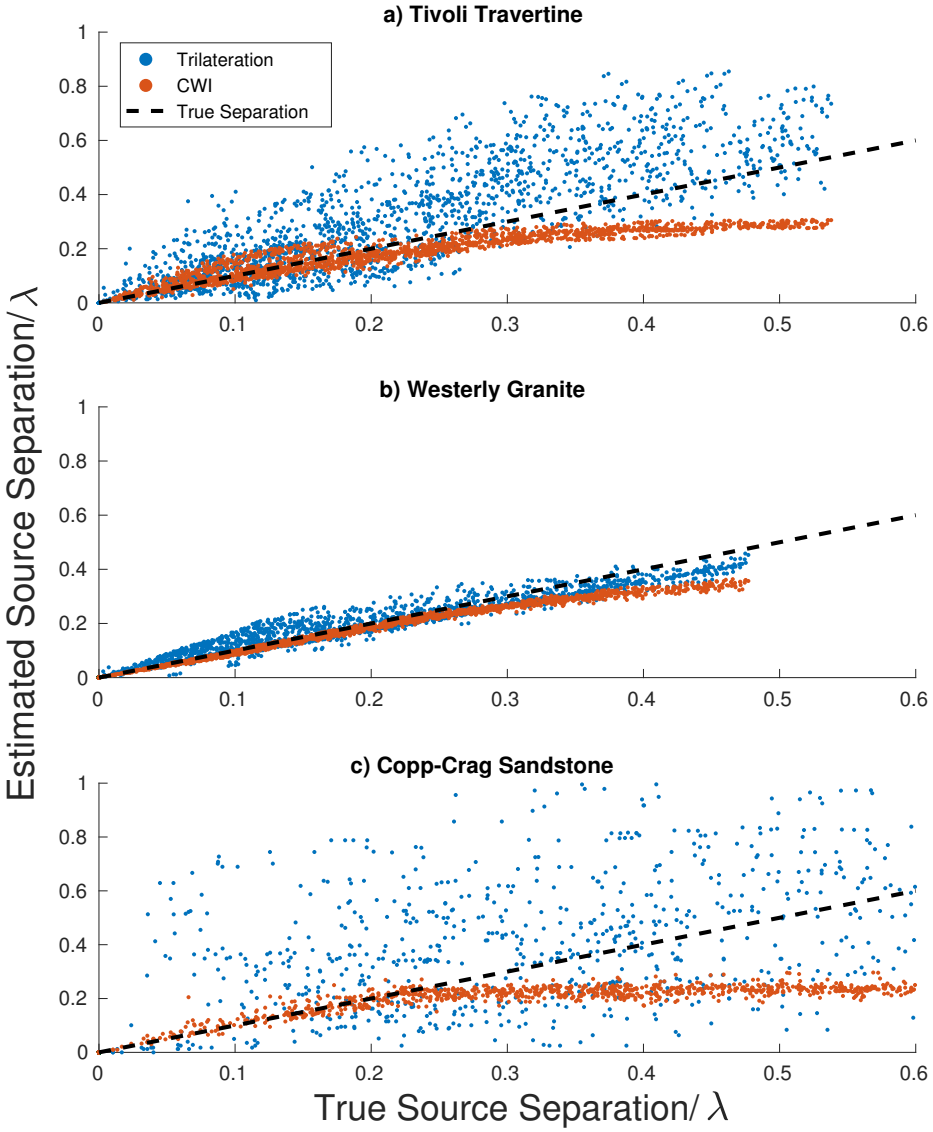

370 **Figure 7.** A comparison of estimated inter-source separation as a function of true inter-source
371 separation for the conventional trilateration method (using arrival times obtained from phase
372 picking of first arrivals) and Coda Wave Interferometry. The true source cluster locations are
373 represented as red dots in Figures 5a, b and c. a) Tivoli Travertine, b) Westerly Granite, and c)
374 Copp-Crag Sandstone. The dashed line indicates the graph locations corresponding to perfect
375 estimates.

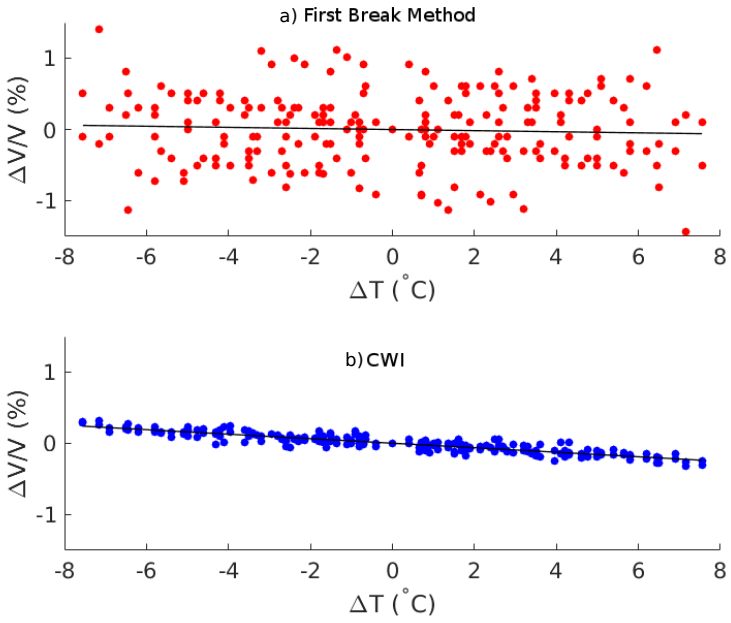

Figure 8. Estimated values of percentage velocity change ($\Delta V/V$) as a function of the change in temperature (ΔT) in a 10 cm^3 sample of Halldale Sandstone, for the standard method of a) picking arrival times and for b) Coda Wave Interferometry. Solid lines are best-fit linear regressions. The zero point on the x axis ($\Delta T = 0$) is arbitrary.

waveform at each receiver is a stack of received waveforms from 25 source pulses with a pulse repetition frequency of 20 kHz.

The change in velocity ($\Delta V/V$) for each temperature change (ΔT) were estimated using both the first-break method and the CWI stretching technique (plotted in Figure 8). There is a large amount of scatter in the $\Delta V/V$ estimates for the first break method, where there is no clear trend that can be resolved above the noise. In contrast, the $\Delta V/V$ estimates using CWI form a clear and coherent response to changes in temperature - a linear, negative correlation due to thermal contraction. This highlights the sensitivity of standard methods to noise, and CWI's ability to resolve small changes in spite of the presence of noise.

A second experiment was carried out where a 38 mm diameter, 90 mm length core of a fine grained laminated carbonate was held at 45 MPa effective pressure, and a differential stress was applied until sample failure. The stress loading history is plotted in

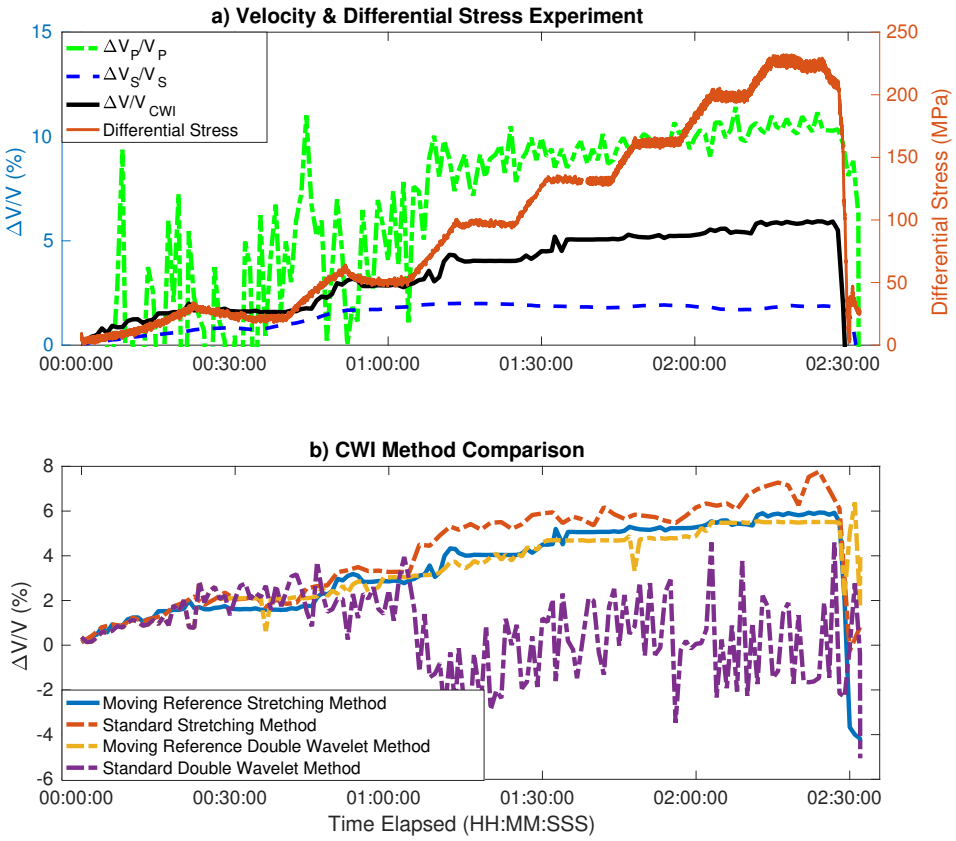

Figure 9. a) Velocity change of a finely laminated carbonate rock during experimental deformation by increasing differential stress (red), with corresponding stress values labeled on the right axis. The response of velocity ($\Delta V/V$), labeled on the left axis, is estimated by the first-break method for P and S wave velocities (dashed lines) and by a CWI moving-reference trace method (black). b) A comparison of CWI algorithms, showing the effect of implementing a moving reference trace (Equation 3) for both the stretching, and double wavelet methods.

Figure 9a, where pauses in loading are periods during which the permeability of the sample was measured. The variation of velocity during the experiment is estimated using the standard first break method for estimating P and S wave velocities, and the CWI moving reference trace method (from Equations 1, 2 and 3). In Figure 9a we see CWI provides a much clearer and more consistent response to external stress changes compared against the change in P wave velocity estimated using first-breaks, accurately mirroring the stepped stress program with far less scatter in the estimated $\Delta V/V$ values, most strikingly for the earlier stress steps. First-break S wave velocities exhibit a smoother response (less scatter), but also fail to mirror the stepped stress program. $\Delta V/V$ estimates from CWI approximately mark the average between changes in P and S wave velocities and we discuss the way that CWI averages in section 4. The higher $\Delta V_P/V_P$ in the conventional method estimates may also reflect the bias towards higher velocities, as the first arriving waves follow only the fastest ray path. As deformation (e.g., compaction) occurs, damage is localized to specific regions of the sample; if the fastest travel path samples such regions, the estimated change in velocity ($\Delta V_P/V_P$) would be larger using first-breaks than estimates using CWI which is representative of the changing bulk properties of sample.

As CWI uses a cross-correlation function, the method breaks down if there are very large changes in the medium due to wave paths being significantly altered and (if the medium fractures) new scattering points being introduced. This means that a single reference trace is not appropriate for CWI in such deformation experiments where the rock structure is significantly deformed. This effect can be seen in Figure 9b, where different CWI algorithms are compared. The "double wavelet" method (Snieder et al., 2002) measures delay times ($\delta\tau$) for multiple time windows down the coda: these relate to the velocity perturbation by $\Delta V/V = -\delta\tau/t$. It is clear that at later stages in the experiment (after 1 hour), the estimates of $\Delta V/V$ using the double wavelet method with a fixed reference trace (dashed purple line) are heavily distorted due to the deformation occurring within the sample. The large amount of scatter exhibited by this method highlights the problem of large changes occurring in the medium. The stretching method, without implementing a moving reference trace (dashed red line), provides more consistent estimates of $\Delta V/V$ than the double wavelet method, estimating a consistent increase in velocity. At later stages in the experiment, these estimates of $\Delta V/V$ become more scattered and the mirroring of the stepped stress program becomes less clear. For both meth-

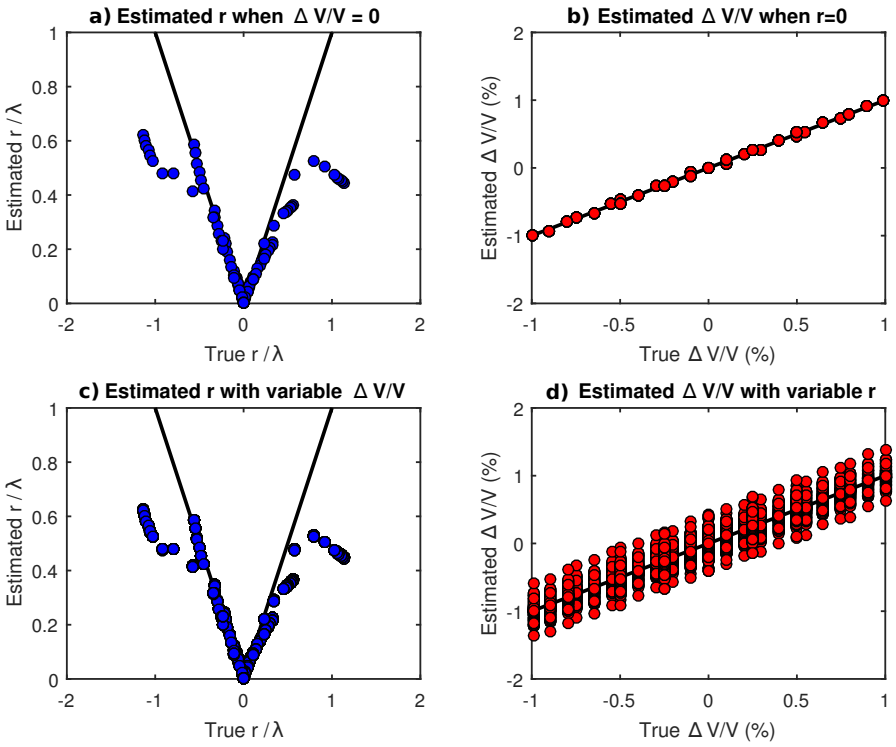

460 **Figure 10.** Assessing the ability of CWI to estimate velocity changes $\Delta V/V$ and inter-source
461 separation r simultaneously in the presence of both velocity and source location perturbations. a)
462 Estimated r when velocity is not perturbed. b) Estimated $\Delta V/V$ when the source location is not
463 perturbed. c) Estimates of r with simultaneous velocity perturbations. d) Estimates of $\Delta V/V$
464 with simultaneous perturbations of source location.

455 ods, implementing the moving reference trace method (Equation 3) combines limiting
456 estimates for small changes in velocity, for which CWI remains accurate, to obtain an
457 overall estimate in $\Delta V/V$ that shows a much clearer stepped response, suggesting the
458 moving reference trace method can account for the extreme changes in the medium.

459 ### 3.4 Joint Estimation of Source Separation and Velocity Change

465 Since CWI estimates of the bulk velocity change ($\Delta V/V$) and source separation
466 (r) are derived from different information (the phase and maximum value of correlation
467 as shown in equations 2 and 9, respectively), estimates can be made independently when
468 both effects occur simultaneously. This has significant experimental advantages, as fixed

source and receiver locations might no longer be necessary for continuous velocity measurements, and in deformation experiments when acoustic emissions might accompany bulk velocity changes these two effects could be analyzed independently - all using a single receiver.

We test the accuracy of these estimates using a series of finite-difference simulations with source locations changing by up to 1.2λ and simultaneous velocity perturbations of up to 1%. Figures 10a and b show estimates of source separation (r) where no velocity perturbation occurs, and the reverse - changes in velocity when the source remains stationary. These represent the best possible estimates from CWI, as only one perturbation type occurs at a time. The additional errors associated with simultaneous perturbations of r and V are shown in Figures 10c and d. We see that estimates of source perturbation are barely affected by the presence of a velocity perturbation: the stretching method of CWI removes the effect of any velocity perturbation. However, estimates of velocity perturbation are far more sensitive to source location perturbations, giving errors of 0.5% for a source displacement of around one wavelength (a relatively large error given the accuracy otherwise expected from CWI). The additional error appears to stem from the effect of cycle skipping in the cross-correlation function.

These results also show that in the case of simultaneous perturbations of source location and velocity, source separation can be estimated much more accurately than estimates of the change in velocity. Therefore, we would expect that the 3D network of relative locations of acoustic emissions that occur during deformation can be estimated robustly using laboratory datasets even if velocity changes occur in the medium (Zhao & Curtis, 2018; Zhao et al., 2017). This is demonstrated in the following section.

3.5 Relocating relative source locations from inter-source distance

Using the inter-source distances or separations between many pairs of sources, it is possible to find the relative locations of a cluster of sources, providing inter-source distances are within the working range of CWI (D. J. Robinson, Sambridge, Snieder, & Hauser, 2013; Zhao & Curtis, 2018; Zhao et al., 2017). However as we see in Figure 7, CWI provides a slightly biased estimate of these separations. The relocation method solves for the relative location of a cluster of sources in a probabilistic framework within which it is possible to correct this bias to a significant extent. For one pair of events, according

to Bayes' theorem

$$P(\tilde{\delta}_t|\tilde{\delta}_{CWI}) \propto P(\tilde{\delta}_{CWI}|\tilde{\delta}_t) \times P(\tilde{\delta}_t) \tag{13}$$

where the posterior probability $P(\tilde{\delta}_t|\tilde{\delta}_{CWI})$ is the probability of the true separation having value $\tilde{\delta}_t$ given the estimated separation from CWI is $\tilde{\delta}_{CWI}$. This is proportional to the likelihood $P(\tilde{\delta}_{CWI}|\tilde{\delta}_t)$ of having observed $\tilde{\delta}_{CWI}$ in the case that the true separation is $\tilde{\delta}_t$, multiplied by the prior probability $P(\tilde{\delta}_t)$ which describes any available information about event locations known prior to the location process. The likelihood function $P(\tilde{\delta}_{CWI}|\tilde{\delta}_t)$ describes the bias in separations estimated by CWI, and can be approximated by a Gaussian probability density function whose mean and standard deviation are described by the empirical functions derived by D. Robinson et al. (2011). The tilde over parameters indicates that the separation quantities are used in normalized form - they are the true values divided by the dominant wavelength recorded in the seismogram coda.

For multiple events, Equation 13 holds for each event pair. The separation estimated from CWI for a cluster of events can be incorporated into a joint posterior function by multiplying the formulae for all available event pairs, assuming they are independent of one another (D. J. Robinson et al., 2013):

$$P(\boldsymbol{e}_1, \ldots, \boldsymbol{e}_n|\tilde{\delta}_{CWI}) = c\prod_{i=1}^{n} P(\boldsymbol{e}_i) \times \prod_{i=1}^{n-1}\prod_{j=i+1}^{n} P(\tilde{\delta}_{CWI,ij}|\boldsymbol{e}_i, \boldsymbol{e}_j) \tag{14}$$

where c is a constant, n is the number of events, $\boldsymbol{e}_i = (x_i, y_i, z_i)$ is the location of event i. Within the last term we use the locations of the ith and jth events ($\boldsymbol{e}_i$ and $\boldsymbol{e}_j$) from which we can calculate their true separation $\delta_{t,ij} = ||\boldsymbol{e}_i - \boldsymbol{e}_j||_2$, and thus we implicitly include equation 13. The most probable set of the event locations can be found where the joint posterior function attains its maximum. Therefore, the event locations can be estimated by solving an optimization problem. The optimization problem is converted to a minimization problem by taking the negative logarithm of Equation 14:

$$-ln[P(\boldsymbol{e}_1, \ldots, \boldsymbol{e}_n|\tilde{\delta}_{CWI})] = -ln[c] - \sum_{i=1}^{n} ln[P(\boldsymbol{e}_i)] - \sum_{i=1}^{n-1}\sum_{j=i+1}^{n} ln[P(\tilde{\delta}_{CWI,ij}|\boldsymbol{e}_i, \boldsymbol{e}_j)] \tag{15}$$

A uniform prior $P(\boldsymbol{e}_i)$ is considered in this work, so the terms containing $ln[P(\boldsymbol{e}_i)]$ are constant, and the term $ln[c]$ can be ignored in the minimization problem. Thus, the objective function becomes:

$$L(\boldsymbol{e}_1, \ldots, \boldsymbol{e}_n) = -\sum_{i=1}^{n-1}\sum_{j=i+1}^{n} ln[P(\tilde{\delta})_{CWI,ij}|\boldsymbol{e}_i, \boldsymbol{e}_j)] \tag{16}$$

The function can be minimized using a conjugate gradient algorithm (Press, Flannery, Teukolsky, & Vetterling, 1986).

We test this location method using the Tivoli Travertine model shown in Figure 2b, and source locations shown in Figure 11a, simulating a cluster of acoustic emissions around a fracture. We divided the events into multiple sub-clusters with 20 overlapping event locations, where the maximum separations in each sub-cluster remained roughly within or just outside of the working range of CWI (approximately 0.5λ). For each sub-cluster, we solved for the relative event locations by minimizing equation 16 using the publicly available CWI-relocation code package of Zhao and Curtis (2018), taking the CWI separation estimates as inputs. We conducted the location process five times with different randomly distributed initial event locations to ensure convergence to the global minimum of the objective function (Equation 15). The optimizations all converge to the same minimum to within trivial numerical differences. Receiver locations follow the same configuration as shown in Figure 5a. Since absolute event locations remain unknown in this method, we then rotate and translate the resulting sub-clusters to match locations of the overlapping sources. For comparison, we also performed the conventional method for locating sources, using phase-picking of first-break arrivals for multiple receivers, and trilateration to estimate locations of sources. The results of trilateration and CWI relocations are shown in Figure 11b and c, respectively.

We note immediately that the cluster of events from trilateration in Figure 11b is rotated by 45° relative to the true locations due to velocity heterogeneity in the sample. Since CWI only provides *relative* locations, the cluster of CWI location in panel c has been rotated to best match the results in panel b for fair comparison. The spatial area of events in panel c appears to be more rectangular (like the true shape of the area in panel a) than the area in panel b. Nevertheless, it is difficult to decide which of Figure 11b and c is better from these plots alone so Figure 12 shows the source separation values of these two clusters as a function of true source separation. This highlights the improvement of accuracy and precision offered by the CWI source relocation procedure. It is also important to note from Figure 12 that using the sub-cluster matching methods, source cluster size can extend well beyond the usual working range of CWI and the source-separation bias can be largely corrected, providing there are overlapping sources between sub-clusters.

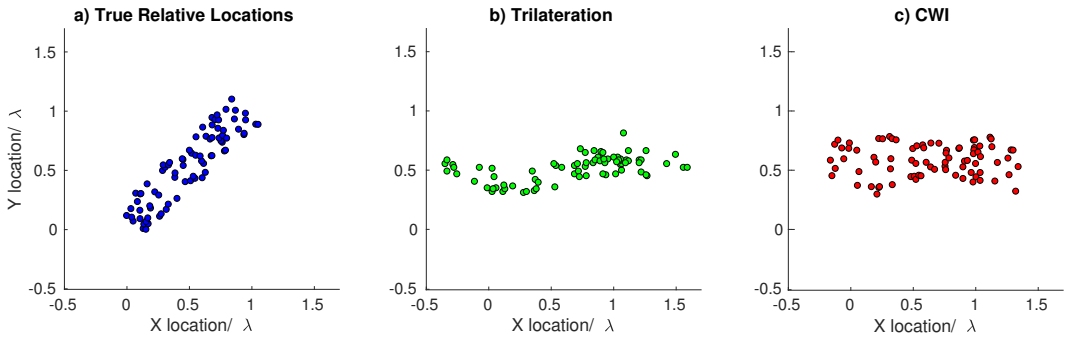

Figure 11. a) True locations of a cluster of acoustic emissions simulated in the Tivoli Travertine μCT slice in Figure 2b. b) The estimated cluster locations using the conventional method of first-break arrival times and trilateration using the receiver geometry in Figure 5a. c) The estimated relative locations found by implementing the CWI-based optimization algorithm described in Zhao et al. (2017), using the inter-source separations estimated from CWI using the same receiver geometry (note these locations have been rotated in plane to best fit the locations in panel b for fair for comparison, as the optimization provides only relative locations).

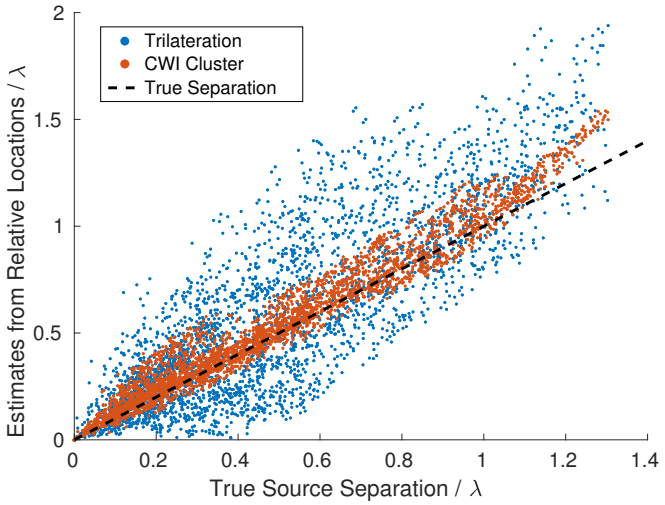

Figure 12. Source separation values from the estimated location clusters shown in Figures 11b and c, as a function of true source separation. The dashed line shows where true separation estimates would lie.

3.6 Sensitivity to Noise

In order to test the ability of CWI to estimate changes in velocity and in source or receiver location when using noise-contaminated data, we generate a synthetic record of noise which is superimposed onto the numerically simulated signals used above. We generate realistic noise as follows: 1) measure a long noise record in the Edinburgh rock physics laboratory, and process it to create a record of de-meaned and de-trended seismic noise. 2) Take the Fourier Transform of the noise recording, and smooth the record in the Fourier domain to ensure there are no spectral gaps (frequency bands without noise). 3) Convolve the resulting spectrum with a sample of random Gaussian white noise so that generated noise is uncorrelated. The resulting signal is therefore a randomly generated recording of realistic noise, which can be superimposed on the effectively noise-less waveforms generated from synthetic finite difference simulations. The signal-to-noise ratio (SNR) is calculated as $SNR = P_{signal}/P_{noise}$, where P is the average power. We superimpose the noise at different SNR values onto a range of numerically simulated signals where the velocity has been perturbed from 0 - 10% and where the source location is perturbed by 0.01λ. Estimates of the range of velocity perturbations are calculated using CWI, as well as by using conventional phase-picking methods (both automatically and manually picked) for each level of noise contamination. These estimates are shown for low noise contamination (SNR=8) and high noise contamination (SNR=0.43) in Figure 13. The total error at each SNR value, calculated as the sum of residuals of each estimate to the true $\Delta V/V$ value is shown in Figure 14a. We find that at high SNR values, all estimates for $\Delta V/V$ show a clear response to the increasing velocity perturbation, though CWI estimates are over an order of magnitude more accurate. At low SNR values, conventional methods based on phase-picking show much more scatter in the estimates of $\Delta V/V$, whereas CWI is much more precise, and is mostly unaffected by the increased contamination of noise. The first-break arrivals are of lower amplitude and are therefore more susceptible to contamination by noise, whereas CWI uses the entire signal, including many more data points, and is therefore more robust in the presence of noise.

For estimation of source separation in the presence of noise (see Figure 14b), the absolute locations of sources within a small cluster were estimated by trilateration by assuming a constant, isotropic P-wave velocity. However, because CWI does not provide absolute source locations but instead gives the separation between two sources, r, we es-

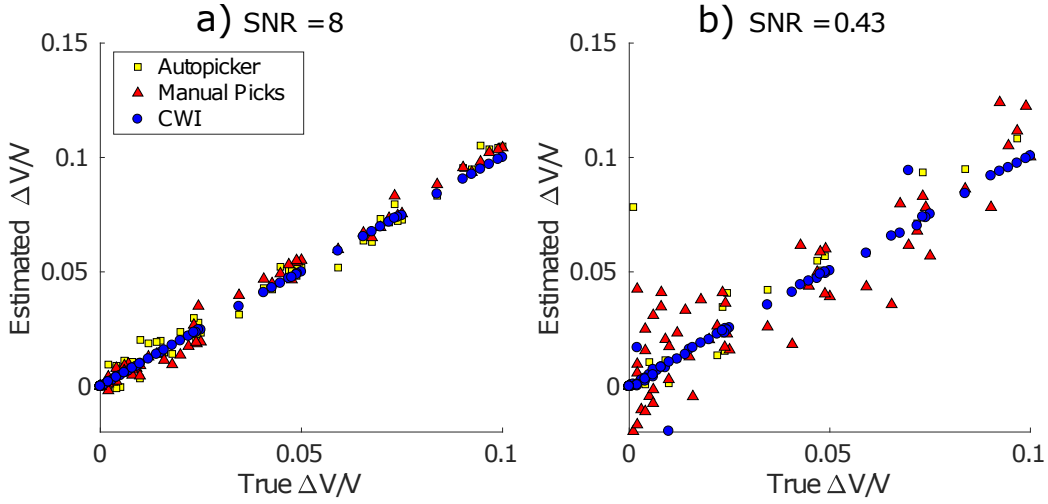

572 **Figure 13.** Estimated $\Delta V/V$ from Coda Wave Interferometry, and from travel times obtained
573 by auto-picking and manual picks, estimated at a) SNR = 8 and b) SNR = 0.43 and plotted as a
574 function of the true velocity change.

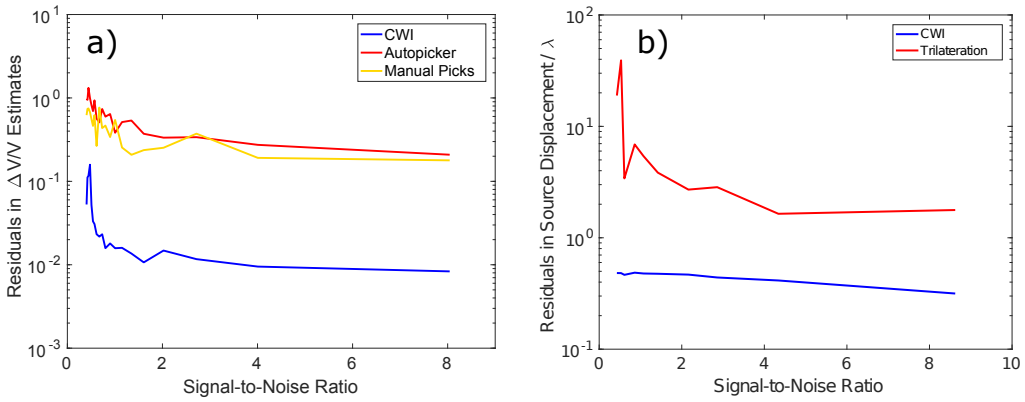

603 **Figure 14.** a) Residuals between true and estimated velocity change ($\Delta V/V$) as a function
604 of signal-to-noise ratio. b) Residuals between true and estimated source displacement r/λ as a
605 function of signal-to-noise ratio.

timate the separation between pairs of absolute locations from trilateration for comparison. We compare this to the r estimate from CWI for each pair of sources, and plot the sum of individual residuals for all source pairs and for each method in Figure 14. We find that at high SNR values, CWI and trilateration estimates are comparable, where both estimations are within 0.05λ of the true separation. However, with increasing contamination of noise, CWI residuals increase by a factor of two, whereas trilateration estimates increase by a factor of ¿10. These results show that CWI is a more robust way to characterize changes in a medium's velocity or in relative source locations in the presence of noise. Since no phase picking is necessary for CWI, this also means that less pre-processing of data is required before analysis.

4 Discussion

While we have demonstrated that using Coda Wave Interferometry for experimental applications can provide significant improvements over conventional methods, particularly in the accuracy and precision of estimates of changes in velocity and source locations, there are several limitations to be considered. First, the result of CWI only gives a measure of the change in velocity and not the absolute velocity itself. In itself this is not of particular concern since in many real-world problems, such as those relating to the interpretation of 4D seismic data, we seek to characterize the dynamic dependence of velocity on changes in external properties (Landrø & Stammeijer, 2004). However, ΔV/V estimates from CWI are more difficult to interpret than separate estimates of V_P and V_S that are obtainable from conventional methods. Given an estimate of density, V_P and V_S estimates allow bulk and shear moduli to be estimated, and these are parameters that appear in the majority of rock physics models. CWI estimates of $\Delta V/V$ reflect a combination of P- and S-velocity information due to the multiple phase conversions that occur during wave propagation.

To aid the interpretation of CWI $\Delta V/V$ estimates, consider the scattering model presented by Snieder (2002). This model represents P and S states as balls of energy traveling with velocities V_P and V_S. When a ball of P energy travels distance a (the average distance between scatterers), it has a probability p_{PS} of converting to an S state; likewise a ball of S energy has a probability p_{SP} of converting to the P state. Over a time interval dt, a ball in the P state encounters $V_P dt/a$ scatterers, meaning that in a system with N_P and N_S balls in the P and S states, the reduction in P balls due to $P-$

642 $to - S$ conversions is given by $-2p_{PS}N_PV_Pdt/a$ and the increase due to $S - to - P$
643 conversions is given by $p_{SP}N_SV_Sdt/a$. Following from this, Snieder (2002) derives the
644 following system of differential equations:

645 $$\dot{N}_P = \frac{1}{a}(p_{SP}V_SN_S - 2p_{PS}V_PN_P) \tag{17}$$

646 $$\dot{N}_S = \frac{1}{a}(2p_{PS}V_PN_P - p_{SP}V_SN_S) \tag{18}$$

652 where the dot over N_P and N_S on the left side indicates a rate of change over time. Now
653 consider a receiver not co-located with the source, at which the time of first arriving en-
654 ergy in the signal is comprised of only P state energy. After this time the proportions
655 of P and S wave energy can be calculated using equations 18 and 18, and therefore so
656 can the proportions of *changes* in P-wave velocity ($\Delta V_P/V_P$) and S-wave velocity ($\Delta V_S/V_S$).
657 The way in which these proportions of $\Delta V/V$ vary as a function of time is shown in Fig-
658 ure 15. For time values to be independent of the scattering properties of the medium,
659 time is normalized by the travel time of one mean free path ($\tau_P = l_P/V_P$), where the
660 mean free path l_P is defined as $l_P = a/(2P_{PS})$. In practice, the mean free path of a
661 scattering medium can be estimated from the attenuation of energy in recorded signals
662 (Anugonda, Wiehn, & Turner, 2001). Figure 15 shows how the proportions of $\Delta V_P/V_P$
663 and $\Delta V_S/V_S$ change depend on the V_P/V_S ratio. At equilibrium, the proportion of $\Delta V_S/V_S$
664 is higher than $\Delta V_P/V_P$, even at very low V_P/V_S ratios (Figure 15a), explained by S hav-
665 ing two states (S_1 and S_2, which represent the two polarizations of S waves) where P
666 only has one state. As V_P/V_S increases, so does the proportion of $\Delta V_S/V_S$ at equilib-
667 rium, as energy in S waves are traveling more slowly than P waves so are spending more
668 time in that state before encountering scatterers.

678 We can use this model to estimate the independent changes of P and S wave ve-
679 locity. Define $q(t, \gamma)$ to be the relative contribution of $\Delta V_S/V_S$ (the red curves in Fig-
680 ure 15), where $\gamma = V_P/V_S$. The function q depends on time t and on the V_P/V_S ra-
681 tio γ, and the relative contribution of $\Delta V_P/V_P$ (blue curves in Figure 15) is $1-q(t, \gamma)$.
682 If P and S wave velocities change by different amounts, the measured change in veloc-
683 ity from CWI ($[\Delta V/V]_{CWI}$) therefore varies as a function of time along the coda by

684 $$\left[\frac{\Delta V}{V}\right]_{CWI}(t) = [1 - q(t, \gamma)]\left[\frac{\Delta V_P}{V_P}\right] + q(t, \gamma)\left[\frac{\Delta V_S}{V_S}\right] \tag{19}$$

685 For a single time window, this equation has two unknown parameters, $\Delta V_P/V_P$ and $\Delta V_S/V_S$;
686 the value of $[\Delta V/V]_{CWI}$ can be measured and $q(t, \gamma)$ is known (from Figure 15). Mea-
687 suring $[\Delta V/V]_{CWI}$ in multiple time windows along the coda therefore gives multiple equa-

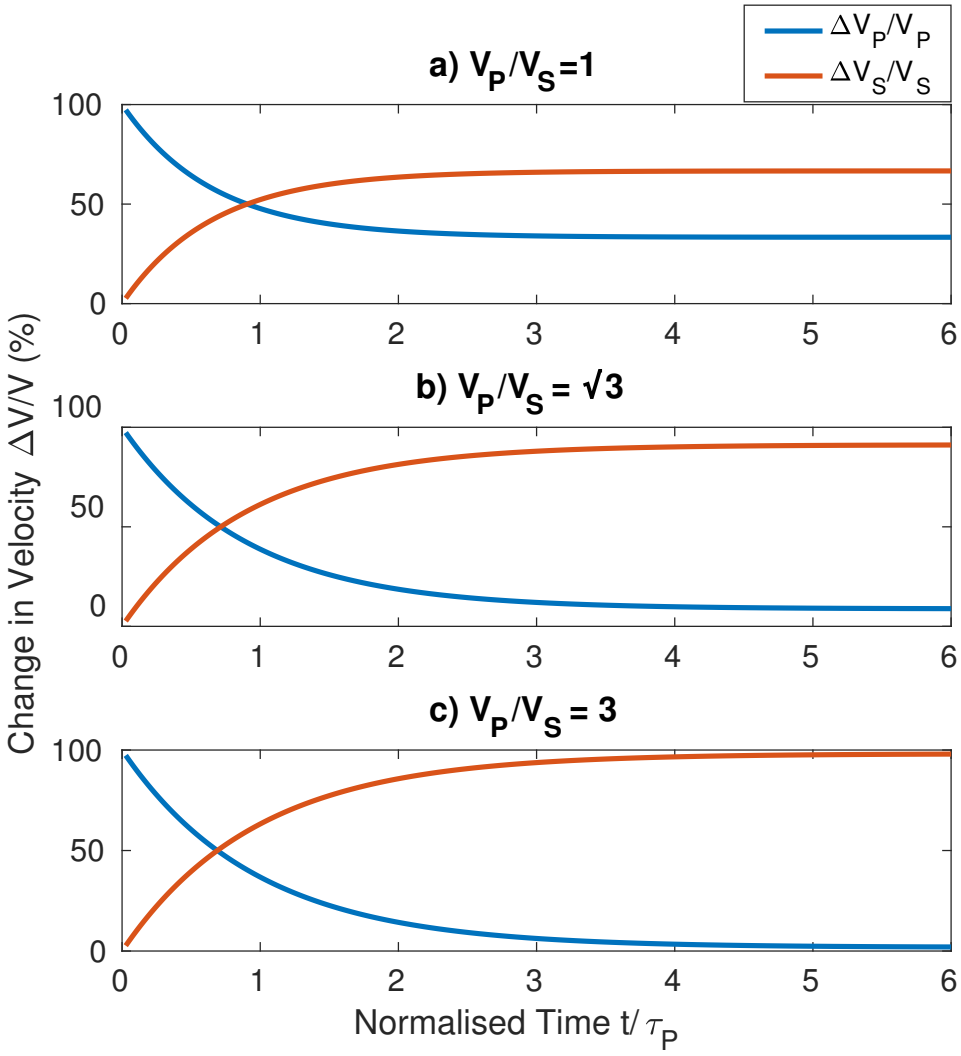

Figure 15. Relative proportions of changes in P-wave velocity ($\Delta V_P/V_P$) and S-wave velocity ($\Delta V_S/V_S$) which make up the change in velocity estimated from CWI ($\Delta V/V$) as a function of time along the coda, using equations 18 and 18 from Snieder (2002). Multiple relations are shown for media of varying V_P/V_S ratios: a) b) $V_P/V_S = 1$, b) $V_P/V_S = \sqrt{3}$, c) $V_P/V_S = 3$. Time is normalized by dividing time t by the transit time of one mean free path ($\tau_P = l_P/V_P$).

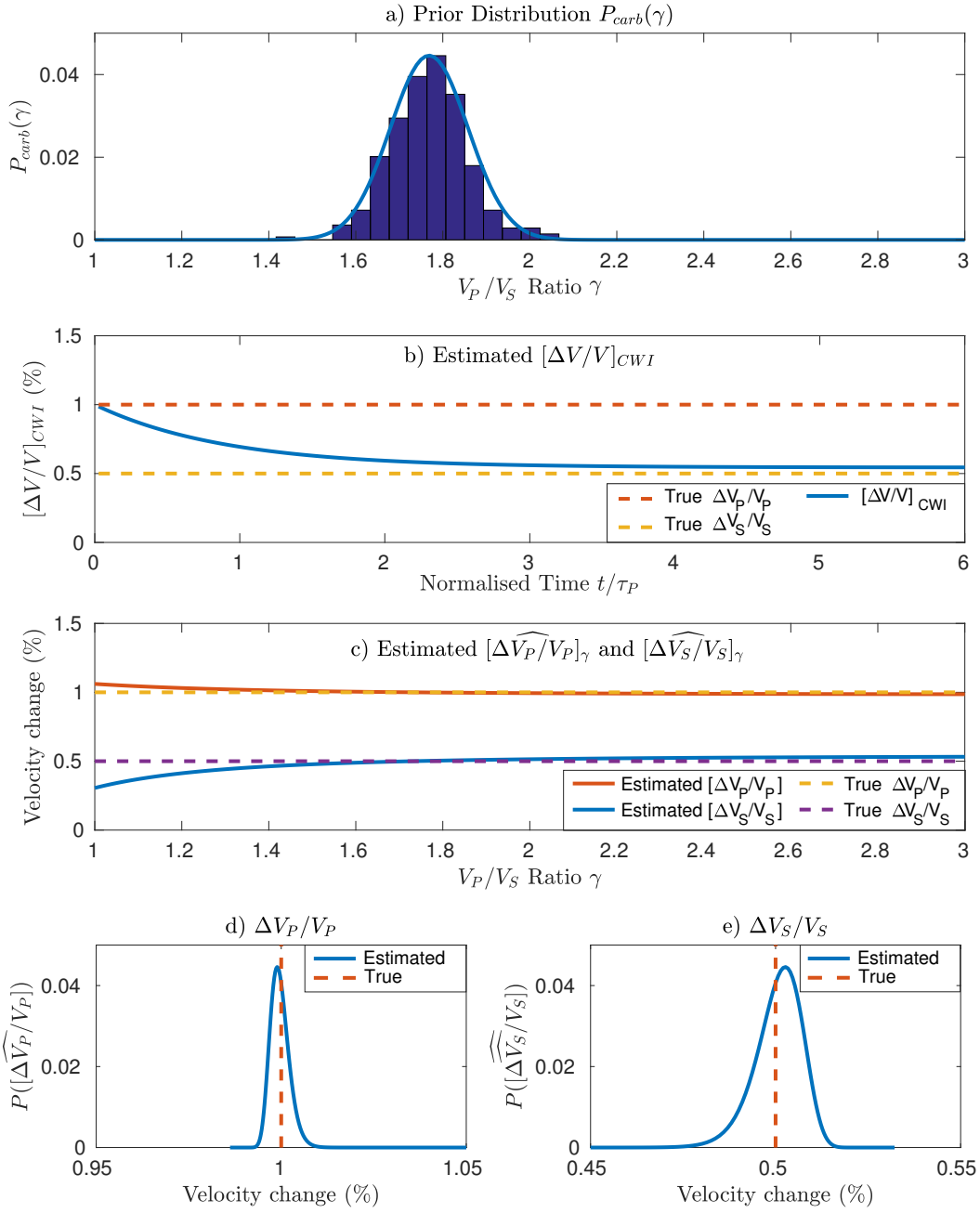

Figure 16. a) Prior distribution of V_P/V_S ratios from measured dry carbonate data compiled from Bakhorji (2010), Fournier et al. (2011) and Verwer et al. (2008). The curve shows the best fitting normal distribution function of the histogram. b) Synthetic $[\Delta V/V]_{CWI}$ data generated using Equation 19, where $\Delta V_P/V_P = 1\%$, $\Delta V_S/V_S = 0.5\%$ and $\gamma = \sqrt{3}$). c) Estimated $[\Delta\widehat{V_P/V_P}]_\gamma$ and $[\Delta\widehat{V_S/V_S}]_\gamma$ from an ordinary least squares inversion of the forward modeled $[\Delta V/V]_{CWI}$ data in panel b, as a function of the V_P/V_S ratio used in the inversion. d) and e) show the probability density functions (solid blue lines) for estimates of $\Delta V_P/V_P$ and $\Delta V_S/V_S$, the dashed red lines represent the true changes in velocity ($\Delta V_P/V_P = 1\%$, $\Delta V_S/V_S = 0.5\%$), using Equations 20 and 21.

tions, the same number as there are time windows. Quantities $\Delta V_P/V_P$ and $\Delta V_S/V_S$ can be estimated using an ordinary least squares inversion approach to solve the system: $d = Am$, where d is a matrix of measured values of $[\Delta V/V]_{CWI}$ for each time window, and A is matrix of $(1-q)$ and q values expected at each time window for a given V_P/V_S ratio γ. The resulting vector m contains estimates of $\Delta V_P/V_P$ and $\Delta V_S/V_S$ for a given V_P/V_S ratio, and we denote these estimates by $[\Delta\widehat{V_P/V_P}]_\gamma$ and $[\Delta\widehat{V_S/V_S}]_\gamma$, respectively. Clearly, in order to estimate the changes of V_P and V_S independently we need to be able to estimate $\gamma = V_P/V_S$.

One way to estimate γ would be to use the conventional experimental method to estimate V_P and V_S, but as we have shown herein, those methods are less accurate than CWI for subtle changes in the medium so it is desirable to find alternative methods. As Figure 15 shows, values for $q(t)$ can vary significantly depending on the V_P/V_S ratio. Given the knowledge of a rock type (e.g., if the rock is a carbonate) we can refine estimates of $\Delta V_P/V_P$ and $\Delta V_S/V_S$ within a probabilistic framework. We demonstrate this by compiling a database of 296 measured V_P/V_S ratios for dry carbonates combining data from Bakhorji (2010), Fournier et al. (2011) and Verwer et al. (2008). From this, we create a prior distribution of V_P/V_S ratios γ for carbonate rocks $P_{carb}(\gamma)$, shown in Figure 16a. In order to test the method we also calculate synthetic $[\Delta V/V]_{CWI}$ data using Equation 19 with a change in P wave velocity of 1%, a change in S wave velocity of 0.5%, and a V_P/V_S ratio equal to $\sqrt{3}$ ($\Delta V_P/V_P = 1\%$, $\Delta V_S/V_S = 0.5\%$, $\gamma = \sqrt{3}$), which gives $[\Delta V/V]_{CWI}$ as a function of time (Figure 16b. The method then proceeds as follows: using the generated $[\Delta V/V]_{CWI}$ data and the known values for $q(t,\gamma)$, we invert for $[\Delta\widehat{V_P/V_P}]_\gamma$ and $[\Delta\widehat{V_S/V_S}]_\gamma$ for a range of values of V_P/V_S ratios (γ), shown in Figure 16c. However, given the knowledge that the sample is a carbonate, not all of these values are equally likely. We should therefore weight this set of solutions by the probability that each V_P/V_S ratio is the one in our sample - the probability distribution in Figure 16a. Thus we can generate probability density functions for estimates of $\Delta V_P/V_P$ and $\Delta V_S/V_S$ with the following equations:

$$P\left(\frac{\Delta V_P}{V_P}\right) = \int_{\gamma\in R_\gamma} \delta\left(\frac{\Delta V_P}{V_P} - \left[\frac{\widehat{\Delta V_P}}{V_P}\right]_\gamma\right) \cdot P_{carb}(\gamma)d\gamma \tag{20}$$

$$P\left(\frac{\Delta V_S}{V_S}\right) = \int_{\gamma\in R_\gamma} \delta\left(\frac{\Delta V_S}{V_S} - \left[\frac{\widehat{\Delta V_S}}{V_S}\right]_\gamma\right) \cdot P_{carb}(\gamma)d\gamma \tag{21}$$

where R_γ is the prior range of V_P/V_S ratios γ. In the case where $\Delta V_P/V_P = 1\%$ and $\Delta V_S/V_S = 0.5\%$, the resulting probability distributions for changes in P and S wave

velocities are shown in Figures 16d and e. For both changes in P and S wave velocity, the method accurately estimates the velocity change. The probability distribution change in P wave velocity $\Delta V_P/V_P$ is relatively precise, with almost possible estimates within $\pm 0.01\%$ of the true value for velocity change. The distribution of change in S wave velocity has a wider spread, though still significant precision when compared to standard methods, with the majority of estimates within $\pm 0.03\%$ of the true velocity change. From this we can see that it is possible to estimate independent changes in P and S wave velocity using CWI given only the knowledge that the rock is a carbonate.

Another important aid in the interpretation of CWI estimates is an understanding of the type of spatial average of material parameters that is implicit in the CWI estimate. To examine this, another experiment is conducted using the μCT derived velocity and density models of the Tivoli Travertine (Figure 2a). The fluid velocity is perturbed by a range of values (up to a +150 m/s perturbation), and CWI is used to estimate the velocity perturbation of the bulk medium. As the exact amount of calcite and pore fluid phases are known, as well as their properties, the change in the average properties of the medium can be calculated with various methods: here we use the arithmetic ($\bar{V}_A = \frac{1}{n}(\sum_{i=1}^{n} V_i)$), geometric ($\bar{V}_G = (\prod_{i=1}^{n} V_i)^{1/n}$), and harmonic ($\bar{V}_H = n(\sum_{i=1}^{n} \frac{1}{V_i})^{-1}$) means. A comparison of how these different measures spatially average the medium is shown in Figure 17. Of the different methods used, the harmonic mean shows the closest estimate of the true velocity in Figure 17a, and of the CWI estimates for velocity change in Figure 17b. The harmonic mean, which is in fact the same calculation as the Wyllie time average (Mavko et al., 2009), is equivalent to taking the velocity from the entire medium stretched into a single 1-dimensional line, and calculating the mean velocity of a wave passing through every point along the line.

The use of CWI estimates in current rock physics protocols is therefore possible because the appropriate information required for many rock physics models is available: the relative proportions of P and S wave velocity changes (Figure 16) given prior knowledge of V_P/V_S ratios of the medium (based for instance on rock type as in the example above), and how CWI averages the bulk velocity change properties of a medium spatially (Figure 17).

The method of CWI used here (Equation 1) is known as trace stretching and has some underlying assumptions and limitations. Namely it assumes that the velocity per-

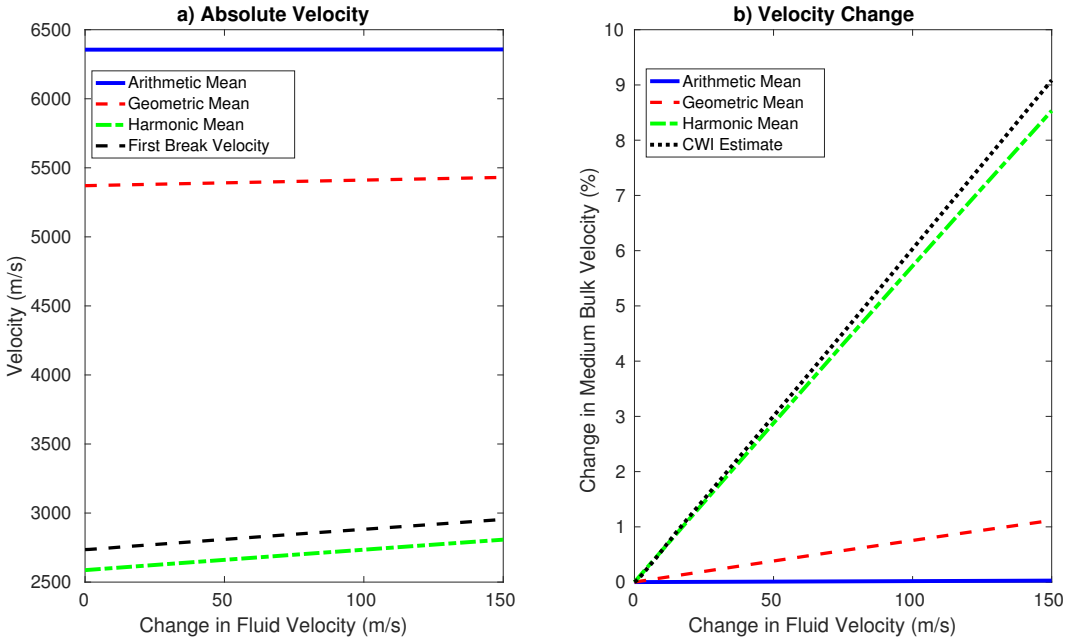

744 **Figure 17.** a) Calculated average velocity for the Tivoli Travertine digital rock sample fol-
745 lowing multiple perturbation of fluid velocity. The medium velocity is averaged using arithmetic
746 $\bar{V}_A$ (solid blue), geometric $\bar{V}_G$ (solid red), and harmonic means $\bar{V}_H$ (dashed yellow). The velocity
747 is also estimated using the first break method (dashed black). b) The change in bulk velocity
748 ($\Delta V/V$) as a function of fluid velocity perturbation, calculated with the multiple averages. The
749 dotted black line is the estimate of velocity change ($\Delta V/V$) attained using CWI.

turbation is uniform across the entire medium so that all arriving energy is perturbed at the same temporal rate, and therefore the trace is stretched linearly in time along the seismogram. Mikesell, Malcolm, Yang, and Haney (2015) provides a comparison of different methods to estimate changes in velocity for CWI, and suggests dynamic time warping method as a solution for inhomogeneous velocity perturbations.

As we have shown, CWI is able to resolve both changes in velocity and changes in source and/or receiver locations, allowing for the estimation of relative source locations. However CWI is also able to resolve another type of perturbation on which we have not focused: the average displacement of all scatterers, δ, illustrated in Figure 1c (Snieder et al., 2002). This value is related to the variance of travel time perturbations by

$$\sigma_\tau^2 = \frac{2\delta^2 t}{v l_\star} \tag{22}$$

where $l_\star$ is the transport mean free path. It would be interesting to monitor how this parameter varies during experimental rock physics and geomechanics experiments. For example, it may be possible to monitor changes in the average distance between scattering points, which could act as a proxy measure for inter-pore distance, itself a strong control on the time of failure (Vasseur et al., 2017). During the confining or varying of fluid pressure in an isotropic sample, scattering points would be displaced in all directions, and this displacement might be measured by CWI. Similar effects occur at reservoir scale where fluid injection or extraction can lead to seismically observable volumetric expansion of the reservoir. We leave this for future research.

5 Conclusion

Conventional first-break methods based on phase-picking provide an estimate of seismic velocity that is not representative of the bulk medium. Such estimates of seismic velocity, changes in velocity, and source location are highly variable even for a single sample, and depend on the specific source/receiver path of the first arriving wave. They are therefore inadequate for characterizing the bulk properties of a rock sample, particularly those with complicated pore structures. By contrast, Coda Wave Interferometry is an effective method for countering these problems because coda waves sample the entire medium, and sample the same regions multiple times. CWI is shown to provide an increase in precision by an order of magnitude in the absence of noise, and to be a robust and accurate method for estimating both bulk velocity changes and per-

turbations of the source or receiver locations when compared with standard methods in both synthetic digital rock physics and laboratory experimental data. When noise is present, CWI remains far more accurate than conventional methods, even at very low signal-to-noise ratios. Additionally, when velocity and source/receiver location perturbations occur simultaneously CWI can still estimate velocity and source separation under some conditions: source separation estimates are mostly unaffected by the velocity perturbation, but velocity change estimates are much more sensitive and become inaccurate in the presence of larger source perturbations, possibly due to cycle-skipping. Using source separation estimates, relative locations of a cluster of sources can be estimated using a single receiver, and show higher precision and accuracy compared to conventional methods. CWI estimates a combination of changes in both P and S wave velocities, and we demonstrate a model for the equilibration of the contributions from P and S waves as a function of time, and show how the independent changes in P and S wave velocity can be measured, given probabilistic *a priori* information about the V_P/V_S ratio. Overall these results show significant potential for the use of CWI to characterize changes in porous media undergoing changes in effective stress and strain, and in temperature.

Acknowledgments

The authors would like to thank Petrobras and Shell for their sponsorship of the International Centre for Carbonate Reservoirs (ICCR), and for permission to publish this work from the 4DRP project. We are also grateful to Ian Butler, Florian Fussies, Phil Cilli, Angus Lomas, and Roseanne Clement for their helpful scientific input and comments. The MATLAB code package is available at https://edin.ac/2OhWHFP. The code package of Zhao and Curtis (2018) is available at https://www.geos.ed.ac.uk/eip/codes.html.

References

Anugonda, P., Wiehn, J. S., & Turner, J. A. (2001). Diffusion of ultrasound in concrete. *Ultrasonics*, *39*(6), 429–435.

Arts, R., Eiken, O., Chadwick, A., Zweigel, P., Van der Meer, L., & Zinszner, B. (2004). Monitoring of co2 injected at sleipner using time-lapse seismic data. *Energy*, *29*(9-10), 1383–1392.

Bakhorji, A. M. (2010). *Laboratory measurements of static and dynamic elastic properties in carbonate.*

Brown, L. T. (2002). *Integration of rock physics and reservoir simulation for the interpretation of time-lapse seismic data at weyburn field, saskatchewan* (Unpublished doctoral dissertation). Colorado School of Mines. Arthur Lakes Library.

Christensen, N. I. (1966). Shear wave velocities in metamorphic rocks at pressures to 10 kilobars. *Journal of Geophysical Research*, *71*(14), 3549–3556.

Fournier, F., Leonide, P., Biscarrat, K., Gallois, A., Borgomano, J., & Foubert, A. (2011). Elastic properties of microporous cemented grainstones. *Geophysics*, *76*(6), E211–E226.

Grêt, A., Snieder, R., & Özbay, U. (2006). Monitoring in situ stress changes in a mining environment with coda wave interferometry. *Geophysical Journal International*, *167*(2), 504–508.

Guilbot, J., & Smith, B. (2002). 4-d constrained depth conversion for reservoir compaction estimation: Application to ekofisk field. *The Leading Edge*, *21*(3), 302–308.

Herwanger, J. V., & Horne, S. A. (2009). Linking reservoir geomechanics and time-lapse seismics: Predicting anisotropic velocity changes and seismic attributes. *Geophysics*, *74*(4), W13–W33.

James, S., Knox, H., Abbott, R., & Screaton, E. (2017). Improved moving window cross-spectral analysis for resolving large temporal seismic velocity changes in permafrost. *Geophysical Research Letters*, *44*(9), 4018–4026.

Landrø, M., & Stammeijer, J. (2004). Quantitative estimation of compaction and velocity changes using 4d impedance and traveltime changes. *Geophysics*, *69*(4), 949–957.

Larose, E., & Hall, S. (2009). Monitoring stress related velocity variation in concrete with a 2× 10- 5 relative resolution using diffuse ultrasound. *The Journal of the Acoustical Society of America*, *125*(4), 1853–1856.

Lockner, D. (1993). The role of acoustic emission in the study of rock fracture. In *International journal of rock mechanics and mining sciences & geomechanics abstracts* (Vol. 30, pp. 883–899).

Lockner, D., Byerlee, J., Kuksenko, V., Ponomarev, A., & Sidorin, A. (1992). Observations of quasistatic fault growth from acoustic emissions. *International Geophysics*, *51*, 3–31.

Madonna, C., Almqvist, B. S., & Saenger, E. H. (2012). Digital rock physics: numerical prediction of pressure-dependent ultrasonic velocities using micro-ct imaging. *Geophysical Journal International*, *189*(3), 1475–1482.

Margrave, G. F. (2007). Methods of seismic data processing. *Geophysics*, *557*, 657.

Mavko, G., Mukerji, T., & Dvorkin, J. (2009). *The rock physics handbook: Tools for seismic analysis of porous media*. Cambridge university press.

McLaskey, G. C., & Glaser, S. D. (2012). Acoustic emission sensor calibration for absolute source measurements. *Journal of Nondestructive Evaluation*, *31*(2), 157–168.

Mikesell, T. D., Malcolm, A. E., Yang, D., & Haney, M. M. (2015). A comparison of methods to estimate seismic phase delays: Numerical examples for coda wave interferometry. *Geophysical Journal International*, *202*(1), 347–360.

Moczo, P., Robertsson, J. O., & Eisner, L. (2007). The finite-difference time-domain method for modeling of seismic wave propagation. *Advances in Geophysics*, *48*, 421–516.

Mordret, A., Mikesell, T. D., Harig, C., Lipovsky, B. P., & Prieto, G. A. (2016). Monitoring southwest greenlands ice sheet melt with ambient seismic noise. *Science advances*, *2*(5), e1501538.

Planès, T., & Larose, E. (2013). A review of ultrasonic coda wave interferometry in concrete. *Cement and Concrete Research*, *53*, 248–255.

Press, W. H., Flannery, B. P., Teukolsky, S. A., & Vetterling, W. T. (1986). Numerical recipes: The art of scientific computing.

Pyrak-Nolte, L. J., Myer, L. R., & Cook, N. G. (1990). Transmission of seismic waves across single natural fractures. *Journal of Geophysical Research: Solid Earth*, *95*(B6), 8617–8638.

Robinson, D., Sambridge, M., & Snieder, R. (2011). A probabilistic approach for estimating the separation between a pair of earthquakes directly from their coda waves. *Journal of Geophysical Research: Solid Earth*, *116*(B4).

Robinson, D., Snieder, R., & Sambridge, M. (2007). Using coda wave interferometry for estimating the variation in source mechanism between double couple events. *Journal of Geophysical Research: Solid Earth*, *112*(B12).

Robinson, D. J., Sambridge, M., Snieder, R., & Hauser, J. (2013). Relocating a cluster of earthquakes using a single seismic station. *Bulletin of the Seismological*

Society of America, *103*(6), 3057–3072.

Saenger, E. H., Madonna, C., Osorno, M., Uribe, D., & Steeb, H. (2014). Digital carbonate rock physics. In *Seg technical program expanded abstracts 2014* (pp. 2915–2919). Society of Exploration Geophysicists.

Sams, M., Neep, J., Worthington, M., & King, M. (1997). The measurement of velocity dispersion and frequency-dependent intrinsic attenuation in sedimentary rocks. *Geophysics*, *62*(5), 1456–1464.

Sato, H., Fehler, M. C., & Maeda, T. (2012). *Seismic wave propagation and scattering in the heterogeneous earth* (Vol. 484). Springer.

Saxena, N., & Mavko, G. (2016). Estimating elastic moduli of rocks from thin sections: Digital rock study of 3d properties from 2d images. *Computers & Geosciences*, *88*, 9–21.

Sayers, C., & Kachanov, M. (1995). Microcrack-induced elastic wave anisotropy of brittle rocks. *Journal of Geophysical Research: Solid Earth*, *100*(B3), 4149–4156.

Sell, K., Saenger, E. H., Falenty, A., Chaouachi, M., Haberthür, D., Enzmann, F., ... Kersten, M. (2016). On the path to the digital rock physics of gas hydrate-bearing sediments-processing of in situ synchrotron-tomography data. *Solid Earth*, *7*(4), 1243.

Sens-Schönfelder, C., & Wegler, U. (2006). Passive image interferometry and seasonal variations of seismic velocities at merapi volcano, indonesia. *Geophysical research letters*, *33*(21).

Snieder, R. (2002). Coda wave interferometry and the equilibration of energy in elastic media. *Physical review E*, *66*(4), 046615.

Snieder, R. (2006). The theory of coda wave interferometry. *Pure and Applied Geophysics*, *163*(2-3), 455–473.

Snieder, R., Grêt, A., Douma, H., & Scales, J. (2002). Coda wave interferometry for estimating nonlinear behavior in seismic velocity. *Science*, *295*(5563), 2253–2255.

Snieder, R., & Vrijlandt, M. (2005). Constraining the source separation with coda wave interferometry: Theory and application to earthquake doublets in the hayward fault, california. *Journal of Geophysical Research: Solid Earth*, *110*(B4).

Stork, A. L., Allmark, C., Curtis, A., Kendall, J.-M., & White, D. J. (2018). Assessing the potential to use repeated ambient noise seismic tomography to detect co 2 leaks: Application to the aquistore storage site. *International Journal of Greenhouse Gas Control*, *71*, 20–35.

Toksöz, M., Johnston, D. H., & Timur, A. (1979). Attenuation of seismic waves in dry and saturated rocks: I. laboratory measurements. *Geophysics*, *44*(4), 681–690.

Vasseur, J., Wadsworth, F. B., Heap, M. J., Main, I. G., Lavallée, Y., & Dingwell, D. B. (2017). Does an inter-flaw length control the accuracy of rupture forecasting in geological materials? *Earth and Planetary Science Letters*, *475*, 181–189.

Verwer, K., Braaksma, H., & Kenter, J. A. (2008). Acoustic properties of carbonates: Effects of rock texture and implications for fluid substitution. *Geophysics*, *73*(2), B51–B65.

Vlastos, S., Liu, E., Main, I., Schoenberg, M., Narteau, C., Li, X., & Maillot, B. (2006). Dual simulations of fluid flow and seismic wave propagation in a fractured network: effects of pore pressure on seismic signature. *Geophysical Journal International*, *166*(2), 825–838.

Vlastos, S., Liu, E., Main, I. G., & Narteau, C. (2007). Numerical simulation of wave propagation in 2-d fractured media: scattering attenuation at different stages of the growth of a fracture population. *Geophysical Journal International*, *171*(2), 865–880.

Wang, Z. (2001). Fundamentals of seismic rock physics. *Geophysics*, *66*(2), 398–412.

Zhao, Y., & Curtis, A. (2018). Relative source location using coda wave interferometry: method, code package and application to mining induced earthquakes. *Submitted to Geophysics*.

Zhao, Y., Curtis, A., & Baptie, B. (2017). Locating microseismic sources with a single seismometer channel using coda wave interferometry. *Geophysics*, *82*(3), A19–A24.